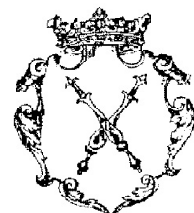


Jagiellonian University
Marian Smoluchowski Institute of Physics



**Electromagnetic processes
in few-nucleon systems
within the Chiral Perturbation Theory**

presented by

Dagmara Rozpędzik

Ph.D. Dissertation
written under the supervision of Dr. habil. Jacek Golak

Cracow 2010

*For My Darling
who has always been “the wind beneath my wings”...*

Abstract

The Chiral Effective Field Theory (ChEFT) is a modern framework to analyze properties of few-nucleon systems in the low-energy regime. It is based on the most general effective Lagrangian for pions and nucleons consistent with the chiral symmetry of QCD. For energies below the pion-production threshold it is possible to eliminate the pionic degrees of freedom and derive nuclear potentials and nuclear current operators solely in terms of nucleonic degrees of freedom. This is very important because, despite many efforts in the past, the consistence between two-nucleon forces, many-nucleon forces and corresponding current operators has not been achieved yet.

In this thesis, we consider recently derived long-range two-pion exchange (TPE) contributions to the nuclear current operator which appear at higher order chiral expansions. These operators do not contain any new free parameters. Based on ChEFT dynamical picture, we study their role in the electron and photon scattering reactions and compare chiral predictions with those obtained in the conventional framework and to the existing experimental data. The bound and scattering states are calculated with five different chiral nucleon-nucleon potentials leading to the so-called theoretical uncertainty bands for the predicted observables.

Contents

1	Introduction	1
2	Basic properties of the chiral potential	5
3	Operator structure of the nuclear electromagnetic current	11
3.1	One-body currents	13
3.2	Two-body currents	15
3.2.1	Leading order one-pion exchange currents	18
3.2.2	Two-pion exchange currents at NLO	20
3.2.3	Preliminary results for other parts of current	25
4	Formalism for selected electromagnetic two-nucleon reactions	31
4.1	Matrix elements for the two-nucleon current operator	41
5	Electron-deuteron scattering	45
5.1	Elastic electron scattering off deuteron	48
5.1.1	Kinematics	49
5.1.2	The Rosenbluth cross section	50
5.1.3	Tensor analyzing powers	54
5.1.4	The deuteron elastic form factors	56
5.1.5	Helicity asymmetry of the cross section	58
5.2	Electrodisintegration of the deuteron	61
5.2.1	Kinematics	61
5.2.2	Unpolarized exclusive cross section	63
5.2.3	Deuteron analyzing powers	64
5.2.4	Helicity asymmetry of the cross section	68
5.2.5	Outgoing nucleon polarization	69
5.2.6	Inclusive cross section	70
6	Deuteron photodisintegration and radiative capture reactions	73
6.1	Deuteron photodisintegration	73
6.1.1	Kinematics	74
6.1.2	Exclusive cross section	75
6.1.3	Photon analyzing power	76
6.1.4	Outgoing nucleon polarization	79

6.1.5	Deuteron tensor analyzing powers	79
6.1.6	Total cross section	82
6.2	Neutron-proton capture reaction	83
6.2.1	Kinematics	84
6.2.2	Inclusive cross section	86
6.2.3	Nucleon analyzing powers	87
7	Formalism for three-nucleon reactions	89
8	Electron scattering of ${}^3\text{He}$	101
8.1	Elastic electron scattering	102
8.2	Electrodisintegration of ${}^3\text{He}$	102
9	Photodisintegration of ${}^3\text{He}$	111
10	Summary and conclusions	117
A	Schrödinger equation for the deuteron	121
B	Numerical solutions of the Lippmann-Schwinger equation	127
C	Symbolic algebra calculation of the nuclear matrix elements	139
D	Low energy constants C'_1 and d_9 – estimation procedure	145

Chapter 1

Introduction

Chiral Effective Field Theory (ChEFT) provides a systematic and model-independent framework to analyze various low-energy hadronic processes in agreement with the spontaneously broken approximate chiral symmetry of Quantum Chromodynamics (QCD). It is a very powerful tool at low energy where the perturbative expansion of QCD in powers of the coupling constant cannot be applied. Starting from the most general effective Lagrangian for Goldstone bosons (pions in the two-flavor case of u and d quarks) and matter fields (nucleons and recently also Δ) consistent with the symmetries of QCD, the hadronic S-matrix elements are obtained via a simultaneous expansion in the low external momenta and quark masses.

This perturbative scheme works well in the pion-pion and pion-nucleon domains where, in the chiral limit, the interaction becomes very small at vanishing external momenta. In the case of few interacting nucleons one has to deal with non-perturbative problems. Indeed, perturbation theory is expected to fail already at low energy due to the presence of the shallow few-nucleon bound states. A suitable non-perturbative approach was proposed by Weinberg [1], who showed that the strong enhancement of the few-nucleon scattering amplitude arises from purely nucleonic intermediate states. Weinberg suggested to apply ChEFT to the kernel of the corresponding scattering equation, which can be understood as an effective nuclear potential. Power counting is a crucial ingredient of any effective field theory which allows to organize various contributions to the scattering amplitude according to their relevance. Traditionally, chiral power counting is formulated in terms of topological quantities such as the number of loops and, in the few-nucleon sector, the number of participating nucleons and disconnected pieces [1, 2, 3]. The expansion parameter is given by Q/Λ , where Q is the so-called soft scale associated with the pion mass M_π and/or typical external momenta involved in the process, and Λ is the so-called hard scale of the order of the nucleon mass. For a given connected irreducible diagram with N nucleons, L pion loops and V_i vertices of type i , the parameter ν , which determines its importance can be obtained as

$$\nu = -4 + 2N + 2L + \sum_i V_i \Delta_i, \quad \Delta_i = d_i + \frac{1}{2} n_i - 2, \quad (1.1)$$

where n_i is the number of nucleon field operators and d_i the number of derivatives and/or insertions of M_π . The spontaneously broken chiral symmetry of QCD guarantees that $\Delta_i \geq 0$. Consequently, the chiral parameter ν is bounded from below and a finite number of diagrams contributes at a given order. It is very important that this scheme explains the dominant role of two-nucleon interactions in the nuclear Hamiltonian (they appear at $\nu = 0$) and, more generally, the so-called hierarchy of nuclear forces.

No wonder then that Weinberg's idea has been explored in the last two decades by many authors. Ordóñez and co-workers derived a nucleon–nucleon (NN) potential up to next-to-next-to-leading order (N2LO) in the chiral expansion and performed a numerical analysis of the two-nucleon (2N) system [4]. The explicit energy dependence of the effective potential derived in [4] led, however, to difficulties in applications to $> 2N$ systems but could be eliminated by different techniques. The corresponding energy-independent expressions for the NN potential were first given in Ref. [5] and later in Refs [6, 7] using different methods. They served as a basis for the N2LO analyses of the 2N system [8, 9], see also [10] for related application, as well as three nucleon (3N) and four nucleon (4N) systems [11, 12] including the corresponding 3N forces.

Chiral 3N forces start to contribute at N2LO and are given by two-pion exchange (TPE), one-pion exchange (OPE) and 3N contact interaction itself. In turn, chiral 4N forces come only at N3LO [13], which confirms the so-called hierarchy of the nuclear forces. The strength of ChEFT is that it provides a framework to derive the few-nucleon forces in a systematic way, fully consistent with the 2N forces.

In order to arrive at effective nuclear forces (and later also at effective nuclear current operators), the pion degrees of freedom have to be eliminated. In the modern framework of ChEFT, the most frequently used methods are time-ordered perturbation theory, S-matrix and the unitary transformation. Only the S-matrix and the unitary transformation methods lead to energy-independent interactions [14]. The energy independence of the potential is a crucial feature which enables applications to three- and more-nucleon systems. In the S-matrix scheme, the nuclear potential is defined through matching the scattering amplitude to the iterated Lippmann-Schwinger equation. In the unitary transformation approach, the potential is obtained by applying an appropriately chosen unitary transformation to the underlying pion-nucleon Hamiltonian which eliminates the coupling between the purely nucleonic Fock space states and the ones which contain pions.

Not only the nuclear forces but also exchange vector and axial currents in nuclei have been studied in the framework of ChEFT. Park, Min and Rho applied heavy-baryon chiral perturbation theory to derive exchange axial [15] and vector [16] currents at the one-loop level for small values of the photon momentum. These calculations were carried out employing time-ordered perturbation theory to extract non-iterative contributions to the amplitude. The derived exchange vector currents were applied within a hybrid approach to analyze observables in radiative capture of thermal neutrons on light nuclei [16, 17, 18, 19, 20] and other reactions of astrophysical interest [21, 22, 23, 24, 25]. Deuteron electromagnetic properties [26, 27, 28, 29, 30], Compton

scattering on the deuteron [31, 32] and on ^3He [33] as well as pion electro- and photo-production and the corresponding capture reactions [34, 35, 36, 37, 38, 39] have also been studied in the framework of ChEFT.

The leading two-nucleon contributions to the exchange current arise from one-pion exchange and are well known. However, the corrections at the one-loop level have not yet been completely worked out. An important step in this direction was made by Pastore et al. [40, 41] who considered the electromagnetic two-body current density at the leading one-loop order based on time-ordered perturbation theory.

In the recent work, Kölling et al. [42] calculated the leading two-pion exchange two-nucleon four-current operator based on the same method of unitary transformation which had been used in Refs [7, 8, 9, 43, 13] to derive nuclear forces. This guarantees for the first time consistence between the forces and current operators. This work provided also completely new results for the exchange charge density. It is also very important that the authors evaluated analytically all loop integrals to obtain a representation in momentum space which can be easily treated numerically.

In this thesis we apply the forces and currents derived using the method of unitary transformation to various electromagnetic processes in the 2N system, and to some extent, also in the 3N system. By using this method, the effective potential and current are hermitian operators which are independent of energy. The approach presented in the method of unitary transformation is quite different from that used in the old-fashioned time-ordered perturbation theory, where the resulting potential explicitly depends on energy, which makes it difficult (if not impossible) to make the calculations for few nucleon systems.

The primary objective of this thesis is to investigate the long-range two-pion exchange (TPE) contribution to the nuclear current operator. Expressions for TPE current operators are parameters free. We study for the first time effects of the leading TPE exchange currents [42] and some other parts of the 2N current operator of Kölling et al. [44]. We compare our predictions for various observables obtained with the consistent ingredients from ChEFT to the more conventional results based on the AV18 potential [45] and related exchange currents [46, 47, 48]. We present also the very first results based on the new pieces of the current operator corresponding to the OPE loop corrections at NLO, relativistic corrections and short-range parts from [44]. The new pieces of the current operator contain unknown parameters, which must be fitted to the experimental data.

The thesis is organized as follows. The operator structure of the potential and the current operator are described in Chapters 2 and Chapter 3, respectively. They are used in our formalism for the electromagnetic reactions with two- and three-nucleon system, as generally described in Chapters 4 and 7. Then Chapter 5 deals specifically with elastic and inelastic electron-deuteron scattering. We study the effects induced by different parts of the current operator not only in the cross sections but also in various polarization observables. In Chapter 6 we describe the deuteron photodisintegration and (closely related by time-reversal symmetry) neutron-proton radiative capture reactions. In both cases we show many results for different observables and compare our predictions to the recent experimental data.

The formalism for selected reactions with 3N systems is briefly given in Chapter 8. Next, in Chapter 9, this formalism is applied to electrodisintegration and photodisintegration of ${}^3\text{He}$. We consider reactions with two and three nuclear fragments in the final state and again show examples for several observables. Finally, we summarize in Chapter 10.

This thesis has four appendices. The first one describes how we solve the Schrödinger equation for the deuteron. The second appendix deals with the numerical solution of the Lippmann-Schwinger equation for the two-nucleon half-shell T -matrix. An exemplary *Mathematica* ©[49] script used in our new method of partial wave decomposition is introduced in Appendix C. Finally, in Appendix D, we describe the estimation procedure necessary to fix two unknown parameters in the current operator.

Chapter 2

Basic properties of the chiral potential

The chiral nucleon-nucleon (NN) potential can be cast in the general form

$$V = V_{\text{pion}} + V_{\text{cont}}, \quad (2.1)$$

where V_{pion} denotes the long-range terms associated with the one-pion-exchange (ope), two-pion-exchange (tpe) and more-pion-exchange contributions

$$V_{\text{pion}} = V_{\text{ope}} + V_{\text{tpe}} + \dots \quad (2.2)$$

and V_{cont} corresponds to the short-range part represented by NN contact interactions. In this thesis, we restricted ourselves to the forces obtained at next-to-leading order (NLO) and next-to-next-to-leading order (N2LO) of the chiral expansion by E. Epelbaum *et al.* (c.f.[50] and references therein.) The NN potential has been obtained even at next-to-next-to-next-to-leading order (N3LO) [51] but the current operator we have at our disposal [42, 44] would be highly inconsistent with such a potential.

We will now give the reader only very basic information about the NN potentials at the different orders of chiral expansion and refer to [50] for the details of the derivation. At the leading order (LO), as shown schematically in Figure 2.1, the NN force comprises the well known one-pion exchange potential and a contact part with two low-energy constants (LEC):

$$V_{\text{ope}}^{(0)} = - \left(\frac{g_A}{2F_\pi} \right)^2 \tau_1 \cdot \tau_2 \frac{\vec{\sigma}_1 \cdot \vec{q} \vec{\sigma}_2 \cdot \vec{q}}{q^2 + M_\pi^2}, \quad (2.3)$$

$$V_{\text{cont}}^{(0)} = C_S + C_T \vec{\sigma}_1 \cdot \vec{\sigma}_2, \quad (2.4)$$

where \vec{p} and \vec{p}' are the initial and final relative momenta of the two nucleons, $\vec{q} \equiv \vec{p}' - \vec{p}$ and $\vec{\sigma}_i(\vec{\tau}_i)$ denote the Pauli spin (isospin) matrices acting in the space of nucleon i . Further, $F_\pi = 92.4$ MeV and g_A are the pion-decay constant and the nucleon axial coupling constant, respectively. Finally, $M_\pi = 138.57$ MeV is the (average) pion mass. The low-energy constants C_S and C_T determine the strength of the leading NN short-range interaction and have to be obtained from the experimental data. Note that (2.3) and similar expressions defining the potentials should be understood as matrix elements in the momentum space and operators in the spin-isospin space.

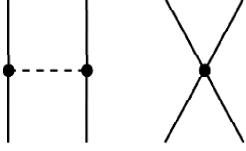


Figure 2.1: The LO structure of the NN force. Solid and dashed lines are nucleons and pions, respectively.

At the next-to-leading order (NLO) a renormalization of the low energy constants is required and the contribution from the Goldberger-Treiman discrepancy leads to a modified value of $g_A = 1.29$ [50]. The remaining contributions to the NN potential at this order (see Figure 2.2) come from two-pion exchanges and contact interactions of a new type. The leading TPE part is given by

$$\begin{aligned} V_{tpe}^{(2)} = & - \frac{\tau_1 \cdot \tau_2}{384\pi^2 F_\pi^4} L^{\tilde{\Lambda}}(q) \left(4M_\pi^2(5g_A^4 - 4g_A^2 - 1) + q^2(23g_A^4 - 10g_A^2 - 1) + \frac{48g_A^4 M_\pi^4}{4M_\pi^2 + q^2} \right) \\ & - \frac{3g_A^4}{64\pi^2 F_\pi^4} L^{\tilde{\Lambda}}(q) (\vec{\sigma}_1 \cdot \vec{q} \vec{\sigma}_2 \cdot \vec{q} - q^2 \vec{\sigma}_1 \cdot \vec{\sigma}_2) , \end{aligned} \quad (2.5)$$

where $q \equiv |\vec{q}|$ and the cut-off regularized loop function $L^{\tilde{\Lambda}}(q)$,

$$L^{\tilde{\Lambda}}(q) = \theta(\tilde{\Lambda} - 2M_\pi^2) \frac{\omega}{2q} \ln \frac{\tilde{\Lambda}^2 \omega^2 + q^2 s^2 + 2\tilde{\Lambda} q \omega s}{4M_\pi^2(\tilde{\Lambda}^2 + q^2)}, \quad (2.6)$$

is defined with a help of the step function $\theta(x)$ and the following abbreviations:

$$\begin{aligned} \omega &= \sqrt{q^2 + 4M_\pi^2}, \\ s &= \sqrt{\tilde{\Lambda}^2 - 4M_\pi^2}. \end{aligned} \quad (2.7)$$

Here, $\tilde{\Lambda}$ denotes the ultraviolet cutoff in the mass spectrum of the two-pion-exchange potential. The new short-range contact terms at this order are [50]

$$\begin{aligned} V_{cont}^{(2)} = & C_1 \vec{q}^2 + C_2 \vec{k}^2 + (C_3 \vec{q}^2 + C_4 \vec{k}^2)(\vec{\sigma}_1 \cdot \vec{\sigma}_2) + iC_5 \frac{1}{2} (\vec{\sigma}_1 + \vec{\sigma}_2) \cdot (\vec{q} \times \vec{k}) \\ & + C_6 (\vec{q} \cdot \vec{\sigma}_1)(\vec{q} \cdot \vec{\sigma}_2) + C_7 (\vec{k} \cdot \vec{\sigma}_1)(\vec{k} \cdot \vec{\sigma}_2), \end{aligned} \quad (2.8)$$

where $\vec{k} = \frac{1}{2}(\vec{p}' + \vec{p})$. The LECs C_T, C_S and C_1, \dots, C_7 are fixed from a fit to the nucleon-proton scattering phase shifts and mixing parameters for the laboratory energies below 100 MeV.

The contributions at next-to-next-to-leading order (N2LO) lead first of all to the renormalization and/or redefinition of the LECs $C_S, C_T, C_1, \dots, C_7$. Secondly, we

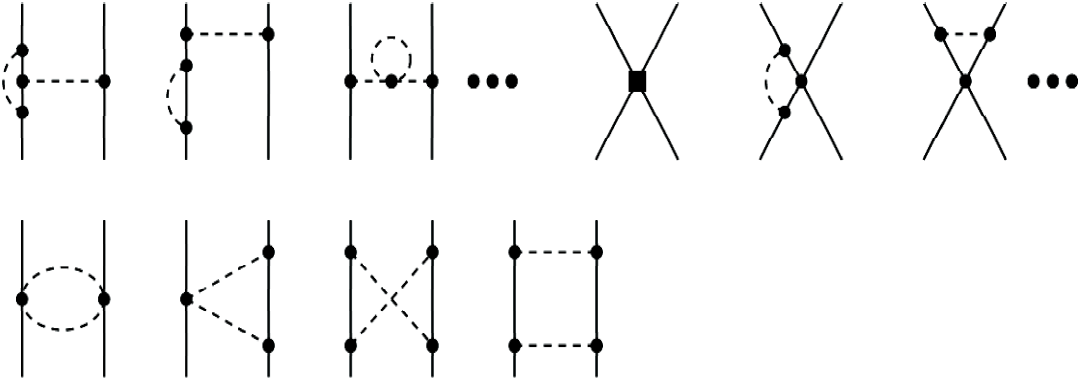


Figure 2.2: The NLO structure of the NN force. Solid dots and squares denote vertices with $\Delta_i = 0, 2$, respectively.

encounter a new momentum dependence due to the following terms:

$$\begin{aligned}
 V_{tpe}^{(3)} &= -\frac{3g_A^2}{16\pi F_\pi^4} \\
 &\quad \left\{ -\frac{g_A^2 M_\pi^5}{16M_N(4M_\pi^2 + q^2)} + \left(2M_\pi^2(2c_1 - c_3) - q^2 \left(c_3 + \frac{3g_A^2}{16M_N} \right) \right) (2M_\pi^2 + q^2) A^{\tilde{\Lambda}}(q) \right\} \\
 &- \frac{g_A^2}{128\pi M_N F_\pi^4} (\boldsymbol{\tau}_1 \cdot \boldsymbol{\tau}_2) \\
 &\quad \left\{ -\frac{3g_A^2 M_\pi^5}{4M_\pi^2 + q^2} + (4M_\pi^2 + 2q^2 - g_A^2(4M_\pi^2 + 3q^2)) (2M_\pi^2 + q^2) A^{\tilde{\Lambda}}(q) \right\} \\
 &+ \frac{9g_A^4}{512\pi M_N F_\pi^4} \left((\vec{\sigma}_1 \cdot \vec{q})(\vec{\sigma}_2 \cdot \vec{q}) - q^2(\vec{\sigma}_1 \cdot \vec{\sigma}_2) \right) (2M_\pi^2 + q^2) A^{\tilde{\Lambda}}(q) \\
 &- \frac{g_A^2}{32\pi F_\pi^4} (\boldsymbol{\tau}_1 \cdot \boldsymbol{\tau}_2) \left((\vec{\sigma}_1 \cdot \vec{q})(\vec{\sigma}_2 \cdot \vec{q}) - q^2(\vec{\sigma}_1 \cdot \vec{\sigma}_2) \right) \\
 &\quad \times \left\{ \left(c_4 + \frac{1}{4M_N} \right) (4M_\pi^2 + q^2) - \frac{g_A^2}{8M_N} (10M_\pi^2 + 3q^2) \right\} A^{\tilde{\Lambda}}(q) \\
 &- \frac{3g_A^4}{64\pi M_N F_\pi^4} i(\vec{\sigma}_1 + \vec{\sigma}_2) \cdot (\vec{p}' \times \vec{p}) (2M_\pi^2 + q^2) A^{\tilde{\Lambda}}(q) \\
 &- \frac{g_A^2(1 - g_A^2)}{64\pi M_N F_\pi^4} (\boldsymbol{\tau}_1 \cdot \boldsymbol{\tau}_2) i(\vec{\sigma}_1 + \vec{\sigma}_2) \cdot (\vec{p}' \times \vec{p}) (4M_\pi^2 + q^2) A^{\tilde{\Lambda}}(q), \tag{2.9}
 \end{aligned}$$

where M_N in the nucleon mass and

$$A^{\tilde{\Lambda}}(q) = \theta(\tilde{\Lambda} - 2M_\pi) \frac{1}{2q} \arctan \frac{q(\tilde{\Lambda} - 2M_\pi)}{q^2 + 2\tilde{\Lambda}M_\pi}. \tag{2.10}$$

Although in this expression new LECs appear, c_1 , c_3 , c_4 , they are already known from πN scattering. Following [50], we use: $c_1 = -0.81 \text{ GeV}^{-1}$, $c_3 = -3.4 \text{ GeV}^{-1}$,

Table 2.1: Ranges of the LECs corresponding to the cut-off parameters $(\Lambda, \tilde{\Lambda})$ from Table 2.2 obtained from fits to the neutron-proton phase shift parameters up to laboratory energies of 100 MeV. The values C_S and C_T are given in GeV^{-2} and the other values in GeV^{-4} .

V-CUT	C_S	C_T	C_1	C_2	C_3	C_4	C_5	C_6	C_7
NLO-1	-139.346	-4.844	155.226	11.436	-138.929	-594.815	-534.069	87.642	-1065.242
NLO-2	-100.977	-17.300	147.246	282.745	-233.231	-839.756	-477.219	130.024	-1038.657
NLO-3	-106.667	-11.597	118.980	167.898	-234.305	-847.827	-476.715	142.438	-1025.798
NLO-4	-139.219	-4.845	119.563	-120.311	-167.749	-708.079	-543.216	113.123	-1048.608
NLO-5	-109.681	-8.419	103.202	104.254	-233.819	-849.293	-476.938	149.132	-1018.453
N2LO-1	-132.407	-3.386	449.616	668.296	-84.3236	-561.362	-577.698	27.865	-1516.096
N2LO-2	-102.493	-5.461	376.731	759.802	-146.175	-665.533	-698.465	75.941	-1501.418
N2LO-3	-117.259	0.662	443.401	806.555	-103.432	-659.295	-715.454	24.638	-1481.817
N2LO-4	-133.960	-3.980	572.018	960.757	-72.241	-625.106	-662.657	-3.182	-1674.360
N2LO-5	-112.932	2.602	385.633	1343.493	-121.543	-614.322	-1269.039	-26.488	-1385.119

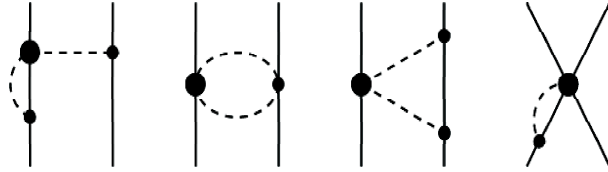


Figure 2.3: Diagrammatic representation of the N2LO corrections to the NN potential. Filled circles denotes vertices with $\Delta_i = 1$.

$c_4 = 3.4 \text{ GeV}^{-1}$. So both at NLO and at N2LO we are left with a relatively small number (nine) of unknown parameters. The potential we consider either at NLO or at N2LO still requires regularization when inserted into the Lippmann-Schwinger equation, which is achieved by introducing a regulated potential $V_{reg}(\vec{p}', \vec{p})$ of the form

$$V_{reg}(\vec{p}', \vec{p}) \equiv f_{reg}(\vec{p}') V(\vec{p}', \vec{p}) f_{reg}(\vec{p}), \quad (2.11)$$

where f_{reg} is a regulator function which dumps the potential at higher momenta. We perform the regularization using the exponential regulator function

$$f_{reg}(\vec{p}) = \exp\left(-\frac{p^4}{\Lambda^4}\right). \quad (2.12)$$

Due to a different form of the Schrödinger and Lippmann–Schwinger equations used by E. Epelbaum and collaborators, the regulated potential has to be multiplied by the factor of $\frac{1}{(2\pi)^3}$.)

Finally, it should be clear that at the given order of the chiral expansion we do not have unique predictions and instead of one chiral potential, we use several (five) potentials with different parameters in order to account for the theoretical uncertainty.

In practice, for a given $(\Lambda, \tilde{\Lambda})$ pair, the set of nine parameters is obtained from a fit to NN scattering data [43]. The $(\Lambda, \tilde{\Lambda})$ pairs and the corresponding parameters of the five NLO and five N2LO potentials we use in this thesis are given in Table 2.2.

Table 2.2: The NLO and N2LO cut-off values [52]. The cut-off values vary between 500 and 700 MeV for Λ and between 450 and 600 MeV for $\tilde{\Lambda}$. For these choices we followed Ref. [43].

V-CUT	Λ [MeV]	$\tilde{\Lambda}$ [MeV]	V-CUT	Λ [MeV]	$\tilde{\Lambda}$ [MeV]
NLO-1	400	500	N2LO-1	450	500
NLO-2	550	500	N2LO-2	600	500
NLO-3	550	600	N2LO-3	550	600
NLO-4	400	700	N2LO-4	450	700
NLO-5	550	700	N2LO-5	600	700

Chapter 3

Operator structure of the nuclear electromagnetic current

The effective electromagnetic current operator of the two-nucleon system contains, in general, one-body and two-body terms

$$J^\mu(x) = J_1^\mu(x) + J_2^\mu(x) + J_{12}^\mu(x). \quad (3.1)$$

The single nucleon current operator, $J_1^\mu(x) + J_2^\mu(x)$, is the sum of independent contributions from nucleons 1 and 2. The two-body term $J_{12}^\mu(x)$ acts on the degrees of freedom of both nucleons and consists of the meson exchange (mec) and contact (cont) parts

$$J_{12}^\mu(x) = J_{mec}^\mu(x) + J_{cont}^\mu(x), \quad (3.2)$$

where, in turn, $J_{mec}^\mu(x)$ comprises contributions from the exchange of different numbers of pions

$$J_{mec}^\mu(x) = J_{ope}^\mu(x) + J_{tpe}^\mu(x) + \dots \quad (3.3)$$

In this thesis, we consider only NLO contributions to the 2N chiral current operator so, in Equation (3.3), we will encounter one-pion exchange (OPE) parts ($J_{ope}^\mu(x)$) and two-pion exchange (TPE) contributions ($J_{tpe}^\mu(x)$). The contribution from the exchange of bigger number of pions appears at higher order of the chiral expansion.

The one-pion exchange charge density operator consists of two parts [44]

$$J_{ope}^0(x) = J_{rel}^0(x) + J_{nope}^0(x), \quad (3.4)$$

where $J_{rel}^0(x)$ are relativistic corrections and $J_{nope}^0(x)$ stand for new contributions arising only at NLO. In the vector part we have

$$\vec{J}_{ope}(x) = \vec{J}_{lope}(x) + \vec{J}_{nlope}(x), \quad (3.5)$$

where $\vec{J}_{lope}(x)$ are well known leading one-pion-exchange terms and $\vec{J}_{nlope}(x)$ are additional contributions, which appear at NLO.

Short-range terms J_{sr}^0 in the two-nucleon charge density operator are one-loop currents involving the LECs, C_S and C_T [44]

$$J_{sr}^0(x) = J_{opext}^0(x). \quad (3.6)$$

In the vector \vec{J}_{sr} we find contributions of two types,

$$\vec{J}_{sr}(x) = \vec{J}_{cont}(x) + \vec{J}_{opect}(x), \quad (3.7)$$

where $\vec{J}_{cont}(x)$ are tree short-range current operators comprising known and also unknown parameters and $\vec{J}_{opect}(x)$ stem from a short-range loop graphs corrections from one-pion-exchange [44]. All the contributions to the 2N current operator mentioned in this subsection will be discussed in detail in the following subsections.

The two-nucleon current operator should be derived consistently with the chiral potential. The basic requirement is that the continuity equation must be fulfilled

$$\vec{\nabla} \cdot \vec{J}(x) = -\frac{\partial \rho}{\partial t} = -i[H, \rho] \equiv -i[H_0 + V, \rho], \quad (3.8)$$

where $\rho = \rho(x) \equiv J^0(x)$ is the charge density. The presence of the two-body interaction V in the Hamiltonian H generates, due to momentum and isospin dependent terms in V , two-body contributions in the electromagnetic current operator. The continuity equation provides a powerful check for the theoretical models of the forces and currents. In this thesis, due to the lack of contact terms in the current operator, the continuity equation is fulfilled with respect to the corresponding one-pion, two-pion parts and short-range parts at NLO, provided all the terms from [44] are taken into account.

In fact, we would like to require even more from the matrix elements of the nuclear current operator, namely the so-called gauge independence, which reads

$$q_\mu \langle f | J^\mu(0) | i \rangle = 0, \quad (3.9)$$

where q_μ is the four-momentum transfer and $|i\rangle$ ($|f\rangle$) is the general initial (final) nuclear state. The electromagnetic current operator is taken at $x = 0$. As it is well known (see for example [53, 54]), Equation (3.9) holds if the continuity is fulfilled and the nuclear states $|i\rangle$ and $|f\rangle$ are exact eigenstates of the full Hamiltonian, H .

Throughout this thesis we work in momentum space. Since the current operators depend on the spin and isospin degrees of freedom, many expressions that appear in next sub-sections should be understood as matrix elements in the momentum space and operators in the spin-isospin space, exactly like for the NN potentials.

3.1 One-body currents

In the Hamiltonian formalism the nucleons are on the mass shell. The standard single nucleon current at space-time point zero $J_1^\mu(0)$ calculated between the nucleon initial $p \equiv (p_0 = \sqrt{M_N^2 + \vec{p}^2}, \vec{p})$ and final $p' \equiv (p_0' = \sqrt{M_N^2 + \vec{p}'^2}, \vec{p}')$ four momenta is

$$\begin{aligned} \left\langle \vec{p}' \left| \frac{1}{e} J_1^\mu(0) \right| \vec{p} \right\rangle &= \bar{u}(\vec{p}') s' (\gamma^\mu F_1 + i\sigma^{\mu\nu}(p' - p)_\nu F_2) u(\vec{p}s) \\ &= \bar{u}(\vec{p}') s' (G_M \gamma^\mu - F_2(p' + p)^\mu) u(\vec{p}s). \end{aligned} \quad (3.10)$$

Here u are Dirac spinors, $F_1((p' - p)^2)$ and $F_2((p' - p)^2)$ the Dirac and Pauli nucleon form factors and $G_M \equiv F_1 + 2M_N F_2$ the magnetic form factor of the nucleon. (We extract the proton charge e from the matrix element.) In this thesis we adopt only the nonrelativistic limit of Equation (3.10) which leads to well known expressions for the nucleon charge density operator as well as the convection and spin current operators

$$\begin{aligned} \left\langle \vec{p}' \left| \frac{1}{e} J_1^0(0) \right| \vec{p} \right\rangle &= G_E, \\ \left\langle \vec{p}' \left| \frac{1}{e} \vec{J}_1(0) \right| \vec{p} \right\rangle &= G_E \frac{\vec{p} + \vec{p}'}{2M_N} + \frac{i}{2M_N} G_M \vec{\sigma} \times (\vec{p}' - \vec{p}), \\ &\equiv \left\langle \vec{p}' \left| \frac{1}{e} \vec{J}_1^{conv}(0) \right| \vec{p} \right\rangle + \left\langle \vec{p}' \left| \frac{1}{e} \vec{J}_1^{spin}(0) \right| \vec{p} \right\rangle, \end{aligned} \quad (3.11)$$

where $G_E \equiv F_1 + \frac{(p' - p)^2}{2M_N} F_2$ is the electric form factor. The neutron (n) and proton (p) form factors G_E and G_M , are normalized as

$$\begin{aligned} G_E^n(0) &= 0 \\ G_E^p(0) &= 1 \\ G_M^n(0) &= -1.913 \\ G_M^p(0) &= 2.793 \end{aligned} \quad (3.12)$$

and these values correspond to point-like nucleons. All the form factors depend on the four momentum transfer squared $(p' - p)^2$, but in the nonrelativistic regime usually this argument is replaced by the three momentum transfer squared, $-(\vec{p}' - \vec{p})^2$, or is even set to zero for interactions with real photons. The properties of the electromagnetic nucleon form factors have been studied both theoretically and experimentally by many authors, see for example [55, 56, 57, 58].

As already mentioned, expressions given in Equation (3.11) are matrix elements in the momentum space and operators in the spin space. Treating nucleons as identical particles, it is convenient to introduce the isospin projection operators for the proton (Π^p) and for the neutron (Π^n):

$$\begin{aligned} \Pi^p &\equiv \frac{1}{2} \left(1 + (\tau)_3 \right), \\ \Pi^n &\equiv \frac{1}{2} \left(1 - (\tau)_3 \right). \end{aligned} \quad (3.13)$$

where τ_3 is the third cartesian component of the isospin operator. This leads to a modification of Equation (3.11)

$$\begin{aligned} \left\langle \vec{p}' \left| \frac{1}{e} J_1^0(0) \right| \vec{p} \right\rangle &= (G_E^p \Pi^p + G_E^n \Pi^n), \\ \left\langle \vec{p}' \left| \frac{1}{e} \vec{J}_1(0) \right| \vec{p} \right\rangle &= \frac{\vec{p} + \vec{p}'}{2M_N} (G_E^p \Pi^p + G_E^n \Pi^n) + \frac{i}{2M_N} (G_M^p \Pi^p + G_M^n \Pi^n) \vec{\sigma} \times (\vec{p}' - \vec{p}). \end{aligned} \quad (3.14)$$

For two nucleons (see Figure 3.1) the single-nucleon current operator consists of two

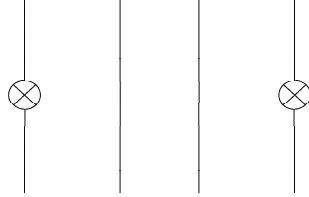


Figure 3.1: Total single nucleon current is the sum of the current of nucleon 1 (J_1^μ) and the current of nucleon 2 (J_2^μ). Crosses in circles denote photon coupling to either of the two nucleons.

parts and the corresponding matrix elements in the two-nucleon space are given as

$$\begin{aligned} \langle \vec{p}_1' \vec{p}_2' | J_{single}^\mu(0) | \vec{p}_1 \vec{p}_2 \rangle &\equiv \langle \vec{p}_1' \vec{p}_2' | J_1^\mu(0) + J_2^\mu(0) | \vec{p}_1 \vec{p}_2 \rangle \\ &= \delta(\vec{p}_2' - \vec{p}_2) \langle \vec{p}_1' | J_1^\mu(0) | \vec{p}_1 \rangle + \delta(\vec{p}_1' - \vec{p}_1) \langle \vec{p}_2' | J_2^\mu(0) | \vec{p}_2 \rangle. \end{aligned} \quad (3.15)$$

In the following we will consider matrix elements of the current operator between the two-nucleon initial (subscript i) and final (subscript f) states which are characterized by an internal state $|\Psi\rangle$ and total momentum, \vec{P} . Since the internal states are assumed to be antisymmetric with respect to the exchange of nucleons 1 and 2, it is sufficient to consider only the contribution from one of the particles, here from nucleon 2 as shown in Figure 3.2:

$$\langle \Psi_f \vec{P}_f | J_1^\mu(0) + J_2^\mu(0) | \Psi_i \vec{P}_i \rangle = 2 \langle \Psi_f \vec{P}_f | J_2^\mu(0) | \Psi_i \vec{P}_i \rangle. \quad (3.16)$$

In the nonrelativistic approximation we have additionally the following factorization

$$\langle \vec{p}_1 \vec{p}_2 | \Psi_i \vec{P} \rangle = \langle \vec{p} | \Psi_i \rangle \delta(\vec{p}_1 + \vec{p}_2 - \vec{P}), \quad (3.17)$$

where $\vec{p} \equiv \frac{1}{2}(\vec{p}_1 - \vec{p}_2)$ is the relative momentum of the two nucleons. Given that, we can obtain the following result for the general matrix element of the single-nucleon current

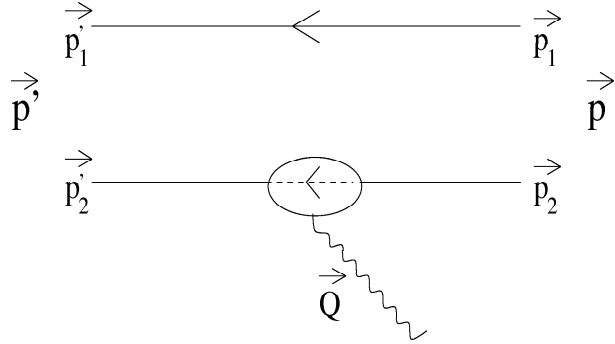


Figure 3.2: General single current diagram for $J_2^\mu(x = 0)$.

operator between the two-nucleon states

$$\begin{aligned} \left\langle \Psi_f \vec{P}_f \left| \frac{1}{e} \left(J_1^0(0) + J_2^0(0) \right) \right| \Psi_i \vec{P}_i \right\rangle = \\ 2 \int d\vec{p} \langle \Psi_f | \vec{p} \rangle (G_E^p \Pi^p + G_E^n \Pi^n) \left\langle \vec{p} + \frac{1}{2} \vec{Q} \middle| \Psi_i \right\rangle, \end{aligned} \quad (3.18)$$

$$\begin{aligned} \left\langle \Psi_f \vec{P}_f \left| \frac{1}{e} \left(\vec{J}_1^{conv}(0) + \vec{J}_2^{conv}(0) \right) \right| \Psi_i \vec{P}_i \right\rangle = \\ 2 \int d\vec{p} \langle \Psi_f | \vec{p} \rangle (G_E^p \Pi^p + G_E^n \Pi^n) \left(\frac{-\vec{p}}{M_N} \right) \left\langle \vec{p} + \frac{1}{2} \vec{Q} \middle| \Psi_i \right\rangle \\ + 2 \left(\frac{\vec{P}_i}{2M_N} \right) \int d\vec{p} \langle \Psi_f | \vec{p} \rangle (G_E^p \Pi^p + G_E^n \Pi^n) \left\langle \vec{p} + \frac{1}{2} \vec{Q} \middle| \Psi_i \right\rangle, \end{aligned} \quad (3.19)$$

$$\begin{aligned} \left\langle \Psi_f \vec{P}_f \left| \frac{1}{e} \left(\vec{J}_1^{spin}(0) + \vec{J}_2^{spin}(0) \right) \right| \Psi_i \vec{P}_i \right\rangle = \\ 2 \int d\vec{p} \langle \Psi_f | \vec{p} \rangle (G_M^p \Pi^p + G_M^n \Pi^n) \left(\frac{i\vec{\sigma}_2 \times \vec{Q}}{2M_N} \right) \left\langle \vec{p} + \frac{1}{2} \vec{Q} \middle| \Psi_i \right\rangle, \end{aligned} \quad (3.20)$$

where $\vec{Q} \equiv \vec{P}_f - \vec{P}_i$. Note that the second term in Equation (3.19) is zero in the laboratory frame, where the initial total momentum $\vec{P}_i = 0$.

3.2 Two-body currents

The corresponding matrix elements of the two-body current at space-time point $x = 0$, $J_{12}^\mu(0)$, do not contain any δ -function and can be written as

$$\left\langle \vec{p}_1' \vec{p}_2' \left| \frac{1}{e} J_{12}^\mu(0) \right| \vec{p}_1 \vec{p}_2 \right\rangle = J^\mu(\vec{q}_1, \vec{q}_2) \quad (3.21)$$

where, as explained in Figure 3.3, \vec{p}_1, \vec{p}_2 (\vec{p}'_1, \vec{p}'_2) are individual momenta of the two nucleons in the initial (final) state. The two vectors \vec{q}_1 and \vec{q}_2 are fractional momentum transfers, defined as

$$\vec{q}_1 = \vec{p}'_1 - \vec{p}_1 \quad (3.22)$$

$$\vec{q}_2 = \vec{p}'_2 - \vec{p}_2. \quad (3.23)$$

They can be written in terms of the relative momenta in the initial (\vec{p}) and final state (\vec{p}')

$$\vec{q}_1 = \vec{p}' - \vec{p} + \frac{1}{2}\vec{Q}, \quad (3.24)$$

$$\vec{q}_2 = \vec{p} - \vec{p}' + \frac{1}{2}\vec{Q}, \quad (3.25)$$

where

$$\vec{Q} \equiv \vec{p}'_1 + \vec{p}'_2 - \vec{p}_1 - \vec{p}_2 = \vec{q}_1 + \vec{q}_2. \quad (3.26)$$

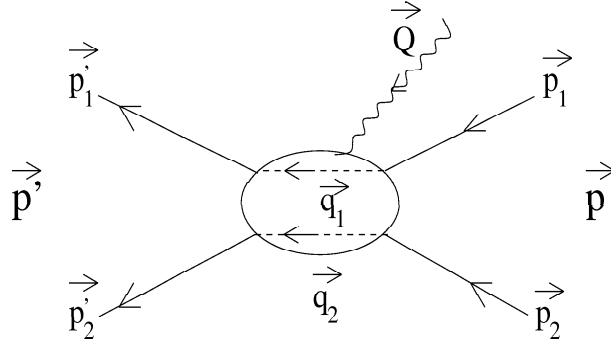


Figure 3.3: Diagram for the current operator of nucleon 2 J_2^μ in the 2N space. The quantum numbers of nucleon 1 are not affected.

The most general form of the two-nucleon current operator is [59], [42]

$$\vec{J}(\vec{q}_1, \vec{q}_2) = \sum_{i=1}^5 \sum_{j=1}^{24} f_i^j(\vec{q}_1, \vec{q}_2) T_i \vec{O}_j, \quad (3.27)$$

$$J^0(\vec{q}_1, \vec{q}_2) = \sum_{i=1}^5 \sum_{j=1}^8 f_i^{jS}(\vec{q}_1, \vec{q}_2) T_i O_j^S, \quad (3.28)$$

where $f_i^j(\vec{q}_1, \vec{q}_2)$ and $f_i^{jS}(\vec{q}_1, \vec{q}_2)$ are scalar functions. The spin-momentum operators for the current \vec{O}_i and for the charge density O_i^S are given by

$$\begin{aligned}
\vec{O}_1 &= \vec{q}_1 + \vec{q}_2, \\
\vec{O}_2 &= \vec{q}_1 - \vec{q}_2, \\
\vec{O}_3 &= [\vec{q}_1 \times \vec{\sigma}_2] + [\vec{q}_2 \times \vec{\sigma}_1], \\
\vec{O}_4 &= [\vec{q}_1 \times \vec{\sigma}_2] - [\vec{q}_2 \times \vec{\sigma}_1], \\
\vec{O}_5 &= [\vec{q}_1 \times \vec{\sigma}_1] + [\vec{q}_2 \times \vec{\sigma}_2], \\
\vec{O}_6 &= [\vec{q}_1 \times \vec{\sigma}_1] - [\vec{q}_2 \times \vec{\sigma}_2], \\
\vec{O}_7 &= \vec{q}_1 (\vec{q}_1 \cdot [\vec{q}_2 \times \vec{\sigma}_2]) + \vec{q}_2 (\vec{q}_1 \cdot [\vec{q}_2 \times \vec{\sigma}_1]), \\
\vec{O}_8 &= \vec{q}_1 (\vec{q}_1 \cdot [\vec{q}_2 \times \vec{\sigma}_2]) - \vec{q}_2 (\vec{q}_1 \cdot [\vec{q}_2 \times \vec{\sigma}_1]), \\
\vec{O}_9 &= \vec{q}_2 (\vec{q}_1 \cdot [\vec{q}_2 \times \vec{\sigma}_2]) + \vec{q}_1 (\vec{q}_1 \cdot [\vec{q}_2 \times \vec{\sigma}_1]), \\
\vec{O}_{10} &= \vec{q}_2 (\vec{q}_1 \cdot [\vec{q}_2 \times \vec{\sigma}_2]) - \vec{q}_1 (\vec{q}_1 \cdot [\vec{q}_2 \times \vec{\sigma}_1]), \\
\vec{O}_{11} &= (\vec{q}_1 + \vec{q}_2) (\vec{\sigma}_1 \cdot \vec{\sigma}_2), \\
\vec{O}_{12} &= (\vec{q}_1 - \vec{q}_2) (\vec{\sigma}_1 \cdot \vec{\sigma}_2), \\
\vec{O}_{13} &= \vec{q}_1 (\vec{q}_1 \cdot \vec{\sigma}_1) (\vec{q}_1 \cdot \vec{\sigma}_2) + \vec{q}_2 (\vec{q}_2 \cdot \vec{\sigma}_1) (\vec{q}_2 \cdot \vec{\sigma}_2), \\
\vec{O}_{14} &= \vec{q}_1 (\vec{q}_1 \cdot \vec{\sigma}_1) (\vec{q}_1 \cdot \vec{\sigma}_2) - \vec{q}_2 (\vec{q}_2 \cdot \vec{\sigma}_1) (\vec{q}_2 \cdot \vec{\sigma}_2), \\
\vec{O}_{15} &= (\vec{q}_1 + \vec{q}_2) (\vec{q}_2 \cdot \vec{\sigma}_1) (\vec{q}_1 \cdot \vec{\sigma}_2), \\
\vec{O}_{16} &= (\vec{q}_1 - \vec{q}_2) (\vec{q}_2 \cdot \vec{\sigma}_1) (\vec{q}_1 \cdot \vec{\sigma}_2), \\
\vec{O}_{17} &= (\vec{q}_1 + \vec{q}_2) (\vec{q}_1 \cdot \vec{\sigma}_1) (\vec{q}_2 \cdot \vec{\sigma}_2), \\
\vec{O}_{18} &= (\vec{q}_1 - \vec{q}_2) (\vec{q}_1 \cdot \vec{\sigma}_1) (\vec{q}_2 \cdot \vec{\sigma}_2), \\
\vec{O}_{19} &= \vec{\sigma}_1 (\vec{q}_1 \cdot \vec{\sigma}_2) + \vec{\sigma}_2 (\vec{q}_2 \cdot \vec{\sigma}_1), \\
\vec{O}_{20} &= \vec{\sigma}_1 (\vec{q}_1 \cdot \vec{\sigma}_2) - \vec{\sigma}_2 (\vec{q}_2 \cdot \vec{\sigma}_1), \\
\vec{O}_{21} &= \vec{\sigma}_1 (\vec{q}_2 \cdot \vec{\sigma}_2) + \vec{\sigma}_2 (\vec{q}_1 \cdot \vec{\sigma}_1), \\
\vec{O}_{22} &= \vec{\sigma}_1 (\vec{q}_2 \cdot \vec{\sigma}_2) - \vec{\sigma}_2 (\vec{q}_1 \cdot \vec{\sigma}_1), \\
\vec{O}_{23} &= \vec{q}_1 (\vec{q}_2 \cdot \vec{\sigma}_1) (\vec{q}_2 \cdot \vec{\sigma}_2) + \vec{q}_2 (\vec{q}_1 \cdot \vec{\sigma}_1) (\vec{q}_1 \cdot \vec{\sigma}_2), \\
\vec{O}_{24} &= \vec{q}_1 (\vec{q}_2 \cdot \vec{\sigma}_1) (\vec{q}_2 \cdot \vec{\sigma}_2) - \vec{q}_2 (\vec{q}_1 \cdot \vec{\sigma}_1) (\vec{q}_1 \cdot \vec{\sigma}_2),
\end{aligned} \tag{3.29}$$

and

$$\begin{aligned}
O_1^S &= \mathbb{1}, \\
O_2^S &= \vec{q}_1 \cdot [\vec{q}_2 \times \vec{\sigma}_2] + \vec{q}_1 \cdot [\vec{q}_2 \times \vec{\sigma}_1], \\
O_3^S &= \vec{q}_1 \cdot [\vec{q}_2 \times \vec{\sigma}_2] - \vec{q}_1 \cdot [\vec{q}_2 \times \vec{\sigma}_1], \\
O_4^S &= \vec{\sigma}_1 \cdot \vec{\sigma}_2, \\
O_5^S &= (\vec{q}_1 \cdot \vec{\sigma}_2) (\vec{q}_2 \cdot \vec{\sigma}_1), \\
O_6^S &= (\vec{q}_1 \cdot \vec{\sigma}_1) (\vec{q}_2 \cdot \vec{\sigma}_2), \\
O_7^S &= (\vec{q}_2 \cdot \vec{\sigma}_1) (\vec{q}_2 \cdot \vec{\sigma}_2) + (\vec{q}_1 \cdot \vec{\sigma}_1) (\vec{q}_1 \cdot \vec{\sigma}_2), \\
O_8^S &= (\vec{q}_2 \cdot \vec{\sigma}_1) (\vec{q}_2 \cdot \vec{\sigma}_2) - (\vec{q}_1 \cdot \vec{\sigma}_1) (\vec{q}_1 \cdot \vec{\sigma}_2).
\end{aligned} \tag{3.30}$$

It turns out that even more complicated "non-local" structures may appear in the 2N current operator, which depend not only on \vec{q}_1 and \vec{q}_2 but, additionally, are

functions of the initial total 2N momentum $\vec{p}_1 + \vec{p}_2$. Operators of this type appear in the relativistic corrections to the one-pion-exchange charge density operator [44]

$$\begin{aligned} A_1^S &= (\vec{q}_1 \cdot \vec{\sigma}_1) (\vec{k}_2 \cdot \vec{\sigma}_2) + (\vec{q}_2 \cdot \vec{\sigma}_2) (\vec{k}_1 \cdot \vec{\sigma}_1), \\ A_2^S &= (\vec{q}_1 \cdot \vec{\sigma}_1) (\vec{k}_2 \cdot \vec{\sigma}_2) - (\vec{q}_2 \cdot \vec{\sigma}_2) (\vec{k}_1 \cdot \vec{\sigma}_1), \\ A_3^S &= (\vec{q}_1 \cdot \vec{\sigma}_2) (\vec{k}_1 \cdot \vec{\sigma}_1) + (\vec{q}_2 \cdot \vec{\sigma}_1) (\vec{k}_2 \cdot \vec{\sigma}_2), \\ A_4^S &= (\vec{q}_1 \cdot \vec{\sigma}_2) (\vec{k}_1 \cdot \vec{\sigma}_1) - (\vec{q}_2 \cdot \vec{\sigma}_1) (\vec{k}_2 \cdot \vec{\sigma}_2), \end{aligned} \quad (3.31)$$

where $\vec{k}_1 = \vec{p}_1 + \vec{p}'_1$ and $\vec{k}_2 = \vec{p}_2 + \vec{p}'_2$.

The five different isospin operators in the two-nucleon isospin space are:

$$\begin{aligned} T_1 &= (\vec{\tau}_1 + \vec{\tau}_2)_3, \\ T_2 &= (\vec{\tau}_1 - \vec{\tau}_2)_3, \\ T_3 &= (\vec{\tau}_1 \times \vec{\tau}_2)_3, \\ T_4 &= \vec{\tau}_1 \cdot \vec{\tau}_2, \\ T_5 &= \mathbb{1}, \end{aligned} \quad (3.32)$$

where $\vec{\tau}_1$ and $\vec{\tau}_2$ are the individual isospin operators and $(\dots)_3$ denotes the third Cartesian components of a given vector.

From these very general formulas we can immediately draw some important observations. First, none of the (T_1, T_2, T_3) structures can contribute to elastic electron scattering off the deuteron because the corresponding isospin matrix elements are zero between two states with the total two-nucleon isospin $t = 0$. Secondly, the T_1 structure plays no role also in the inelastic processes on the deuteron because the deuteron isospin state is antisymmetric with respect to exchange of nucleons 1 and 2. Note that all the above-mentioned operators will be active in the processes with three nucleons, where two-nucleon subsystems in the initial and final state may have $t = 0$ or $t = 1$. Finally, for the typical choice $\vec{Q} \parallel \hat{z}$, the transverse components of the operator \vec{O}_1 will be zero.

The expression corresponding to Equations (3.18)–(3.20) given for the single nucleon current reads

$$\left\langle \Psi_f \vec{P}_f \left| \frac{1}{e} J_{12}^\mu(0) \right| \Psi_i \vec{P}_i \right\rangle = \int d\vec{p}' \int d\vec{p} \langle \Psi_f | \vec{p}' \rangle J^\mu(\vec{q}_1, \vec{q}_2) \langle \vec{p} | \Psi_i \rangle, \quad (3.33)$$

where \vec{q}_1 and \vec{q}_2 are defined in Equations (3.24) and (3.25).

3.2.1 Leading order one-pion exchange currents

Having presented the general form of the two-nucleon current operator, we can now discuss the specific expressions derived consistently with the nucleon-nucleon force

within the Chiral Effective Field Theory [60]. Of course, a complete two-nucleon current operator must, first of all, contain a single-nucleon part. This part is taken in the form of the nonrelativistic single-nucleon current for point-like nucleons.

The first nontrivial contribution to the 2N current operator comes from the one-pion exchange already at lowest order (LO), where three classes of one-pion-exchange diagrams have been considered. One of them, however, gives no contribution to the current operator. The other two classes yield expected contributions in the form of the so-called seagull current, $\vec{J}_{ope}^{seagull}$, and the pion-in-flight current, \vec{J}_{ope}^{pionic} , which have been known for a long time [61].

The diagrams representing contributing classes are shown in Figure 3.4 and the corresponding expressions read:

$$\vec{J}_{ope}^{seagull} = -i \left(\frac{g_A}{2F_\pi} \right)^2 \vec{\sigma}_1 [\vec{\tau}_1 \times \vec{\tau}_2]_3 \frac{\vec{\sigma}_2 \cdot \vec{q}_2}{\vec{q}_2^2 + M_\pi^2} + (1 \leftrightarrow 2) \quad (3.34)$$

and

$$\vec{J}_{ope}^{pionic} = i \left(\frac{g_A}{2F_\pi} \right)^2 \frac{\vec{\sigma}_1 \cdot \vec{q}_1}{\vec{q}_1^2 + M_\pi^2} \frac{\vec{\sigma}_2 \cdot \vec{q}_2}{\vec{q}_2^2 + M_\pi^2} [\vec{\tau}_1 \times \vec{\tau}_2]_3 (\vec{q}_1 - \vec{q}_2). \quad (3.35)$$

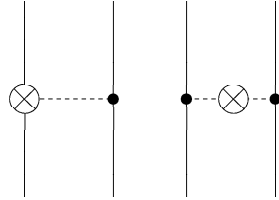


Figure 3.4: Diagrams corresponding to the leading OPE current operators: $\vec{J}_{ope}^{seagull}$ (left) and \vec{J}_{ope}^{pionic} (right).

Thus the leading one-pion-exchange current operator can be expressed in terms of the basis operators from Equation (3.5) as

$$\begin{aligned} \vec{J}_{lope} &= \vec{J}_{ope}^{seagull} + \vec{J}_{ope}^{pionic} = \\ f_3^{21}(\vec{q}_1, \vec{q}_2) T_3 \vec{O}_{21} - f_3^{22}(\vec{q}_1, \vec{q}_2) T_3 \vec{O}_{22} + f_3^{18}(\vec{q}_1, \vec{q}_2) T_3 \vec{O}_{18} \end{aligned} \quad (3.36)$$

with

$$f_3^{21}(\vec{q}_1, \vec{q}_2) = \frac{i}{2} \left(\frac{g_A}{2F_\pi} \right)^2 \left(\frac{1}{\vec{q}_1^2 + M_\pi^2} - \frac{1}{\vec{q}_2^2 + M_\pi^2} \right), \quad (3.37)$$

$$f_3^{22}(\vec{q}_1, \vec{q}_2) = \frac{i}{2} \left(\frac{g_A}{2F_\pi} \right)^2 \left(\frac{1}{\vec{q}_2^2 + M_\pi^2} + \frac{1}{\vec{q}_1^2 + M_\pi^2} \right), \quad (3.38)$$

$$f_3^{18}(\vec{q}_1, \vec{q}_2) = i \left(\frac{g_A}{2F_\pi} \right)^2 \frac{1}{(\vec{q}_1^2 + M_\pi^2)(\vec{q}_2^2 + M_\pi^2)}. \quad (3.39)$$

3.2.2 Two-pion exchange currents at NLO

The two-pion-exchange (TPE) contributions to the nuclear current operator are derived in [42]. They result from several classes of diagrams shown in Figure 3.5 and are written as

$$J_{tpe}^\mu = \sum_{X=c1}^{c7} J_X^\mu, \quad (3.40)$$

where J_X denotes the current and charge densities coming from the individual classes. Further, $(1 \leftrightarrow 2)$ refers to the part arising from the interchange of the nucleon labels. As emphasized in [42] the diagrams in the method of unitary transformation serve merely to visualize the topology corresponding to a given sequence of the field-theoretical operators.

In the following we do not show the contributions from the individual classes obtained in [42] but display the final expressions in terms of the basis operators introduced in (3.29) and (3.30). The non-vanishing contributions to the scalar functions $f_i^j \equiv f_i^j(\vec{q}_1, \vec{q}_2)$ due to two-pion exchange calculated using dimensional regularization are [42]

$$\begin{aligned} f_1^3 &= \frac{ig_A^2(g_A^2 + 1)}{256\pi^2 F_\pi^4} + \frac{ig_A^2 L(q_1)}{128\pi^2 F_\pi^4} \left[\frac{g_A^2(8M_\pi^2 + 3q_1^2)}{4M_\pi^2 + q_1^2} - 1 \right] + (1 \leftrightarrow 2), \\ f_1^4 &= \frac{ig_A^2 L(q_1)}{128\pi^2 F_\pi^4} \left[\frac{g_A^2(8M_\pi^2 + 3q_1^2)}{4M_\pi^2 + q_1^2} - 1 \right] - (1 \leftrightarrow 2), \\ f_1^5 &= -\frac{ig_A^4}{128\pi^2 F_\pi^4} + \frac{ig_A^4 L(k)}{32\pi^2 F_\pi^4} - \frac{ig_A^4 L(q_1)}{64\pi^2 F_\pi^4} + \frac{g_A^2 \pi}{2F_\pi^4} \left[g_A^2(-M_\pi^2) I_{(1,1,2)}^{(d+2)} \right. \\ &\quad \left. + 4\pi g_A^2 q_1 I_{(2,1,2)}^{(d+4)}(q_1 - q_2 z) + (g_A^2 - 1) I_{\text{red}(1,1,0)}^{(d+2)} \right] + (1 \leftrightarrow 2), \\ f_1^6 &= -\frac{ig_A^4 L(q_1)}{64\pi^2 F_\pi^4} - \frac{2g_A^4 \pi^2}{F_\pi^4} I_{(2,1,2)}^{(d+4)} q_1 (q_1 + q_2 z) - (1 \leftrightarrow 2), \\ f_1^7 &= \frac{g_A^2 \pi}{2F_\pi^4} \left[8\pi g_A^2 (q_1^2 - 2M_\pi^2) I_{(3,1,2)}^{(d+4)} - g_A^2 M_\pi^2 I_{(2,1,2)}^{(d+2)} + 192\pi^2 g_A^2 q_1^2 I_{(4,1,2)}^{(d+6)} - 64\pi^2 g_A^2 q_1 q_2 z \right. \\ &\quad \left. I_{(3,2,2)}^{(d+6)} + 8\pi g_A^2 I_{(2,1,2)}^{(d+4)} + (g_A^2 - 1) I_{(2,1,0)}^{(d+2)} + 16\pi(g_A^2 - 1) I_{(3,1,0)}^{(d+4)} \right] - (1 \leftrightarrow 2), \\ f_1^8 &= \frac{ig_A^4}{32\pi^2 F_\pi^4 Q^2} - \frac{ig_A^4 L(Q)}{32\pi^2 F_\pi^4 Q^2} + \frac{g_A^2 \pi}{4F_\pi^4} \left[16\pi g_A^2 (q_1^2 - 2M_\pi^2) I_{(3,1,2)}^{(d+4)} - 2g_A^2 M_\pi^2 I_{(2,1,2)}^{(d+2)} \right. \\ &\quad \left. + 384\pi^2 g_A^2 q_1^2 I_{(4,1,2)}^{(d+6)} - 8\pi g_A^2 q_1 q_2 z I_{(2,2,2)}^{(d+4)} - 128\pi^2 g_A^2 q_1 q_2 z I_{(3,2,2)}^{(d+6)} + g_A^2 I_{(1,1,2)}^{(d+2)} \right. \\ &\quad \left. + 16\pi g_A^2 I_{(2,1,2)}^{(d+4)} + 2(g_A^2 - 1) I_{(2,1,0)}^{(d+2)} + 32\pi(g_A^2 - 1) I_{(3,1,0)}^{(d+4)} \right] + (1 \leftrightarrow 2), \end{aligned}$$

$$\begin{aligned}
f_1^9 &= \frac{g_A^2 \pi}{2F_\pi^4} \left[g_A^2 M_\pi^2 I_{(2,1,2)}^{(d+2)} - 8\pi g_A^2 q_1^2 I_{(3,1,2)}^{(d+4)} - 64\pi^2 g_A^2 q_1 I_{(3,2,2)}^{(d+6)} (q_1 + q_2 z) \right. \\
&\quad \left. + 4\pi g_A^2 I_{(2,1,2)}^{(d+4)} + (1 - g_A^2) I_{(2,1,0)}^{(d+2)} \right] - (1 \leftrightarrow 2), \\
f_1^{10} &= \frac{ieg_A^4}{32\pi^2 F_\pi^4 Q^2} - \frac{ig_A^4 L(Q)}{32\pi^2 F_\pi^4 Q^2} - \frac{g_A^2 \pi}{4F_\pi^4} \left[-8\pi g_A^2 I_{(2,2,2)}^{(d+4)} (2M_\pi^2 + q_1 q_2 z) - 2g_A^2 M_\pi^2 I_{(2,1,2)}^{(d+2)} \right. \\
&\quad \left. + 16\pi g_A^2 q_1^2 I_{(3,1,2)}^{(d+4)} + 128\pi^2 g_A^2 q_1 I_{(3,2,2)}^{(d+6)} (q_1 - q_2 z) + g_A^2 I_{(1,1,2)}^{(d+2)} + 8\pi g_A^2 I_{(2,1,2)}^{(d+4)} \right. \\
&\quad \left. + 2(g_A^2 - 1) I_{(2,1,0)}^{(d+2)} + 16\pi(g_A^2 - 1) I_{(2,2,0)}^{(d+4)} \right] + (1 \leftrightarrow 2), \\
f_3^1 &= \frac{ig_A^2 L(q_1)}{128\pi^2 F_\pi^4} \left[\frac{g_A^2 (8M_\pi^2 + 3q_1^2)}{4M_\pi^2 + q_1^2} - 1 \right] + \frac{\pi}{F_\pi^4} \left[g_A^4 M_\pi^4 I_{(2,1,2)}^{(d+2)} + 4\pi g_A^4 M_\pi^2 q_1^2 I_{(2,2,2)}^{(d+4)} \right. \\
&\quad \left. - 8\pi g_A^4 M_\pi^2 q_1 I_{(3,1,2)}^{(d+4)} (q_1 - q_2 z) - 96\pi^2 g_A^4 q_1^3 q_2 z I_{(4,1,2)}^{(d+6)} \right. \\
&\quad \left. + 32\pi^2 g_A^4 q_1^2 q_2 I_{(3,2,2)}^{(d+6)} (q_1 z + q_2 z^2 + q_2) - 2\pi g_A^4 q_1 I_{(2,1,2)}^{(d+4)} (q_1 + 2q_2 z) \right. \\
&\quad \left. - 2(g_A^2 - 1) g_A^2 M_\pi^2 \times I_{(2,1,0)}^{(d+2)} - 4\pi(g_A^2 - 1) g_A^2 q_1^2 I_{(2,2,0)}^{(d+4)} \right. \\
&\quad \left. + 8\pi(g_A^2 - 1) g_A^2 q_1 I_{(3,1,0)}^{(d+4)} (q_1 - q_2 z) - 2\pi(g_A^2 - 1)^2 I_{\text{red}(2,1,0)}^{(d+4)} \right] - (1 \leftrightarrow 2), \\
f_3^2 &= \frac{ig_A^2 (g_A^2 + 1)}{256\pi^2 F_\pi^4} + \frac{ig_A^2 L(q_1)}{128\pi^2 F_\pi^4} \left[\frac{g_A^2 (8M_\pi^2 + 3q_1^2)}{4M_\pi^2 + q_1^2} - 1 \right] \\
&\quad + \frac{1}{8F_\pi^4} \left[-64\pi^2 g_A^4 q_1 I_{(3,1,2)}^{(d+4)} (M_\pi^2 (q_1 - q_2 z) + q_1^2 q_2 z) \right. \\
&\quad \left. + 16\pi^2 g_A^4 q_1 I_{(2,2,2)}^{(d+4)} (q_1 q_2^2 (z^2 + 1) - 2M_\pi^2 (q_1 - q_2 z)) - 2\pi g_A^4 I_{(1,1,2)}^{(d+2)} (2M_\pi^2 + q_1 q_2 z) \right. \\
&\quad \left. + 8\pi g_A^4 M_\pi^2 I_{(2,1,2)}^{(d+2)} (M_\pi^2 + q_1 (q_2 z - q_1)) - 768\pi^3 g_A^4 q_1^3 q_2 z I_{(4,1,2)}^{(d+6)} \right. \\
&\quad \left. - 256\pi^3 g_A^4 q_1^2 q_2 I_{(3,2,2)}^{(d+6)} (q_1 z - q_2 (z^2 + 1)) + 16\pi^2 g_A^4 q_1 I_{(2,1,2)}^{(d+4)} (q_1 - 2q_2 z) \right. \\
&\quad \left. + 2\pi(g_A^2 - 1) I_{\text{red}(1,1,0)}^{(d+2)} - 8\pi(g_A^2 - 1) g_A^2 I_{(2,1,0)}^{(d+2)} (2M_\pi^2 + q_1 (q_2 z - q_1)) \right. \\
&\quad \left. + 32\pi^2(g_A^2 - 1) g_A^2 q_1 I_{(2,2,0)}^{(d+4)} (q_1 - q_2 z) + 64\pi^2(g_A^2 - 1) g_A^2 q_1 I_{(3,1,0)}^{(d+4)} (q_1 - q_2 z) \right. \\
&\quad \left. - 16\pi^2(g_A^2 - 1)^2 I_{\text{red}(2,1,0)}^{(d+4)} + g_A^4 M_\pi^4 I_{(1,1,2)}^{(4)} - 2(g_A^2 - 1) g_A^2 M_\pi^2 I_{(1,1,0)}^{(4)} \right] + (1 \leftrightarrow 2). \tag{3.41}
\end{aligned}$$

The non-zero f_2^j functions are obtained using the following relations

$$\begin{aligned}
f_2^3 &= f_1^4, & f_2^4 &= f_1^3, & f_2^5 &= -f_1^6, & f_2^6 &= -f_1^5, \\
f_2^7 &= f_1^8, & f_2^8 &= f_1^7, & f_2^9 &= f_1^{10}, & f_2^{10} &= f_1^9. \tag{3.42}
\end{aligned}$$

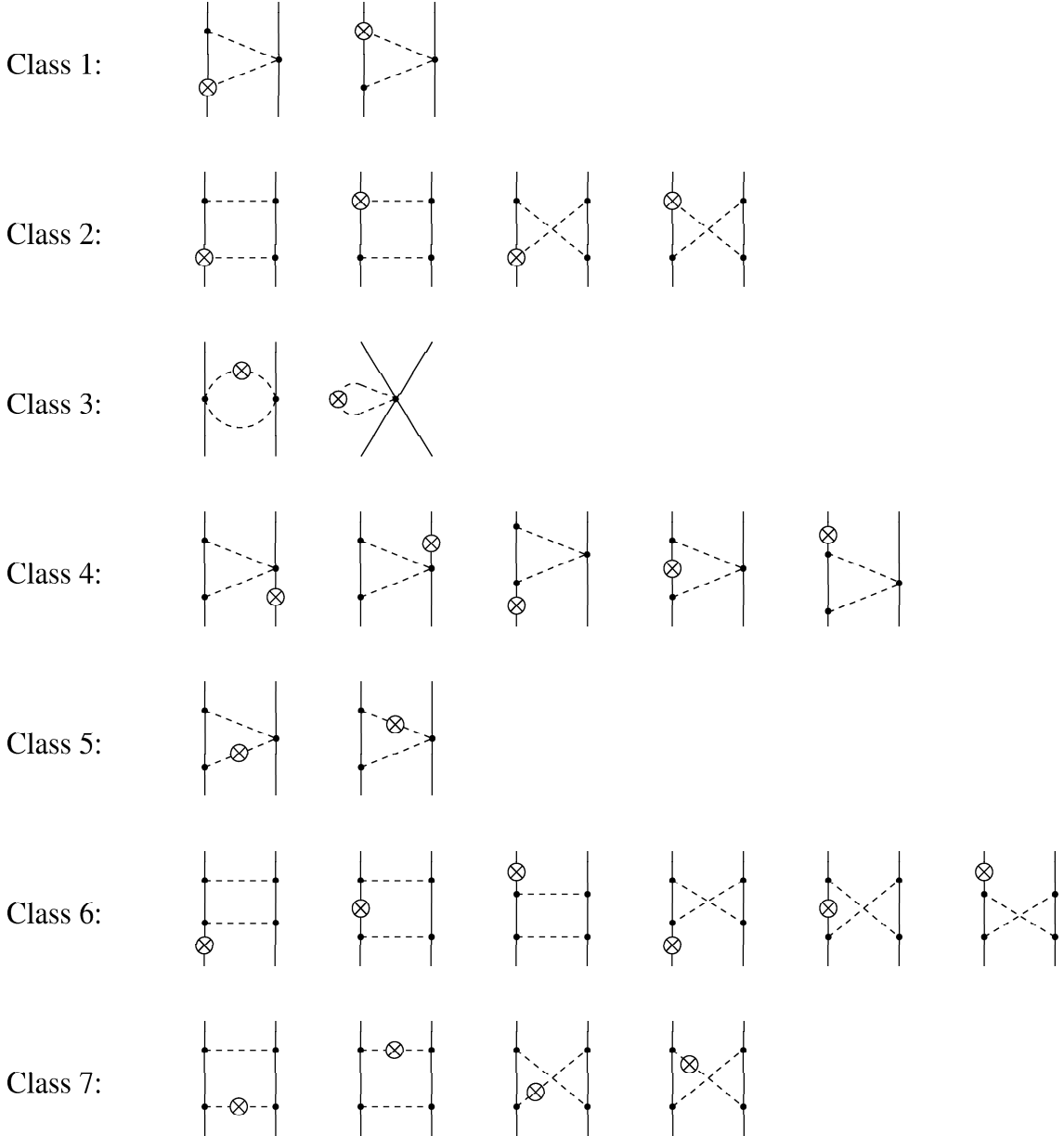


Figure 3.5: Diagrams showing contributions to the leading two-pion exchange currents. Solid and dashed lines refer to nucleons and pions, respectively. Solid dots are the lowest-order vertices from the effective Lagrangian while the crosses represent insertions of the electromagnetic vertices as explained in [42].

In the above equations $z \equiv \hat{q}_1 \cdot \hat{q}_2$, $q_i \equiv |\vec{q}_i|$, $Q \equiv |\vec{q}_1 + \vec{q}_2|$ and the loop functions $L(q)$ and $A(q)$ are defined by

$$\begin{aligned} L(q) &= \frac{1}{2} \frac{s}{q} \ln \left(\frac{s+q}{s-q} \right), \quad \text{with } s = \sqrt{q^2 + 4M_\pi^2}, \\ A(q) &= \frac{1}{2q} \arctan \left(\frac{q}{2M_\pi} \right). \end{aligned} \quad (3.43)$$

Furthermore, the function I corresponds to the three-point functions via

$$I_{(\nu_1, \nu_2, \nu_3)}^{(d)} \equiv I(d; 0, 1; q_1, \nu_1; -q_2, \nu_2; 0, \nu_3) \quad \text{with} \quad q_i = (0, \vec{q}_i) \quad (3.44)$$

and

$$\begin{aligned} I(d; p_1, \nu_1; p_2, \nu_2; p_3, \nu_3; p_4, \nu_4) = \\ \mu^{4-d} \int \frac{d^d \ell}{(2\pi)^d} \frac{1}{[(\ell + p_1)^2 - M_\pi^2]^{\nu_1} [(\ell + p_2)^2 - M_\pi^2]^{\nu_2} [(\ell + p_3)^2 - M_\pi^2]^{\nu_3} [v \cdot (\ell + p_4)]^{\nu_4}}. \end{aligned} \quad (3.45)$$

In Equation (3.45) all propagators have an infinitesimal positive imaginary part. It turns out all functions $I_{(\nu_1, \nu_2, \nu_3)}^{(d+n)}$ which enter the above equations except $I_{(1,1,0)}^{(d+2)}$, $I_{(2,1,0)}^{(d+4)}$ and $I_{(1,2,0)}^{(d+4)}$ are finite in dimensional regularization in the limit $d \rightarrow 4$. For the three exceptions, the so-called reduced functions are introduced [42]

$$\begin{aligned} I_{\text{red } (1,1,0)}^{(d+2)} &= I_{(1,1,0)}^{(d+2)} - \frac{i}{4\pi} L(\mu) - \frac{i}{128\pi^3} \ln \left(\frac{M_\pi^2}{\mu^2} \right), \\ I_{\text{red } (2,1,0)}^{(d+4)} &= I_{(2,1,0)}^{(d+4)} + \frac{i}{48\pi^2} L(\mu) + \frac{i}{1536\pi^4} \ln \left(\frac{M_\pi^2}{\mu^2} \right), \\ I_{\text{red } (1,2,0)}^{(d+4)} &= I_{(1,2,0)}^{(d+4)} + \frac{i}{48\pi^2} L(\mu) + \frac{i}{1536\pi^4} \ln \left(\frac{M_\pi^2}{\mu^2} \right), \end{aligned} \quad (3.46)$$

where

$$L(\mu) = \frac{\mu^{d-4}}{16\pi^2} \left[\frac{1}{d-4} + \frac{1}{2} (\gamma_E - 1 - \ln(4\pi)) \right]. \quad (3.47)$$

Here, μ is the scale introduced in dimensional regularization and $\gamma_E = -\Gamma'(1) \simeq 0.577$. The detailed evaluation of the three-point functions was done in [42].

Finally, for scalar functions contributing to the charge density we obtain the following expressions:

$$\begin{aligned} f_3^{2S} &= \frac{g_A^4 A(k)}{64\pi F_\pi^4} + \frac{i\pi^2 g_A^4}{F_\pi^4} \left[-2M_\pi^2 I_{(2,1,3)}^{(d+4)} + 16\pi q_1^2 I_{(3,1,3)}^{(d+6)} - 8\pi q_1 q_2 z I_{(2,2,3)}^{(d+6)} + I_{(1,1,3)}^{(d+4)} \right] \\ &\quad + (1 \leftrightarrow 2), \\ f_3^{3S} &= \frac{2i\pi^2 g_A^4}{F_\pi^4} \left[8\pi q_1^2 I_{(3,1,3)}^{(d+6)} - M_\pi^2 I_{(2,1,3)}^{(d+4)} \right] - (1 \leftrightarrow 2), \end{aligned}$$

$$\begin{aligned}
f_1^{1S} &= \frac{g_A^4 M_\pi (12M_\pi^4 + 7M_\pi^2 q_1^2 + q_1^2 q_2^2)}{64\pi F_\pi^4 (4M_\pi^2 + q_1^2)(4M_\pi^2 + q_2^2)} - \frac{g_A^4 A(k) (2M_\pi^2 + q_1^2)}{16\pi F_\pi^4} + \frac{g_A^4 A(q_1) (2M_\pi^2 + q_1^2)}{32\pi F_\pi^4} \\
&\quad + \frac{i g_A^4 \pi}{F_\pi^4} \left[M_\pi^4 (-I_{(1,1,3)}^{(d+2)}) + 8\pi M_\pi^2 q_1 I_{(2,1,3)}^{(d+4)} (q_1 - q_2 z) + 64\pi^2 q_1^3 q_2 z I_{(3,1,3)}^{(d+6)} \right. \\
&\quad \left. - 16\pi^2 q_1^2 q_2^2 (z^2 + 1) I_{(2,2,3)}^{(d+6)} + 2\pi q_1 q_2 z I_{(1,1,3)}^{(d+4)} \right] + (1 \leftrightarrow 2), \\
f_1^{4S} &= -\frac{g_A^4 q_1^2 A(q_1)}{64\pi F_\pi^4} - \frac{2i g_A^4 \pi^2}{F_\pi^4} \left[8\pi q_1^2 q_2^2 (z^2 - 1) I_{(2,2,3)}^{(d+6)} - q_1 q_2 z I_{(1,1,3)}^{(d+4)} \right] + (1 \leftrightarrow 2), \\
f_1^{5S} &= \frac{2i g_A^4 \pi^2}{F_\pi^4} \left[8\pi q_1 q_2 z I_{(2,2,3)}^{(d+6)} - I_{(1,1,3)}^{(d+4)} \right] + (1 \leftrightarrow 2), \\
f_1^{6S} &= \frac{16i\pi^3 e g_A^4}{F_\pi^4} q_1 q_2 z I_{(2,2,3)}^{(d+6)} + (1 \leftrightarrow 2), \\
f_1^{7S} &= \frac{g_A^4 A(q_1)}{128\pi F_\pi^4} - \frac{16i\pi^3 g_A^4}{F_\pi^4} q_1^2 I_{(2,2,3)}^{(d+6)} + (1 \leftrightarrow 2), \\
f_1^{8S} &= -\frac{g_A^4 A(q_1)}{128\pi F_\pi^4} - \frac{16i\pi^3 g_A^4}{F_\pi^4} q_1^2 I_{(2,2,3)}^{(d+6)} - (1 \leftrightarrow 2), \\
f_2^{1S} &= \frac{g_A^4 M_\pi^3 q_1^2}{64\pi F_\pi^4 (4M_\pi^2 + q_1^2)(4M_\pi^2 + q_2^2)} + \frac{g_A^2 (g_A^2 - 1) A(q_1) (2M_\pi^2 + q_1^2)}{32\pi F_\pi^4} - (1 \leftrightarrow 2), \\
f_2^{7S} &= -\frac{g_A^4 A(q_1)}{128\pi F_\pi^4} - (1 \leftrightarrow 2), \\
f_2^{8S} &= \frac{g_A^4 A(q_1)}{128\pi F_\pi^4} + (1 \leftrightarrow 2).
\end{aligned} \tag{3.48}$$

Note that since the nucleon-nucleon potential is regularized and high momenta are thus truncated in the initial and final nuclear states, there is no need for additional regularization of the chiral current operator and the form factors given above are used without any extra damping.

In fact, some of these form factors ($f_2^6 = -f_1^5$, $f_2^4 = f_1^3$, f_3^2 , f_1^{1S}) induce short-range corrections to the current operator which are not absorbed into re-definitions of the low-energy constants. In our calculations, following [52], we first skipped these short-range terms in the TPE current operator and performed calculations with the long-range one-pion-exchange and two-pion-exchange operators. Only when we introduced other short-range terms, which come from one-pion-exchange at NLO and/or arise from relativistic corrections [44], the short-range terms in the TPE current operator were also taken into account.

The form factors specified in Equations (3.41) and (3.48) can be given in many different, formally equivalent ways. Not all of them are, however, well suited for numerical treatment. We had a chance to work with other tentative expressions from [44], which turned out numerically unstable. We give just two examples, f_1^{5S} and f_1^7

$$\begin{aligned}
f_1^{5S} = & \frac{g_A^4 z (-2q_1^2 - 2q_2^2 + q_1 q_2 z (-5 + z^2)) A(k)}{32 F_\pi^4 \pi q_1 q_2 (-1 + z^2)^2} + \frac{g_A^4 (q_2 + 2q_1 z + q_2 z^2) A(q_1)}{32 F_\pi^4 \pi q_2 (-1 + z^2)^2} \\
& + \frac{q_2 (q_1 + 2q_2 z + q_1 z^2) A(q_2)}{32 F_\pi^4 \pi q_1 (-1 + z^2)^2} + \frac{1}{8 F_\pi^4 (-1 + z^2)^2} (i g_A^4 (-4 M_\pi^2 (-1 + z^2) \\
& + q_1^2 (1 + z^2) + q_2^2 (1 + z^2) + q_1^2 q_2^2 z (3 + z^2)) I_{(1,1,1)}^{(4)}) , \tag{3.49}
\end{aligned}$$

$$\begin{aligned}
f_1^7 = & g_A^2 (q_1 - q_2) (q_1 + q_2) (i(-1 + g_A^2) q_1 q_2 (-1 + z^2) - (-i(-(-1 + g_A^2) \\
& (q_1^2 + q_2^2 + 2q_1 q_2 z) (2q_1 q_2 + 3(q_1^2 + q_2^2)z + 4q_1 q_2 z^2) + 4M_\pi^2 (-1 + z^2) \\
& (2(-1 + 2g_A^2) q_1 q_2 + (-3 + 5g_A^2)(q_1^2 + q_2^2)z + 2(-2 + 3g_A^2) q_1 q_2 z^2)) L(k) \\
& + i q_1 (-(-1 + g_A^2) (q_1^2 + q_2^2 + 2q_1 q_2 z) (q_2 + 3q_1 z + 2q_2 z^2) + 4M_\pi^2 (-1 + z^2) \\
& ((-3 + 5g_A^2) q_1 z + q_2 (-1 + g_A^2 + 2(-1 + 2g_A^2)z^2))) L(q_1) + q_2 (i(-(-1 + g_A^2) \\
& (q_1^2 + q_2^2 + 2q_1 q_2 z) (q_1 + 3q_2 z + 2q_1 z^2) + 4M_\pi^2 (-1 + z^2) ((-3 + 5g_A^2) q_2 z \\
& + q_1 (-1 + g_A^2 + 2(-1 + 2g_A^2)z^2))) L(q_2) + 8\pi^2 q_1 (q_1^2 + q_2^2 + 2q_1 q_2 z \\
& - 4M_\pi^2 (-1 + z^2)) (-4(-1 + 3g_A^2) M_\pi^2 (-1 + z^2) + (-1 + g_A^2) \\
& (q_1^2 + q_2^2 + 4q_1 q_2 z + 2(q_1^2 + q_2^2)z^2 + 2q_1 q_2 z^3)) I_{(1,1,1)}^{(4)} / \\
& (q_1^2 + q_2^2 + 2q_1 q_2 z - 4M_\pi^2 (-1 + z^2)))) / (256 F_\pi^4 \pi^2 q_1^3 q_2^3 (-1 + z^2)^2) , \tag{3.50}
\end{aligned}$$

where $I_{(1,1,1)}^{(4)}$ is the three-point function defined in (3.45). We show the behavior of these two functions in Figure 3.6 in the vicinity of $z \equiv \hat{q}_1 \cdot \hat{q}_2 = \pm 1$, for other arguments fixed in such a way that $|\vec{q}_1 + \vec{q}_2| = Q$. We see a rapid unphysical change in the value which led to completely wrong results for the current matrix elements. Since the functions and their derivatives have finite value at $z \pm 1$, we tried to use the Taylor expansions with just two terms

$$f(z) \approx f(\pm 1) + f'(\pm 1)(z \mp 1) \tag{3.51}$$

and then to glue together this prescription with the general formula (see Figure 3.6). This required considering very many different cases for many scalar functions: $f_1^5, f_1^6, f_1^7, f_1^8, f_1^9, f_1^{10}, f_1^{2S}, f_1^{3S}, f_1^{4S}, f_1^{5S}, f_1^{6S}, f_2^6, f_2^7, f_2^8, f_2^9, f_2^{10}, f_3^2, f_3^{7S}, f_3^{8S}$ for each Q separately! Despite many efforts, even apparently stable results could not be considered without a shadow of doubt. We informed the authors about this problem and they rewrote the expressions for the form factors to the form given finally in [42]. We could thus make sure that our "regularization" scheme was correct (see Figure 3.7) and thus also the results presented in [62]. Of course, as soon as the new forms of the form factors became available, we started using these safer expressions.

3.2.3 Preliminary results for other parts of current

In more a complete calculation, one has to supplement the leading OPE and TPE current operators with new terms, which arrise at the same (NLO) order of chiral expansion. This section deals with very recent results from [44]. We give general expressions for new parts of currents, however, we show only these which we used in calculations: the form factors corresponding to the new parts of current according to the T_4 and T_5 isospin structure operator.

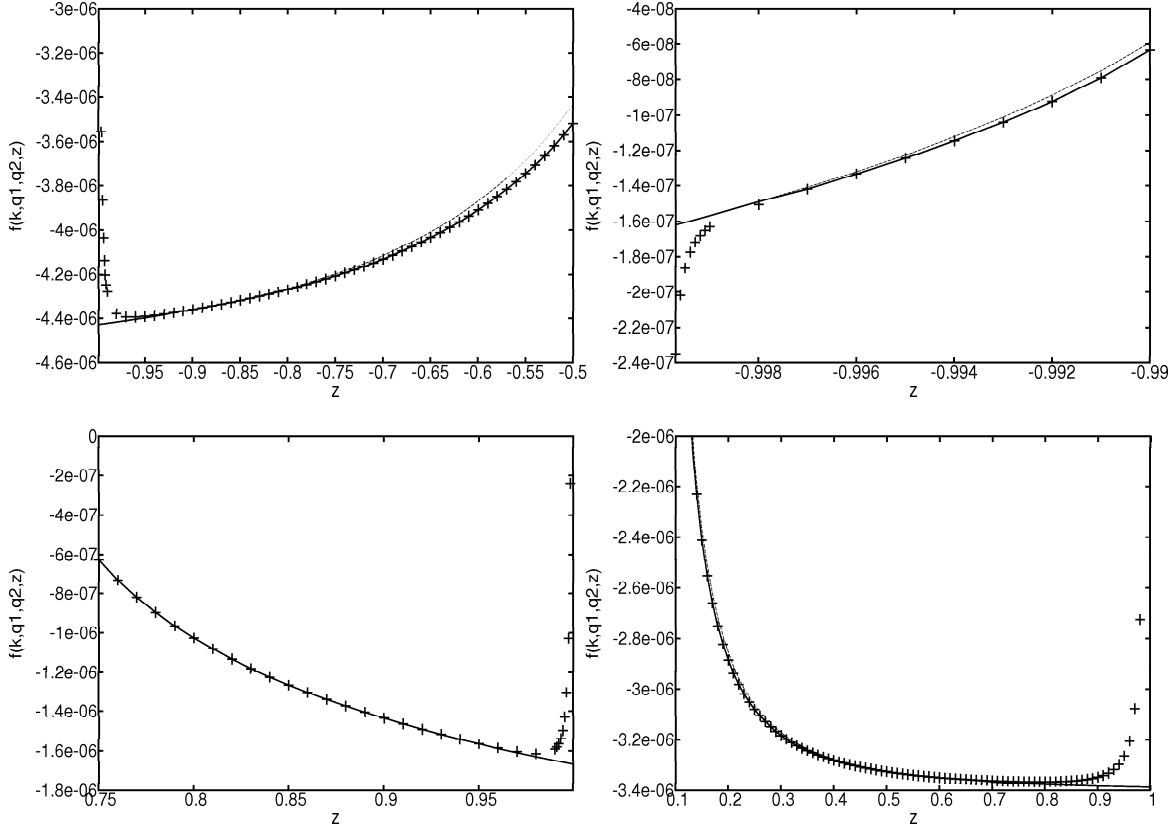


Figure 3.6: Tentative form of two scalar functions f_1^7 (left) and f_1^{5S} (right) showing unstable behaviour for $z \approx \pm 1$ (see text). Dotted lines correspond directly to Equations (3.50) and (3.49). Dashed lines represent the approximate form based on (3.51). Solid lines show results of our regularization.

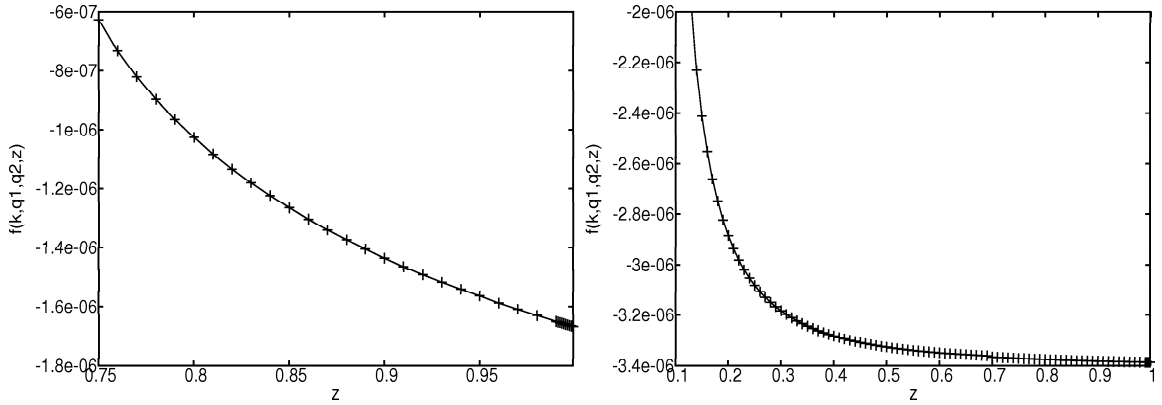


Figure 3.7: Two scalar functions f_1^7 (left) and f_1^{5S} (right). Comparison of the final formulas from [42] (solid lines) with the regularization prescription shown in Figure 3.6 (crosses).

One-pion exchange currents at NLO

At NLO we encounter one-loop OPE corrections, which are $(\frac{Q}{\Lambda})^4$ suppressed. Considered OPE expressions at NLO involve the new LECs: d_8 , d_9 . Therefore the calculation of these corrections will depend on the choice of constants. The contribution from the one-pion exchange density at NLO is represented by the sum of following structures

$$J_{n\text{ope}}^0 = \sum_{i=1,2} \sum_{j=6,7,8} g_i^{jS}(\vec{q}_1, \vec{q}_2) T_i O_j^S, \quad (3.52)$$

where $g_i^j(\vec{q}_1, \vec{q}_2)$ correspond to the scalar functions. The new terms in the vector part of the OPE current operator at NLO are given by

$$\vec{J}_{n\text{ope}} = \sum_{i=1,2,4} \sum_{j=3,4,5,6,9,10} g_i^j(\vec{q}_1, \vec{q}_2) T_i \vec{O}_j. \quad (3.53)$$

The form factors $g_1^j(g_2^j)$ correspond to $(T_1)T_2$ isospin operator and involve d_8 . For the operator T_4 the form factors $g_4^j(\vec{q}_1, \vec{q}_2) \equiv g_4^j$ are

$$\begin{aligned} g_4^3 &= \frac{id_9 g_A}{2F_\pi^2} (2q_1^2 q_2^2 + M^2(q_1^2 + q_2^2)) \frac{1}{M_\pi^2 + q_1^2} \frac{1}{M_\pi^2 + q_2^2} + (1 \leftrightarrow 2), \\ g_4^4 &= \frac{id_9 g_A}{2F_\pi^2} M_\pi^2 \frac{1}{M_\pi^2 + q_1^2} - (1 \leftrightarrow 2), \\ g_4^5 &= -\frac{id_9 g_A}{F_\pi^2} (\vec{q}_1 \cdot \vec{q}_2) \frac{1}{M_\pi^2 + q_1^2} + (1 \leftrightarrow 2), \\ g_4^6 &= -\frac{id_9 g_A}{F_\pi^2} (\vec{q}_1 \cdot \vec{q}_2) \frac{1}{M_\pi^2 + q_1^2} - (1 \leftrightarrow 2), \\ g_4^9 &= -\frac{id_9 g_A}{2F_\pi^2} \frac{1}{M_\pi^2 + q_1^2} - (1 \leftrightarrow 2), \\ g_4^{10} &= \frac{id_9 g_A}{2F_\pi^2} \frac{1}{M_\pi^2 + q_1^2} + (1 \leftrightarrow 2). \end{aligned} \quad (3.54)$$

One-pion exchange relativistic correction

There are several types of graphs that can contribute to the OPE relativistic corrections. From [44] we obtain the following non-vanishing relativistic corrections to the charge density

$$\begin{aligned} J_{rel}^0 &= \sum_{i=1,2,4} \sum_{j=6,7,8} r_i^{jS}(\vec{q}_1, \vec{q}_2) T_i O_j^S \\ &+ \sum_{j=7,8} r_3^{jS}(\vec{q}_1, \vec{q}_2) T_3 O_j^S + \sum_{k=1}^4 r_3^{kS}(\vec{q}_1, \vec{q}_2) T_3 A_k^S, \end{aligned} \quad (3.55)$$

where the form factors contained in T_4 of the structure operator have the form:

$$\begin{aligned}
r_4^{6S} &= -\frac{g_A^2(2M_\pi^2 + q_1^2 + q_2^2)(-1 + 2\alpha_8)}{16F_\pi^2 M_n(M_\pi^2 + q_1^2)(M_\pi^2 + q_2^2)}, \\
r_4^{7S} &= \frac{g_A^2}{32F_\pi^2 M_n(M_\pi^2 + q_1^2)^2(M_\pi^2 + q_2^2)^2} \left(2M_\pi^4(q_1 q_2 z(-1 + 2\alpha_7) + q_1^2(1 + \alpha_7 - 3\alpha_8) \right. \\
&\quad + q_2^2(1 + \alpha_7 - 3\alpha_8)) + M_\pi^2(2q_1^3 q_2 z(-1 + 2\alpha_7) + 2q_1 q_2^3 z(-1 + 2\alpha_7) + q_1^4(1 - 2\alpha_8) \\
&\quad + q_2^4(1 - 2\alpha_8) + 8q_1^2 q_2^2(\alpha_7 - \alpha_8)) + q_1 q_2(q_1^4 z(-1 + 2\alpha_7) + q_2^4 z(-1 + 2\alpha_7) \\
&\quad \left. + 2q_1^3 q_2(\alpha_7 - \alpha_8) + 2q_1 q_2^3(\alpha_7 - \alpha_8)) + M_\pi^6(2 - 4\alpha_8) \right), \\
r_4^{8S} &= \frac{g_A^2(q_1^2 - q_2^2)}{32F_\pi^2 M_n(M_\pi^2 + q_1^2)^2(M_\pi^2 + q_2^2)^2} \left(M_\pi^2(2q_1 q_2 z(-1 + 2\alpha_7) + q_1^2(1 - 2\alpha_8) \right. \\
&\quad + q_2^2(1 - 2\alpha_8)) + (q_1 q_2(q_1^2 z(-1 + 2\alpha_7) \\
&\quad \left. + q_2^2 z(-1 + 2\alpha_7) + 2q_1 q_2(\alpha_7 - \alpha_8)) - 2M_\pi^4(-1 + \alpha_7 + \alpha_8) \right). \tag{3.56}
\end{aligned}$$

The r_i^{jS} form factors depend on new parameters: α_6 , α_7 and α_8 . In calculations, we used for r_4^j the following values [52]: $\alpha_7 = 1/4$ and $\alpha_8 = 0$. This is consistent with the chiral potential.

Short-range currents

An important contribution to the nuclear Hamiltonian is derived from the short-range interactions. Contact graphs representing such effects appear already in the first order of chiral expansion, so it is important to take into account these contributions in the description of dynamics. The short-range contributions to currents consist of: one-loop short-range currents that involve C_T , tree short-range currents resulting from gauging C_1, \dots, C_7 terms (with fixed coefficients) and additional short-range currents whose strength is not fixed by gauge invariance. The corresponding two LECs have to be adjusted to the data. The one-loop short-range contribution for the charge density and the vector part of current are represented by the structures:

$$J_{opect}^0 = \sum_{j=4,5,6,7} w_1^j(\vec{q}_1, \vec{q}_2) T_1 O_j^S, \vec{J}_{opect} = \sum_{j=4,6} w_2^j(\vec{q}_1, \vec{q}_2) T_2 O_j \tag{3.57}$$

where $w_i^j(\vec{q}_1, \vec{q}_2)$ are scalar functions corresponding to the $T_1(T_2)$ isospin operator for given spin operators.

Contact current operators start to appear at the same order as the TPE contributions, i.e. they are order $(\frac{Q}{\Lambda})^4$ suppressed compared to the leading single-nucleon charge density. The expression involves the following LECs: C_2, C_4, C_5, C_7, C'_1 and C'_2 . For C_2, C_4, C_5 and C_7 we use the same values as those used in the calculation of the potential (see Chapter 2). The C'_1 and C'_2 are related to the constants C'_{15} and C'_{16} of

Girlanda et al. [63].

$$\begin{aligned} \vec{J}_{cont} = & \sum_{j=4,6} h_2^j(\vec{q}_1, \vec{q}_2) T_2 O_j + \sum_{k=2,12,20,22} h_3^k(\vec{q}_1, \vec{q}_2) T_3 O_k \\ & + \sum_{n=3,5} h_5^n(\vec{q}_1, \vec{q}_2) T_5 O_n, \end{aligned} \quad (3.58)$$

where scalar form factors according to T_5 isospin structure are given by

$$h_5^3 = h_5^5 = 2C'_1. \quad (3.59)$$

Work on including all of these new parts of current to the formalism of electromagnetic reactions is in progress. However, this requires an estimation of many LECs, what is not trivial. In this thesis, we attempt to estimate the two LECs, C'_1 and d_9 , which appear in the operator structure of the current giving a contribution to the elastic electron scattering on deuteron. In case of this reaction, this is the overall contribution from the chiral electromagnetic currents at NLO.

Chapter 4

Formalism for selected electromagnetic two-nucleon reactions

As shown in the previous chapter, the general form of the nuclear matrix element is given as

$$N^\mu = \left\langle \Psi_f \vec{P}_f \left| \frac{1}{e} J^\mu(0) \right| \Psi_i \vec{P}_i \right\rangle \equiv \left\langle \Psi_f \left| J^\mu(\vec{Q}) \right| \Psi_i \right\rangle, \quad (4.1)$$

where it is understood that the current operator $J^\mu(\vec{Q})$ acts now between the internal initial and final two-nucleon states and e is the magnitude of the elementary charge. In this thesis we restrict ourselves to electron and photon scattering on the deuteron below the pion production threshold. In the case of electron scattering we assume that equation (3.9) holds for our non-relativistic framework. It can be written as

$$\omega N^0 - \vec{Q} \cdot \vec{N} = 0, \quad (4.2)$$

where (ω, \vec{Q}) is the four-momentum transferred to the nuclear system or, in other words, the four-momentum of the virtual photon. In the following we put $\vec{Q} \parallel \hat{z}$ and use the spherical unit vectors to expand \vec{N} as:

$$\vec{N} = \hat{e}_{+1}^* N_{+1} + \hat{e}_{-1}^* N_{-1} + \hat{z} N_z. \quad (4.3)$$

This allows us to express N_z in terms of the matrix element of the charge density operator, N^0 :

$$N_z = \frac{\omega}{|\vec{Q}|} N^0. \quad (4.4)$$

This means that for electron scattering processes we have to calculate three types of matrix elements: N^0 and $N_{\pm 1} \equiv \hat{e}_{\pm 1} \cdot \vec{N}$. For the photo-absorption processes, where we deal with real transverse photons, only $N_{\pm 1}$ will appear in the calculations. In the case of elastic electron-deuteron scattering both initial and final states are the deuteron states with the magnetic quantum numbers m_d (m'_d) in the initial (final) state

$$N_{ELAS}^\mu = \left\langle \Psi_{deut} m'_d \left| J^\mu(\vec{Q}) \right| \Psi_{deut} m_d \right\rangle. \quad (4.5)$$

The deuteron bound state is the solution to the Schrödinger equation

$$H |\Psi_{deut} m_d\rangle \equiv (H_0 + V) |\Psi_{deut} m_d\rangle = E_{deut} |\Psi_{deut} m_d\rangle, \quad (4.6)$$

where E_{deut} is the (negative) deuteron binding energy, V is the nucleon-nucleon potential and H_0 is the operator of the non-relativistic internal kinetic energy, given as

$$H_0 = \frac{\hat{p}^2}{M_N}, \quad (4.7)$$

where \hat{p} is the operator of the relative momentum in the two-nucleon system.

For inelastic electron-deuteron scattering or photo-disintegration of the deuteron we need matrix elements

$$N^\mu = \left\langle \Psi_{scatt} m_p m_n \left| J^\mu(\vec{Q}) \right| \Psi_{dcut} m_d \right\rangle, \quad (4.8)$$

which contain now the scattering state of two nucleons with the spin magnetic quantum numbers for the outgoing proton (m_p) and neutron (m_n). The scattering state is the solution of the Schrödinger equation for the positive internal energy, $E_{np} = \frac{\vec{p}_0^2}{M_N}$

$$(H_0 + V) |\Psi_{scatt} m_p m_n\rangle = E_{np} |\Psi_{scatt} m_p m_n\rangle, \quad (4.9)$$

where \vec{p}_0 is the asymptotic relative momentum of the proton-neutron system. The scattering state, $|\Psi_{scatt} m_p m_n\rangle$ can be defined as

$$|\Psi_{scatt} m_p m_n\rangle^{(-)} = \lim_{\epsilon \rightarrow 0^+} \frac{-i\epsilon}{E_{np} - i\epsilon - iH} \left| \phi m_p m_n \right\rangle_a, \quad (4.10)$$

where $|\phi m_p m_n\rangle_a$ is the antisymmetrized plane wave state describing the free relative motion (with momentum \vec{p}_0) of the proton and neutron with the spin projections m_p and m_n , respectively. It is convenient to introduce the scattering $T(z)$ -matrix, which satisfies the Lippmann-Schwinger equation

$$T(z) = V + T(z)G_0(z)V, \quad (4.11)$$

with $G_0(z)$ being the free two-nucleon propagator

$$G_0(z) \equiv \frac{1}{z - H_0}. \quad (4.12)$$

Using $T(z)$, we can write $|\Psi_{scatt} m_p m_n\rangle^{(-)}$ as

$$|\Psi_{scatt} m_p m_n\rangle^{(-)} = \lim_{\epsilon \rightarrow 0^+} (1 + G_0(E_{np} - i\epsilon) T(E_{np} - i\epsilon)) |\phi m_p m_n\rangle_a. \quad (4.13)$$

Thus the matrix element (4.8) can be written as

$$\begin{aligned} & \left\langle \Psi_{scatt} m_p m_n \left| J^\mu(\vec{Q}) \right| \Psi_{dcut} m_d \right\rangle = \\ & \lim_{\epsilon \rightarrow 0^+} {}_a \left\langle \phi m_p m_n \left| (1 + T(E_{np} + i\epsilon) G_0(E_{np} + i\epsilon)) J^\mu(\vec{Q}) \right| \Psi_{deut} m_d \right\rangle, \end{aligned} \quad (4.14)$$

which we split into the plane wave part

$$\begin{aligned} N_{PW}^\mu &\equiv {}_a \left\langle \phi m_p m_n \left| J^\mu(\vec{Q}) \right| \Psi_{deut} m_d \right\rangle, \\ &\equiv {}_a \left\langle \vec{p}_0 m_1 m_2 \nu_1 \nu_2 \left| J^\mu(\vec{Q}) \right| \Psi_{deut} m_d \right\rangle \end{aligned} \quad (4.15)$$

and the rescattering part

$$\begin{aligned} N_{RSC}^\mu &\equiv \lim_{\epsilon \rightarrow 0^+} {}_a \left\langle \phi m_p m_n \left| T(E_{np} + i\epsilon) G_0(E_{np} + i\epsilon) J^\mu(\vec{Q}) \right| \Psi_{deut} m_d \right\rangle \\ &\equiv \lim_{\epsilon \rightarrow 0^+} {}_a \left\langle \vec{p}_0 m_1 m_2 \nu_1 \nu_2 \left| T(E_{np} + i\epsilon) G_0(E_{np} + i\epsilon) J^\mu(\vec{Q}) \right| \Psi_{deut} m_d \right\rangle. \end{aligned} \quad (4.16)$$

Note that in the second lines of (4.15) and (4.16) we introduced the spin (m_i) and isospin (ν_i) projections of the two nucleons treated as identical particles.

In order to calculate (4.5), (4.15) and (4.16) we have to choose basis states necessary to represent all the relevant operators and states in the two-nucleon systems. As already stated, we work in the momentum space. In principle it would be possible to work directly with three-dimensional vectors [64], the nuclear forces and states are usually given in the so-called partial wave representation. Thus instead of employing the three-dimensional basis states $|\vec{p}\rangle$, which fulfill

$$\int d^3 p |\vec{p}\rangle \langle \vec{p}| = 1 \quad (4.17)$$

and

$$\langle \vec{p}' | \vec{p} \rangle = \delta^3(\vec{p}' - \vec{p}), \quad (4.18)$$

the bulk of our calculations is performed using a complete set

$$|p\alpha_2\rangle \equiv |p(ls)jm_j\rangle |tm_t\rangle \quad (4.19)$$

where p is the magnitude of the relative momentum, l and s , j , m_j are the orbital angular momentum, spin, total angular momentum and its projection on the quantisation axis \hat{z} . The isospin of the two-nucleon system and its projection are denoted by t and m_t . More explicitly we write

$$|p(ls)jm_j\rangle = \sum_{m_l=-l}^l c(l, s, j; m_l, m_j - m_l, m_j) |plm_l\rangle |sm_j - m_l\rangle, \quad (4.20)$$

$$|sm_s\rangle = \sum_{m_1=-\frac{1}{2}}^{\frac{1}{2}} c\left(\frac{1}{2}, \frac{1}{2}, s; m_1, m_s - m_1, m_s\right) \left|\frac{1}{2}m_1\right\rangle \left|\frac{1}{2}m_s - m_1\right\rangle \quad (4.21)$$

and similarly

$$|tm_t\rangle = \sum_{\nu_1=-\frac{1}{2}}^{\frac{1}{2}} c\left(\frac{1}{2}, \frac{1}{2}, t; \nu_1, m_t - \nu_1, m_t\right) \left|\frac{1}{2}\nu_1\right\rangle \left|\frac{1}{2}m_t - \nu_1\right\rangle, \quad (4.22)$$

where $c(j_1, j_2, j; m_1, m_2, m)$ is the Clebsch-Gordan coefficient [65]. In Equations (4.21) and (4.22) the spins (isospins) of individual nucleons are coupled to the total spin (isospin), respectively. Note that in our notation the isospin projection $\nu = \frac{1}{2}$ corresponds to the proton and $\nu = -\frac{1}{2}$ to the neutron. Thus for the proton-neutron system $m_t = 0$.

The momentum part of states (4.19) is normalised as

$$\langle \vec{p}' | p l m_l \rangle = \frac{\delta(p - p')}{pp'} Y_{lm_l}(\hat{p}'), \quad (4.23)$$

where $Y_{lm_l}(\hat{p})$ is the spherical harmonic [65]. The corresponding completeness relation reads

$$\sum_{\alpha_2} \int dp p^2 |p\alpha_2\rangle \langle p\alpha_2| = 1, \quad (4.24)$$

where, in principle, we need infinitely many $|\alpha_2\rangle$ states. In practice, however, we restrict ourselves to a finite number of basis vectors by demanding that the total angular momentum of the system is $j_{max} \geq 0$. Since the two-nucleon states are antisymmetric for the system of two identical fermions, we make also a restriction which allows us to reduce the number of the basis states (4.19)

$$(-1)^{l+s+t} = -1. \quad (4.25)$$

Thus we work with $N_{\alpha_2} = 2 + 4j_{max}$ states, where j_{max} is set according the given reaction kinematics and we always make sure that a sufficient number of channels guarantees the convergence of results. In the kinematical regime where our theory is applicable it is sufficient to consider $j_{max} \leq 10$.

In order to evaluate (4.5), (4.15) and (4.16) we represent first the deuteron state $|\Psi_{deut}m_d\rangle$ in our basis (4.19)

$$\begin{aligned} |\Psi_{deut}m_d\rangle &= \sum_{\alpha_2} \int_0^\infty dpp^2 |p\alpha_2\rangle \langle p\alpha_2| \Psi_{deut}m_d \rangle \\ &= \int_0^\infty dpp^2 (|p(01)1m_d\rangle |00\rangle \varphi_0(p) + |p(21)1m_d\rangle |00\rangle \varphi_2(p)), \end{aligned} \quad (4.26)$$

where we inserted the information about the deuteron quantum numbers ($l = 0, 2$, $s = 1$, $j = 1$, $t = 0$) and denoted the S - and D -components of the deuteron as $\varphi_0(p)$ and $\varphi_2(p)$, respectively. The way we obtain $\varphi_l(p)$ numerically will be outlined in Appendix A.

Next we calculate matrix elements of the single-nucleon current operator. For the charge density we obtain

$$\begin{aligned} & \left\langle p' (l' s') j' m'_j t' m'_t \left| J^0 (\vec{Q} \parallel \hat{z}) \right| \Psi_{dcut} m_d \right\rangle = \\ & 2 \left(\frac{1}{2} (G_E^p + G_E^n) \delta_{t',0} + \frac{1}{2} (G_E^n - G_E^p) \delta_{t',1} \right) \delta_{s',1} \delta_{m',m_d} \\ & \sum_{m'_l=-l'}^{l'} \sum_{l=0,2} \sum_{m_l=-l}^l \delta_{m'-m'_l, m_d-m_l} c(l', s', j'; m'_l, m' - m'_l, m') \\ & c(l, 1, 1; m_l, m_d - m_l, m_d) \int d\hat{p}' Y_{l'm'_l}^* (\hat{p}') Y_{lm_l} \left(\widehat{\vec{p}' + \frac{1}{2}\vec{Q}} \right) \varphi_l \left(\left| \vec{p}' + \frac{1}{2}\vec{Q} \right| \right), \quad (4.27) \end{aligned}$$

where $\widehat{\vec{a} + \vec{b}}$ denotes the direction of the unit vector $\frac{\vec{a} + \vec{b}}{|\vec{a} + \vec{b}|}$. For the spherical component $\tau = \pm 1$ of the convection current we get

$$\begin{aligned} & \left\langle p' (l' s') j' m'_j t' m'_t \left| J_\tau^{conv} (\vec{Q} \parallel \hat{z}) \right| \Psi_{dcut} m_d \right\rangle = \\ & 2 \left(\frac{1}{2} (G_E^p + G_E^n) \delta_{t',0} + \frac{1}{2} (G_E^n - G_E^p) \delta_{t',1} \right) \left(-\sqrt{\frac{4\pi}{3}} \frac{p'}{M_N} \right) \delta_{s',1} \delta_{m',m_d+\tau} \\ & \sum_{m'_l=-l'}^{l'} \sum_{l=0,2} \sum_{m_l=-l}^l \delta_{m'-m'_l, m_d-m_l} c(l', s', j'; m'_l, m' - m'_l, m') \\ & c(l, 1, 1; m_l, m_d - m_l, m_d) \int d\hat{p}' Y_{l'm'_l}^* (\hat{p}') Y_{1\tau} \left(\hat{p}' \right) Y_{lm_l} \left(\widehat{\vec{p}' + \frac{1}{2}\vec{Q}} \right) \varphi_l \left(\left| \vec{p}' + \frac{1}{2}\vec{Q} \right| \right). \quad (4.28) \end{aligned}$$

Finally, for the spherical component τ of the spin current we get

$$\begin{aligned} & \left\langle p' (l' s') j' m'_j t' m'_t \left| J_\tau^{spin} (\vec{Q} \parallel \hat{z}) \right| \Psi_{deut} m_d \right\rangle = \\ & 2 \left(\frac{1}{2} (G_M^p + G_M^n) \delta_{t',0} + \frac{1}{2} (G_M^n - G_M^p) \delta_{t',1} \right) \frac{Q}{2M_N} \tau \delta_{m',m_d+\tau} \\ & \sum_{m'_l=-l'}^{l'} \sum_{l=0,2} \sum_{m_l=-l}^l c(l', s', j'; m'_l, m' - m'_l, m') c(l, 1, 1; m_l, m_d - m_l, m_d) \\ & c(1, 1, s'; \tau, m_d - m_l, m' - m'_l) \sqrt{18} \left\{ \begin{array}{ccc} \frac{1}{2} & 1 & \frac{1}{2} \\ s' & \frac{1}{2} & 1 \end{array} \right\} \\ & \int d\hat{p}' Y_{l'm'_l}^* (\hat{p}') Y_{lm_l} \left(\widehat{\vec{p}' + \frac{1}{2}\vec{Q}} \right) \varphi_l \left(\left| \vec{p}' + \frac{1}{2}\vec{Q} \right| \right). \quad (4.29) \end{aligned}$$

The calculation of the corresponding matrix elements for the two-nucleon current is performed in two steps. In the first step, which is described in detail in Section 4.1,

we evaluate matrix elements

$$\left\langle p' (l's') j'm'_j t'm'_t \left| J_{12}^0 (\vec{Q} \parallel \hat{z}) \right| p (ls) jm_j tm_t \right\rangle \quad (4.30)$$

and

$$\left\langle p' (l's') j'm'_j t'm'_t \left| J_{12\tau} (\vec{Q} \parallel \hat{z}) \right| p (ls) jm_j tm_t \right\rangle. \quad (4.31)$$

Then the application to the deuteron state is straightforward and using an obvious shorthand notation reads

$$\begin{aligned} & \left\langle p' (l's') j'm'_j t'm'_t \left| J_{12}^\mu (\vec{Q} \parallel \hat{z}) \right| \Psi_{dcut} m_d \right\rangle = \\ & \sum_{\alpha_2} \int_0^\infty dp p^2 \left\langle p' (l's') j'm'_j t'm'_t \left| J_{12}^\mu (\vec{Q} \parallel \hat{z}) \right| p\alpha_2 \right\rangle \langle p\alpha_2 | \Psi_{deut} m_d \rangle. \end{aligned} \quad (4.32)$$

In the following we assume that the matrix elements of the full current operator contain contributions from the single nucleon current and the two-nucleon part. It is important to realize that the choice $\vec{Q} \parallel \hat{z}$ leads to relations between the current matrix elements. Namely,

$$\begin{aligned} & \left\langle p' (l's') j'm'_j t'm'_t \left| J^0 (\vec{Q} \parallel \hat{z}) \right| \Psi_{dcut} - m_d \right\rangle = \\ & (-1)^{l'+j'+1} \left\langle p' (l's') j'm'_j t'm'_t \left| J^0 (\vec{Q} \parallel \hat{z}) \right| \Psi_{dcut} m_d \right\rangle \end{aligned} \quad (4.33)$$

and

$$\begin{aligned} & \left\langle p' (l's') j'm'_j t'm'_t \left| J_{-1} (\vec{Q} \parallel \hat{z}) \right| \Psi_{deut} m_d \right\rangle = \\ & (-1)^{l'+j'+1} \left\langle p' (l's') j'm'_j t'm'_t \left| J_{+1} (\vec{Q} \parallel \hat{z}) \right| \Psi_{dcut} - m_d \right\rangle. \end{aligned} \quad (4.34)$$

At this point we have all ingredients necessary to calculate the matrix elements for the elastic process (4.5). They take the following form

$$N_{ELAS}^\mu = \sum_{\alpha'_2} \int_0^\infty dp' p'^2 \langle \Psi_{deut} m'_d | p'\alpha'_2 \rangle \left\langle p'\alpha'_2 \left| J^\mu (\vec{Q} \parallel \hat{z}) \right| \Psi_{deut} m_d \right\rangle. \quad (4.35)$$

Note that because of the deuteron properties, in (4.32) and (4.35) only two states contribute.

Let us now turn to the inelastic reactions. In this case we distinguish between the plane wave and the rescattering parts. In the latter case we solve first the Lippmann-Schwinger equation in the partial wave representation (see Appendix B) to get

$$\lim_{\epsilon \rightarrow 0^+} \langle p'\alpha'_2 | T(E_{np} + i\epsilon) | p\alpha_2 \rangle \quad (4.36)$$

and then evaluate (4.16) (the limit is understood implicitly) with the following result:

$$\begin{aligned} & \left\langle p''\alpha_2'' \left| T(E_{np} + i\epsilon) G_0(E_{np} + i\epsilon) J^\mu(\vec{Q} \parallel \hat{z}) \right| \Psi_{deut} m_d \right\rangle = \\ & M_N \sum_{\alpha'_2} \int_0^{\bar{p}} dp' p'^2 \frac{\langle p''\alpha_2'' | T | p'\alpha'_2 \rangle \langle p'\alpha'_2 | J^\mu(\vec{Q} \parallel \hat{z}) | \Psi_{deut} m_d \rangle}{p_0^2 - p'^2 + i\epsilon} = \\ & M_N \sum_{\alpha'_2} \left[\int_0^{\bar{p}} dp' \frac{p'^2 f_{\alpha'_2}(p') - p_0^2 f_{\alpha'_2}(p_0)}{p_0^2 - p'^2} + \frac{1}{2} p_0 f_{\alpha'_2}(p_0) \left(\ln \left| \frac{\bar{p} + p_0}{\bar{p} - p_0} \right| - i\pi \right) \right], \quad (4.37) \end{aligned}$$

where

$$f_{\alpha_2}(p') \equiv \langle p''\alpha_2'' | T | p'\alpha'_2 \rangle \langle p'\alpha'_2 | J^\mu(\vec{Q} \parallel \hat{z}) | \Psi_{deut} m_d \rangle. \quad (4.38)$$

We used the fact that $G_0(z)$ is diagonal

$$\langle p'\alpha'_2 | G_0(z) | p\alpha_2 \rangle = \delta_{\alpha'_2, \alpha_2} \frac{\delta(p' - p)}{pp'} \frac{1}{z - \frac{p^2}{M_N}} \quad (4.39)$$

and treated the resulting Cauchy singularity by subtraction. We introduced the upper limit for the p' integration, \bar{p} , because, due to the properties of the T -matrix elements (see Appendix B), contributions to the integral for larger momenta are negligible. With this result we can easily write the rescattering amplitude as

$$\begin{aligned} N_{RSC}^\mu &= {}_a \left\langle \vec{p}_0 m_1 m_2 \nu_1 \nu_2 \left| T(E_{np} + i\epsilon) G_0(E_{np} + i\epsilon) J^\mu(\vec{Q}) \right| \Psi_{deut} m_d \right\rangle \\ &\equiv \left\langle \vec{p}_0 m_1 m_2 \nu_1 \nu_2 \left| \frac{1 - P_{12}}{2} T(E_{np} + i\epsilon) G_0(E_{np} + i\epsilon) J^\mu(\vec{Q}) \right| \Psi_{deut} m_d \right\rangle \\ &= \sum_{\alpha''_2} \int dp'' p''^2 \langle \vec{p}_0 m_1 m_2 \nu_1 \nu_2 | p''\alpha''_2 \rangle \\ &\quad \left\langle p''\alpha''_2 \left| \frac{1 - P_{12}}{2} T(E_{np} + i\epsilon) G_0(E_{np} + i\epsilon) J^\mu(\vec{Q}) \right| \Psi_{deut} m_d \right\rangle \\ &= \sum_{\alpha''_2} \int dp'' p''^2 \langle \vec{p}_0 m_1 m_2 \nu_1 \nu_2 | p''\alpha''_2 \rangle \\ &\quad \left\langle p''\alpha''_2 | T(E_{np} + i\epsilon) G_0(E_{np} + i\epsilon) J^\mu(\vec{Q}) | \Psi_{deut} m_d \right\rangle. \quad (4.40) \end{aligned}$$

We could remove the permutation operator $\frac{1}{2}(1 - P_{12})$ because the $| p\alpha_2 \rangle$ states are already antisymmetric and

$$\left\langle p''\alpha''_2 \left| \frac{1 - P_{12}}{2} \right. \right\rangle = \left\langle p''\alpha''_2 \right|. \quad (4.41)$$

Using the very definition of the $|\alpha_2\rangle$ states and (4.23), the overlap $\langle \vec{p}_0 m_1 m_2 \nu_1 \nu_2 | p'' \alpha_2'' \rangle$ takes the form

$$\begin{aligned} \langle \vec{p}_0 m_1 m_2 \nu_1 \nu_2 | p'' \alpha_2'' \rangle &= \frac{\delta(p_0 - p'')}{p_0^2} \sum_{m_l'' = -l''}^{l''} c(l'', s'', j''; m_l'', m_j'' - m_l'', m_j'') \\ &\quad Y_{l'' m_l''}(\hat{p}_0) c\left(\frac{1}{2}, \frac{1}{2}, s''; m_1, m_2, m_j'' - m_l''\right) c\left(\frac{1}{2}, \frac{1}{2}, t''; \nu_1, \nu_2, m_t''\right) \end{aligned} \quad (4.42)$$

and finally

$$\begin{aligned} N_{RSC}^\mu &= \sum_{\alpha_2''} \left\langle p_0 \alpha_2'' \left| T(E_{np} + i\epsilon) G_0(E_{np} + i\epsilon) J^\mu(\vec{Q}) \right| \Psi_{dcut} m_d \right\rangle \\ &\quad \sum_{m_l'' = -l''}^{l''} c(l'', s'', j''; m_l'', m_j'' - m_l'', m_j'') Y_{l'' m_l''}(\hat{p}_0) \\ &\quad c\left(\frac{1}{2}, \frac{1}{2}, s''; m_1, m_2, m_j'' - m_l''\right) c\left(\frac{1}{2}, \frac{1}{2}, t''; \nu_1, \nu_2, m_t''\right). \end{aligned} \quad (4.43)$$

We could, in principle, use the same formula for the plane wave amplitude, N_{PW}^μ . We would just make a replacement in (4.43)

$$\left\langle p_0 \alpha_2'' \left| T(E_{np} + i\epsilon) G_0(E_{np} + i\epsilon) J^\mu(\vec{Q}) \right| \Psi_{dcut} m_d \right\rangle \longrightarrow \left\langle p_0 \alpha_2'' \left| J^\mu(\vec{Q}) \right| \Psi_{dcut} m_d \right\rangle$$

which yields

$$\begin{aligned} N_{PW}^\mu &= \sum_{\alpha_2''} \left\langle p_0 \alpha_2'' \left| J^\mu(\vec{Q}) \right| \Psi_{dcut} m_d \right\rangle \\ &\quad \sum_{m_l'' = -l''}^{l''} c(l'', s'', j''; m_l'', m_j'' - m_l'', m_j'') Y_{l'' m_l''}(\hat{p}_0) \\ &\quad c\left(\frac{1}{2}, \frac{1}{2}, s''; m_1, m_2, m_j'' - m_l''\right) c\left(\frac{1}{2}, \frac{1}{2}, t''; \nu_1, \nu_2, m_t''\right). \end{aligned} \quad (4.44)$$

It turns out, however, that for the single-nucleon current operator Equation (4.44) requires that very many basis states have to be taken in the sum over α_2'' . That is why we decided to calculate this part of N_{PW}^μ using directly Equations (3.18), (3.19) and (3.20) in their integral form. Taking into account that

$$_a\left\langle \vec{p}_0 m_1 m_2 \nu_1 \nu_2 \right| = \frac{1}{2} \left\langle \vec{p}_0 m_1 m_2 \nu_1 \nu_2 \right| - \frac{1}{2} \left\langle -\vec{p}_0 m_2 m_1 \nu_2 \nu_1 \right| \quad (4.45)$$

we obtain for the charge density the following equation

$$\begin{aligned} N_{1;PW}^0 \equiv & {}_a \left\langle \vec{p}_0 m_1 m_2 \nu_1 \nu_2 = -\nu_1 \left| J^0(1; \vec{Q} \parallel \hat{z}) \right| \Psi_{dcut} m_d \right\rangle = \\ & 2H(\nu_1) \sum_{l=0,2} \sum_{m_l=-l}^l c(l, 1, 1; m_l, m_d - m_l, m_d) \\ & c\left(\frac{1}{2}, \frac{1}{2}, 1; m_1, m_2, m_d - m_l\right) Y_{lm_l}\left(\vec{p}_0 + \widehat{\frac{1}{2}\vec{Q}}\right) \varphi_l\left(\left|\vec{p}_0 + \frac{1}{2}\vec{Q}\right|\right) \\ & -2H(-\nu_1) \sum_{l=0,2} \sum_{m_l=-l}^l c(l, 1, 1; m_l, m_d - m_l, m_d) \\ & c\left(\frac{1}{2}, \frac{1}{2}, 1; m_2, m_1, m_d - m_l\right) Y_{lm_l}\left(-\vec{p}_0 + \widehat{\frac{1}{2}\vec{Q}}\right) \varphi_l\left(\left|-\vec{p}_0 + \frac{1}{2}\vec{Q}\right|\right), \end{aligned} \quad (4.46)$$

where the matrix element in the isospin space is

$$H(\nu_1) \equiv \begin{cases} \frac{G_E^n}{\sqrt{2}}, \nu_1 = \frac{1}{2} \\ -\frac{G_E^p}{\sqrt{2}}, \nu_1 = -\frac{1}{2} \end{cases} \quad (4.47)$$

For the convection current we get

$$\begin{aligned} N_{conv;\tau;PW} \equiv & {}_a \left\langle \vec{p}_0 m_1 m_2 \nu_1 \nu_2 = -\nu_1 \left| J_{conv;\tau}(\vec{Q} \parallel \hat{z}) \right| \Psi_{dcut} m_d \right\rangle = \\ & 2H(\nu_1) \left(-\frac{p_0}{M_N} \sqrt{\frac{4\pi}{3}} Y_{1\tau}(\hat{p}_0) \right) \sum_{l=0,2} \sum_{m_l=-l}^l c(l, 1, 1; m_l, m_d - m_l, m_d) \\ & c\left(\frac{1}{2}, \frac{1}{2}, 1; m_1, m_2, m_d - m_l\right) Y_{lm_l}\left(\vec{p}_0 + \widehat{\frac{1}{2}\vec{Q}}\right) \varphi_l\left(\left|\vec{p}_0 + \frac{1}{2}\vec{Q}\right|\right) \\ & -2H(-\nu_1) \left(-\frac{p_0}{M_N} \sqrt{\frac{4\pi}{3}} Y_{1\tau}(-\hat{p}_0) \right) \sum_{l=0,2} \sum_{m_l=-l}^l c(l, 1, 1; m_l, m_d - m_l, m_d) \\ & c\left(\frac{1}{2}, \frac{1}{2}, 1; m_2, m_1, m_d - m_l\right) Y_{lm_l}\left(-\vec{p}_0 + \widehat{\frac{1}{2}\vec{Q}}\right) \varphi_l\left(\left|-\vec{p}_0 + \frac{1}{2}\vec{Q}\right|\right), \end{aligned} \quad (4.48)$$

and for the spin current reads

$$\begin{aligned}
N_{spin;\tau;PW} \equiv {}_a \left\langle \vec{p}_0 m_1 m_2 \nu_1 \nu_2 = -\nu_1 \left| J_{spin;\tau}(\vec{Q} \parallel \hat{z}) \right| \Psi_{deut} m_d \right\rangle = \\
2W(\nu_1) \left(\frac{|\vec{Q}|}{2M_N} \tau \right) \sum_{l=0,2} \sum_{m_l=-l}^l c(l, 1, 1; m_l, m_d - m_l, m_d) \\
c \left(\frac{1}{2}, \frac{1}{2}, 1; m_1, m_d - m_l - m_1, m_d - m_l \right) (-\sqrt{3}) c \left(1, \frac{1}{2}, \frac{1}{2}; \tau, m_d - m_l - m_1, m_2 \right) \\
Y_{lm_l} \left(\widehat{\vec{p}_0 + \frac{1}{2}\vec{Q}} \right) \varphi_l \left(\left| \vec{p}_0 + \frac{1}{2}\vec{Q} \right| \right) \\
-2W(-\nu_1) \left(\frac{|\vec{Q}|}{2M_N} \tau \right) \sum_{l=0,2} \sum_{m_l=-l}^l c(l, 1, 1; m_l, m_d - m_l, m_d) \\
c \left(\frac{1}{2}, \frac{1}{2}, 1; m_2, m_d - m_l - m_2, m_d - m_l \right) (-\sqrt{3}) c \left(1, \frac{1}{2}, \frac{1}{2}; \tau, m_d - m_l - m_2, m_1 \right) \\
Y_{lm_l} \left(\widehat{-\vec{p}_0 + \frac{1}{2}\vec{Q}} \right) \varphi_l \left(\left| -\vec{p}_0 + \frac{1}{2}\vec{Q} \right| \right), \tag{4.49}
\end{aligned}$$

where

$$W(\nu_1) \equiv \begin{cases} \frac{G_M^n}{\sqrt{2}}, \nu_1 = \frac{1}{2} \\ -\frac{G_M^p}{\sqrt{2}}, \nu_1 = -\frac{1}{2} \end{cases} \tag{4.50}$$

and we used

$$\langle m' | \sigma_\tau | m \rangle = (-\sqrt{3}) c \left(1, \frac{1}{2}, \frac{1}{2}; \tau, m, m' \right). \tag{4.51}$$

4.1 Matrix elements for the two-nucleon current operator

Different contributions to the two-nucleon current operator were discussed in the previous chapters. Also the most general form of the two-nucleon current was introduced both for the charge density and for other components of (3.27). Those expressions were given in the three-dimensional form. For our calculations it is necessary to find the following matrix elements:

$$\left\langle p'\alpha'_2 \left| J_{12}^\mu(\vec{Q} \parallel \hat{z}) \right| p\alpha_2 \right\rangle = \int d\vec{p}' \int d\vec{p} \langle p'\alpha'_2 | \vec{p}' \rangle \left\langle \vec{p}' \left| J_{12}^\mu(\vec{Q} \parallel \hat{z}) \right| \vec{p} \right\rangle \langle \vec{p} | p\alpha_2 \rangle. \quad (4.52)$$

It is clear that contrary to the traditional approach, where the number of spin-isospin structures in $J_{12}^\mu(\vec{Q})$ was rather limited, in the chiral framework we can expect very many different contributions. The traditional way of partial wave decomposition [66] could be in principle employed but this would be a formidable task. Thus we decided from the very beginning to use a completely new, automated method, which was also successfully tested in partial wave decomposition of few-nucleon forces [67].

Let us consider a single term in Equations (3.27) and (3.28), $f_i^j(\vec{q}_1, \vec{q}_2) \hat{T}_i \hat{O}_j$ or $f_i^{jS}(\vec{q}_1, \vec{q}_2) \hat{T}_i \hat{O}_j^S$ and insert it in Equation (4.52). We obtain

$$\begin{aligned} & \left\langle p'(l's')j'm'_j; t'm'_t \left| J_i^j(\vec{Q} \parallel \hat{z}) \right| p(ls)jm_j; tm_t \right\rangle = \\ & \int d\hat{p}' \int d\hat{p} \sum_{m'_l} \sum_{m_l} c(l', s', j'; m'_l, m' - m'_l, m'_j) \\ & c(l, s, j; m_l, m - m_l, m_j) Y_{l'm'_l}^*(\hat{p}') Y_{lm_l}(\hat{p}) f_i^j(\vec{q}_1, \vec{q}_2) \\ & \langle s'm'_s - m'_l | \hat{O}_j | sm_s - m_l \rangle \langle t'm'_t | \hat{T}_i | tm_t \rangle. \end{aligned} \quad (4.53)$$

The main point of our new method is the observation that the spin and isospin matrix elements in Equation (4.53), $\langle s'm'_s | \hat{O}_j | sm_s \rangle$ and $\langle t'm'_t | \hat{T}_i | tm_t \rangle$, can be calculated analytically. We used *Mathematica* \textcircled{C} [49] scripts not only to get all spin (isospin) matrix elements but also to directly produce essential parts of the Fortran code. In order to calculate the four-fold integrals in Equation (4.53) for the whole grids of p and p' points and all non-vanishing $(\alpha'_2, \alpha_2, m_j)$ combinations we used the powerful parallel computers of the Jülich Supercomputing Center (JSC) in Germany.

We prepared different versions of *Mathematica* \textcircled{C} scripts. The calculations proved particularly simple with the concept of the Kronecker product which makes such matrix elements simple matrix elements in the four-dimensional space. An example of such a script is given in Appendix C.

At this point we would like to make the following remark. In particular, performing calculations with several thousands of processors requires in particular careful preparations. It is also necessary to be able to compare output from the new system with well established results. Such double-checking proved to be necessary in the case of our calculations, because we discovered a compiler error on the most important JSC

computer. Thus before we started "production" of totally new results, we carefully compared matrix elements of the leading one-pion-exchange current operator, calculated in a traditional partial wave decomposition with the results from the parallel machine.

In the following figures we show directly the most important ingredients of our scheme, namely

$$\langle p\alpha_2 | J_{+1}(\vec{Q} \parallel \hat{z}) | \psi_{deut} m_d \rangle \quad (4.54)$$

as a function of p for $m_d = +1$ and several α_2 "channels". This serves two purposes. First, we used to look at such matrix elements in order to check the numerical stability and accuracy of our results. Secondly, we wanted to compare contributions from the single-nucleon (known), leading one-pion-exchange (known) and leading two-pion-exchange (unknown !) current operators. Since the two latter contributions are zero for α_2 channels with $t = 0$, we choose three α_2 examples with $t = 1$. We restrict ourselves to $+1$ spherical component of the vector current operator because it appears both in the description of the electro- and photo-disintegration reactions.

In the case of $\alpha_2 = \{l = 0, s = 0, j = 0\}$ the main contribution comes from the spin part of the single-nucleon current. (The convection part is zero.) The corrections from OPE and TPE are hardly visible. For $\alpha_2 = \{l = 1, s = 1, j = 0\}$ the situation is quite different. At least in a certain range of p we can clearly separate contributions from the convection and spin parts of the single-nucleon current as well as from the OPE and TPE operators. For the highest considered p values TPE contributions are, in fact, dominant. Finally, for $\alpha_2 = \{l = 3, s = 1, j = 2\}$ for very small p values the single-nucleon current (in fact its spin part) is the most important. But already for $p \approx 0.5 \text{ fm}^{-1}$ the OPE contribution is overwhelming. We get only small corrections from TPE in this case. We show matrix elements (4.54) for two Q values and see no quantitative difference, at least between 30 and 60 MeV/c. Of course, in other α_2 "channels" this picture might look differently.

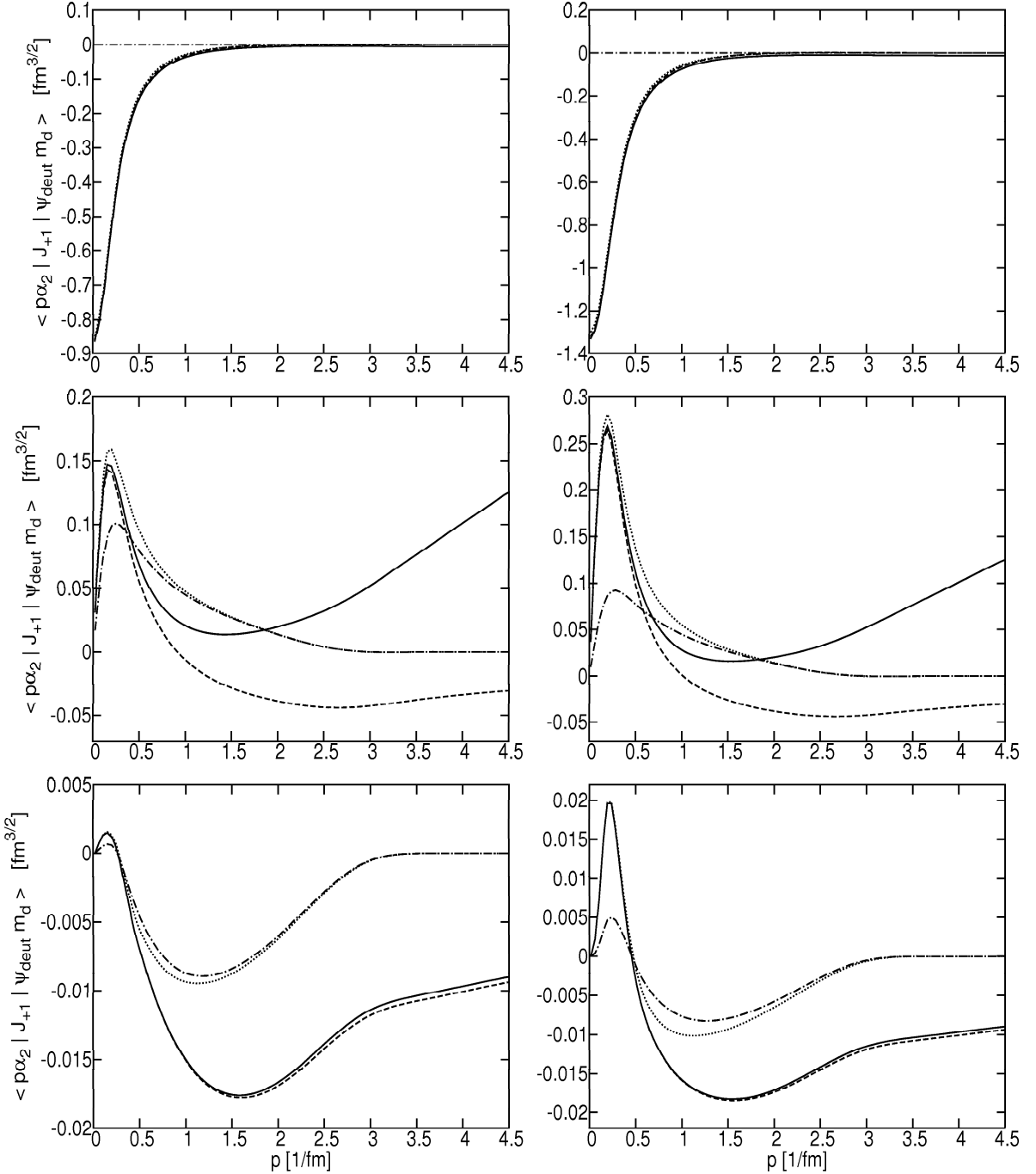


Figure 4.1: Different contributions to the matrix elements given in Equation (4.54) for $m_d = 1$ and $\alpha_2 = \{l = 0, s = 0, j = 0\}$ (upper row), $\alpha_2 = \{l = 1, s = 1, j = 0\}$ (middle row) and $\alpha_2 = \{l = 3, s = 1, j = 2\}$ (lower row) as a function of p (see text). The left (right) panel is for $Q = 30 \text{ MeV}/c$ ($Q = 60 \text{ MeV}/c$). Dash-dotted lines show contribution from the convection current, dotted lines display results from the total single nucleon current operator (convection + spin). Results obtained with the sum of the single nucleon current and the leading OPE current operators are represented with dashed lines. Finally, we add the leading long-range TPE currents which leads to predictions shown with solid lines.

Chapter 5

Electron-deuteron scattering

Electron scattering from nuclei has a long and rich history. It is a powerful tool for obtaining information on many important properties of nuclei, for example on their charge distributions. This idea was postulated long time ago [68, 69, 70, 71] and electron scattering by nuclei has been studied both experimentally and theoretically for many years.

At present electron scattering is studied with the aim to probe the nuclear wave functions and obtain information about the nuclear current operator. In this context, the few-body systems ($A \leq 3$) are particularly important since the two- and three-nucleon bound and scattering states, at least nonrelativistically, can be calculated accurately for any given two- and three-body interactions. First, elastic and inelastic electron scattering from the deuteron has been measured and analyzed by many authors. The deuteron is the only two nucleon bound state of two nucleons and thus it is the most fundamental system in nuclear physics. Deuteron electromagnetic form factors calculated for elastic electron-deuteron scattering provide a crucial test for any model of the deuteron [72, 73]. Experimental studies of inelastic electron-deuteron scattering inspired many theoretical efforts and have greatly contributed to our understanding of the nucleon-nucleon interaction and the role of the meson exchange current or relativistic corrections in the nuclear systems. Recent review articles [74, 75, 76, 77, 78] illustrate the present state of knowledge on the structure of the deuteron and, more generally, on the dynamical picture of the electron-deuteron scattering reactions.

Much later, exact solutions of the Schrödinger equations for the three-nucleon bound and scattering states became available, which resulted in many experimental and theoretical investigations of elastic and inelastic electron scattering on ${}^3\text{He}$ and ${}^3\text{H}$ [54].

Since the electromagnetic interaction is relatively weak, it can be treated perturbatively. This leads to the so-called one-photon exchange approximation, which we use in this thesis. The scattering amplitude is then written as a contraction of the electron part with the nuclear matrix element supplemented by the virtual photon propagator

$$M = -\frac{e^2}{\mathbf{q}^2} \left[\bar{u}(k', h') \gamma_\mu u(k, h) \right] \left\langle \Psi_f m_f \left| J^\mu(\vec{Q}) \right| \Psi_{deut} m_d \right\rangle, \quad (5.1)$$

which is schematically given in Figure 5.1. The expressions for both the photon propagator and the so-called "electron arm" are analytically known [79]. In the electron

part one finds the Dirac spinors representing the electron in the initial state (with the four-momentum k and the helicity h) and in the final state (with the four-momentum k' and the helicity h') as well as the standard γ^μ -matrix [79]. Usually the electron mass

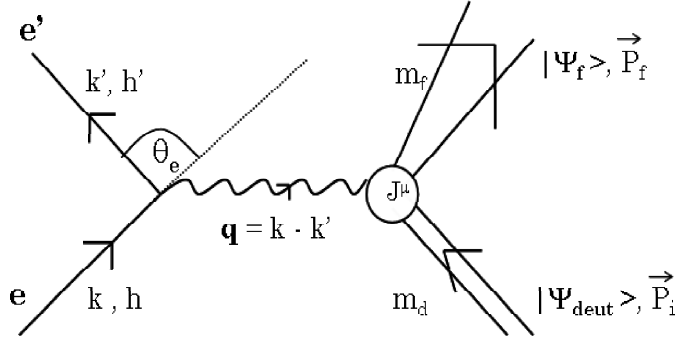


Figure 5.1: General diagram for electron-deuteron scattering which leads to the final state $|\Psi_f\rangle$ with the total momentum P_f and the set of spin magnetic quantum numbers m_f .

is very small compared to its total energy in the initial state ($k_0 \equiv E$) and in the final state ($k'_0 \equiv E'$) and can be neglected, which leads to simple expressions for the energy transfer, ω , and the three-momentum transfer \vec{Q}

$$\omega = k_0 - k'_0 \equiv E - E' \approx |\vec{k}| - |\vec{k}'|, \quad (5.2)$$

$$\vec{Q} = \vec{k} - \vec{k}'.$$

The four-momentum transfer squared

$$\mathbf{q}^2 \equiv \omega^2 - \vec{Q}^2 \quad (5.4)$$

is often expressed in terms of the initial electron energy, the final electron energy and the electron scattering angle θ_e

$$\mathbf{q}^2 = -4EE' \sin^2 \frac{\theta_e}{2}. \quad (5.5)$$

In the following we will often use two abbreviations: $Q \equiv |\vec{Q}|$ and $\mathbf{q} \equiv \sqrt{-\mathbf{q}^2}$.

Following Donnelly and Raskin [80], we write the cross section for electron-nucleus scattering in a very general form as

$$\sigma = \Sigma + h\Delta, \quad (5.6)$$

where we only assume that the final electron helicity h' is not observed. Otherwise this formula holds both for the elastic and inelastic processes and can contain all information about the spin projections in the initial and final nuclear state. The dependence on the initial electron helicity h is given explicitly, which means that for the unpolarized electron in the initial state the term with Δ does not contribute. The Σ and Δ parts of the cross section can be written as

$$\Sigma = \sigma_{Mott} (v_L R_L + v_T R_T + v_{TT} R_{TT} + v_{TL} R_{TL}) \rho, \quad (5.7)$$

and

$$\Delta = \sigma_{Mott} (v_{T'} R_{T'} + v_{TL'} R_{TL'}) \rho. \quad (5.8)$$

The Mott cross section

$$\sigma_{Mott} = \frac{\alpha^2 \cos^2(\frac{\theta_e}{2})}{4E^2 \sin^4(\frac{\theta_e}{2})}, \quad (5.9)$$

contains, in particular, the fine structure constant $\alpha \approx \frac{1}{137}$ and ρ – the appropriate phase space factor. For example, in the case of elastic electron-deuteron scattering

$$\rho = \frac{E'}{E} \frac{E'_d}{M_d}. \quad (5.10)$$

The kinematical functions v are

$$\begin{aligned} v_L &= \frac{(\mathbf{q}^2)^2}{Q^4}, \\ v_T &= -\frac{1}{2} \frac{\mathbf{q}^2}{Q^2} + \tan^2 \frac{\theta_e}{2}, \\ v_{TT} &= \frac{1}{2} \frac{\mathbf{q}^2}{Q^2}, \\ v_{TL} &= \frac{1}{\sqrt{2}} \frac{\mathbf{q}^2}{Q^2} \left[-\frac{\mathbf{q}^2}{Q^2} + \tan^2 \frac{\theta_e}{2} \right]^{1/2}, \\ v_{T'} &= \tan \frac{\theta_e}{2} \left[-\frac{\mathbf{q}^2}{Q^2} + \tan^2 \frac{\theta_e}{2} \right]^{1/2}, \\ v_{TL'} &= \frac{1}{\sqrt{2}} \frac{\mathbf{q}^2}{Q^2} \tan \frac{\theta_e}{2}, \end{aligned} \quad (5.11)$$

and the nuclear response functions R can be expressed in terms of the nuclear matrix elements N^0 and $N_{\pm 1}$

$$\begin{aligned} R_L &= |N^0|^2, \\ R_T &= |N_{+1}|^2 + |N_{-1}|^2, \\ R_{TT} &= 2\text{Re}(N_{+1} N_{-1}^*), \\ R_{TL} &= -2\text{Re}(N^0(N_{+1} - N_{-1})^*), \\ R_{T'} &= |N_{+1}|^2 - |N_{-1}|^2, \\ R_{TL'} &= -2\text{Re}(N^0(N_{+1} + N_{-1})^*), \end{aligned} \quad (5.12)$$

where $\text{Re}(z)$ denotes the real part of z .

5.1 Elastic electron scattering off deuteron

In the case of elastic electron-deuteron scattering both the initial and final 2N states have isospin $t = 0$. In the matrix elements

$$N_{ELAS}^0 = \langle \Psi_{deut} m'_d | J^0(\vec{Q}) | \Psi_{deut} m_d \rangle \quad (5.13)$$

and

$$N_{\pm 1,ELAS} = \langle \Psi_{deut} m'_d | J_{\pm 1}(\vec{Q}) | \Psi_{deut} m_d \rangle \quad (5.14)$$

we thus find contributions from the single nucleon current operator and from these relatively few parts of the 2N current operator with the T_4 and T_5 isospin operators. Namely, for this elastic process we encounter (in the charge density matrix element N_{ELAS}^0) contributions from the single nucleon charge density $J_{single}^0(\vec{Q})$ and from the relativistic corrections to the 2N one-pion-exchange current operator $J_{rel}^0(\vec{Q})$

$$N_{ELAS}^0 = \langle \Psi_{deut} m'_d | J_{single}^0(\vec{Q}) + J_{rel}^0(\vec{Q}) | \Psi_{deut} m_d \rangle, \quad (5.15)$$

where (as given in Chapter 3):

$$J_{rel}^0 = \sum_{j=6,7,8} r_4^{jS} T_4 O_j^S \quad (5.16)$$

and r_4^{jS} are, as usual, scalar functions.

In the vector matrix element $N_{\pm 1,ELAS}$ we have the single nucleon part $J_{\pm 1,single}(\vec{Q})$ as well as inputs from the one-pion-exchange current operator at NLO $J_{\pm 1,nope}(\vec{Q})$ and the so-called contact current operators $J_{\pm 1,cont}(\vec{Q})$

$$N_{\pm 1,ELAS} = \langle \Psi_{deut} m'_d | J_{\pm 1,single}(\vec{Q}) + J_{\pm 1,nope}(\vec{Q}) + J_{\pm 1,cont}(\vec{Q}) | \Psi_{deut} m_d \rangle, \quad (5.17)$$

where

$$\vec{J}_{nope} = \sum_{j=3,4,5,6,9,10} g_4^j T_4 \vec{O}_j, \quad (5.18)$$

$$\vec{J}_{cont} = \sum_{j=3,5} w_5^j T_5 \vec{O}_j \quad (5.19)$$

and the corresponding form factors g_4^j and w_5^j are defined in Chapter 3.

In this thesis for the first time, we calculate contribution from new parts of current, which affect elastic scattering on deuteron. Previous calculations included only contributions from single nucleon current [81]. However, as we could see in Subsection 3.2.3 the form factors g_4^j and w_5^j contain two low-energy constants: C'_1 and d_9 . These LECs are not related to the NN potential and have to be determined by a fit to experimental data for electromagnetic reactions. There is some estimate of the value of these constants in the literature [63]. However, the values depend on the Λ parameter, which regularized potential. We use a different method of regularization of the potential than the one adopted in Ref. [63], so we can not use the constant

values given therein. An attempt to the best estimate these two parameters from the cross section and the structure function in elastic electron-deuteron scattering is described in Appendix D. We obtained some preliminary values of these parameters: for two pairs of cut-off values, N2LO-1 and N2LO-4 (see Tables 2.2, D.1), we get $C'_1 = 0.500 \text{ fm}^{-4}$, $d_9 = 0.210 \text{ fm}^{-2}$. For the other two pairs N2LO-2 and N2LO-5, we obtain $C'_1 = 0.900 \text{ fm}^{-4}$, $d_9 = -0.045 \text{ fm}^{-2}$. For the remaining N2LO-3 we get $C'_1 = 0.200 \text{ fm}^{-4}$, $d_9 = -0.195 \text{ fm}^{-2}$. These values are used in this chapter.

5.1.1 Kinematics

Elastic electron-deuteron scattering is shown schematically in Figure 5.2, assuming the one-photon-exchange approximation. We describe this process in the laboratory

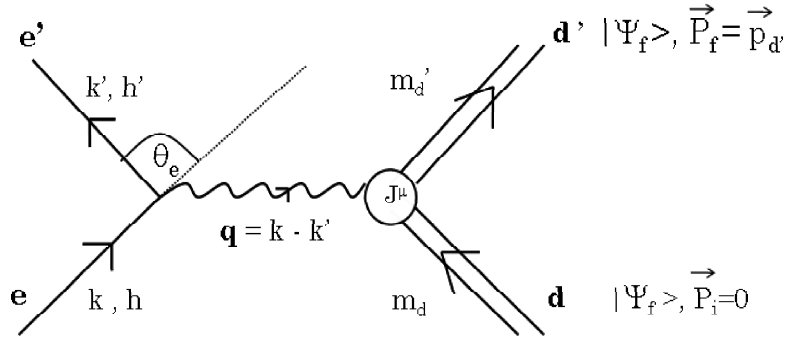


Figure 5.2: Diagram for elastic electron-deuteron scattering in the laboratory frame.

frame, where the initial deuteron momentum \vec{P}_i is zero. The energy and momentum conservation reads (we use $\hbar = c = 1$)

$$\begin{cases} E + M_d = E' + E'_d \\ \vec{k} + \vec{P}_i = \vec{k} = \vec{k}' + \vec{p}_{d'} \end{cases}, \quad (5.20)$$

where $E'_d = \sqrt{M_d^2 + \vec{p}_{d'}^2}$. The system of Equations (5.20) can be easily solved for a given electron scattering angle θ_e , which yields

$$E' = \frac{E}{1 + \frac{E}{M_d}(1 - \cos \theta_e)}. \quad (5.21)$$

This formula is derived from relativistic kinematics. Since we treat our dynamics in the nonrelativistic framework, we would like to use consistently also (approximate) nonrelativistic kinematics. It is then natural to require that various kinematical quantities calculated with nonrelativistic kinematics agree well with their corresponding relativistic counterparts. In Figure 5.3 we show the outgoing electron energy as a function of the electron scattering angle θ_e for $E = 300 \text{ MeV}$ calculated both relativistically and nonrelativistically. We see that at this initial electron energy the nonrelativistic approximation is indeed justified. Of course, once the outgoing electron energy is determined

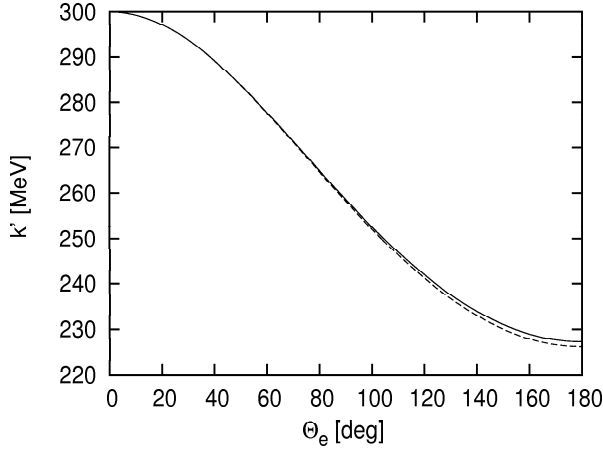


Figure 5.3: Final electron energy in the laboratory frame as a function of the electron scattering angle θ_e for the initial electron energy $E = 300$ MeV calculated relativistically (solid line) and nonrelativistically (dashed line).

for this two-body kinematics, we can calculate the energy E'_d and the scattering angle of the outgoing deuteron θ_d :

$$\begin{aligned} |\vec{p}_d'| &= |\vec{k} - \vec{k}'| = \sqrt{E^2 + E'^2 - 2EE' \cos \theta_e}, \\ \cos \theta_d &= \frac{E - E' \cos \theta_e}{|\vec{p}_d'|}, \\ E'_d &= \sqrt{M_d^2 + \vec{p}_d'^2} \approx M_d + \frac{\vec{p}_d'^2}{2M_d}. \end{aligned} \quad (5.22)$$

Very often results for electron-deuteron scattering are presented in the Breit frame, where the energy transfer is zero and the three-momentum transfer squared is equal to the (negative) four-momentum transfer squared. In Figure 5.4 we demonstrate that in the laboratory frame (provided the initial electron energy is small) we are very close to that condition, because $|\vec{Q}| \approx \mathbf{q} \equiv \sqrt{\vec{Q}^2 - \omega^2}$. We use this fact and later compare our results obtained in the laboratory frame with the results given in the Breit frame. Also in this case we show our calculations based on the relativistic and nonrelativistic formulae and find relativistic effects to be very small.

5.1.2 The Rosenbluth cross section

The formula for the differential cross section in elastic scattering of unpolarized electrons from an unpolarized nucleus was derived by M. N. Rosenbluth in 1950 [82]. It reads

$$\frac{d\sigma}{d\Omega_e} = \sigma_{Mott} \left[A(\mathbf{q}^2) + B(\mathbf{q}^2) \tan^2 \frac{\theta_e}{2} \right] \rho, \quad (5.23)$$

where σ_{mott} and ρ have been already defined and the structure functions $A(\mathbf{q}^2)$ and $B(\mathbf{q}^2)$ can be related to the charge and magnetic moment distributions of the target.

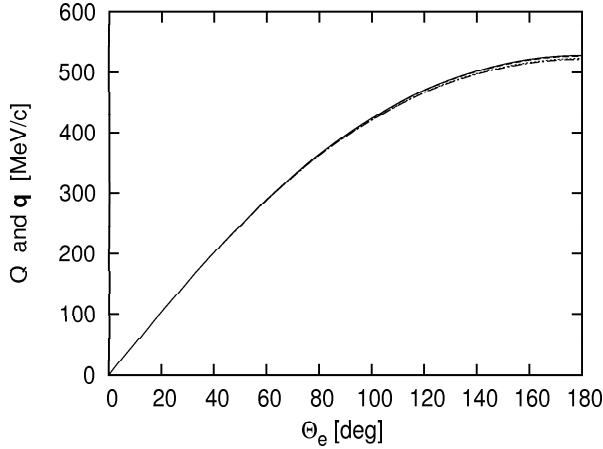


Figure 5.4: Solid (dashed) line represents Q calculated relativistically (nonrelativistically) and the dotted (dash-dotted) line shows the relativistic (nonrelativistic) version of \mathbf{q} . All the four lines practically overlap.

Since Eqs. (5.6)–(5.12) are general, we can re-express the A and B structure functions as

$$A(\mathbf{q}^2) = v_L \frac{1}{3} \sum_{m_d} \sum_{m'_d} R_L - \frac{1}{2} \frac{\mathbf{q}^2}{Q^2} \frac{1}{3} \sum_{m_d} \sum_{m'_d} R_T, \quad (5.24)$$

$$B(\mathbf{q}^2) = \frac{1}{3} \sum_{m_d} \sum_{m'_d} R_T, \quad (5.25)$$

where the dependence on the initial and final deuteron spin projections is given explicitly. Note that A and B given in Equation (5.23) are functions of the four-momentum transfer squared only. In particular, they do not depend on the initial electron energy and on the electron scattering angle. In our nonrelativistic framework this is fulfilled only approximately.

The structure functions A and B have been measured at many facilities. High precision data for small \mathbf{q}^2 come from [83, 84, 85, 86]. For more information about experimental results, also for higher \mathbf{q}^2 see [87, 88, 89, 90, 91].

There are many theoretical frameworks (non-relativistic [92], relativistic [93], quark-hadron models [94], the Skyrme model [95], models based on perturbative QCD [96] and chiral calculations [29, 81]), which give predictions for these observables. Our predictions for the structure functions A and B are based on Equations (5.24) and (5.25), respectively. First, we consider the longitudinal structure function $A(\mathbf{q}^2)$. Our results are presented in Figure 5.5. The left panel on this figure shows results obtained with the single nucleon current. The right panel displays results for the sum of the single nucleon current (single), the long-range contributions from OPE corrections at NLO (nope), OPE relativistic corrections (rel) and short-range contact currents (cont). The sum of above parts will be called “total”. Note that the presented results depend on the choice of the cut-off values. Therefore chiral predictions are shown as bands.

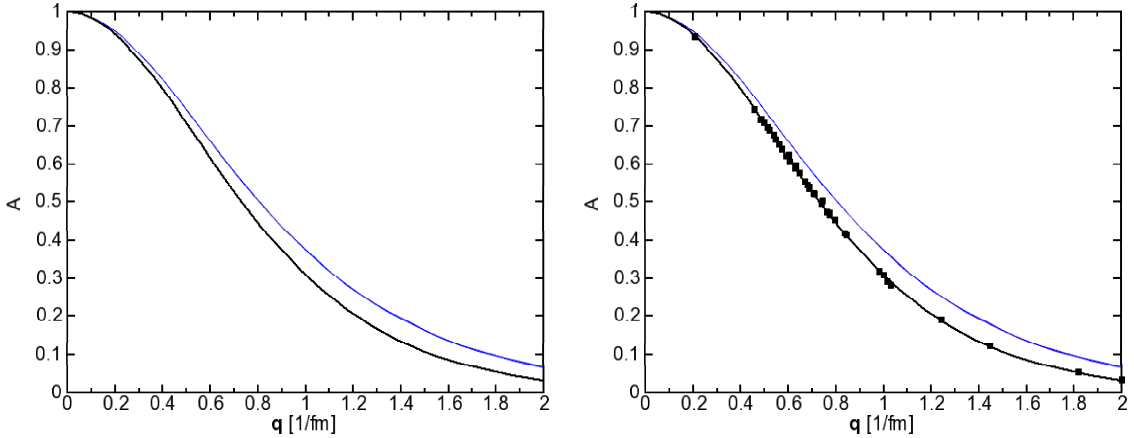


Figure 5.5: Structure functions $A(q^2)$ as a function of q . In the left panel results for the single nucleon current at NLO (grey band), at N2LO (blue band) and for AV18 (black line) are shown. Note the two bands practically overlap. In the right panel we show the results at N2LO and compare the predictions based on the single nucleon current alone (blue band), with the predictions where additional contributions (see text) to the current operator are included (pink band). The two bands overlap. The black line represents predictions obtained with AV18. Data come from [84] and references therein.

The results with the AV18 potential (only for the single nucleon current) are in a good agreement with the experimental data. The chiral predictions give only a fair description of the data. There is practically no difference between NLO and N2LO results. The main contribution to the structure function A comes from the single nucleon current operators while adding the two-nucleon current operators leads to negligible corrections. Table 5.1 compares the structure functions for the “total” current with the AV18 results and the experimental data from [84].

Table 5.1: Range of the structure function $A(q^2)$ calculated at N2LO for a different cut-off values from Table 2.2. Experimental data are from Ref. [84]. Experimental errors (not shown) are very small.

Q [MeV/c]	N2LO1-N2LO5	Exp.	AV18
41.35	0.9454	0.9358	0.9378
90.65	0.7757–0.7759	0.7450	0.7459
96.05	0.7537–0.7540	0.7201	0.7212
101.24	0.7323–0.7326	0.6979	0.6973
110.98	0.6920–0.6923	0.6519	0.6524
119.82	0.6554–0.6557	0.6080	0.6119
140.45	0.5721–0.5723	—	0.5205

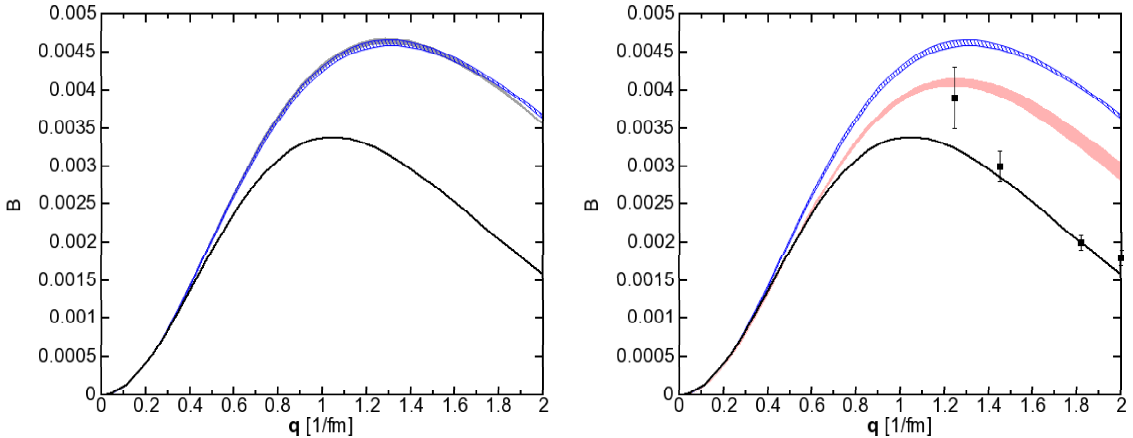


Figure 5.6: Structure functions $B(\mathbf{q}^2)$ as a function of \mathbf{q} . In the left panel results for the single nucleon current at NLO (grey band), at N2LO (blue band) and for AV18 (black line) are shown. Note the two bands practically overlap. In the right panel we show results at N2LO and compare predictions based on the single nucleon current alone (blue band), to the predictions where additional contributions (see text) to the current operator are included (pink band). The black line represents predictions obtained with AV18. Data come from [84].

Next, the transverse structure function $B(\mathbf{q}^2)$, which carries information about the magnetic moment distribution, is discussed. The low \mathbf{q}^2 data on B structure function come from the experiments carried out at: Stanford[97], [98], Orsay[99], [86], Naval Research Lab[100] and Mainz[84]. Our results are shown in Figure 5.6. They are shown in the same way as for A in Figure 5.5.

There is no difference between the NLO and N2LO results. The difference between the chiral and AV18 predictions is very big for $\mathbf{q} > 0.5 \text{ fm}^{-1}$. For small \mathbf{q} values the chiral and AV18 results overlap. The contributions, which come on top of the single nucleon current in the chiral case are well visible for the higher \mathbf{q} values, although the single nucleon current operator still plays a dominant role. Adding new parts (single, nope, rel and cont) leads to a better, but still unsatisfactory, agreement with the experimental data.

Calculations of the unpolarized cross section for one electron energy and several scattering angles θ_e are shown in Table 5.2. While the chiral predictions slightly overshoot the data, AV18 results give a good description. Table 5.3 presents summarized results for the three unpolarized observables: the structure functions A and B and the differential cross section. Results were obtained for the three values of \mathbf{q} : 40, 90, 120 MeV/c at the fixed angle $\theta_e = 70^\circ$ for N2LO. This table presents contributions of the individual parts of the current operator. We see clearly that all the results receive dominant contributions from the single nucleon current operator. All the remaining parts of the current operator give very small corrections to the differential cross section. In the structure function A we see some effects coming from the relativistic corrections (rel). This happens only for the two higher values of Q . In the case of structure functions B the situation is more interesting: contributions from the relativistic correction

Table 5.2: Results for the differential cross section $d\sigma/d\Omega_e(E, \theta_e)$ in the units of $10^{-30} \text{ cm}^2/\text{sr}$ for $E = 80.1 \text{ MeV}$ calculated at N2LO for different cut-off values from Table 2.2. Experimental data are from Ref. [84]. Predictions based on AV18 are added for comparison.

θ_e [deg]	Q [MeV/c]	N2LO1-N2LO5	Exp.	Stat.error	AV18
30	41.35	158.0–158.1	156.380	0.250	156.80
70	90.65	3.789–3.791	3.635	0.011	3.644
75	96.05	2.714–2.715	2.583	0.008	2.597
80	101.24	1.972–1.973	1.876	0.006	1.878
90	110.98	1.078	1.014	0.004	1.017
100	119.82	0.610	0.565	0.002	0.570
130	140.45	0.1175	0.1072	0.0002	0.1070

Table 5.3: Predictions for the differential cross section $d\sigma/d\Omega_e(E, \theta_e)$ in the units of $10^{-30} \text{ cm}^2/\text{sr}$ and the structure functions A and B based on the selected (N2LO-3) chiral potential with different ingredients in the current operator.

Q [MeV/c]	contributions	$d\sigma/d\Omega_e [10^{-30} \times \text{cm}^2/\text{sr}]$	A	B
41.35 $(\theta_e = 30^\circ)$	single	158.1	0.9455	0.4475E-03
	sig+nope	158.1	0.9455	0.4466E-03
	sig+nope+rel	158.0	0.9454	0.4466E-03
	single+nope+rel+cont	158.0	0.9454	0.4213E-03
90.65 $(\theta_e = 70^\circ)$	single	3.793	0.7763	0.1781E-02
	single+nope	3.793	0.7763	0.1777E-02
	single+nope+rel	3.790	0.7758	0.1777E-02
	sig+nope+rel+cont	3.790	0.7757	0.1663E-02
119.82 $(\theta_e = 100^\circ)$	single	0.611	0.6565	0.2653E-02
	single+nope	0.611	0.6565	0.2647E-02
	single+nope+rel	0.610	0.6556	0.2647E-02
	single+nope+rel+cont	0.610	0.6556	0.2462E-02

are not visible but the results are affected by the OPE corrections at NLO and contact terms in the current operator.

5.1.3 Tensor analyzing powers

In order to describe general polarization states of a deuteron target we introduce the system of coordinates following the Madison convention [101] (c.f. Figure 5.7). The scattering xz plane is spanned by the \vec{k} and \vec{k}' vectors, where \hat{z} is parallel to the three-momentum transfer $\vec{k} - \vec{k}'$, \hat{y} is parallel to $\vec{k} \times \vec{k}'$ and $\hat{x} = \hat{y} \times \hat{z}$.

The deuteron is polarized in the direction given by the polar angle θ^* and the azimuthal angle ϕ^* . We assume that spin projection on that axis is equal 1. Such a deuteron state can be obtained from the states with definite projections on the z axis

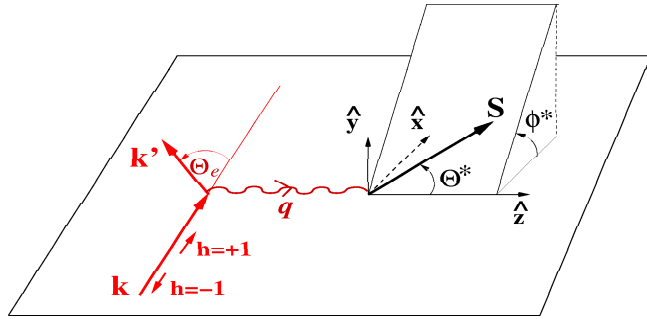


Figure 5.7: Definition of the two angles (θ^*, ϕ^*) used to specify the initial deuteron polarization.

using the Wigner D -matrix for spin 1 [65, 69]

$$|\Psi_{deut}\rangle_{(\theta^*, \phi^*)} = \sum_{m_d=-1,0,1} D_{m_d 1}^{(1)}(\phi^*, \theta^*, 0) |\Psi_{deut m_d}\rangle. \quad (5.26)$$

The expression for the cross section for a polarized target of spin 1, in spherical tensor notation and assuming parity conservation, takes the form [102]

$$\sigma = \sigma_0 [1 + 2\text{Re}(iT_{11})iT_{11} + t_{20}T_{20} + 2\text{Re}(t_{21})T_{21} + 2\text{Re}(t_{22})T_{22}], \quad (5.27)$$

where σ_0 is the so-called "unpolarized" cross section, t_{kq} are tensor components of the target polarization and T_{kq} are the tensor analyzing powers. There are many ways to calculate and measure T_{kq} (see for example [103]). In this thesis we express them in terms of the cross sections obtained for some selected cases of the initial deuteron spin direction, while the initial electron is not polarized and no polarization degrees of freedom are observed in the final state. To this aim we define four deuteron spin directions given by four (θ^*, ϕ^*) pairs:

$$\begin{aligned} \text{up} \equiv u &\leftrightarrow (\theta^* = 90^\circ, \phi^* = 90^\circ) \\ \text{down} \equiv d &\leftrightarrow (\theta^* = 90^\circ, \phi^* = 270^\circ) \\ \text{in plane1} \equiv p1 &\leftrightarrow (\theta^* = 90^\circ, \phi^* = 0^\circ) \\ \text{in plane2} \equiv p2 &\leftrightarrow (\theta^* = 45^\circ, \phi^* = 0^\circ). \end{aligned} \quad (5.28)$$

and obtain

$$\begin{aligned} iT_{11} &= \frac{\sigma_u - \sigma_d}{2\sqrt{3}\sigma_0}, \\ T_{20} &= \frac{4\sigma_0 - \sigma_u - \sigma_d - 2\sigma_{p1}}{\sqrt{2}\sigma_0}, \\ T_{21} &= \frac{6\sigma_0 - \sigma_u - \sigma_d - 4\sigma_{p2}}{2\sqrt{3}\sigma_0}, \\ T_{22} &= \frac{-\sigma_u - \sigma_d + 2\sigma_{p1}}{2\sqrt{3}\sigma_0}, \end{aligned} \quad (5.29)$$

where using Equation (5.7)

$$\sigma_i = \sigma_{Mott} [v_L(R_L)_i + v_T(R_T)_i + v_{TT}(R_{TT})_i + v_{TL}(R_{TL})_i] \rho \quad (5.30)$$

and in the calculation of the response functions $(R)_i$ in (5.12), the deuteron state $|\Psi_{deut}m_d\rangle$ is replaced by $|\Psi_{deut}\rangle_{i\leftrightarrow(\theta^*,\phi^*)}$. Note that for elastic electron-deuteron scattering the analyzing power iT_{11} vanishes and only T_{20} , T_{21} and T_{22} appear in Equation (5.27).

The deuteron tensor analyzing powers give important information about the NN interaction. There is plenty of experimental data available, but almost none for the low energy region, where one can use ChPT.

Tensor analyzing powers were calculated for $\theta_e=70^\circ$. Results are presented in Figure 5.8. Plots in the left panel correspond to the single nucleon current at NLO and N2LO. In the right panel one can see the results for the “total” current at N2LO, the single nucleon current at N2LO and AV18 results for reference. In the left panel, we see only very small differences between the results obtained at NLO and N2LO. Only for T_{20} for larger values of \mathbf{q} the N2LO band is visible and broader than the NLO one.

Let us now focus on the right panel. The best experimentally known tensor analyzing power is T_{20} (see Figure 5.8, the plots in the upper row). For all these observables, a very good agreement is observed among different predictions for small \mathbf{q} . For higher values of \mathbf{q} one can see some differences. The analyzing power T_{21} is not sensitive to the additional contributions, what is seen in the middle row. This behavior is similar to the one for the structure function A .

In the case of T_{22} two bands of chiral predictions and the line for AV18 results overlap for very small \mathbf{q} . For higher values of \mathbf{q} , T_{22} appears to be sensitive to the smaller components of the “total” current operator. This shift towards higher values resembles the behavior of the structure function B .

5.1.4 The deuteron elastic form factors

In former subsections we introduced several quantities discussed for the elastic electron-deuteron scattering. In fact, for this specific reaction, $A(\mathbf{q}^2)$, $B(\mathbf{q}^2)$, $T_{20}(\mathbf{q}^2, \theta_e)$, $T_{21}(\mathbf{q}^2, \theta_e)$ and $T_{22}(\mathbf{q}^2, \theta_e)$ are not independent. They all can be expressed in terms of the deuteron charge $G_C(\mathbf{q}^2)$, magnetic $G_M(\mathbf{q}^2)$ and quadrupole $G_Q(\mathbf{q}^2)$ form factors [78]. The latter quantities are dimensionless and normalized at $\mathbf{q}^2 = 0$ to the static moments:

$$\begin{aligned} G_C(\mathbf{q}^2 \rightarrow 0) &= 1, \\ G_Q(\mathbf{q}^2 \rightarrow 0) &= M_d^2 Q_d = 25.83, \\ G_M(\mathbf{q}^2 \rightarrow 0) &= \mu_d \frac{M_d}{M_n} = 1.714, \end{aligned} \quad (5.31)$$

where $Q_d = 0.2859 \text{ fm}^2$ [104] is the deuteron quadrupole moment and $\mu_d = 0.85741$ [105] is the deuteron magnetic moment in units of nuclear magnetons. In particular,

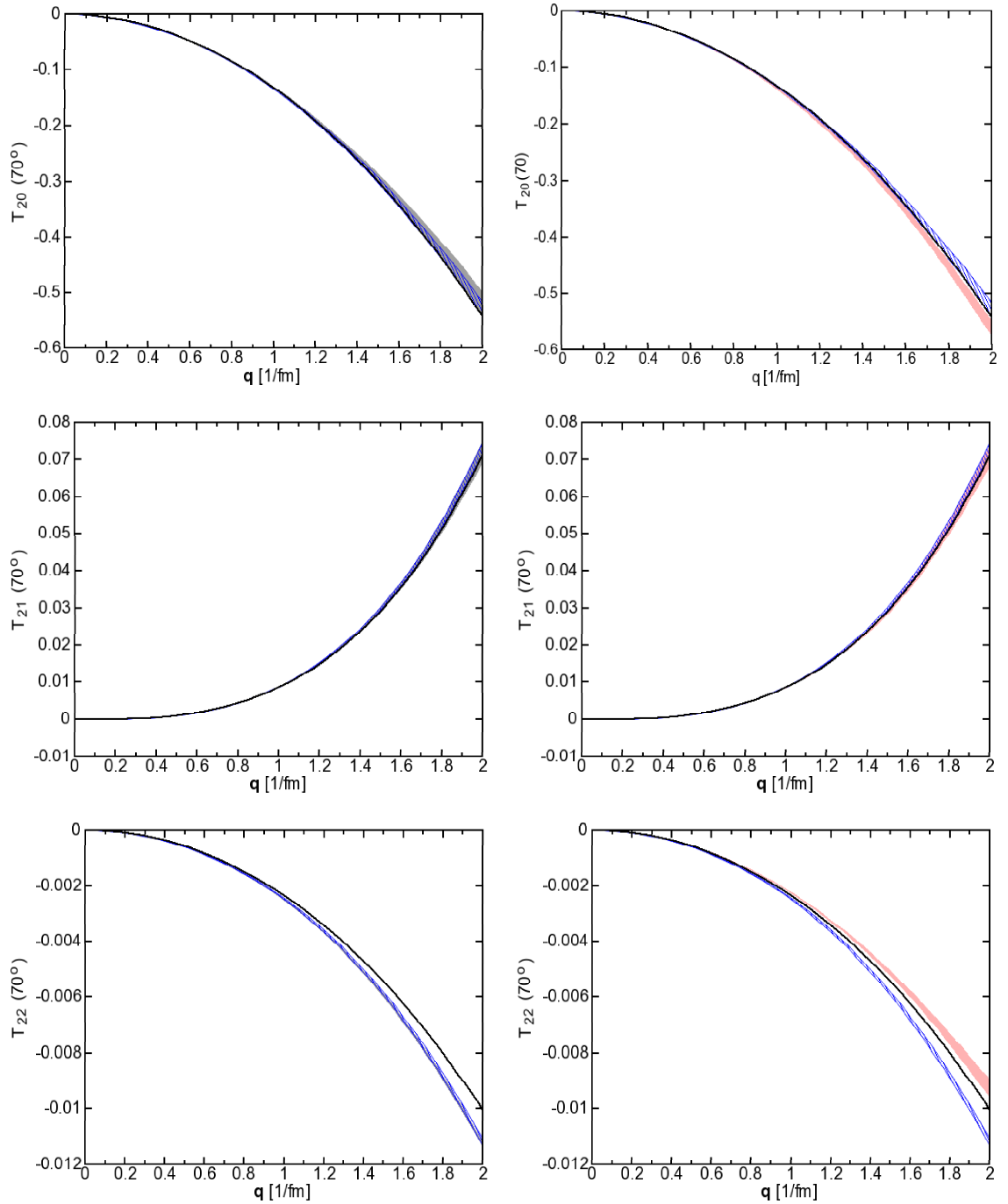


Figure 5.8: Deuteron analyzing powers T_{20}, T_{21}, T_{22} as functions of q at one specific electron scattering angle $\theta_e = 70^\circ$. The left and right panels as well as the bands and lines have the same meaning as in Figures 5.5–5.6.

the structure functions can be written in the form:

$$A(\mathbf{q}^2) = G_C^2 + \frac{2}{3}\eta G_M^2 + \frac{8}{9}\eta^2 M_d^4 G_Q^2, \quad (5.32)$$

$$B(\mathbf{q}^2) = \frac{4}{3}\eta(1+\eta)G_M^2, \quad (5.33)$$

where

$$\eta = \frac{-\mathbf{q}^2}{4M_d^2}. \quad (5.34)$$

While G_M can be independently obtained from B , we need some polarization observable to separate G_C and G_Q . Following [106, 107] we use

$$T_{20} = -\sqrt{2}\frac{1}{S} \left(\frac{4}{3}\eta G_C G_Q + \frac{4}{9}\eta^2 G_Q^2 + \frac{1}{6}\eta \left[1 + 2(1+\eta) \tan^2 \frac{\theta_e}{2} \right] G_M^2 \right), \quad (5.35)$$

where $S(\mathbf{q}^2, \theta_e) \equiv A(\mathbf{q}^2) + B(\mathbf{q}^2) \tan^2 \frac{\theta_e}{2}$. Equations (5.32), (5.33) and (5.35) are then used to obtain the deuteron form factors, G_C , G_M and G_Q . (Note that some unphysical solutions have to be rejected.) Other polarization observables also can be written in terms of the elastic form factors:

$$T_{21} = -\frac{\sqrt{2}\eta}{S} \left(\frac{4}{3}G_C G_Q + \frac{4}{9}G_Q^2 + \frac{1}{6}(1 + (\eta + 1) \tan^2(\frac{\theta_e}{2})) G_M^2 \right), \quad (5.36)$$

$$T_{22} = -\frac{\eta}{2\sqrt{3}S} G_M^2. \quad (5.37)$$

These elastic form factors have been subject of the intensive experimental and theoretical studies for several decades [74, 78, 75]. They can be related to the properties of the nucleon-nucleon interaction. For example, the quantity G_Q is sensitive to the tensor force. Their sensitivity to the different components of the 2N current operator has also been investigated. As it is shown in this thesis, they get contributions from the OPE parts of the current operator at NLO and from the relativistic corrections to the same operator. Figures 5.9 presents calculations for the deuteron elastic form factors. Left plots show results with the single nucleon current at NLO and N2LO. Right plots represent preliminary results with new contributions from two-nucleon currents at N2LO. The difference between NLO and N2LO predictions are negligible. G_C results show similar behavior as for the structure function A , which proves that A receives dominant contributions from G_C . G_M results are similar to T_{20} and G_M results are similar to B and T_{22} results.

5.1.5 Helicity asymmetry of the cross section

Finally, we consider a polarization observable, which requires both the initial electron and the target to be polarized. This is the so-called spin dependent helicity asymmetry,

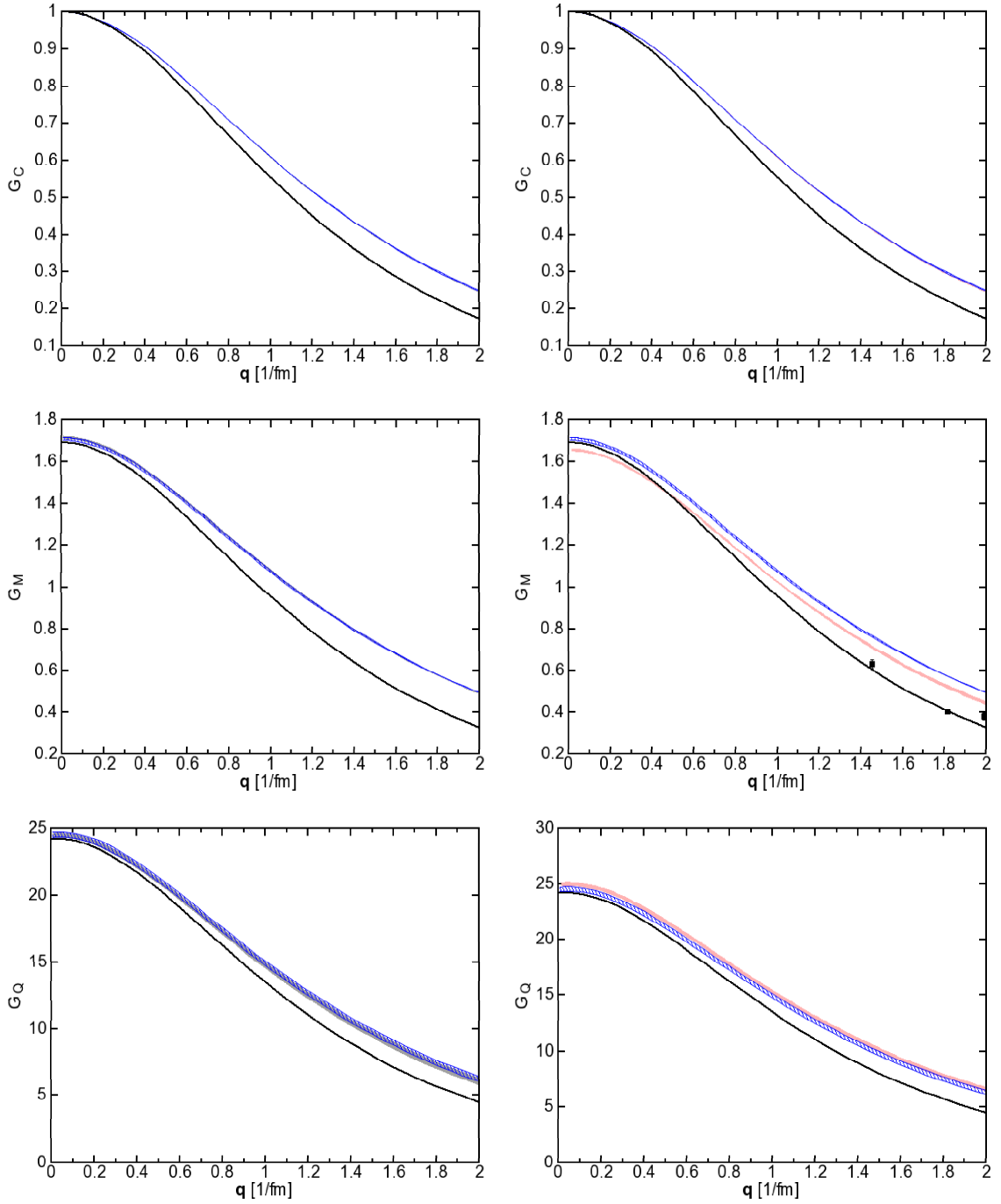


Figure 5.9: Calculations for the magnetic, electric monopole and quadrupole form factors G_M , G_C , G_Q are presented vs. the four momentum transfer q . The left and right panels as well as the bands and lines have the same meaning as in Figures 5.5–5.8. Data shown only in the middle right panel are from [84].

directly related to Equation (5.6). Namely, if no polarization in the final state is considered, the cross section for electron-nucleus scattering can be written as

$$\sigma(h, \theta^*, \phi^*) = \Sigma(\theta^*, \phi^*) + h\Delta(\theta^*, \phi^*), \quad (5.38)$$

where the dependence on the initial electron helicity h and the deuteron spin direction is shown explicitly. It is then straightforward to define the asymmetry $A(\theta^*, \phi^*)$

$$A(\theta^*, \phi^*) \equiv \frac{\sigma(h = +1, \theta^*, \phi^*) - \sigma(h = -1, \theta^*, \phi^*)}{\sigma(h = +1, \theta^*, \phi^*) + \sigma(h = -1, \theta^*, \phi^*)} = \frac{\Delta(\theta^*, \phi^*)}{\Sigma(\theta^*, \phi^*)}. \quad (5.39)$$

For elastic electron-deuteron scattering the nuclear response function R_{TT} and R_{TL} , which enter $\Sigma(\theta^*, \phi^*)$, are zero so we obtain

$$A(\theta^*, \phi^*) = \frac{v_{T'}R_{T'}(\theta^*, \phi^*) + v_{TL'}R_{TL'}(\theta^*, \phi^*)}{v_L R_L(\theta^*, \phi^*) + v_T R_T(\theta^*, \phi^*)}. \quad (5.40)$$

In Figure 5.10 we show an example of $A(\theta^*, \phi^*)$ for cases $A_{||} \equiv A(\theta^* = 0^\circ, \phi^* = 0^\circ)$ and $A_{\perp} \equiv A(\theta^* = 90^\circ, \phi^* = 0^\circ)$ where $\theta_e = 70^\circ$ is fixed. The prediction bands obtained with the NLO potential and the N2LO potential overlap. The prediction bands lie below AV18 line (see left panels). In right panels, for both asymmetries, after adding new parts of currents we find increased values for $q > 1.2 \text{ fm}^{-1}$, higher than the AV18 reference line.

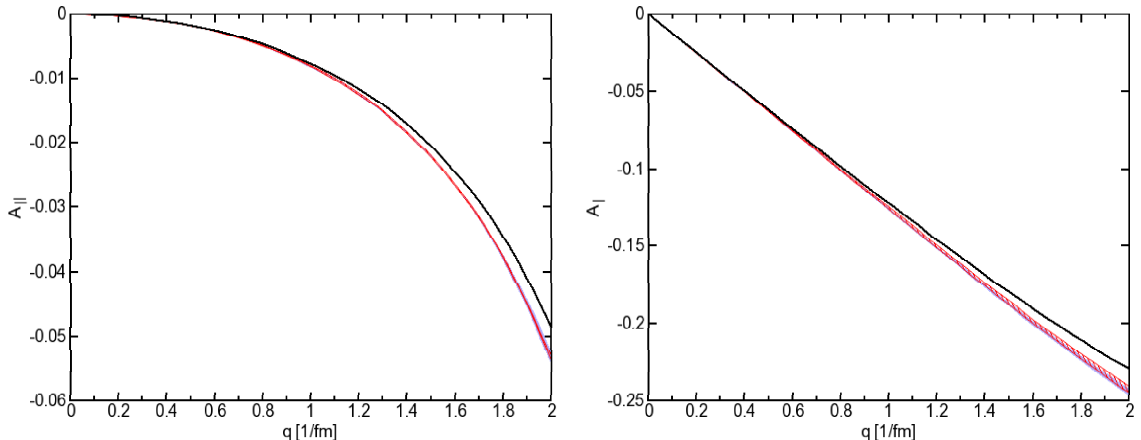


Figure 5.10: Spin dependent helicity asymmetry of the elastic electron-deuteron cross section. The bands and lines have the same meaning as in Figures 5.5–5.8.

5.2 Electrodisintegration of the deuteron

Inclusive and exclusive deuteron electrodisintegration has been studied systematically for many years using the traditional approach [108, 109, 110, 111, 112, 113, 114, 115, 77]. The special emphasis has been on polarization observables focusing on the role of the meson exchange currents, short-range interactions and various relativistic effects. In this thesis we employ, as consistently as it is presently possible, the dynamical ingredients derived within ChEFT and concentrate on the nuclear current operator.

Nuclear matrix elements for inelastic electron-deuteron scattering are:

$$N^0 = \langle \Psi_{scatt} m_p m_n | J^0(\vec{Q}) | \Psi_{deut} m_d \rangle \quad (5.41)$$

and

$$N_{\pm 1} = \langle \Psi_{scatt} m_p m_n | J_{\pm 1}(\vec{Q}) | \Psi_{deut} m_d \rangle, \quad (5.42)$$

where in $J^0(\vec{Q})$ and $J_{\pm 1}(\vec{Q})$ we have contributions from the single-nucleon current, the leading OPE and TPE current operators.

To be more precise, for this inelastic process, in the charge density matrix element N^0 we encounter the following parts

$$N^0 = \langle \Psi_{scatt} m_p m_n | J_{single}^0(\vec{Q}) + J_{tpe}^0(\vec{Q}) | \Psi_{deut} m_d \rangle, \quad (5.43)$$

where the individual inputs to the current operator are defined in Chapter 3.

In the matrix elements of the vector parts of the current operator $N_{\pm 1}$ we have

$$N_{\pm 1} = \langle \Psi_{scatt} m_p m_n | J_{\pm 1,single}(\vec{Q}) + J_{\pm 1,lope}(\vec{Q}) + J_{\pm 1,tpe}(\vec{Q}) | \Psi_{deut} m_d \rangle, \quad (5.44)$$

where the individual parts, $J_{\pm 1,single}(\vec{Q})$, $J_{\pm 1,lope}(\vec{Q})$ and $J_{\pm 1,tpe}(\vec{Q})$ are also specified in Chapter 3.

5.2.1 Kinematics

We describe the kinematics of the $e + {}^2H \rightarrow e' + p + n$ reaction in the laboratory frame, where the initial deuteron is at rest.

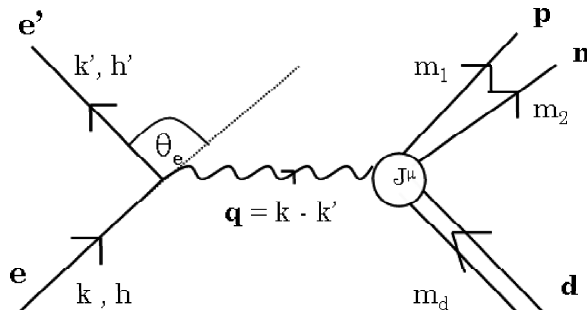


Figure 5.11: Diagram for electrodisintegration of the deuteron.

The four-momentum conservation reads in this case

$$\begin{cases} E + M_d = E' + E_p + E_n \\ \vec{k} = \vec{k}' + \vec{p}_p + \vec{p}_n \end{cases}, \quad (5.45)$$

where E_p (E_n) and \vec{p}_p (\vec{p}_n) are the total energy and the momentum of the outgoing proton (neutron). The remaining quantities have the same meaning as for the elastic process. With

$$\begin{aligned} \omega &= E - E', \\ \vec{Q} &= \vec{k} - \vec{k}', \\ \vec{p}_n &= \vec{Q} - \vec{p}_p \end{aligned} \quad (5.46)$$

we obtain, for fixed (ω, \vec{Q}) , the magnitude of \vec{p}_p as a function of $\cos \theta_p \equiv \hat{Q} \cdot \hat{p}_p$. The equation for $p_p \equiv |\vec{p}_p|$ reads

$$\omega + M_d = \sqrt{M_N^2 + p_p^2} + \sqrt{M_N^2 + Q^2 + p_p^2 - 2Qp_p \cos \theta_p}, \quad (5.47)$$

where both the proton and neutron masses are approximated by the (average) "nucleon mass", M_N . Again we consider additionally the nonrelativistic version of (5.47) which reads

$$\omega + M_d = 2M_N + \frac{p_p^2}{2M_N} + \frac{Q^2 + p_p^2 - 2Qp_p \cos \theta_p}{2M_N}. \quad (5.48)$$

In both cases we deal actually with a quadratic equation which either gives two physical (positive) solutions for p_p in the limited angular range $0 \leq \theta_p \leq \theta_p^{max} < 90^\circ$ or one physical solution for p_p in the whole range of θ_p values, $0 \leq \theta_p \leq 180^\circ$. Nonrelativistically,

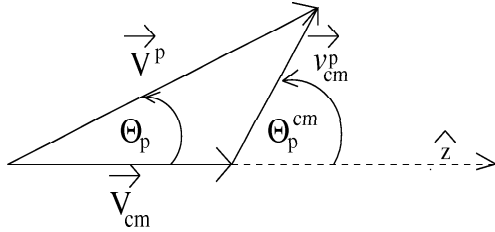


Figure 5.12: Connection between the nonrelativistic center-of-mass and laboratory nucleon velocities.

this can be understood as a result of adding two velocities. The proton velocity in the laboratory system \vec{V}^p is obtained as the sum of the proton velocity in the center of mass frame \vec{v}_{cm}^p and the velocity of the center of mass frame in the laboratory system, \vec{V}_{cm} :

$$\vec{V}^p = \vec{V}_{cm} + \vec{v}_{cm}^p, \quad (5.49)$$

where $v_{cm}^p = p_0/M_n$, $V_{cm} = Q/(2M_N)$, $V^p = p_p/M_N$ and the center of mass nucleon momentum p_0 is given by the neutron-proton energy E_{np} in the center of mass frame:

$$E_{np} = \omega - |E_{deut}| - \frac{1}{4} \frac{Q^2}{M_N} = p_0^2/M_n. \quad (5.50)$$

Of course, this two-body kinematics can be solved (with exactly the same result) for the neutron emission.

In Figure 5.13 we compare the solutions of Equations (5.47) and (5.48) for $\omega = 30$ MeV and $Q = 300$ MeV/c. In this case, the nonrelativistic solution is very close to the relativistic one.

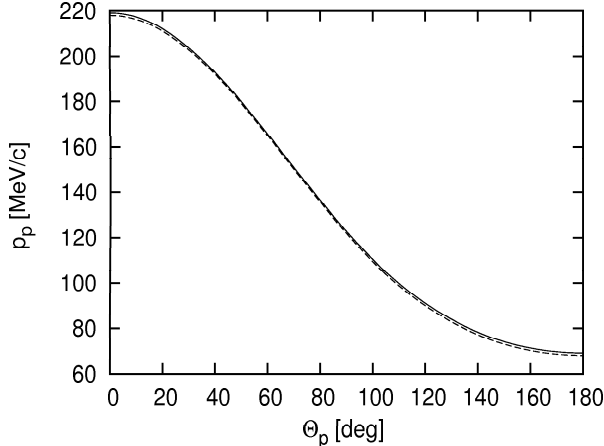


Figure 5.13: Magnitude of the outgoing proton momentum as a function of the proton angle with respect to the three-momentum transfer \vec{Q} calculated relativistically (solid line) and nonrelativistically (dashed line) for $\omega = 30$ MeV and $Q = 300$ MeV/c.

5.2.2 Unpolarized exclusive cross section

First, we consider exclusive reactions for four kinematic configurations as shown in Table 5.4. For these selected electron kinematical configurations we calculated the

Table 5.4: Selected kinematical configurations.

Kinematics	E [MeV]	θ_e [deg]	E' [MeV]	Q [MeV/c]	ω [MeV]
KIN1	62	70	35	60	27
KIN2	105	70	52	100	50
KIN3	140	30	50	100	90
KIN4	270	50	170	206	100

differential cross section and some polarization observables. The angle θ_p used to label the kinematics for the exclusive ${}^2\text{H}(e, e'p)n$ reaction is specified in Figure 5.14. We restrict ourselves to the plane spanned by the \vec{k} and \vec{k}' vectors. Results for the differential cross section as a function of θ_p are presented in Figure 5.15. The cross section is calculated according to the general formula given in Equation 5.23.

For KIN1 we find a very good agreement between chiral calculations and AV18 prediction. For very small angles the predictions for all contributions coincide. A small broadening of TPE predictions can be noticed for the angles greater than 350° . The

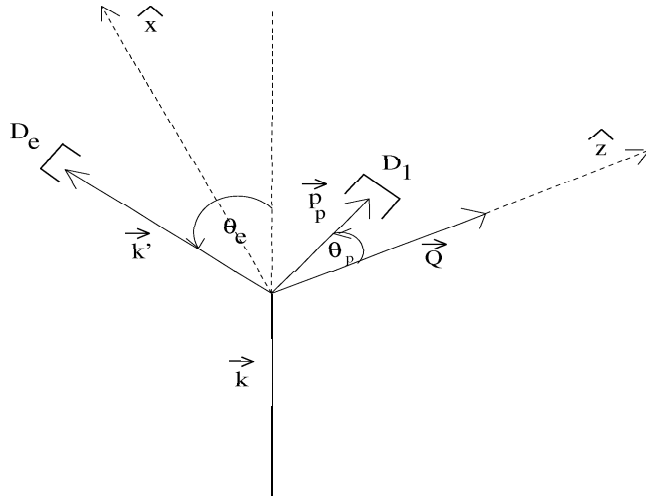


Figure 5.14: Diagram of kinematics for electrodisintegration processes.

similar behavior can be found for KIN2, where the prediction bands are somewhat broader, but still agree with the AV18 results. For $\theta_p > 25^\circ$, significant differences between the contributions from various currents can be observed. Chiral calculations with MEC give larger values of the cross section than the predictions with AV18 potential. The width of the TPE band is much broader than for the OPE current and lies above the OPE band. The KIN2 is set for the same value of Q as the KIN3, but we have now a larger value of ω . We find that larger values of ω cause broadening of the prediction bands for lower values of the cross section. Generally, the chiral bands are much broader than for the previous kinematics. The single nucleon current band and MEC bands are separated and the TPE band is much broader than the OPE one, however it better resembles the shape of the AV18 reference line. The KIN4 is set for a similar value of ω , but has a higher value Q . The picture now is similar to that of KIN1 and KIN2. The bands are narrower and we have reliable agreement between all results.

5.2.3 Deuteron analyzing powers

In this paragraph we present the results for the deuteron analyzing powers. The kinematical configuration are the same as for unpolarized cross section. The analyzing powers are calculated according to Equations 5.29. In this case, all four T_{kq} components appear, among them the vector analyzing power iT_{11} and the tensor analyzing powers: T_{20} , T_{21} and T_{22} .

First, we consider deuteron vector analyzing power iT_{11} (Figure 5.16). In case of KIN1 and KIN2, the TPE bands overlaps with OPE predictions. For the KIN3 we see a large broadening of the prediction bands. OPE predicts wider range of the iT_{11} values than in case of KIN2. Single nucleon current band and the TPE band remain similar as for KIN2. Analogous behaviour of iT_{11} as for KIN1 and KIN2 can be found

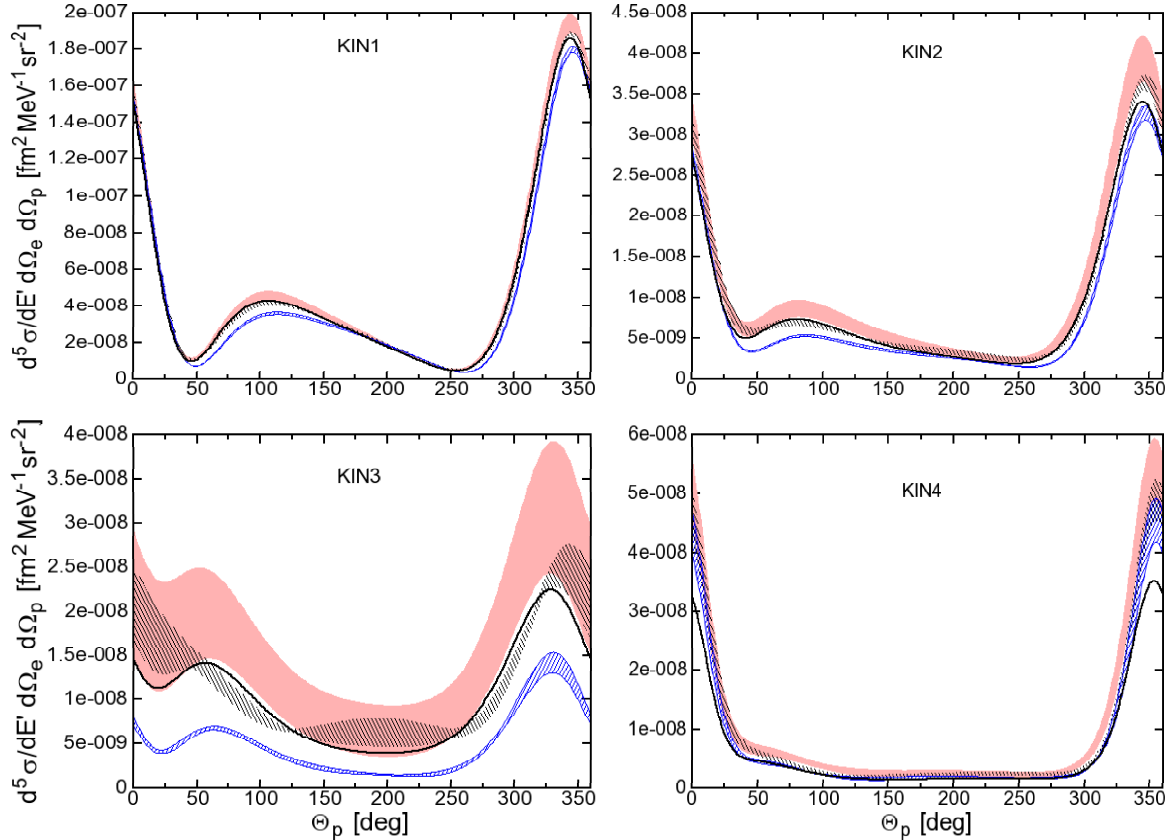


Figure 5.15: Differential cross section as a function of proton outgoing angle for KIN1-KIN4 (see Table 5.4). Results for KIN2 and KIN3 were obtained for the same Q value. We show the results at N2LO. The blue band covers results obtained with the single-nucleon current only, the dark band represents predictions based on the single-nucleon and OPE parts, and the pink band contains additionally TPE parts. The black line represents predictions obtained with AV18.

also for KIN4. Results are compatible in most cases for higher Q values but the bands are broader.

Now, we focus on the tensor analyzing powers shown in Figures 5.16 (lower rows) and 5.17. In case of KIN1 and KIN2, for all observables, the single nucleon bands and the OPE bands have the same width. The TPE bands are broader for KIN2. The single nucleon band gives very similar results as MEC currents. As for the previous observable, for KIN4, we see significant broadening of the prediction bands towards higher values of T_{2q} . In this case, for single nucleon current, the prediction band gives higher values than other calculations. The TPE band overlaps with the OPE band and is much broader than the OPE prediction. In case of T_{21} , a broadening of TPE band for $\theta_p = 20^\circ - 50^\circ$ and $\theta_p = 200^\circ - 220^\circ$ occur. For outgoing proton angles $75^\circ - 120^\circ$ and $275^\circ - 320^\circ$ in all cases the prediction bands are similar and very narrow. For the T_{22} we can observe a broadening of the TPE and the OPE bands for $\theta_p = 50^\circ - 150^\circ$.

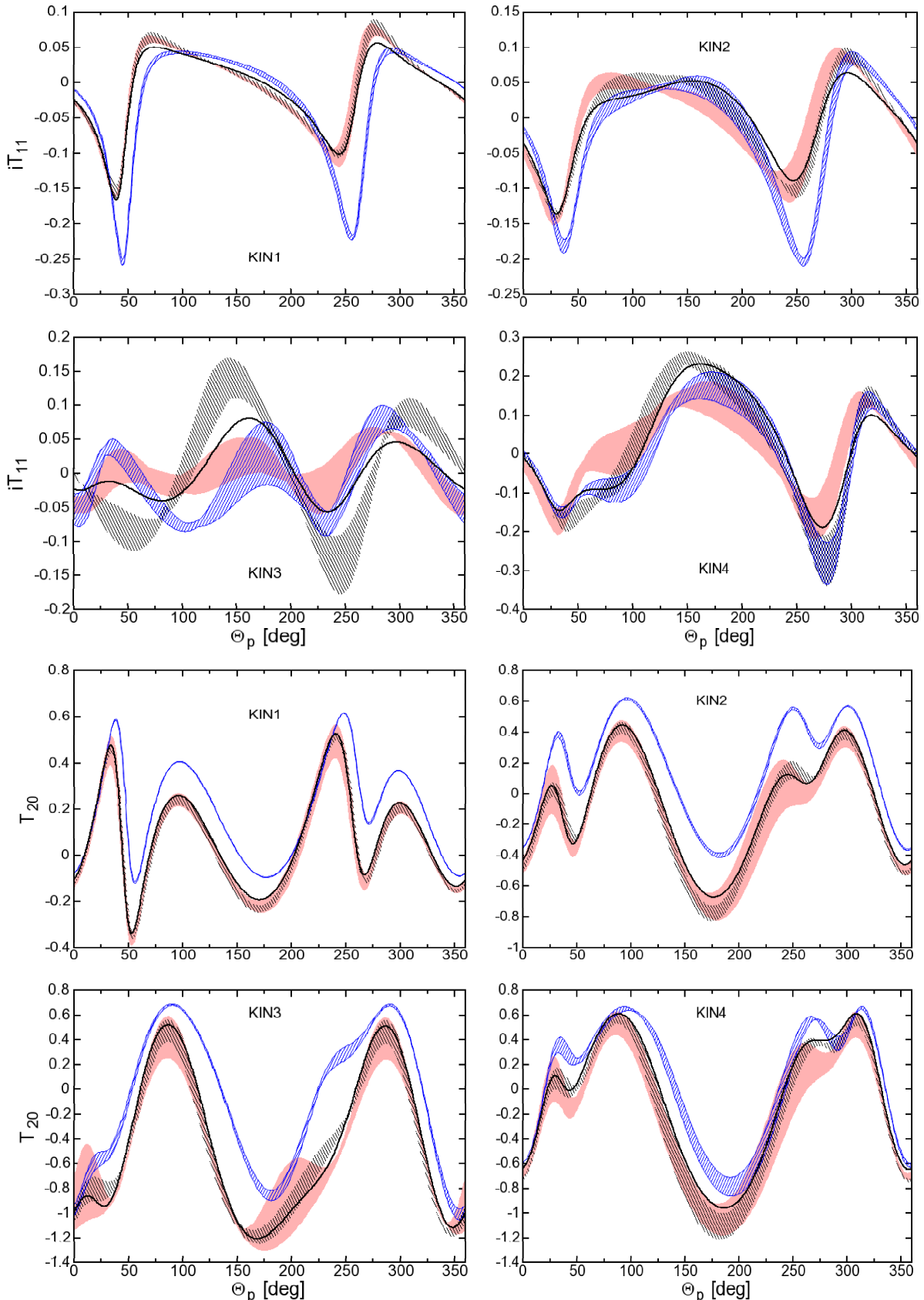


Figure 5.16: Deuteron tensor analyzing powers iT_{11} (upper rows) and T_{20} (lower rows) as a function of outgoing proton angle θ_p . The bands and lines have the same meaning as in Figure 5.15.

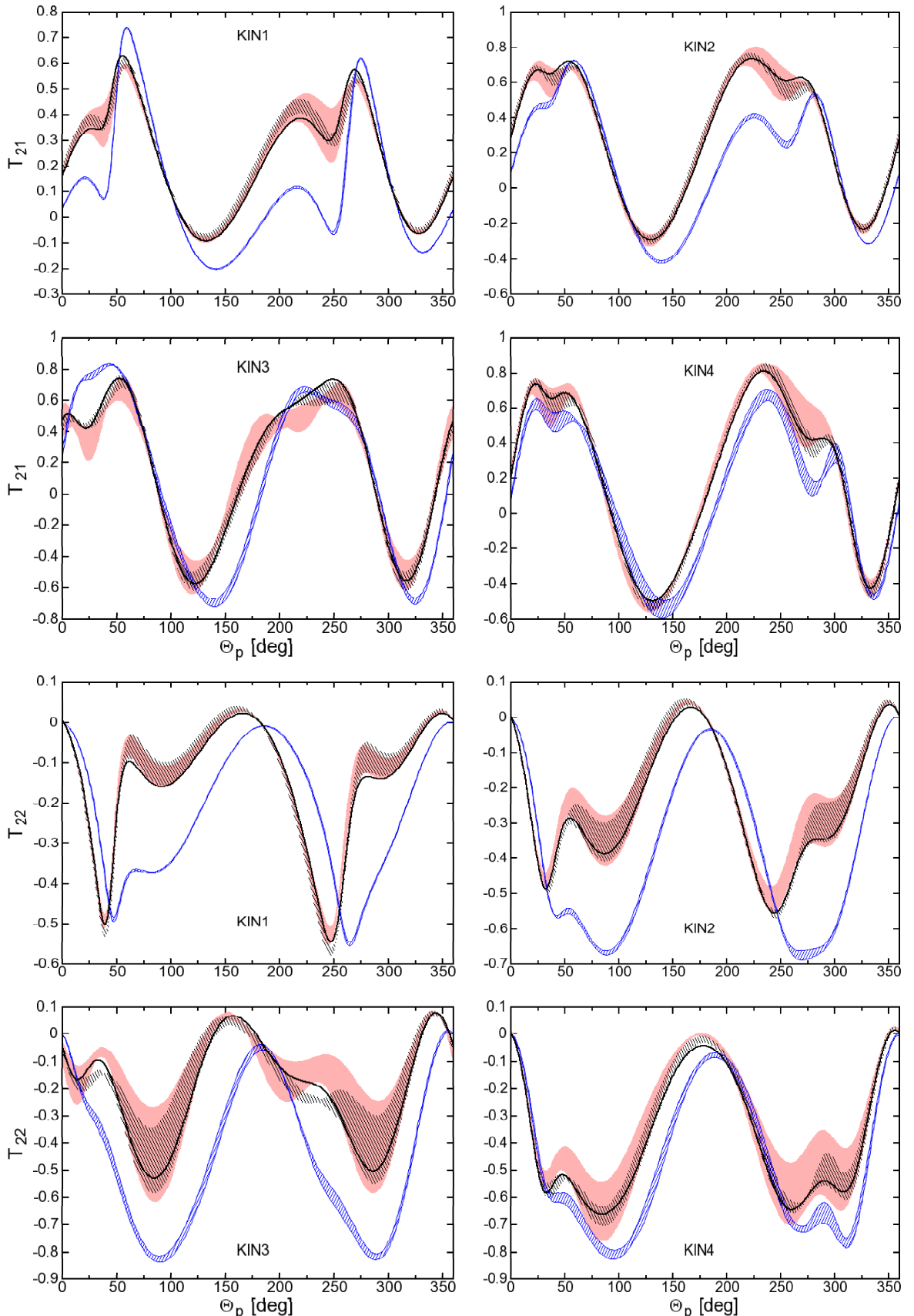


Figure 5.17: Deuteron tensor analyzing powers T_{21} (upper rows) and T_{22} (lower rows) as functions of outgoing proton angle θ_p . The bands and lines have the same meaning as in Figure 5.15.

and $\theta_p = 225^\circ - 325^\circ$ for all kinematical configurations. The AV18 reference is enclosed by MEC bands.

5.2.4 Helicity asymmetry of the cross section

For the electrodisintegration process we investigated also the cross section asymmetries A_\perp and A_\parallel , defined identically as in Equation 5.39, but for inelastic electron-deuteron scattering we obtain

$$A(\theta^*, \phi^*) = \frac{v_{T'}R_{T'}(\theta^*, \phi^*) + v_{TL'}R_{TL'}(\theta^*, \phi^*)}{v_L R_L(\theta^*, \phi^*) + v_T R_T(\theta^*, \phi^*) + v_{TT}R_{TT}(\theta^*, \phi^*) + v_{TL}R_{TL}(\theta^*, \phi^*)}. \quad (5.51)$$

As can be seen in Figure 5.18, in case of A_\perp , for all kinematical configuration we

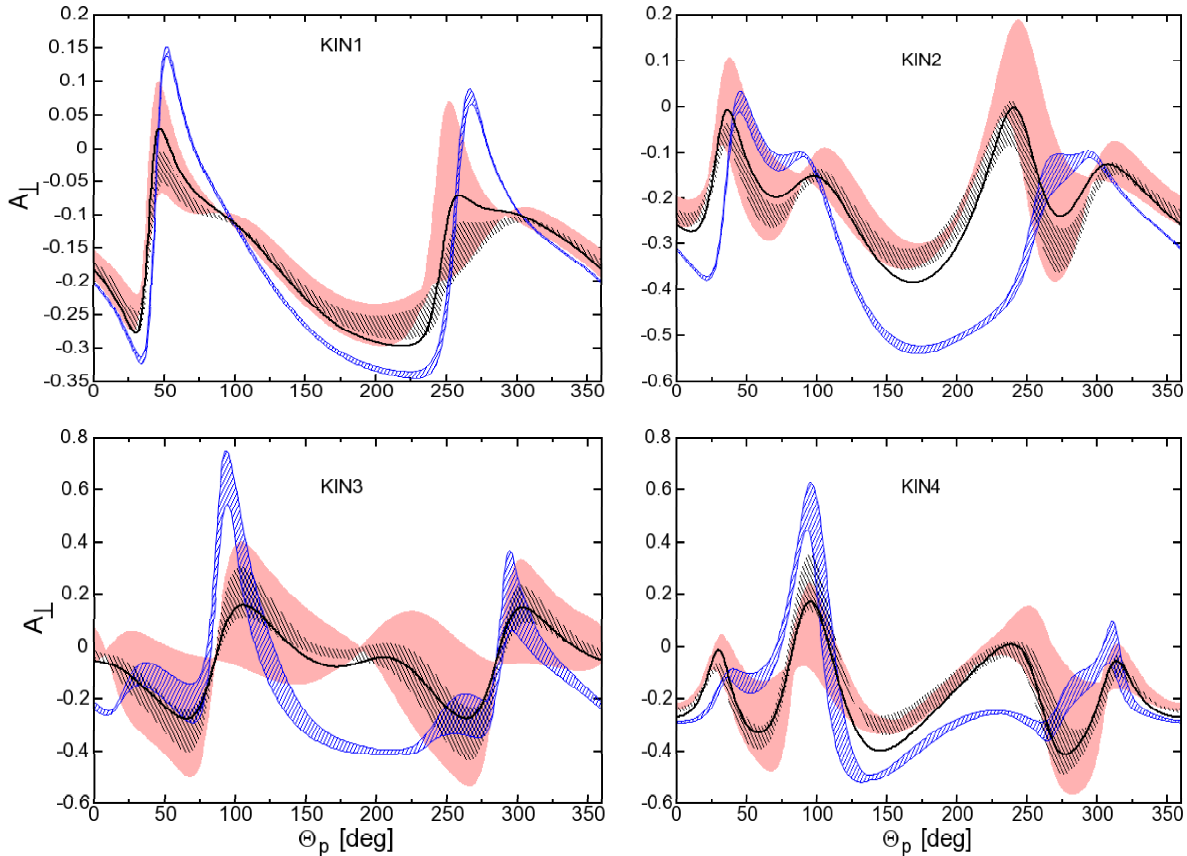


Figure 5.18: Cross section perpendicular helicity asymmetry A_\perp as a function of outgoing proton angle θ_p . The bands and lines have the same meaning as in Figure 5.15.

obtained broader prediction bands for TPE than for OPE currents. Almost for all θ_p angles, the AV18 line and OPE band are contained within the TPE band. Single nucleon current predictions significantly differ from the others, however, the maximum values of A_\perp appears for at same values of θ_p for all currents.

The parallel asymmetry of the cross section, A_\parallel , is shown in Figure 5.19. As for previously discussed observables, the width of the prediction bands increase with

increasing Q value. The TPE bands are the broadest and encompass the OPE bands and the AV18 lines. For all kinematical configurations, we have obtained two maxima at $\theta_p = 70^\circ$ and at $\theta_p = 350^\circ$. With increasing Q value, the minima around $\theta_p = 50^\circ$ and at 250° disappear and a new minimum forms at around 150° .

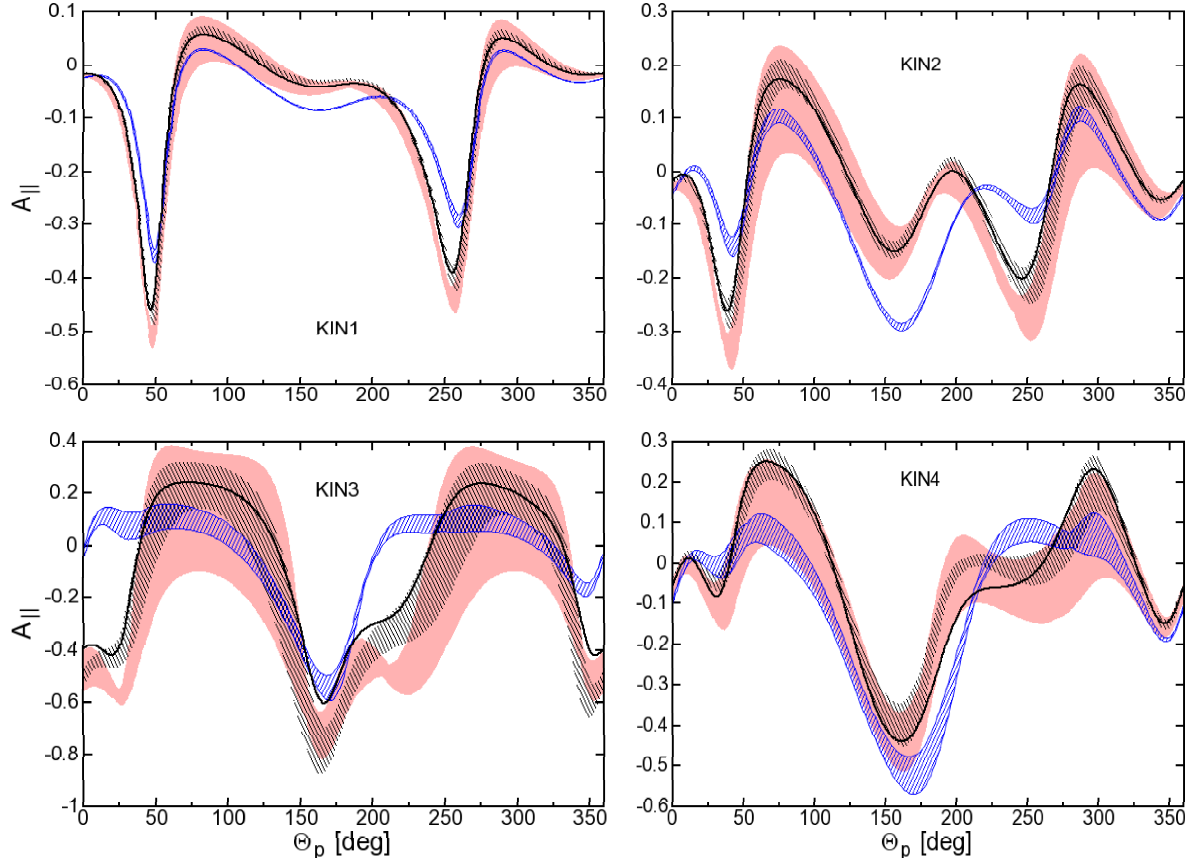


Figure 5.19: Cross section parallel helicity asymmetry A_{\parallel} as a function of outgoing proton angle θ_p . The bands and lines have the same meaning as in Figure 5.15.

5.2.5 Outgoing nucleon polarization

The last analyzed observable was the outgoing proton polarization shown in Figure 5.20. For KIN1 and KIN2 for $\theta_p > 250^\circ$, all prediction bands overlap, while for small angles the results for single nucleon current differ significantly. For higher ω , an addition of MEC currents preserves the shape of the band but shifts it towards smaller angles. With increasing value of Q , the minimum around 200° shifts towards smaller angles and becomes less prominent. For KIN4, the predictions for AV18 and TPE currents differ significantly, thus this case could be interesting for tests of chiral theory.

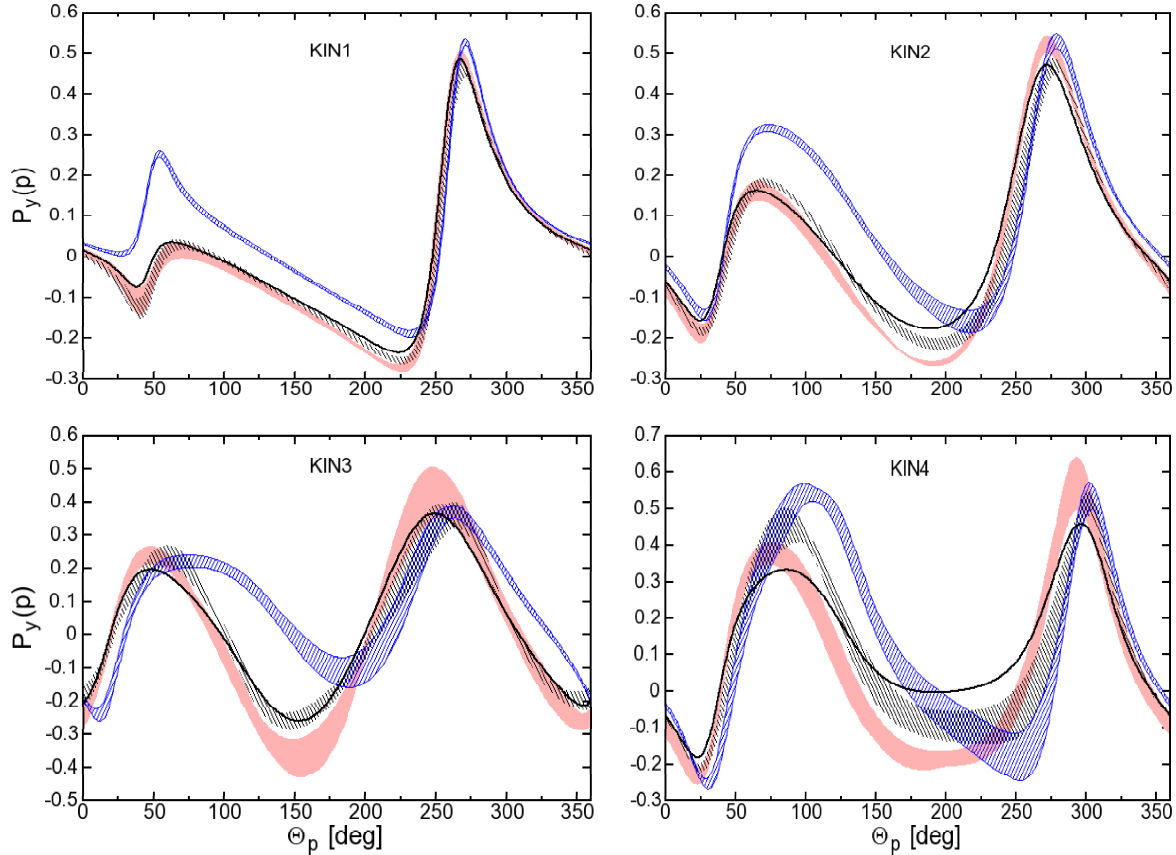


Figure 5.20: Outgoing proton polarization as a function of outgoing proton angle θ_p .

5.2.6 Inclusive cross section

In this section an inclusive reaction for two kinematical configurations ($Q = 100$ MeV and $Q = 206$ MeV, but the same $E = 175$ MeV) is investigated. The inclusive cross section was obtained by integration over the solid angle Ω_{np} . A significant difference between chiral results and AV18 results was obtained for this observable (see Figure 5.21). For higher values of Q (= 206 MeV) these calculations can be compared with experimental data from Ref. [116]. Neither the chiral results nor the calculation with AV18 potential describe the experimental data accurately, especially for small and large E_{np} value. For small value of $Q = 100$ MeV, the difference between the AV18 and the chiral results is less significant and the cross section maximum is shifted towards smaller values of the nucleon-proton energy E_{np} .

Here is a brief summary of the electron scattering on deuteron discussed in this Chapter. In case of elastic scattering, we realize that addition of new parts of the current improves the description of the experimental data, however, still the picture

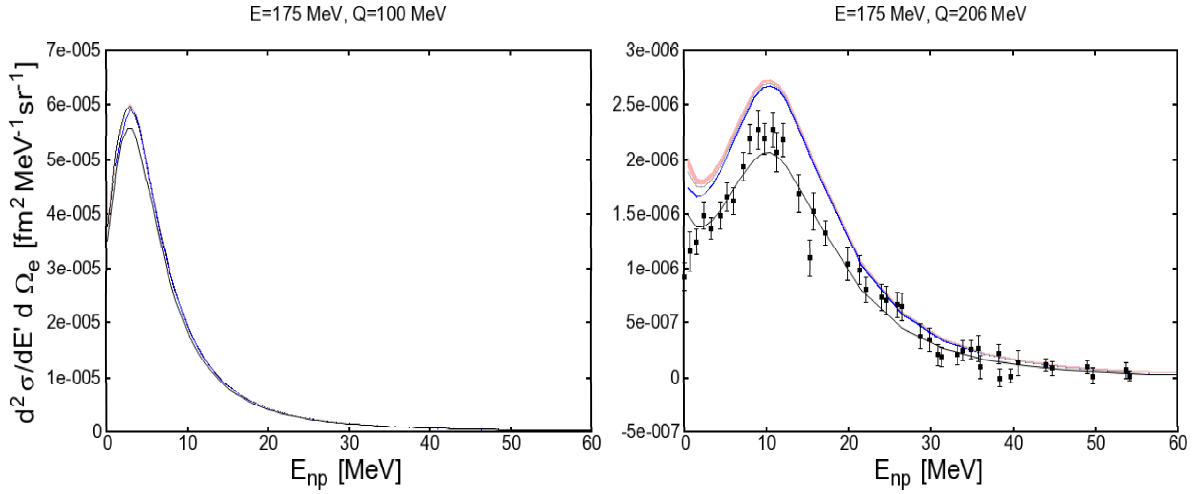


Figure 5.21: Inclusive cross section $d^2\sigma/(dE' d\Omega_e)$ for electrodisintegration of deuteron, as a function of the nucleon-proton energy E_{np} . The color notation is the same as for previous Figures.

is not satisfactory and it is necessary to consider taking into account higher order currents.

For electrodisintegration, for small values of Q and ω , for most observables, we find a good agreement between MEC results and AV18 predictions. With increasing Q , however, the width of the prediction bands increases. We noticed that the predictions strongly depend on ω/Q ratio, and significantly worsen when ω is close to Q ($\omega/Q \approx 1$). This can be seen, especially, in the cross section, $A_{||}$, T_{21} and T_{22} . For low Q values, the bands are narrower, the predictions are more accurate and agree with AV18. As for now, there are insufficient experimental data for low Q values, thus it is impossible to decide which picture, ChEFT or AV18 is better and whether adding TPE current is significant for proper description of the observables. In case of inclusive cross section, for small Q value, we do not see contributions from MEC currents. For higher Q , MEC contributions are very small and noticeable only for small values of E_{NP} .

Chapter 6

Deuteron photodisintegration and radiative capture reactions

6.1 Deuteron photodisintegration

One of the most fundamental processes on the deuteron is the photodisintegration reaction $\gamma + {}^2\text{H} \rightarrow p + n$. It has been a subject of intensive experimental and theoretical research for several decades (see Ref. [117, 118, 119] for a comprehensive review). Especially polarization observables are expected to be sensitive to many dynamical details and provide important tests of different theoretical models. We are aware of many achievements in the theoretical description of this reaction and often compare our results with the ones from [120, 121]. Nuclear matrix elements for photodisintegration

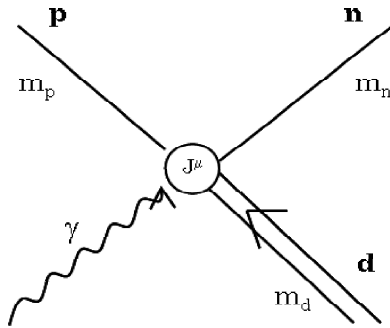


Figure 6.1: Diagram for photodisintegration processes.

of deuteron can be described by the Equation (5.42). We have contributions from the same vector parts of currents operator (5.44) as for electrodisintegration of deuteron.

6.1.1 Kinematics

The kinematics for the photodisintegration process in the laboratory frame is quite similar to the one for electrodisintegration reaction, with one obvious exception. The energy transfer ω and the magnitude of the three-momentum transfer Q cannot be chosen independently and we have $Q = \omega$. There is no restriction on θ_p and for $0 \leq \theta_p \leq 180^\circ$ we get a single value of p_p .

We will describe the photodisintegration process in the center of mass (c.m.) frame (see Figure 6.2). There are two reasons for this change of the reference frame. First,

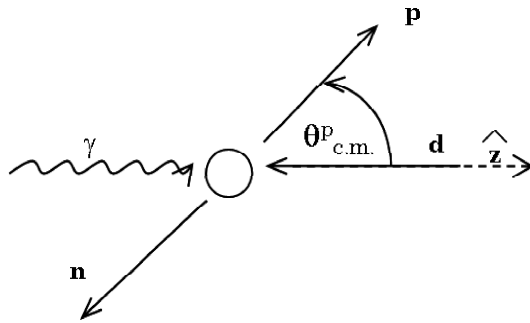


Figure 6.2: Diagram for photodisintegration processes in the center of mass frame.

the bulk of the data available in the literature is given in this frame. Secondly, due to time-reversal invariance, we can easily treat in c.m. the neutron-proton capture process as inverse to the photodisintegration. frame. Given the laboratory photon momentum ω_{lab} , our task is then to calculate the corresponding c.m. photon momentum $\omega_{c.m.}$ and also the momentum of the outgoing nucleons $p_{c.m.}$.

Again we start with relativistic and nonrelativistic formulas for kinematics. In the relativistic case we use the fact that the total four-momentum squared is invariant and can be calculated in any frame yielding the same result

$$\sqrt{(\omega_{lab} + M_d)^2 - \omega_{lab}^2} = \omega_{c.m.} + \sqrt{M_d^2 + \omega_{c.m.}^2}. \quad (6.1)$$

Then we have simply

$$\omega_{c.m.} + \sqrt{M_d^2 + \omega_{c.m.}^2} = 2\sqrt{M_N^2 + p_{c.m.}^2}. \quad (6.2)$$

In the nonrelativistic case we consider the kinetic energy in the final state to get

$$\omega_{lab} - |E_{deut}| - \frac{\omega_{lab}^2}{4M_N} = \omega_{c.m.} + \frac{\omega_{c.m.}^2}{2M_d} - |E_{deut}| \quad (6.3)$$

(E_{deut} is the deuteron binding energy) and then obtain $p_{c.m.}$ from

$$\omega_{c.m.} + M_d + \frac{\omega_{c.m.}^2}{2M_d} = 2M_N + \frac{p_{c.m.}^2}{M_N}. \quad (6.4)$$

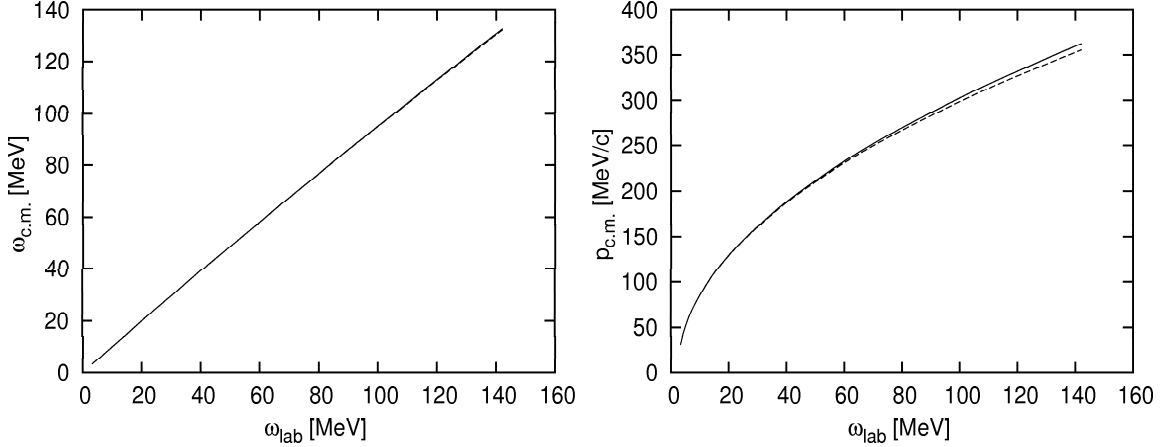


Figure 6.3: (Left panel) The c.m. photon momentum $\omega_{c.m.}$ calculated relativistically (solid line) and nonrelativistically (dashed line) as a function of the laboratory photon momentum ω_{lab} . (Right panel) The c.m. outgoing nucleon momentum $p_{c.m.}$ calculated relativistically (solid line) and nonrelativistically (dashed line) as a function of the laboratory photon momentum ω_{lab} .

In Figure 6.3 (left panel) we compare the photon center-of-mass energy ω_{cm} calculated relativistically and nonrelativistically for a given laboratory photon energy ω_{lab} in order to make sure that the nonrelativistic approximation is very accurate. In the same way we check the validity of the nonrelativistic kinematics calculating the center-of-mass proton momentum. Again, in Figure 6.3 (right panel) we see practically no difference between relativistic and nonrelativistic results.

6.1.2 Exclusive cross section

For unpolarized beam and deuteron target we calculate differential cross section according to the form

$$\frac{d^2\sigma}{d\Omega_p} = 2\pi^2 \alpha \frac{2}{3} \sum_{m'_1, m'_2} \sum_{m_d} R_T F_s \rho_f \quad (6.5)$$

where F_s is the flux factor and ρ_f is the phase shift factor which are defined as

$$F_s = \frac{M_d}{M_d + \omega_{c.m.}}, \quad \rho_f = \frac{M_N p_{c.m.}}{2}. \quad (6.6)$$

Figure 6.4 presents calculations for the unpolarized cross section in the deuteron photodisintegration process for the photon laboratory energies of $E_\gamma = 10, 20, 30, 40, 60$ and 100 MeV displayed as functions of the proton emission angle. All chiral results are obtained with the N2LO potential.

The plots show contributions from different parts of the 2N current: single nucleon currents (blue band), single nucleon current and the leading OPE contributions (dark band). By adding TPE contributions we get predictions for “total” currents represented by the pink band. For comparison, we show the results obtained with AV18 potential

(solid black line). All these predictions are confronted with experimental data from Refs [122, 117]. Note that the results depend on the two cut-off parameters (Λ , $\tilde{\Lambda}$) present in the chiral potential. The bands reflect this dependence for variety of Λ and $\tilde{\Lambda}$ as listed in Table 2.2.

The results obtained with single nucleon currents and OPE contributions do not describe the data as well and significantly differ from the reference AV18 predictions. It can be noticed that the single nucleon current alone is insufficient to describe the experimental data. Thus, it is necessary to include higher order electromagnetic currents. In most cases, the OPE predictions give the cross section values lower than the AV18 prediction. Calculations additionally including the TPE contributions describe the experimental data more accurately and agree with the AV18 predictions. The bands including TPE currents are broad, however, for $E_\gamma = 20, 30$ and 60 MeV they give reasonable description of the experimental data. The prediction bands become narrower for low photon energies, which suggests that the ChEFT works better for small values of E_γ . For photon energies greater than 60 MeV the prediction bands become broad and the ChEFT is still unreliable. For these energies, the AV18 potential is doing the best job.

6.1.3 Photon analyzing power

In this section we describe photon analyzing powers in the deuteron photo-disintegration processes induced by polarized photon. We calculated linear photon analyzing powers according to the following equation

$$\Sigma_l = \sum_{m'_1 m'_2} \sum_{m_d} \frac{2\text{Re}(N_{+1} N_{-1}^*)}{|N_{+1}|^2 + |N_{-1}|^2}. \quad (6.7)$$

For the photon laboratory energies $E_\gamma = 10, 20, 30, 40, 60$ and 100 MeV displayed as functions of the proton emission angle. The results are displayed in Figure 6.5 as a function of the proton emission angle. We use the same notation as in the previous section. The theoretical calculations are compared with experimental data from Refs [122, 117]. Similarly to differential cross section the single nucleon current predictions do not reproduce the experimental data. The prediction band lies above other calculations, are narrow and gets broader with increasing photon energy. The dark band representing the single nucleon currents and OPE contributions is significantly broader than the one including additionally the TPE current operators (pink bands). The chiral results tend to appear below the AV18 calculations for all considered photon energies. The best agreement between these models is obtained at lowest energies. For energies $E_\gamma = 20$ and 30 MeV the experimental data are well described by the AV18 calculations and, within the uncertainty limits, by the TPE predictions. For higher energies ($E_\gamma \geq 60$ MeV) calculations with TPE currents give better agreement with experimental than the AV18 results.

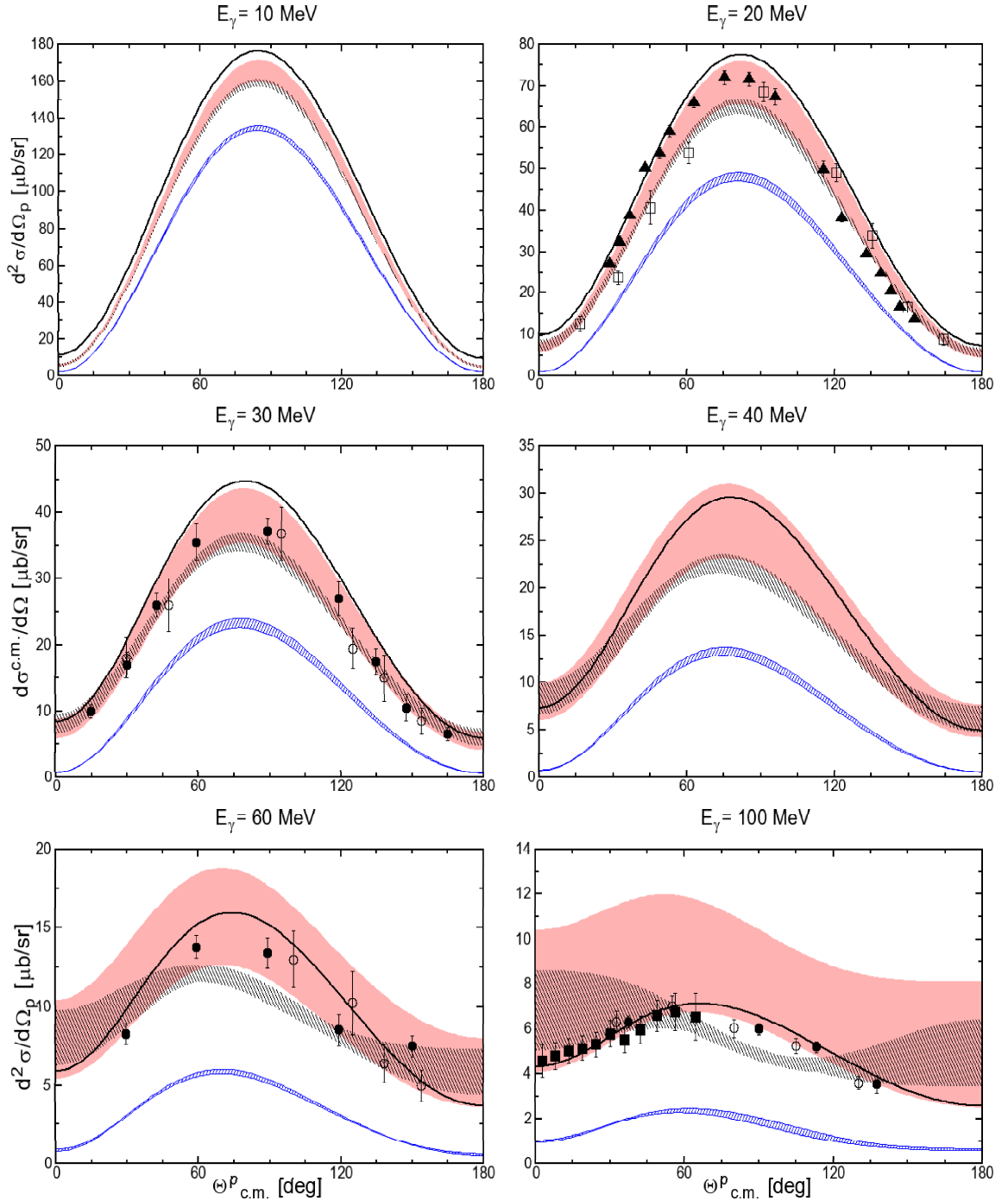


Figure 6.4: Unpolarized cross section in the deuteron photo-disintegration process for the photon laboratory energies of $E_\gamma = 10, 20, 30, 40, 60$ and 100 MeV displayed as functions of the proton emission angle. The solid black line is for the standard calculation based on the AV18 potential, the blue band covers results obtained with the single-nucleon current only, the grey band represents predictions based on the single-nucleon and OPE parts, and the pink band contains additionally TPE parts. The experimental data are the same as in Refs [122, 117].

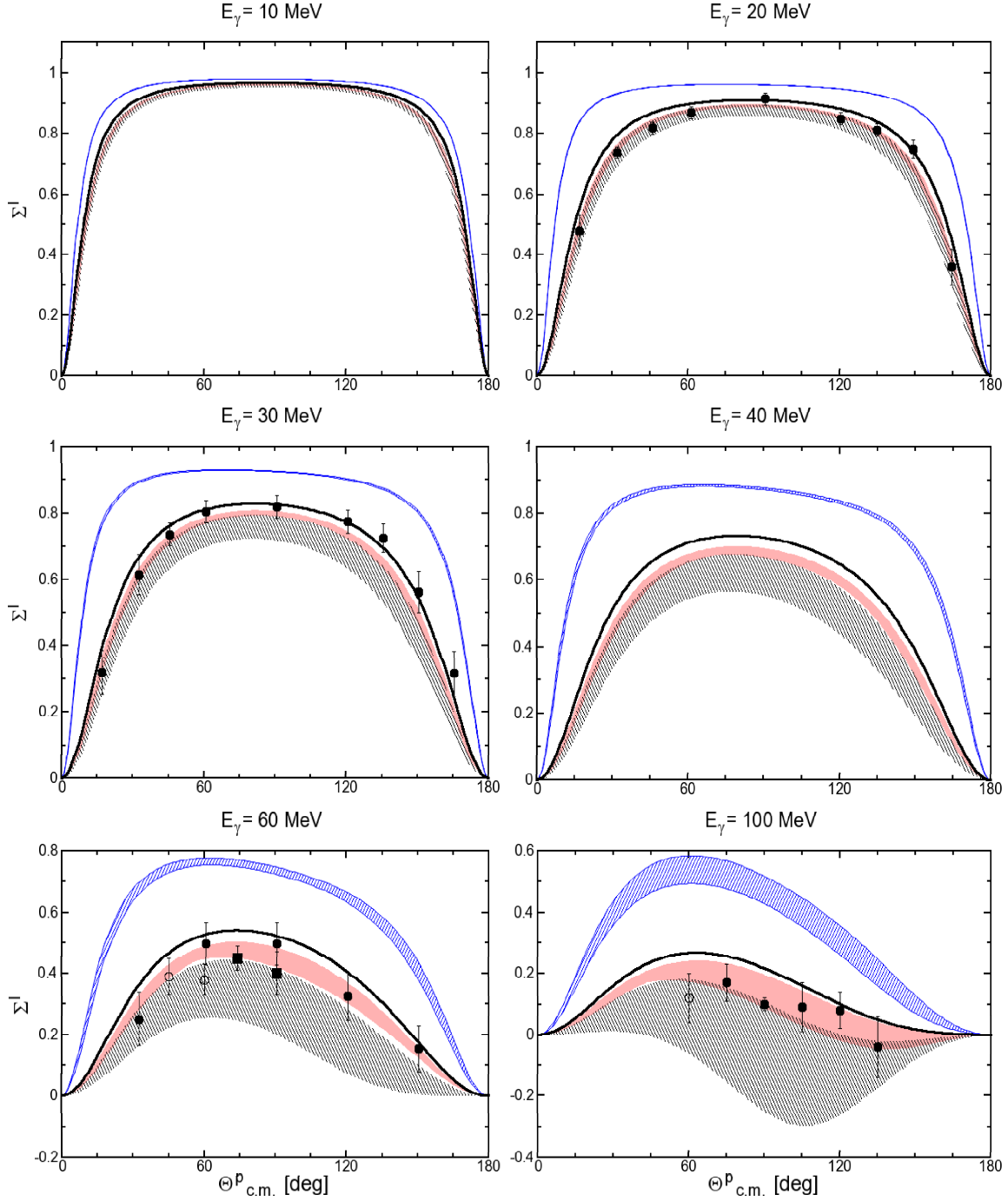


Figure 6.5: Photon analyzing powers in the deuteron photo-disintegration process at the photon laboratory energies of $E_\gamma = 10, 20, 30, 40, 60$ and 100 MeV displayed as functions of the proton emission angle. The solid black line is for the standard calculation based on the AV18 potential, the blue band covers results obtained with the single-nucleon current only, the dark band represents predictions based on the single-nucleon and OPE parts, and the pink band contains additionally TPE parts. The experimental data are the same as in Refs [122, 117].

6.1.4 Outgoing nucleon polarization

An interesting observable, however more difficult to measure is the polarization of the outgoing nucleon. We calculated the outgoing proton and neutron polarizations using the same formula as for electrodisintegration process. The results are shown in Figures 6.6 and 6.7. The color notation is the same as in previous sections. For all photon energies, we can see a good agreement between traditional framework (AV18) and chiral results including MEC. Again, as for photon analyzing powers, the width of the prediction bands all the theories increases with E_γ and the width of the TPE bands is larger than for the OPE bands. The single nucleon current results behave similarly, however the predicted values, especially for the forward and backward outgoing proton angles, significantly differ from other calculations (with the MEC and the AV18 potential).

The results for polarization of outgoing neutron as a function of neutron outgoing angle are presented in Figure 6.7. A similar behaviour as for proton polarization can be noticed. It is worthwhile to note, that the neutron polarizations are generally smaller than the proton ones.

6.1.5 Deuteron tensor analyzing powers

A general expression for the cross section of the two-body photodisintegration of the polarized deuteron is the same as for electrodisintegration processes and was already given in Equation 5.27. The deuteron tensor analyzing powers T_{2q} (where $q=0, 1, 2$) are functions of the photon energy E_γ and the proton emission angle $\theta_{c.m.}^p$. Here, we focus on a comparison of our calculations with recent experimental tensor analyzing powers T_{2q} for low energies from [123] and do not show the results for vector analyzing power iT_{11} as there exist no experimental data for this observable. In order to adjust to the data from [123], our predictions for the exclusive observables have been integrated over relevant intervals of the initial photon energy and over angular regions according to the following formulas:

$$T_{2q} = \frac{1}{\sigma_{incl}} \int_{\Delta E_\gamma} dE_\gamma \int d\theta_{c.m.} \sin \theta_{c.m.}^p \int d\phi T_{2q}(E_\gamma, \theta_{c.m.}^p, \phi) \sigma_0(E_\gamma, \theta_{c.m.}^p, \phi) \quad (6.8)$$

where σ_0 is the unpolarized exclusive cross section and σ_{incl} is the inclusive polarized cross section. First, we present results of the tensor analyzing power components T_{20} , T_{21} and T_{22} which include contribution from two-pion exchange currents. As a reference we use the calculations obtained with the phenomenological AV18 potential with the corresponding exchange currents. In Figure 6.8 the results for the angular distribution at the bin energies of $E_\gamma=25-45$ MeV, $E_\gamma=45-70$ MeV, $E_\gamma=70-100$ MeV and $E_\gamma=100-140$ MeV together with experimental data are presented.

In general, for all the deuteron tensor analyzing powers one achieves quite a good agreement between the AV18 potential prediction, chiral results and experimental data. In case of T_{20} for large $\theta_{c.m.}$ values, a good agreement between all the considered parts of currents and experimental data is obtained. However, the bands for TPE

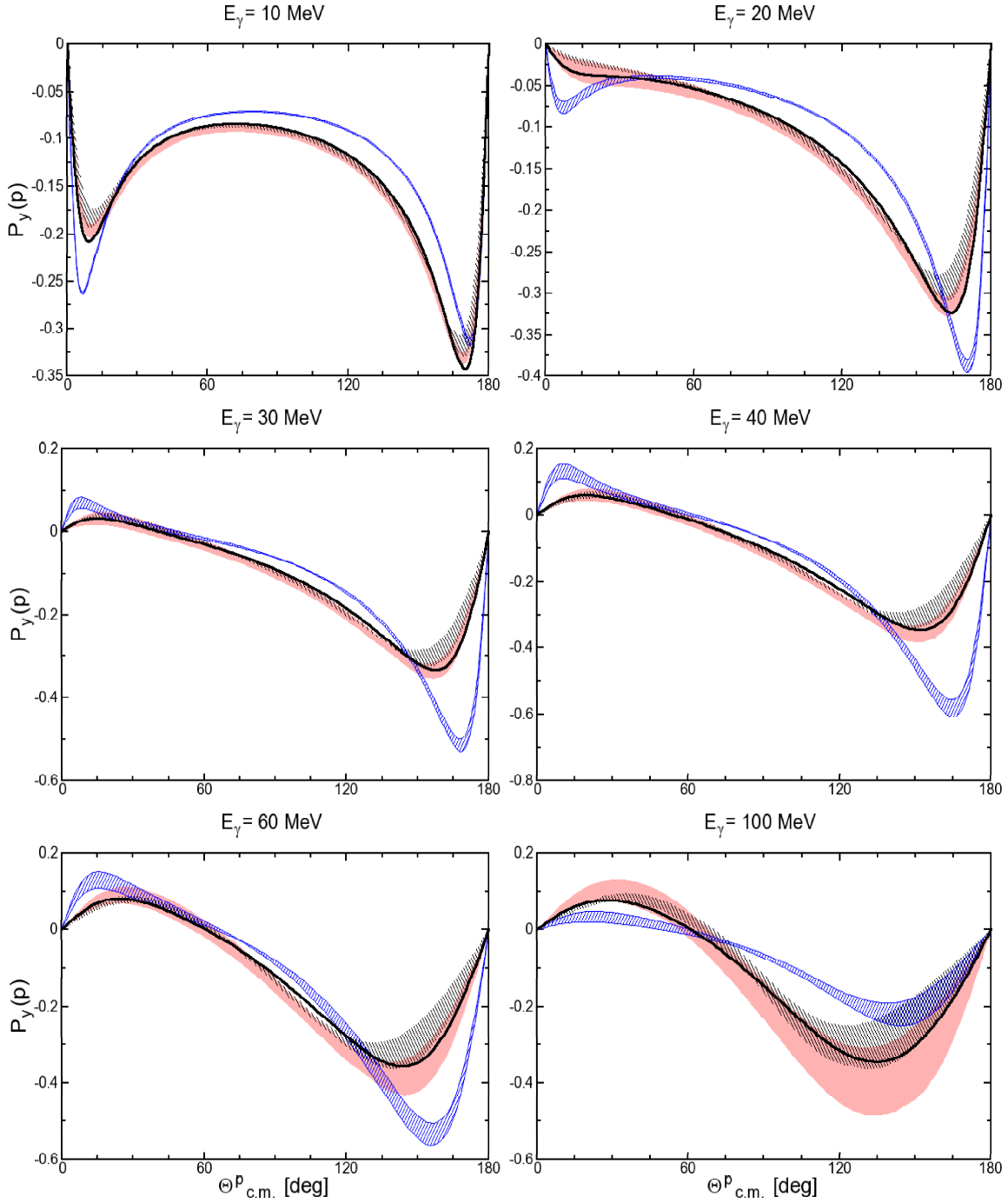


Figure 6.6: Proton polarization in the deuteron photo-disintegration process for the photon laboratory energies of $E_\gamma = 10, 20, 30, 40, 60, 100$ MeV displayed as functions of the proton emission angle. The solid black line is for the standard calculation based on the AV18 potential, the blue band covers results obtained with the single-nucleon current only, the grey band represents predictions based on the single-nucleon and OPE parts, and the pink band contains additionally TPE parts. The experimental data are the same as in Ref. [122].

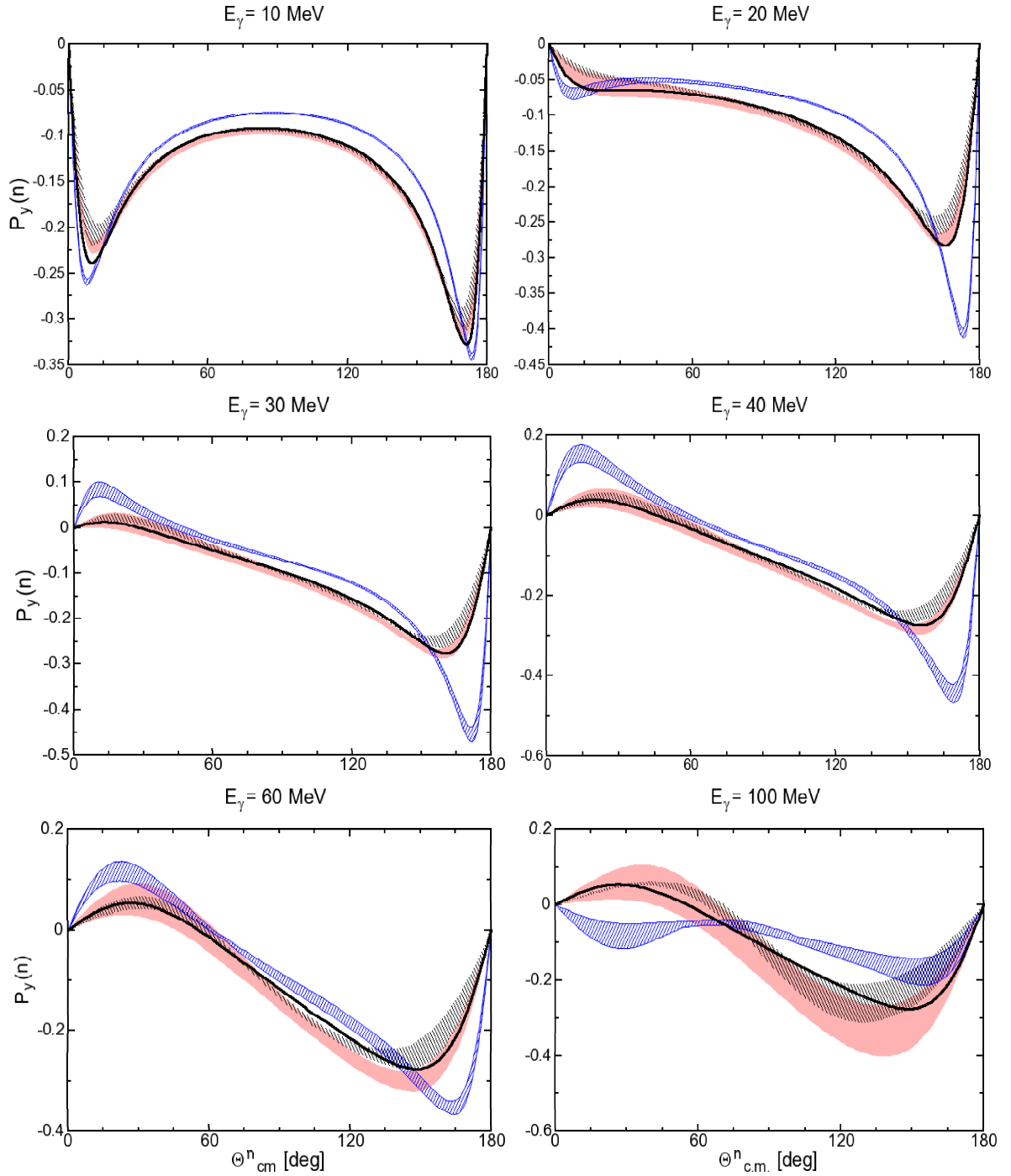


Figure 6.7: Neutron polarization in the deuteron photo-disintegration process for the photon laboratory energies of $E_\gamma = 10, 20, 30, 40, 60, 100$ MeV displayed as functions of the neutron emission angle. The solid black line is for the standard calculation based on the AV18 potential, the blue band covers results obtained with the single-nucleon current only, the grey band represents predictions based on the single-nucleon and OPE parts, and the pink band contains additionally TPE parts. The experimental data are the same as in Ref. [122].

currents are broader than the OPE bands. For high E_γ and low $\theta_{c.m.}^p$, all the theoretical predictions give the T_{20} values smaller than experimental data. For T_{21} , again, all the theoretical predictions give similar results. For $E_\gamma=45\text{--}70$ MeV and $70\text{--}100$ MeV all the calculations reliably describe the experimental data. In case of T_{22} the prediction band for TPE currents is narrower than the OPE bands. For all the energy bins, the experimental T_{22} values for the backward angles are well described.

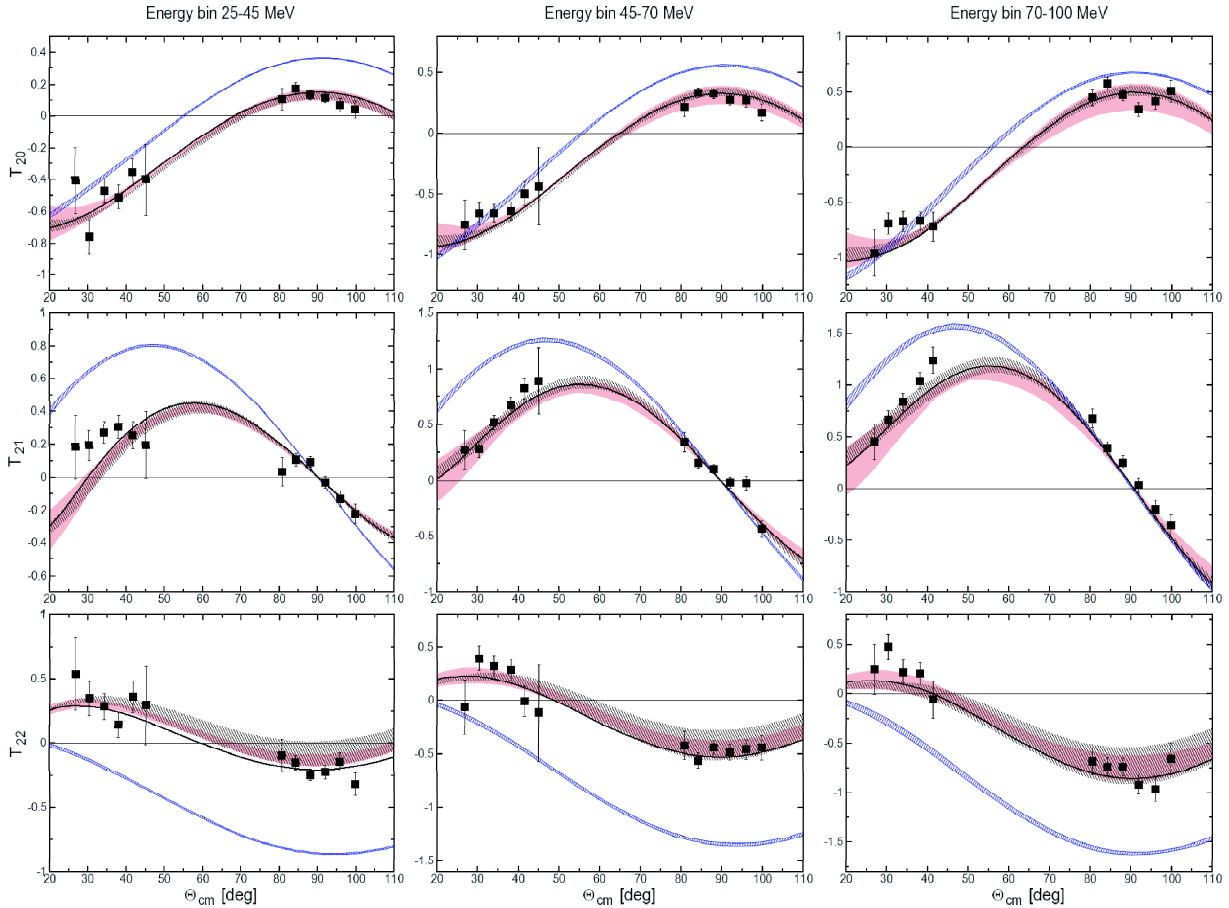


Figure 6.8: Deuteron tensor analyzing powers vs. proton emission angle for three E_γ -energy bins. The solid black line is for the standard calculation based on the AV18 potential, the grey band represents predictions based on the single-nucleon and OPE parts, and the pink band contains additionally TPE parts. Experimental data come from Ref. [123]. Errors bars represent the statistical uncertainty only.

6.1.6 Total cross section

The last observable we calculated was the total cross section. This observable was thoroughly described in many publications using various theories [117]. In Figure 6.9 the total cross section for $E_\gamma \approx 2\text{--}50$ MeV is presented. The experimental data are taken from Ref. [121]. In the left panel, we see the results for the single nucleon and

OPE current. For this particular case the width of the prediction band is negligible. The theoretical predictions agree with the experimental data within the uncertainty limits. The Figure on the right panel shows the TPE calculations, for which the band is somewhat broader but no conclusion can be drawn since experimental data suffer from large uncertainties.

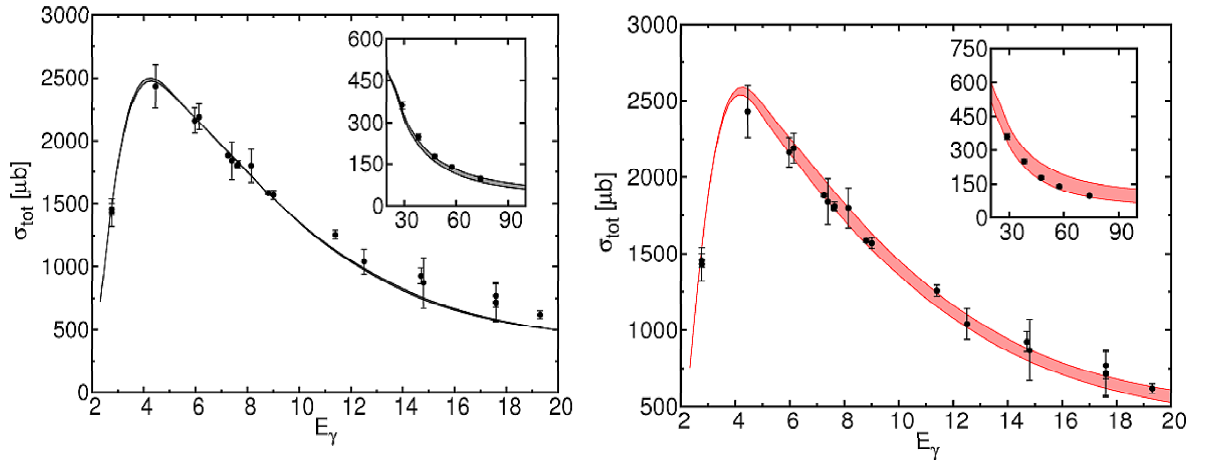


Figure 6.9: Total cross section for photodisintegration of the deuteron as a function of photon energy beam. In the left panel results for single nucleon current and OPE contribution are shown. In the right panel, we can find the results obtained with an additional TPE currents.

Summarizing, for the photodisintegration of the deuteron, especially in case of the low photon energy, addition of the TPE currents significantly improves the theoretical predictions. For all the considered observables the experimental data are well described. For higher energies the prediction bands of TPE are broad. In some cases (differential cross section for $E_\gamma = 20, 30$ MeV and photon analyzing power for $E_\gamma = 60$ MeV) the chiral results are much better than the calculation with the AV18 potential.

6.2 Neutron-proton capture reaction

Radiative neutron-proton capture is one of the key reactions for the Big-Bang Nucleosynthesis (BBN), because it is the starting point of the synthesis of light elements. The cross sections can be measured directly (for example [124, 125]) and via the inverse photodisintegration reaction (for example [126, 127]).

Many theoretical models have been used to describe this capture reaction. In this thesis we calculate the inclusive cross section and selected exclusive polarization observables at BBN energies, using the framework of ChEFT. We also compare our results for the inclusive cross section with other theoretical estimations, the pionless EFT calculation [128], the calculation with the AV18 potential and the meson exchange current [129], and the result of an R-matrix analysis [130] and MCMC analysis [131, 132]. Our results agree quite well with the theoretical models listed above.

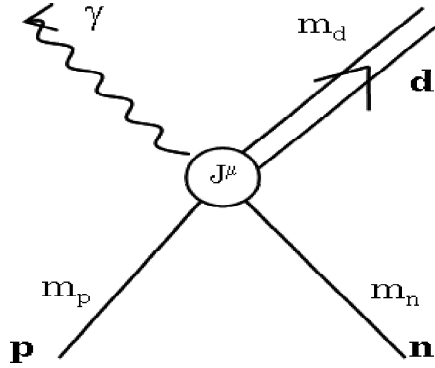


Figure 6.10: Diagram for the np radiative capture reaction.

The exclusive cross section of the capture reaction can be directly obtained from the one for the inverse photodisintegration processes as:

$$\frac{d\sigma}{d\Omega}(np \rightarrow d\gamma) = \frac{3}{2} \left(\frac{\omega_{c.m.}}{p_{p_{c.m.}}} \right)^2 \frac{d\sigma}{d\Omega}(\gamma d \rightarrow np) \quad (6.9)$$

and we do not present it here. In this thesis, we concentrate on the total cross section for capture reaction at BBN energies, and compare our results with various existing theories.

6.2.1 Kinematics

We treat the capture process in the center of mass (c.m.) frame. For a given laboratory nucleon kinetic energy T_{lab} we calculate the corresponding c.m. nucleon momentum $p_{c.m.}$ (in the initial state) and the photon momentum $\omega_{c.m.}$ (in the final state).

Using the relativistic kinematics, we obtain

$$\sqrt{(T_{lab} + 2M_N)^2 - p_{lab}^2} = 2\sqrt{M_N^2 + p_{c.m.}^2} = \omega_{c.m.} + \sqrt{M_d^2 + \omega_{c.m.}^2}, \quad (6.10)$$

where

$$p_{lab} = \sqrt{(T_{lab} + M_N)^2 - M_N^2}. \quad (6.11)$$

In the nonrelativistic case, we have

$$T_{lab} - \frac{p_{lab}^2}{4M_N} + 2M_N = 2M_N + \frac{p_{c.m.}^2}{M_N} = \omega_{c.m.} + M_d + \frac{\omega_{c.m.}^2}{2M_d}, \quad (6.12)$$

where now

$$p_{lab} = \sqrt{2M_N T_{lab}}. \quad (6.13)$$

We show in Figures 6.11–6.12 p_{lab} , $p_{c.m.}$ and $\omega_{c.m.}$ as a function of T_{lab} to check the relevance of the relativistic effects in the kinematics. All the three quantities are calculated relativistically and nonrelativistically. For $T_{lab} \leq 200$ MeV the relativistic

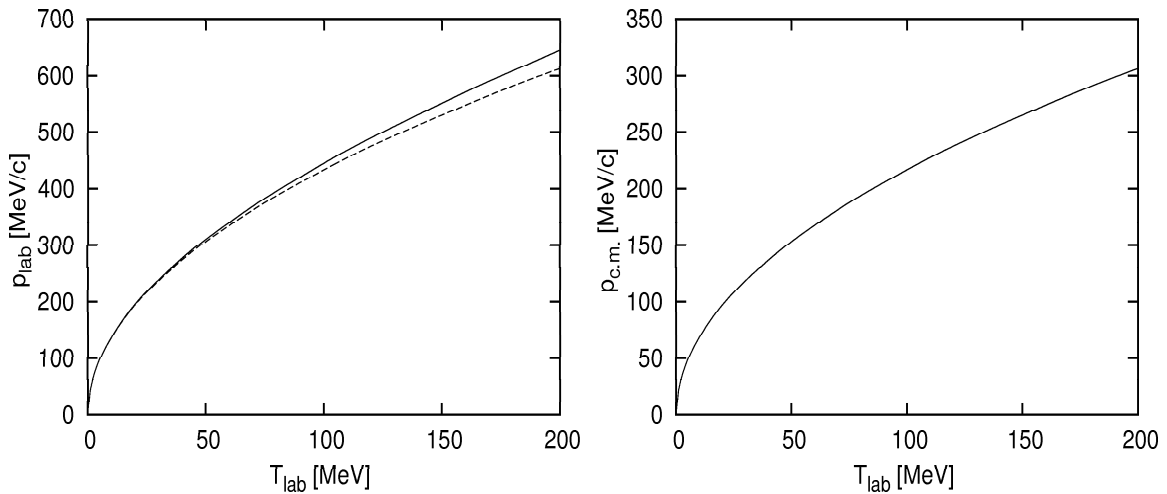


Figure 6.11: (Left panel) Laboratory nucleon momentum p_{lab} calculated relativistically (solid line) and nonrelativistically (dashed line) as a function of the laboratory beam energy T_{lab} . (Right panel) The c.m. initial nucleon momentum $p_{c.m.}$ calculated relativistically (solid line) and nonrelativistically (dashed line) as a function of the laboratory beam energy T_{lab} .

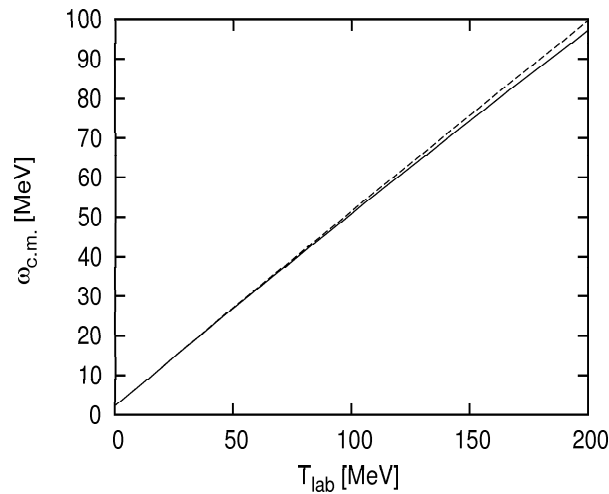


Figure 6.12: The c.m. outgoing photon momentum $\omega_{c.m.}$ calculated relativistically (solid line) and nonrelativistically (dashed line) as a function of the laboratory beam energy T_{lab} .

corrections are small. Thus, in the latter we can safely use the nonrelativistic formulas.

In fact, we can relate not only the unpolarized cross sections but also the more fundamental nuclear matrix elements

$$\langle \Psi_{deut} m_d | J_\tau(\vec{Q}) | \Psi_{scatt} m_p m_n \rangle^{(+)} = \sum_{m'_p, m'_n, m'_d} (-1)^{m_p + m_n + 1 + m_d} D_{m'_d, -m_d}^{(1)}(0, \pi - \theta_{\gamma p}, 0) \\ D_{m'_n, -m_n}^{(1/2)}(0, \pi - \theta_{\gamma p}, 0) D_{m'_p, -m_p}^{(1/2)}(0, \pi - \theta_{\gamma p}, 0)^{(-)} \langle \Psi_{scatt} m'_p m'_n | J_{-\tau}(\vec{Q}) | \Psi_{deut} m_d \rangle \quad (6.14)$$

where using the Wigner D-matrix for spin 1 ($D^{(1)}$) and 1/2 ($D^{(1/2)}$) [65, 69]. Based on the amplitude $\langle \Psi_{deut} m_d | J_\tau(\vec{Q}) | \Psi_{scatt} m_p m_n \rangle^{(+)}$ we can calculate all observables for the capture reaction.

6.2.2 Inclusive cross section

First, we present our numerical results obtained with chiral potential. In Tables 6.1–6.2 we present predictions for the total cross section (in μb) of capture reaction of the neutron as a function of the initial energy for two-nucleon in the center of mass frame: $E_n = 0.1, 0.5, 1.0 \text{ MeV}$ at NLO (Table 6.1) and N2LO (Table 6.2) of chiral expansion. One can recognize that effects from individual currents: single nucleon current, OPE current in LO, two-pion exchange contribution. The values given in Table 6.1 and 6.2 describe the widths of the prediction band. The main contribution comes from single nucleon current. Adding OPE contribution increases the predicted values by $\sim 5.7\%$ for NLO and $\sim 6.3\%$ for N2LO, while addition of the TPE contributions increases the predictions by $\sim 3.0\%$ and $\sim 3.8\%$ for NLO and N2LO, respectively.

Table 6.1: Total cross section of the np-capture reaction at the energy of two nucleons in the center-of-mass frame $E_n=0.1, 0.5$ and 1.0 MeV for NLO potential.

Theory	$E_n = 0.1 \text{ [MeV]}$	$E_n = 0.5 \text{ [MeV]}$	$E_n = 1.0 \text{ [MeV]}$
Single	58.7893–59.4459	31.8747–32.1642	32.3555–32.6074
OPE	62.5215–62.6274	33.8827–34.0609	34.0429–34.3554
TPE	64.3863–65.3418	34.7665–34.8197	35.0500–35.3505

Table 6.2: Total cross section of the np-capture reaction at the energy of two nucleons in the center-of-mass frame $E_n=0.1, 0.5$ and 1.0 MeV for N2LO potential.

Theory	$E_n = 0.1 \text{ [MeV]}$	$E_n = 0.5 \text{ [MeV]}$	$E_n = 1.0 \text{ [MeV]}$
Single	58.7259–59.0605	31.7673–31.9482	32.2647–32.4459
OPE	62.4705–62.4340	33.8626–34.1704	34.1481–34.5082
TPE	64.8853–65.2371	35.0971–35.2765	35.4571–35.7234

The comparison of chiral “total” results (single + OPE + TPE) with those obtained from the calculations of other theories is presented in Table 6.3. Values obtained by

Rupak [128] are from the pionless EFT (without dibaryon fields) up to N4LO and those by Nakamura [129] are from the potential model calculation using wave functions from the AV18 potential and meson exchange currents. The results by Hale are obtained from an R-matrix analysis [130]. The Ando [131] results was done using the Markov Chain Monte Carlo (MCMC) analysis. For $E_n = 0.1$ MeV the chiral results give greater

Table 6.3: Comparison of theoretical predictions for the total cross section (in mb) of the np-capture reaction at the BBN energies. E_n is the energy of two nucleons in the center-of-mass frame.

Theory	$E_n = 0.1$ [MeV]	$E_n = 0.5$ [MeV]	$E_n = 1.0$ [MeV]
Ando[131]	0.0634(2)	0.0343(1)	0.0352(1)
Rupak[128]	0.06352(5)	0.0341(2)	0.0349(3)
Nakamura[129]	0.06366	0.03416	0.03495
Hale[130]	0.0605(10)	0.0338(8)	0.0365(8)
Our results NLO	0.0643–0.0653	0.0348–0.0348	0.0351–0.0353
Our results N2LO	0.0648–0.0652	0.0351–0.0353	0.0355–0.0357

predicted values than other theories. The N2LO band is narrower than the NLO one, and is included within the NLO band. For $E_n = 0.5$ MeV a better agreement with other calculations was obtained, however, our results are still greater than other predictions. The bands are narrower than for the lower energy. For $E_n = 1.0$ MeV case Ando and Rupak theoretical estimations the calculations agree with our NLO results within uncertainty limits, while Hale estimation agrees with N2LO results.

6.2.3 Nucleon analyzing powers

In this section, we focus on the np radiative capture reaction. We calculate several nucleon analyzing powers for radiative capture reaction at energy $T_{lab} = 183$ MeV (which corresponding to 96 MeV for deuteron photodisintegration). The neutron and proton analyzing powers A_n and A_p , are defined as the relative difference in cross sections for the corresponding nucleon spin up (u) vs down (d):

$$A_n(\theta) = \frac{\left(\frac{d\sigma}{d\Omega}\right)_{uu} - \left(\frac{d\sigma}{d\Omega}\right)_{dd} + \left(\frac{d\sigma}{d\Omega}\right)_{ud} - \left(\frac{d\sigma}{d\Omega}\right)_{du}}{\left(\frac{d\sigma}{d\Omega}\right)_{uu} + \left(\frac{d\sigma}{d\Omega}\right)_{dd} + \left(\frac{d\sigma}{d\Omega}\right)_{ud} + \left(\frac{d\sigma}{d\Omega}\right)_{du}} \quad (6.15)$$

$$A_p(\theta) = \frac{\left(\frac{d\sigma}{d\Omega}\right)_{uu} - \left(\frac{d\sigma}{d\Omega}\right)_{dd} - \left(\frac{d\sigma}{d\Omega}\right)_{ud} + \left(\frac{d\sigma}{d\Omega}\right)_{du}}{\left(\frac{d\sigma}{d\Omega}\right)_{uu} + \left(\frac{d\sigma}{d\Omega}\right)_{dd} + \left(\frac{d\sigma}{d\Omega}\right)_{ud} + \left(\frac{d\sigma}{d\Omega}\right)_{du}} \quad (6.16)$$

The results for the neutron and proton analyzing powers at $T_{lab} = 183$ MeV are shown in Figure 6.13. The shape of the prediction bands is similar for all cases. TPE bands is the most broad and much broader than for OPE. The best agreement between theory and experiment for A_n and A_p was obtained for TPE.

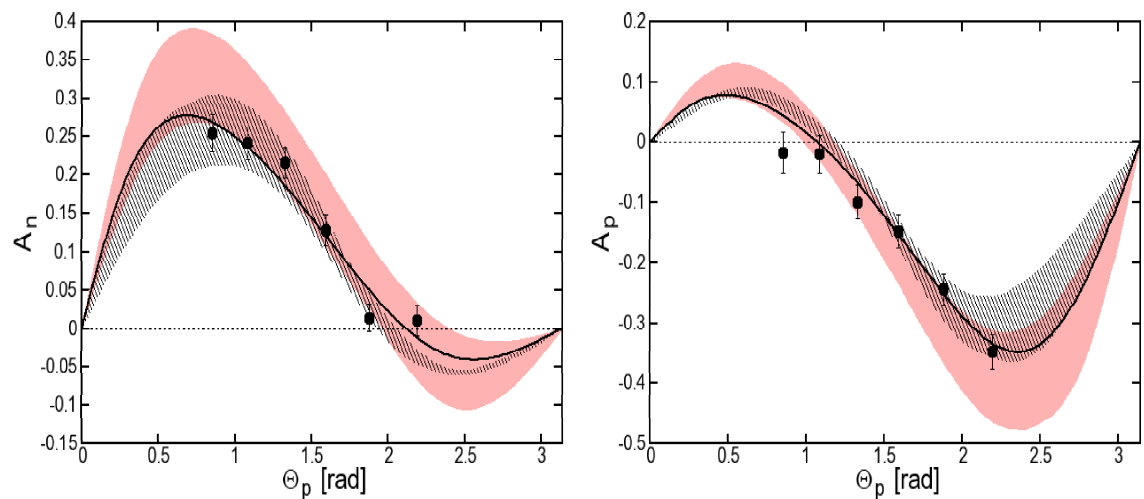


Figure 6.13: Neutron and proton analyzing powers at $T_{lab} = 183$ MeV as a function of the proton emission angle. Data are from Ref. [133].

Chapter 7

Formalism for three-nucleon reactions

For the three-nucleon (3N) reactions considered in this thesis we will only briefly introduce key points and refer the reader to [54] for detailed explanations. Since we use in general the framework and its numerical realization of [54], we will just focus on the way we deal with the current operator in the 3N system.

The starting point is exactly the same as for the 2N reaction. We consider the general matrix element of the current operator

$$N^\mu = \left\langle \Psi_f \vec{P}_f \left| \frac{1}{e} J^\mu(0) \right| \Psi_i \vec{P}_i \right\rangle \equiv \left\langle \Psi_f \left| J^\mu(\vec{Q}) \right| \Psi_i \right\rangle, \quad (7.1)$$

where now \vec{P}_i (\vec{P}_f) is the total initial (final) momentum of the 3N system. As for the 2N case, the magnitude of the elementary charge e is extracted from the current operator. It is also understood that the current operator $J^\mu(\vec{Q})$ acts effectively between the internal initial and final 3N states with $\vec{Q} \equiv \vec{P}_f - \vec{P}_i$.

These internal states are conventionally expressed in momentum space in terms of two (relative) Jacobi momenta, \vec{p} and \vec{q} . The momentum \vec{p} describes a relative motion within a 2N subsystem (here we choose the subsystem consisting of nucleons 2 and 3). The momentum \vec{q} describes the motion of the remaining nucleon (here nucleon 1) with respect to the 2N subsystem:

$$\vec{p} = \frac{1}{2} (\vec{p}_2 - \vec{p}_3), \quad (7.2)$$

$$\vec{q} = \frac{2}{3} \left(\vec{p}_1 - \frac{1}{2} (\vec{p}_2 + \vec{p}_3) \right). \quad (7.3)$$

Thus we use in momentum space the basis states

$$| \vec{p} \vec{q} \rangle \equiv | \vec{p} \rangle | \vec{q} \rangle \quad (7.4)$$

which have to be supplemented by nucleon spin projections (m_1, m_2, m_3) and (treating nucleons as identical particles) also isospin projections (ν_1, ν_2, ν_3). The momentum states are normalized as

$$\langle \vec{p}' \vec{q}' | \vec{p} \vec{q} \rangle = \delta^3(\vec{p}' - \vec{p}) \delta^3(\vec{q}' - \vec{q}) \quad (7.5)$$

and fulfill

$$\int d^3p d^3q |\vec{p}\vec{q}\rangle \langle\vec{p}\vec{q}| = 1. \quad (7.6)$$

Working directly with three-dimensional vectors is very difficult, especially for 3N scattering states. Although first steps in that direction have been already made [134, 135, 136, 137], we will use standard partial wave decomposition [54] and work with the states in the so-called jI coupling:

$$|pq\alpha\rangle \equiv \left| pq(ls)j\left(\lambda\frac{1}{2}\right)I(jI)JM\right\rangle \left|\left(t\frac{1}{2}\right)TM_T\right\rangle \quad (7.7)$$

where p and q are the magnitudes of the Jacobi momenta, l , s , j and t are the orbital angular momentum, spin, total angular momentum and isospin of the 2N subsystem. Additionally, the angular momentum of nucleon 1 is coupled with its spin $\frac{1}{2}$ to the total angular momentum I . Finally, the subsystem total angular momentum j is coupled with I to give the total 3N angular momentum J with the projection M . Similar coupling in the isospin space leads to the total 3N isospin T with the projection M_T . In principle there are infinitely many sets of discrete quantum numbers $\alpha \equiv \{l, s, j, t, \lambda, J, M, T, M_T\}$. In practice, for a given 3N system (for example two neutrons and one proton) a finite set of α is obtained by assuming that $0 \leq j \leq j_{max}$ and $\frac{1}{2} \leq J \leq J_{max}$, where typically $j_{max} = 3$ or 4 and $J_{max} = \frac{15}{2}$. Since we want to represent fully antisymmetric 3N states, from the very beginning we consider only the cases, where

$$(-1)^{l+s+t} = -1, \quad (7.8)$$

which guarantees antisymmetrization of the (2, 3) subsystem.

We consider in this thesis only electron and photon scattering on ${}^3\text{He}$ and ${}^3\text{H}$. This means that the current operator will be applied to the 3N bound state, that is $|\Psi_i\rangle \equiv |\Psi_{bs}\rangle$. For elastic electron scattering also the final state is bound and

$$N_{ELAS}^\mu = \left\langle \Psi_{bs} m'_{bs} \left| J^\mu(\vec{Q}) \right| \Psi_{bs} m_{bs} \right\rangle, \quad (7.9)$$

where m_{bs} (m'_{bs}) is the bound state spin projection in the initial (final) state, respectively. (As in the 2N case the quantization axis is chosen to be parallel to \vec{Q} .) The 3N bound state is the solution of the Schrödinger equation

$$H |\Psi_{bs} m_b\rangle \equiv (H_0 + V) |\Psi_{bs} m_{bs}\rangle = E_{bs} |\Psi_{bs} m_{bs}\rangle, \quad (7.10)$$

where E_{bs} is the ${}^3\text{He}$ (or ${}^3\text{H}$) binding energy, H_0 is the non-relativistic 3N internal kinetic energy, expressed in terms of the Jacobi momenta as

$$H_0 = \frac{\hat{p}^2}{M_n} + \frac{3}{4} \frac{\hat{q}^2}{M_n}. \quad (7.11)$$

and V is the 3N potential energy,

$$V = V_{12} + V_{23} + V_{31} + V_{123}, \quad (7.12)$$

consisting of the pairwise interactions, V_{ij} , and the so-called 3N force, V_{123} .

For inelastic processes two types of 3N scattering states appear. In the first case two nucleons bound in the deuteron emerge with the accompanying third nucleon and the asymptotic motion of this unbound nucleon is described by the Jacobi momentum \vec{q}_0 . It can be formally written as

$$|\Psi_{Nd} m_d m_N\rangle^{(-)} = \lim_{\epsilon \rightarrow 0^+} \frac{-i\epsilon}{E_{Nd} - i\epsilon - H} |\Phi_d m_d \vec{q}_0 m_N\rangle_a, \quad (7.13)$$

where $|\Phi_d\rangle \equiv |\Phi m_d \vec{q}_0 m_N\rangle_a$ is the antisymmetrized product state containing the deuteron state with the spin projection m_d and the plane wave state describing the free relative motion (with momentum \vec{q}_0) of the third nucleon with the spin projection m_N .

In the second case (which requires a slightly higher 3N internal energy) we have three free nucleons in the final state and their asymptotic relative motions are represented by two Jacobi momenta \vec{p} and \vec{q} . In this case we write

$$|\Psi_{Npn} m_1 m_2 m_3\rangle^{(-)} = \lim_{\epsilon \rightarrow 0^+} \frac{-i\epsilon}{E_{Npn} - i\epsilon - H} |\vec{p} \vec{q} m_1 m_2 m_3\rangle_a, \quad (7.14)$$

where $|\Phi_0\rangle \equiv |\vec{p} \vec{q} m_1 m_2 m_3\rangle_a$ is the antisymmetrized product state describing the free motion of three nucleons with the spin projections: m_1 , m_2 and m_3 .

In practice, in order to obtain the 3N bound state, the Schrödinger Equation 7.10 is rewritten in the form of the Faddeev equation [138, 139]

$$|\psi_1\rangle = G_0 T P |\psi_1\rangle + (1 + G_0 T) G_0 V_{123}^{(1)} (1 + P) |\psi_1\rangle, \quad (7.15)$$

where $V_{123}^{(1)}$ is that part of the 3N force which is symmetrical under the exchange of nucleons 2 and 3. The complete 3N force is a sum

$$V_{123} = V_{123}^{(1)} + V_{123}^{(2)} + V_{123}^{(3)}. \quad (7.16)$$

Further, $|\psi_1\rangle$ denotes the corresponding Faddeev component, T is the 2N t-operator, G_0 is the free 3N propagator and P is the permutation operator $P = P_{12}P_{23} + P_{13}P_{23}$. The full 3N bound state is obtained as

$$|\Psi_{bs}\rangle = (1 + P) |\psi_1\rangle. \quad (7.17)$$

In order to calculate the crucial matrix elements N^μ given in 7.1, it is not necessary to solve the corresponding Faddeev equations directly for the 3N scattering states [54]. It is better to obtain, an auxiliary state $|U\rangle$, which obeys the Faddeev-type equation

$$\begin{aligned} |U\rangle &= \left(TG_0 + \frac{1}{2} (1 + P) V_{123}^{(1)} G_0 (1 + TG_0) \right) (1 + P) J^\mu(\vec{Q}) |\Psi_{bs}\rangle \\ &\quad + \left(TG_0 P + \frac{1}{2} (1 + P) V_{123}^{(1)} G_0 (1 + TG_0) P \right) |U\rangle, \end{aligned} \quad (7.18)$$

and construct the nuclear matrix elements as

$$N_{Nd}^\mu = \langle \Phi_d | (1 + P) J^\mu(\vec{Q}) | \Psi_{bs} \rangle + \langle \Phi_d | P | U \rangle \quad (7.19)$$

and

$$\begin{aligned} N_{Npn}^\mu = & \langle \Phi_0 | (1 + P) J^\mu(\vec{Q}) | \Psi_{bs} \rangle + \langle \Phi_0 | TG_0(1 + P) J^\mu(\vec{Q}) | \Psi_{bs} \rangle \\ & + \langle \Phi_0 | P | U \rangle + \langle \Phi_0 | TG_0 P | U \rangle. \end{aligned} \quad (7.20)$$

As mentioned already in the introduction, within the framework of ChEFT not only the 2N forces and 2N currents but also many-nucleon forces are consistently derived. In particular, the 3N force appears only at N2LO of the chiral expansion and thus (at the present stage of our formalizm) should not be introduced. This leads to simpler versions of Equations (7.18) and (7.20), which read correspondingly

$$|U\rangle = TG_0(1 + P) J^\mu(\vec{Q}) | \Psi_{bs} \rangle + TG_0 P | U \rangle, \quad (7.21)$$

$$N_{Npn}^\mu = \langle \Phi_0 | (1 + P) J^\mu(\vec{Q}) | \Psi_{bs} \rangle + \langle \Phi_0 | (1 + P) | U \rangle. \quad (7.22)$$

The equation for N_{Nd}^μ remains unaltered.

In the following we introduce matrix elements of the single-nucleon current acting now in the 3N space. We follow again the steps made for the 2N system. Since the internal 3N states are already totally antisymmetric, it is sufficient to include the contribution from one of the nucleons, here nucleon 1. The expression analogous to Equation (3.16) reads

$$\langle \Psi_f \vec{P}_f | J_1^\mu(0) + J_2^\mu + J_3^\mu(0) | \Psi_i \vec{P}_i \rangle = 3 \langle \Psi_f \vec{P}_f | J_1^\mu(0) | \Psi_i \vec{P}_i \rangle. \quad (7.23)$$

Also now, for the 3N case, we can separate the dependence on the internal momenta from the total 3N momentum and obtain

$$\langle \vec{p}_1 \vec{p}_2 \vec{p}_3 | \Psi \vec{P} \rangle = \langle \vec{p} \vec{q} | \Psi \rangle \delta(\vec{p}_1 + \vec{p}_2 + \vec{p}_3 - \vec{P}), \quad (7.24)$$

where \vec{p} and \vec{q} are defined in Equations (7.2) and (7.3). It is then straightforward to derive expressions which replace Equations (3.18)–(3.20) obtained for the 2N system

$$\begin{aligned} & \langle \Psi_f \vec{P}_f | J_1^0(0) + J_2^0(0) + J_3^0(0) | \Psi_i \vec{P}_i \rangle = \\ & 3 \int d\vec{q} \langle \Psi_f | \vec{q} \rangle (G_E^p \Pi^p + G_E^n \Pi^n) \left\langle \vec{q} - \frac{2}{3} \vec{Q} \middle| \Psi_i \right\rangle, \end{aligned} \quad (7.25)$$

$$\begin{aligned} & \langle \Psi_f \vec{P}_f | \vec{J}_1^{conv}(0) + \vec{J}_2^{conv}(0) + \vec{J}_3^{conv}(0) | \Psi_i \vec{P}_i \rangle = \\ & 3 \int d\vec{q} \langle \Psi_f | \vec{q} \rangle (G_E^p \Pi^p + G_E^n \Pi^n) \left(\frac{\vec{q}}{M_n} \right) \left\langle \vec{q} - \frac{2}{3} \vec{Q} \middle| \Psi_i \right\rangle \\ & + 3 \left(\frac{\vec{P}_i - \frac{1}{2} \vec{P}_f}{2M_n} \right) \int d\vec{q} \langle \Psi_f | \vec{q} \rangle (G_E^p \Pi^p + G_E^n \Pi^n) \left\langle \vec{q} - \frac{2}{3} \vec{Q} \middle| \Psi_i \right\rangle, \end{aligned} \quad (7.26)$$

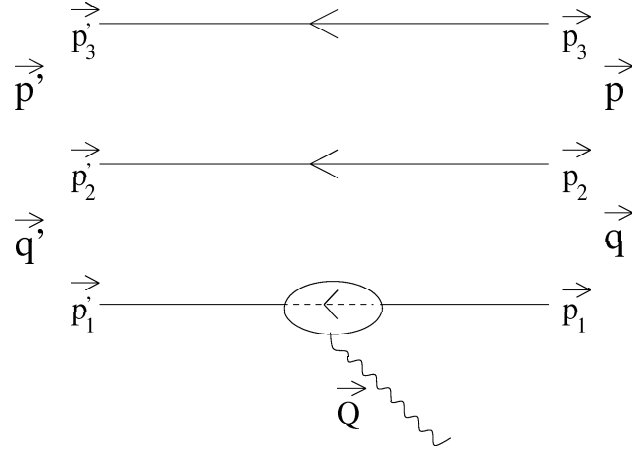


Figure 7.1: General single current diagram for $J_1^\mu(x = 0)$ at the 3N system.

$$\langle \Psi_f \vec{P}_f | \vec{J}_1^{spin}(0) + \vec{J}_2^{spin}(0) + \vec{J}_3^{spin}(0) | \Psi_i \vec{P}_i \rangle = \\ 3 \int d\vec{q} \langle \Psi_f | \vec{q} \rangle (G_M^p \Pi^p + G_M^n \Pi^n) \left(\frac{i\vec{\sigma}_2 \times \vec{Q}}{2M_n} \right) \left\langle \vec{q} - \frac{2}{3}\vec{Q} \middle| \Psi_i \right\rangle, \quad (7.27)$$

The second term in Equation (7.26) can be dropped if $\vec{Q} \parallel \hat{z}$ and we are interested in the spherical components $+1$ and -1 . Note, however, that now the isospin projection operators Π^p and Π^n act in the space of nucleon 1.

In the partial wave representation the 3N bound state is written as

$$|\Psi_{bs} m_{bs} m_T \rangle = \sum_{\alpha_{bs}} \int_0^\infty dp p^2 \int_0^\infty dq q^2 |pq\alpha_{bs}\rangle \langle pq\alpha_{bs}| \Psi_{bs} m_{bs} m_T \rangle \\ \equiv \sum_{\alpha_{bs}} \int_0^\infty dp p^2 \int_0^\infty dq q^2 \Psi(p, q, \alpha_{bs}) |pq\alpha_{bs}\rangle, \quad (7.28)$$

where the set α_{bs} is prepared for $J = \frac{1}{2}$, $T = \frac{1}{2}$ and positive parity $(-1)^{l+\lambda} = 1$. The isospin projection is used to distinguish between ${}^3\text{He}$ ($m_T = \frac{1}{2}$) and ${}^3\text{H}$ ($m_T = -\frac{1}{2}$).

Finally, combining Equations (7.25)–(7.27) with Equation (7.28) we obtain

$$\begin{aligned} \left\langle pq\alpha \left| J^0(\vec{Q}) \right| \Psi_{bs} m_{bs} m_T \right\rangle &= 3 \sum_{\alpha_{bs}} \delta_{l,l_{bs}} \delta_{s,s_{bs}} \delta_{j,j_{bs}} \delta_{t,t_{bs}} I(t, T, m_T) \\ &\quad \sum_{\mu} c \left(j_{bs}, I_{bs}, \frac{1}{2}; \mu, m_{bs} - \mu, m_{bs} \right) c(j, I, J; \mu, m - \mu, m) \\ &\quad \sum_{\nu_{bs}} c \left(\lambda_{bs}, \frac{1}{2}, I_{bs}; \nu_{bs}, m_{bs} - \mu - \nu_{bs}, m_{bs} - \mu \right) \\ &\quad \sum_{\nu} c \left(\lambda, \frac{1}{2}, I; \nu, m - \mu - \nu, m - \mu \right) \delta_{m-\nu, m_{bs}-\nu_{bs}} \\ &\quad \int d\hat{q} Y_{\lambda\nu}^*(\hat{q}) Y_{\lambda_{bs}\nu_{bs}} \left(\widehat{\vec{q} - \frac{2}{3}\vec{Q}} \right) \Psi \left(p, \left| \vec{q} - \frac{2}{3}\vec{Q} \right|, \alpha_{bs} \right), \end{aligned} \quad (7.29)$$

where the integration in (7.29) is carried over all directions of \vec{q} . The isospin factor $I(t, T, m_T)$ arising from the isospin matrix element

$$\left\langle \left(t \frac{1}{2} \right) T m_T \left| G_E^p \frac{1}{2} (1 + \hat{\tau}_z(1)) + G_E^n \frac{1}{2} (1 - \hat{\tau}_z(1)) \right| \left(t_{bs} \frac{1}{2} \right) \frac{1}{2} m_T \right\rangle \quad (7.30)$$

is given as

$$\begin{aligned} I(t, T, m_T) &= \delta_{t,t_{bs}} \left[(G_E^p + G_E^n) \frac{1}{2} \delta_{T,\frac{1}{2}} \right. \\ &\quad \left. - (G_E^p - G_E^n) \sqrt{3} c \left(1, \frac{1}{2}, T; 0, m_T, m_T \right) (-1)^t \left\{ \begin{array}{ccc} t & \frac{1}{2} & \frac{1}{2} \\ 1 & T & \frac{1}{2} \end{array} \right\} \right]. \end{aligned} \quad (7.31)$$

For the spherical component $\tau = \pm 1$ of the convection current we get

$$\begin{aligned} \left\langle pq\alpha \left| J_{\tau}^{conv}(\vec{Q}) \right| \Psi_{bs} m_{bs} m_T \right\rangle &= 3 \sum_{\alpha_{bs}} \delta_{l,l_{bs}} \delta_{s,s_{bs}} \delta_{j,j_{bs}} \delta_{t,t_{bs}} I(t, T, m_T) \\ &\quad \sum_{\mu} c \left(j_{bs}, I_{bs}, \frac{1}{2}; \mu, m_{bs} - \mu, m_{bs} \right) c(j, I, J; \mu, m - \mu, m) \\ &\quad \sum_{\nu_{bs}} c \left(\lambda_{bs}, \frac{1}{2}, I_{bs}; \nu_{bs}, m_{bs} - \mu - \nu_{bs}, m_{bs} - \mu \right) \\ &\quad \sum_{\nu} c \left(\lambda, \frac{1}{2}, I; \nu, m - \mu - \nu, m - \mu \right) \delta_{m-\nu, m_{bs}-\nu_{bs}} \\ &\quad \int d\hat{q} Y_{\lambda\nu}^*(\hat{q}) Y_{\lambda_{bs}\nu_{bs}} \left(\widehat{\vec{q} - \frac{2}{3}\vec{Q}} \right) \Psi \left(p, \left| \vec{q} - \frac{2}{3}\vec{Q} \right|, \alpha_{bs} \right) \frac{q_{\tau}}{M_n} \\ &\quad + \frac{(\vec{P}_i - \frac{1}{3}\vec{P}_f)_{\tau}}{2M_n} \left\langle pq\alpha \left| J^0(\vec{Q}) \right| \Psi_{bs} m_{bs} m_T \right\rangle. \end{aligned} \quad (7.32)$$

Finally, for the spin current matrix elements we get

$$\begin{aligned}
\left\langle pq\alpha \left| J_\tau^{spin}(\vec{Q}) \right| \Psi_{bs} m_{bs} m_T \right\rangle &= \sqrt{2} \sum_{\epsilon} c(1, 1, 1; \epsilon, \tau - \epsilon, \tau) \frac{1}{2M_n} \\
&\quad 3 \sum_{\alpha_{ps}} \delta_{l, l_{bs}} \delta_{s, s_{bs}} \delta_{j, j_{bs}} \delta_{t, t_{bs}} \tilde{I}(t, T, m_T) \\
&\quad \sum_{\mu} c \left(j_{bs}, I_{bs}, \frac{1}{2}; \mu, m_{bs} - \mu, m_{bs} \right) c(j, I, J; \mu, m - \mu, m) \\
&\quad \sum_{\nu_{bs}} c \left(\lambda_{bs}, \frac{1}{2}, I_{bs}; \nu_{bs}, m_{bs} - \mu - \nu_{bs}, m_{bs} - \mu \right) \\
&\quad \sum_{\nu} c \left(\lambda, \frac{1}{2}, I; \nu, m - \mu - \nu, m - \mu \right) \left\langle \frac{1}{2}m - \mu - \nu \left| \sigma_{\epsilon} \left| \frac{1}{2}m_{bs} - \mu - \nu_{bs} \right. \right. \right\rangle \\
&\quad \int d\hat{q} Y_{\lambda \nu}^*(\hat{q}) Y_{\lambda_{bs} \nu_{bs}} \left(\widehat{\vec{q} - \frac{2}{3}\vec{Q}} \right) \Psi \left(p, \left| \vec{q} - \frac{2}{3}\vec{Q} \right|, \alpha_{bs} \right), \quad (7.33)
\end{aligned}$$

where in $\tilde{I}(t, T, m_T)$ G_E are replaced with G_M and the matrix element

$$\left\langle \frac{1}{2}m - \mu - \nu \left| \sigma_{\epsilon} \left| \frac{1}{2}m_{bs} - \mu - \nu_{bs} \right. \right. \right\rangle \quad (7.34)$$

is evaluated as

$$-\sqrt{3} c \left(1, \frac{1}{2}, \frac{1}{2}; \epsilon, m_{bs} - \mu - \nu_{bs}, m - \mu - \nu \right). \quad (7.35)$$

Let us now turn to the partial wave representation of the 2N current operator. There are three pairs in the 3N system but it is sufficient to include a contribution just from one pair, for example pair (2, 3), because the 3N states are fully antisymmetric:

$$\langle \Psi_f \vec{P}_f | J^\mu(2, 3) + J^\mu(3, 1) + J^\mu(1, 2) | \Psi_i \vec{P}_i \rangle = 3 \langle \Psi_f \vec{P}_f | J^\mu(2, 3) | \Psi_i \vec{P}_i \rangle. \quad (7.36)$$

In the 3N space spanned by the Jacobi momenta \vec{p} and \vec{q} the 2N current related to particles 2 and 3 has the form

$$\langle \vec{p}' \vec{q}'' | J(2, 3) | \vec{p} \vec{q} \rangle = \delta \left(\vec{q}' - \vec{q} - \frac{1}{3}\vec{Q} \right) J(\vec{q}_2, \vec{q}_3), \quad (7.37)$$

where

$$\begin{aligned}
\vec{q}_2 &\equiv \vec{p}'_2 - \vec{p}_2 = \frac{1}{2}\vec{Q} + \vec{p}' - \vec{p}, \\
\vec{q}_3 &\equiv \vec{p}'_3 - \vec{p}_3 = \frac{1}{2}\vec{Q} - \vec{p}' + \vec{p},
\end{aligned} \quad (7.38)$$

are the momentum transfers to nucleons 2 and 3. The structure given in Equation (7.37)

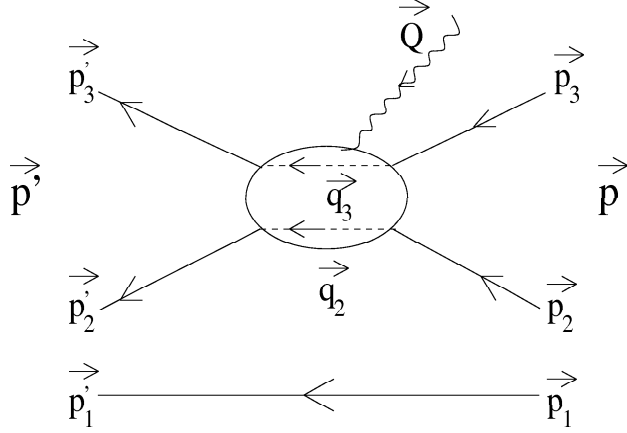


Figure 7.2: General MEC diagram for the 3N system.

shows that the \vec{p} and \vec{q} dependence is separated, what simplifies the partial wave decomposition. We now split the basis states as

$$|pq\alpha\rangle = \left|pq(ls)j\left(\lambda\frac{1}{2}\right)I(jI)Jm\right\rangle \left|\left(t\frac{1}{2}\right)Tm_T\right\rangle \equiv |pq\alpha_J\rangle |\alpha_T\rangle, \quad (7.39)$$

and introduce

$$\mathcal{Y}_{j\mu}(\hat{p}) \equiv \sum_{\mu'} c(lsj; \mu - \mu', \mu', \mu) Y_{l,\mu-\mu'}(\hat{p}) |s\mu'\rangle, \quad (7.40)$$

and

$$\mathcal{Y}_{\lambda\nu}(\hat{q}) \equiv \sum_{\nu'} c\left(\lambda\frac{1}{2}I; \nu - \nu', \nu', \nu\right) Y_{\lambda,\nu-\nu'}(\hat{q}) \left|\frac{1}{2}\nu'\right\rangle. \quad (7.41)$$

Then

$$\begin{aligned}
 & \langle p'q'\alpha' | J(2,3) | pq\alpha \rangle \\
 &= \int d\vec{p}'_1 \int d\vec{q}'_1 \int d\vec{p}_1 \int d\vec{q}_1 \langle p'q'\alpha | \vec{p}'_1 \vec{q}'_1 \rangle \langle \vec{p}'_1 \vec{q}'_1 | j(2,3) | \vec{p}_1 \vec{q}_1 \rangle \langle \vec{p}_1 \vec{q}_1 | pq\alpha \rangle \\
 &= \int d\vec{p}'_1 \int d\vec{q}'_1 \int d\vec{p}_1 \int d\vec{q}_1 \sum_{\mu'\mu} c(j'I'J'; \mu', M' - \mu', M') c(jIJ; \mu, M - \mu, M) \\
 &\quad \times \mathcal{Y}_{j'\mu'}^*(\hat{p}'_1) \frac{\delta(p'_1 - p')}{p'^2_1} \mathcal{Y}_{I',M'-\mu'}^*(\hat{q}'_1) \frac{\delta(q'_1 - q')}{q'^2_1} \delta(\vec{q}_1 - \vec{q}'_1 - \frac{1}{3}\vec{Q}) \\
 &\quad \times J\left(\frac{1}{2}\vec{Q} + \vec{p}'_1 - \vec{p}_1, \frac{1}{2}\vec{Q} - \vec{p}'_1 + \vec{p}_1; 2, 3\right) \\
 &\quad \times I_1\left(q', q, Q; \left(\lambda'\frac{1}{2}\right) I'M' - \mu', \left(\lambda\frac{1}{2}\right) IM - \mu\right) \\
 &\quad \times \mathcal{Y}_{j\mu}(\hat{p}_1) \mathcal{Y}_{I,M-\mu}(\hat{q}_1) \frac{\delta(p_1 - p)}{p^2_1} \frac{\delta(q_1 - q)}{q^2_1} \langle \alpha_{T'} | T_\beta | \alpha_T \rangle, \quad (7.42)
 \end{aligned}$$

where the isospin dependence is separated into the matrix element

$$\langle \alpha_{T'} | T_\beta | \alpha_T \rangle \quad (7.43)$$

and we assume that T_β is one of the five operators defined in Equation (3.32). This leads immediately to

$$\begin{aligned} & \langle p' q' \alpha' | J(2, 3) | pq\alpha \rangle \\ &= \sum_{\mu' \mu} c(j' I' J'; \mu', M' - \mu', M') c(j I J; \mu, M - \mu, M) \\ & \quad \times I_{23}(p', p, Q; (l' s') j' \mu', (ls) j \mu) \\ & I_1 \left(q', q, Q; \left(\lambda' \frac{1}{2} \right) I' M' - \mu', \left(\lambda \frac{1}{2} \right) IM - \mu \right) \langle \alpha_{T'} | T_\beta | \alpha_T \rangle \end{aligned} \quad (7.44)$$

with

$$\begin{aligned} & I_{23}(p', p, Q; (l' s') j' \mu', (ls) j \mu,) \\ &= \int d\hat{p}' \int d\hat{p} \mathcal{Y}_{j' \mu'}^*(\hat{p}') J \left(\frac{1}{2} \vec{Q} + \vec{p}' - \vec{p}, \frac{1}{2} \vec{Q} - \vec{p}' + \vec{p} \right) \mathcal{Y}_{j \mu}(\hat{p}), \end{aligned} \quad (7.45)$$

and

$$\begin{aligned} & I_1 \left(q', q, Q; \left(\lambda' \frac{1}{2} \right) I' M' - \mu', \left(\lambda \frac{1}{2} \right) IM - \mu \right) \\ &= \int d\hat{q}' \mathcal{Y}_{I', M' - \mu'}^*(\hat{q}') \frac{\delta(q - |\vec{q}' + \frac{1}{3} \vec{Q}|)}{q^2} \mathcal{Y}_{I, M - \mu}(\vec{q}' + \widehat{\frac{1}{3} \vec{Q}}). \end{aligned} \quad (7.46)$$

In the last step we prepare an important building block $\langle pq\alpha | J(2, 3) | \Psi \rangle$. We obtain

$$\begin{aligned} \langle p' q' \alpha' | J(2, 3) | \Psi \rangle &= \sum_{\alpha} \int p^2 dp q^2 dq \langle p' q' \alpha' | J(2, 3) | pq\alpha \rangle \langle pq\alpha | \Psi \rangle \\ &= \sum_{\alpha} \int p^2 dp \sum_{\mu \mu'} c(j' I' J'; \mu', M' - \mu', M') c(j I J; \mu, M - \mu, M) \\ & \quad \times I_{23}(p', p, Q; (l' s') j' \mu', (ls) j \mu) \\ & \quad \times \tilde{I}_1 \left(p, q', Q; \left(\lambda' \frac{1}{2} \right) I' M' - \mu', \left(\lambda \frac{1}{2} \right) IM - \mu \right), \end{aligned} \quad (7.47)$$

with

$$\begin{aligned} & \tilde{I}_1 \left(p, q', Q; \left(\lambda' \frac{1}{2} \right) I' M' - \mu', \left(\lambda \frac{1}{2} \right) IM - \mu \right) = \\ & \int d\hat{q}' \mathcal{Y}_{I', M' - \mu'}^*(\hat{q}') \left\langle p, \left| \vec{q}' + \frac{1}{3} \vec{Q} \right|, \alpha \middle| \Psi \right\rangle \mathcal{Y}_{I, M - \mu}(\vec{q}' + \widehat{\frac{1}{3} \vec{Q}}). \end{aligned} \quad (7.48)$$

The angular integration in \tilde{I}_1 can be easily performed and in the I_{23} we recognize the same type of a matrix element we dealt with in the 2N space. Now, however, the isospin part is extracted from I_{23} . This is because in the 3N system we have much more cases than in the processes on the deuteron which has the total isospin zero and only two

states. This separation allows us, for example, to calculate I_{23} once and use it both for the reaction on ${}^3\text{He}$ and ${}^3\text{H}$. It is still important, however, to use the properties of the matrix elements (7.43) in order to reduce the number of necessary four fold integrals in I_{23} , even if the isospin dependence is now treated separately.

For the sake of completeness, we give the matrix elements of the five isospin operators in the 3N isospin space. As already mentioned, we assume that the operators act on the 3N bound state (${}^3\text{H}$ or ${}^3\text{He}$), which has the total isospin $T = \frac{1}{2}$. It is then straightforward to obtain

$$\begin{aligned} & \left\langle \left(t' \frac{1}{2} \right) T' m_{T'} \middle| T_1 \middle| \left(t \frac{1}{2} \right) \frac{1}{2} m_T \right\rangle \\ & \equiv \left\langle \left(t' \frac{1}{2} \right) T' m_{T'} \middle| (\vec{\tau}(2) + \vec{\tau}(3))_3 \middle| \left(t \frac{1}{2} \right) \frac{1}{2} m_T \right\rangle = c \left(1, \frac{1}{2}, T'; 0, m_T, m_{T'} \right) \\ & \quad \sqrt{12} \sqrt{(2t'+1)(2t+1)} \left\{ \begin{array}{ccc} 1 & t & t' \\ \frac{1}{2} & T' & \frac{1}{2} \end{array} \right\} \left\{ \begin{array}{ccc} 1 & \frac{1}{2} & \frac{1}{2} \\ \frac{1}{2} & t' & t \end{array} \right\} \\ & \quad (-1)^{t+t'+\frac{1}{2}+T'} \left(1 + (-1)^{t+t'} \right), \quad (7.49) \end{aligned}$$

$$\begin{aligned} & \left\langle \left(t' \frac{1}{2} \right) T' m_{T'} \middle| T_2 \middle| \left(t \frac{1}{2} \right) \frac{1}{2} m_T \right\rangle \\ & \equiv \left\langle \left(t' \frac{1}{2} \right) T' m_{T'} \middle| (\vec{\tau}(2) - \vec{\tau}(3))_3 \middle| \left(t \frac{1}{2} \right) \frac{1}{2} m_T \right\rangle = c \left(1, \frac{1}{2}, T'; 0, m_T, m_{T'} \right) \\ & \quad \sqrt{12} \sqrt{(2t'+1)(2t+1)} \left\{ \begin{array}{ccc} 1 & t & t' \\ \frac{1}{2} & T' & \frac{1}{2} \end{array} \right\} \left\{ \begin{array}{ccc} 1 & \frac{1}{2} & \frac{1}{2} \\ \frac{1}{2} & t' & t \end{array} \right\} \\ & \quad (-1)^{t+t'+\frac{1}{2}+T'} \left(1 - (-1)^{t+t'} \right), \quad (7.50) \end{aligned}$$

$$\begin{aligned} & \left\langle \left(t' \frac{1}{2} \right) T' m_{T'} \middle| iT_3 \middle| \left(t \frac{1}{2} \right) \frac{1}{2} m_T \right\rangle \\ & \equiv \left\langle \left(t' \frac{1}{2} \right) T' m_{T'} \middle| i(\vec{\tau}(2) \times \vec{\tau}(3))_3 \middle| \left(t \frac{1}{2} \right) \frac{1}{2} m_T \right\rangle = \left(1, \frac{1}{2}, T'; 0, m_T, m_{T'} \right) \\ & \quad 12\sqrt{3} \sqrt{(2t'+1)(2t+1)} \left\{ \begin{array}{ccc} 1 & t & t' \\ \frac{1}{2} & T' & \frac{1}{2} \end{array} \right\} \left\{ \begin{array}{ccc} 1 & 1 & 1 \\ \frac{1}{2} & \frac{1}{2} & t \\ \frac{1}{2} & \frac{1}{2} & t' \end{array} \right\} (-1)^{1+t+\frac{1}{2}+T'}, \quad (7.51) \end{aligned}$$

$$\begin{aligned} & \left\langle \left(t' \frac{1}{2} \right) T' m_{T'} \middle| T_4 \middle| \left(t \frac{1}{2} \right) \frac{1}{2} m_T \right\rangle \\ & \equiv \left\langle \left(t' \frac{1}{2} \right) T' m_{T'} \middle| \vec{\tau}(2) \cdot \vec{\tau}(3) \middle| \left(t \frac{1}{2} \right) \frac{1}{2} m_T \right\rangle = \delta_{m_{T'}, m_T} \delta_{T', \frac{1}{2}} (\delta_{t', 1} \delta_{t, 1} - 3\delta_{t', 0} \delta_{t, 0}), \\ & \quad (7.52) \end{aligned}$$

$$\begin{aligned} & \left\langle \left(t' \frac{1}{2} \right) T' m_{T'} \middle| T_5 \middle| \left(t \frac{1}{2} \right) \frac{1}{2} m_T \right\rangle \\ & \equiv \left\langle \left(t' \frac{1}{2} \right) T' m_{T'} \middle| 1 \middle| \left(t \frac{1}{2} \right) \frac{1}{2} m_T \right\rangle = \delta_{m_{T'}, m_T} \delta_{T', \frac{1}{2}} \delta_{t', t}, \end{aligned} \quad (7.53)$$

Chapter 8

Electron scattering of ^3He

In Chapter 7 we gave formulas for the nuclear matrix elements N^μ in the case of electron scattering on ^3He . The step towards the rich set of observables based on one-photon-exchange is standard [80]. Here, in this thesis, we follow closely the formalism and use numerical experience of [54] and give only very brief information, necessary to understand presented results.

In our potential approach, we are restricted to such energies and momenta of the virtual photon that the three-nucleon c.m. energy in the final state is below the pion mass. We should also choose such electron parameters that a nonrelativistic approach to kinematics (consistent with the dynamics) is well justified. In our calculations we

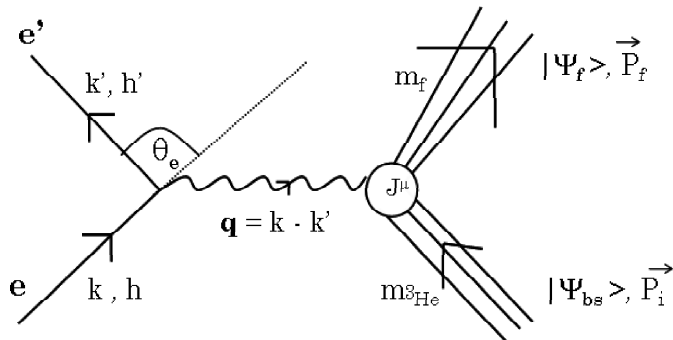


Figure 8.1: General diagram for electron scattering on ^3He . The final state $|\Psi_f\rangle$ can be again $|\Psi_{bs}\rangle$ (elastic scattering), $|\Psi_{pd}\rangle^{(-)}$ (two-body break-up of ^3He) or $|\Psi_{ppn}\rangle^{(-)}$ (three-body break-up of ^3He). Electron scattering on ^3H can be treated accordingly.

neglect the Coulomb force between two-protons in three-nucleon scattering states. The three nucleon matrix elements N^μ are obtained using partial wave decomposition, with the total angular momentum of the three-nucleon system $J \leq \frac{15}{2}$ and including all partial waves with the total angular momentum in the two-body subsystem $j \leq 3$.

8.1 Elastic electron scattering

The differential cross section for unpolarized electron scattering on an unpolarized ^3He target in the laboratory system is usually written in terms of the charge and magnetic form factors [140]

$$\frac{d\sigma}{d\Omega_e} = \sigma_{Mott} \frac{Z^2}{1 + \frac{e}{M_{^3\text{He}}}(1 - \cos \theta_e)} \left[F_C^2 \right. \\ \left. - \frac{\mathbf{q}^2}{4M_{^3\text{He}}^2} F_M^2 (1 + \kappa)^2 \left(1 + 2 \left(1 - \frac{\mathbf{q}^2}{4M_{^3\text{He}}^2} \right) \tan^2 \frac{\theta_e}{2} \right) \right] \frac{1}{1 - \frac{\mathbf{q}^2}{4M_{^3\text{He}}^2}}, \quad (8.1)$$

where Z is the number of protons in the initial target. The form factors are normalized as

$$F_C(\mathbf{q}^2 = 0) = 1 \quad (8.2)$$

$$F_M(\mathbf{q}^2 = 0) = 1, \quad (8.3)$$

such that $(1 + \kappa)$ is the magnetic moment of ^3He in nuclear magnetons $\left(\frac{e}{2M_N}\right)$ [141]. It is known that polarizing the initial electron or initial ^3He does not lead to new independent information [80].

We show individual contributions from isospin operator structures T_1, T_2, T_3 to elastic form factors F_M and F_C . Results are presented in Tables 8.1 and 8.2, where we assume that $T_i \equiv T_i O_j + T_i O_j^S$. As we can find in Table 8.1, for lower values of Q ,

Table 8.1: Individual contributions of the isospin operator structures to the elastic form factors at $Q = 50\text{MeV}$.

Isospin operator structure	$ F_M $	$ F_C $
Single nucleon	0.849–0.870	0.9647–0.9671
Single nucleon + T_3	0.959–0.967	0.9647–0.9671
Single nucleon + $T_3 + T_2$	0.985–1.075	0.9647–0.9671
Single nucleon + $T_3 + T_2 + T_1$	0.985–1.078	0.9600–0.9634

the dominant contributions to F_C come from the structure operators with T_1 isospin operator. The dominant contributions to F_M arise from T_3 isospin operator and we notice some effects coming from T_2 . For higher values of Q , the behavior is similar (see Table 8.2) but the prediction bands are wider.

8.2 Electrodisintegration of ^3He

We use the standard expressions for the cross sections [80] which are analogous to the ones considered for electron-deuteron scattering. Also the definition of the reference

Table 8.2: Individual contributions of the isospin operator structures to the elastic form factors at $Q = 120\text{MeV}$.

Isospin operator structure	$ F_M $	$ F_C $
Single nucleon	0.706–0.735	0.8197–0.8304
Single nucleon + T_3	0.814–0.831	0.8197–0.8277
Single nucleon + $T_3 + T_2$	0.840–0.939	0.8197–0.8305
Single nucleon + $T_3 + T_2 + T_1$	0.840–0.941	0.8162–0.8245

frame is the same. In the case of two-body break-up of ${}^3\text{He}$ we have three particles in the final state. We start with the following formula:

$$d\sigma = \sigma_{\text{Mott}} \frac{1}{(E')^2} \delta^4(P_f - P_i - Q) d^3k' d^3p_p d^3p_d [v_L R_L + v_T R_T + v_{TT} R_{TT} + v_{TL} R_{TL} + h(v_{TL'} R_{TL'} + v_{T'} R_{T'})]. \quad (8.4)$$

Thus the fivefold differential cross section $d^5\sigma/(dE' d\Omega_e d\Omega_p)$ for the two-body break-up process reads

$$\begin{aligned} \frac{d^5\sigma}{dE' d\Omega_e d\Omega_p} = \\ \sigma_{\text{Mott}} [v_L R_L + v_T R_T + v_{TT} R_{TT} + v_{TL} R_{TL} \\ + h(v_{TL'} R_{TL'} + v_{T'} R_{T'})] \rho_f, \end{aligned} \quad (8.5)$$

where the nonrelativistic phase space factor ρ_f is given in terms of the final proton (\vec{p}_p) and deuteron (\vec{p}_d) laboratory momenta

$$\rho_f = \frac{M_N |\vec{p}_p|}{\left| 1 - \frac{M_N}{M_d} \frac{\vec{p}_p \cdot \vec{p}_d}{|\vec{p}_p|^2} \right|} \approx \frac{M_N |\vec{p}_p|}{\left| 1 - \frac{\vec{p}_p \cdot \vec{p}_d}{2|\vec{p}_p|^2} \right|} \quad (8.6)$$

The corresponding phase space factor for the deuteron detection can also be formulated starting from Equation (8.4).

Note that the matrix elements which appear in R_i in Equations (8.4) and (8.5) are calculated for a polarized initial ${}^3\text{He}$ state. If the final polarizations are not measured, we sum the response functions over the proton and deuteron spin magnetic quantum numbers. If the initial ${}^3\text{He}$ state is not polarized we average over its two spin projections.

In Figure 8.2 we defined our way of specifying the kinematics for exclusive two-body break-up of ${}^3\text{He}$. We restrict ourselves to the case where proton momentum lies in the plane given by vectors \vec{k} and \vec{k}' . Since we calculate kinematics nonrelativistically, we check in Figure 8.3 that this approximation is acceptable for the energy and momentum transfers we consider in this thesis.

Also for this reaction we can expect, for some (ω, Q) values, two solutions for the final proton momentum for given θ_p . These two solutions should be then taken into account in all observables, where the final proton is observed at the θ_p angle.

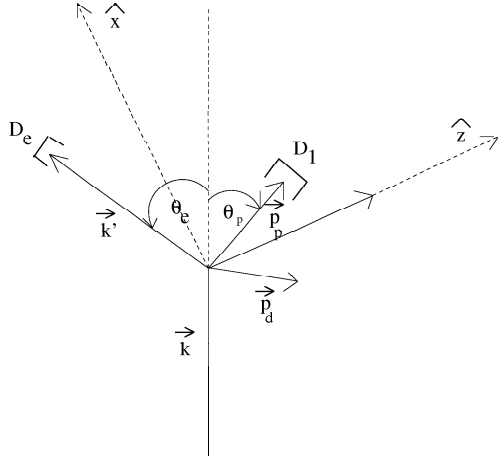


Figure 8.2: Definition of the θ_p angle used to label the exclusive two-body break-up cross section.

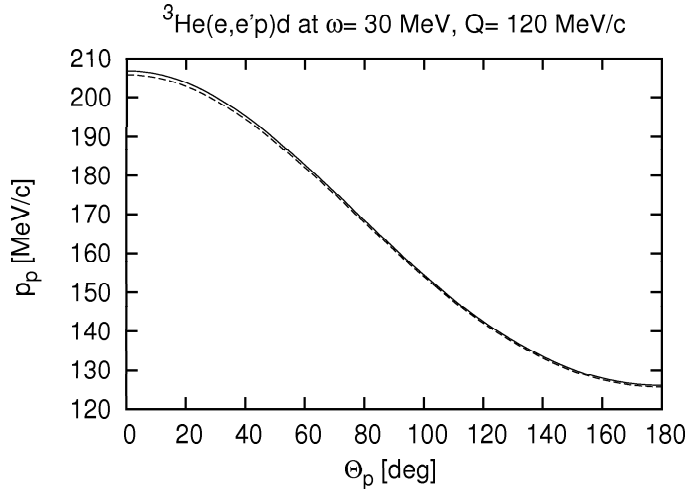


Figure 8.3: Final proton momentum calculated relativistically (solid line) and nonrelativistically (dashed line) for the fixed energy and momentum transfer.

In Figure 8.2 we show the exclusive cross section $d^5\sigma/(dE'd\Omega_e d\Omega_p)$ as a function of the chosen proton scattering angle θ_p defined in Figure 8.3. In the left panel the electron kinematics is: ($E=100$ MeV, $\theta_e=30^\circ$, $E'=80$ MeV), which gives $\omega=20$ MeV, $Q=50$ MeV/c. In the right panel we choose electron parameters ($E=100$ MeV, $\theta_e=88^\circ$, $E'=70$ MeV) which lead to slightly higher values of ω (30 MeV) and Q (120 MeV/c). In both cases we compare predictions based on the AV18 potential (and the corresponding current operator) to our chiral results obtained with the N2LO potentials. In the chiral case we have two groups of predictions. In the first group, in addition to the single nucleon current we included the leading OPE contributions. In the second case our calculations involve also the long-range TPE contributions. For the two electron kinematics we see very good agreement between the traditional approach and the chiral

predictions. For these relatively small momentum transfers the main contribution comes from the single nucleon current. For the smaller Q value TPE effects in the current operator are hardly visible. For the higher Q value we see some small effects for the angular region $100^\circ < \theta_p < 180^\circ$.

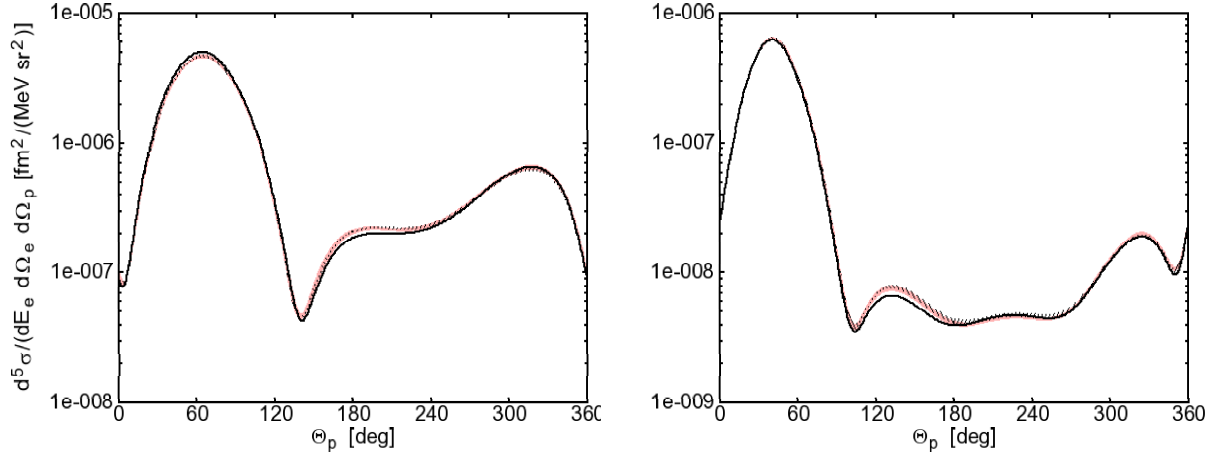


Figure 8.4: Exclusive differential cross section $d^5\sigma/(dE'd\Omega_e d\Omega_p)$ as a function of the proton scattering angle θ_p for two electron kinematical configurations (see text). The black line indicates the AV18 results. The dark band displays predictions with the single-nucleon and leading OPE contributions and the pink band shows the predictions with the additional long-range TPE contributions in the current operator.

Now, we turn to the electron induced three-body break-up reaction. There are clearly infinitely many kinematical configurations in this four-body reaction. Again, we can give only very few examples, in order to demonstrate that also this reaction can be studied within our framework.

First we consider the exclusive situation, where, as usually, the electron kinematics is fixed and, in addition, the directions of two outgoing protons are known (see Figure 8.5).

In the relativistic approach we get in the laboratory frame:

$$E + M_{^3\text{He}} = E' + E_1 + E_2 + E_3 \quad (8.7)$$

$$\vec{k} = \vec{k}' + \vec{p}_1 + \vec{p}_2 + \vec{p}_3 \quad (8.8)$$

where $E_i = \sqrt{M_N^2 + \vec{p}_i^2} \approx M_N + \frac{\vec{p}_i^2}{2M_N}$. Going to the nonrelativistic limit, we have:

$$\omega + M_{^3\text{He}} = 3M_N + \frac{\vec{p}_1^2}{2M_N} + \frac{\vec{p}_2^2}{2M_N} + \frac{\vec{p}_3^2}{2M_N} \quad (8.9)$$

$$\vec{Q} = \vec{p}_1 + \vec{p}_2 + \vec{p}_3 \quad (8.10)$$

$$(8.11)$$

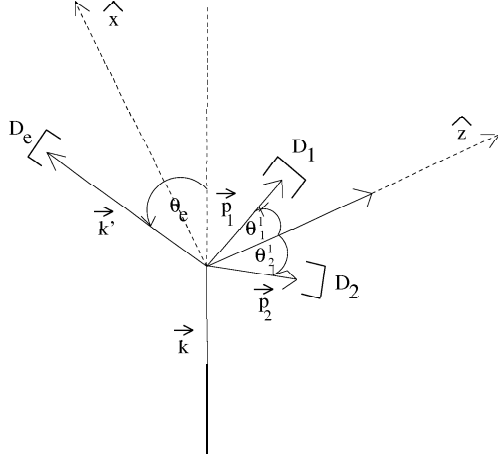


Figure 8.5: Exclusive kinematics for the three-body break-up of ^3He .

With these kinematical conditions in mind, we start from

$$d\sigma = \sigma_{\text{Mott}} \frac{1}{(E')^2} \delta^4(P_f - P_i - Q) d^3k' d^3p_1 d^3p_2 d^3p_3 [v_L R_L + v_T R_T + v_{TT} R_{TT} + v_{TL} R_{TL} + h(v_{TL'} R_{TL'} + v_{T'} R_{T'})] \quad (8.12)$$

and arrive at the eightfold differential cross section $d^8\sigma/(dE' d\Omega_e d\Omega_1 d\Omega_2 dE_1)$ for complete break-up

$$\frac{d^8\sigma}{dE' d\Omega_e d\Omega_1 d\Omega_2 dE_1} = \sigma_{\text{Mott}} [v_L R_L + v_T R_T + v_{TT} R_{TT} + v_{TL} R_{TL} + h(v_{TL'} R_{TL'} + v_{T'} R_{T'})] \rho_f^{3N}, \quad (8.13)$$

where the phase space factor ρ_f^{3N} given in terms of final nucleon laboratory momenta \vec{p}_i reads

$$\rho_f^{3N} = \frac{M_N p_1 p_2^2}{\left| \frac{p_2}{M_N} - \frac{\vec{p}_2 \cdot \vec{p}_3}{M_N p_2} \right|}. \quad (8.14)$$

Again the matrix elements in Equations (8.12) and (8.13) are calculated for a polarized initial ^3He state. If the initial target is unpolarized and no polarization is measured in the final state, the usual average and summations over the spin magnetic quantum numbers must be performed.

At some values of the momenta the denominator in (8.14) can vanish. In order to avoid this singularity, the breakup cross section is represented along the kinematically allowed locus in the $E_1 - E_2$ plane and parameterized by the arc-length S along that locus [102]. This leads to a modified phase space factor

$$\rho_f^{3NS} = \frac{M_N^2 |\vec{p}_1| |\vec{p}_2|}{\sqrt{\left(1 - \frac{\vec{p}_2 \cdot \vec{p}_3}{p_2^2}\right)^2 + \left(1 - \frac{\vec{p}_1 \cdot \vec{p}_3}{p_1^2}\right)^2}}, \quad (8.15)$$

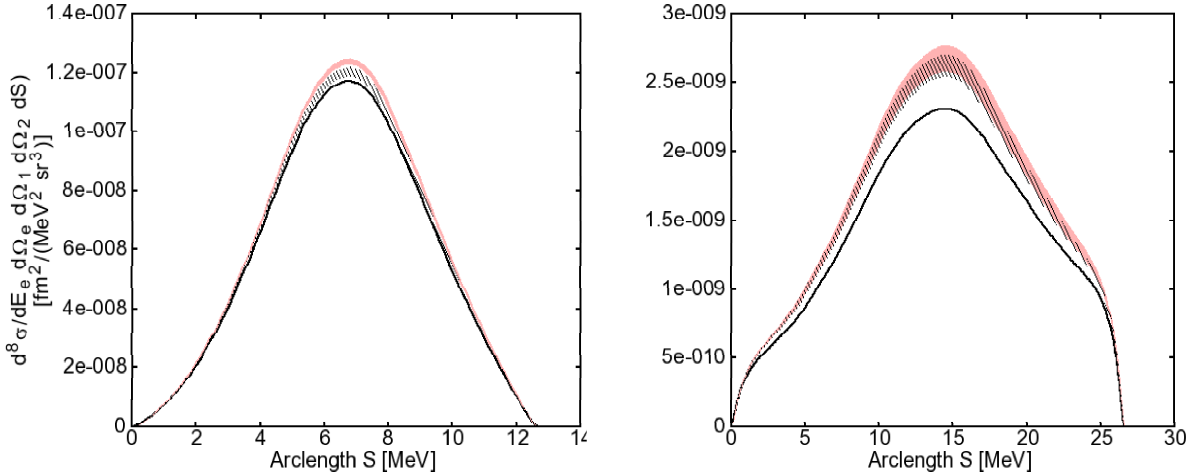


Figure 8.6: Exclusive differential cross section $d^8\sigma/(dE'd\Omega_e d\Omega_1 d\Omega_2 dS)$ as a function of the arc-length S for the two previously considered electron kinematics branches. Two protons in the final state are measured at $\theta_1^l = 20^\circ, \phi_1^l = 0^\circ$ and $\theta_2^l = 20^\circ, \phi_2^l = 180^\circ$. The lines and bands have the same meaning as in Figure 8.2.

and the complete breakup cross section $d^8\sigma/(dE'd\Omega_e d\Omega_1 d\Omega_2 dS)$.

In Figure 8.6 we present the exclusive cross section $d^8\sigma/(dE'd\Omega_e d\Omega_1 d\Omega_2 dS)$ as a function of the arc-length S . The two panels show the same electron kinematics branches as in Figure 8.2. Two protons in the final state are detected at $\theta_1^l = 20^\circ, \phi_1^l = 0^\circ$ and $\theta_2^l = 20^\circ, \phi_2^l = 180^\circ$, respectively. We regard the same theoretical models as in the case of two-body break-up of ${}^3\text{He}$. For the lower Q value (left panel) the predictions are close to each other but do not overlap. The band which includes the TPE current effects gets narrower than the one with the OPE contributions only. For the higher Q value (right plot) the AV18 predictions lie lower than the chiral bands which overlap. In this case, the band including TPE contributions is wider. Measurements of the exclusive three-body break-up cross section are very difficult, because the differential cross section values are very small. Thus, it is more realistic to expect that the so-called semi-exclusive cross sections and other observables of this kind will be measured. We consider the six-fold cross section $\frac{d^6\sigma}{dE'd\Omega_e d\Omega_1 dE_1}$, where the direction and the energy of one nucleon in the final state is known. Figure 8.7 contains just two examples for this observable at two different electron kinematics and different proton angles in the final state. For the lower Q value, the two bands are very narrow and overlap with the line which displays the AV18 predictions. For the higher Q value, in some range of proton energies, we see a difference between the line (AV18) and the chiral bands. Also in this case the band representing the TPE effects in the current operator is broader.

The second and third observables we investigate here are special cases of the helicity asymmetry $A(\vec{S})$, introduced already for electron-deuteron scattering,

$$A(\vec{S}) \equiv \frac{\sigma(\vec{S}, h = +1) - \sigma(\vec{S}, h = -1)}{\sigma(\vec{S}, h = +1) + \sigma(\vec{S}, h = -1)}, \quad (8.16)$$

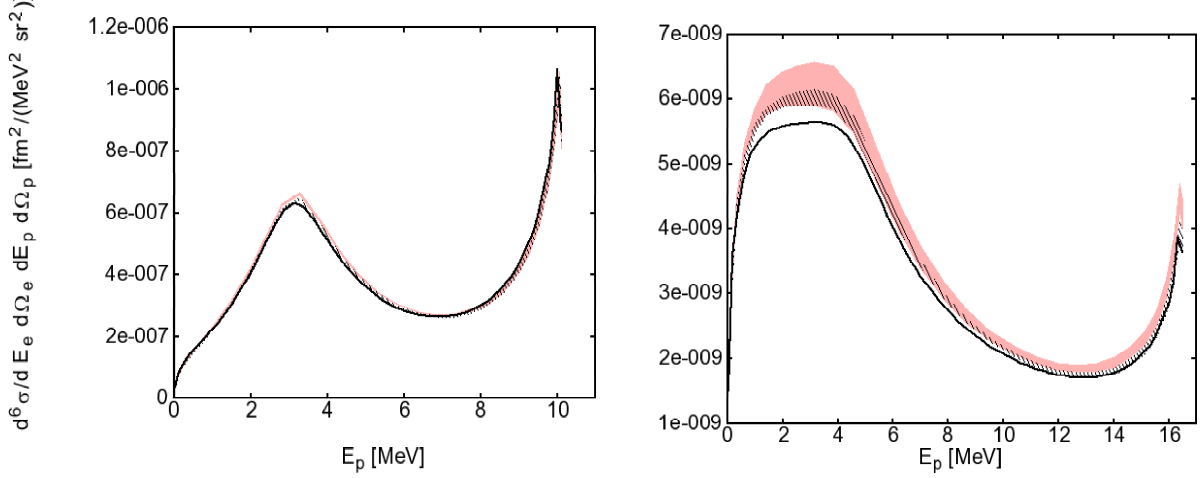


Figure 8.7: Semi-exclusive differential cross section (one proton is detected) $\frac{d^6\sigma}{dE'd\Omega_e d\Omega_1 dE_1}$ as a function of the outgoing proton energy E_p . The same electron kinematics is considered in the left and right panels as in Figure 8.2. The proton is detected at $\theta_1^l = 12^\circ, \phi_1^l = 0^\circ$ (left panel) and at $\theta_1^l = 145^\circ, \phi_1^l = 180^\circ$ (right panel). The meaning of lines and bands are the same as in Figure 8.2.

where now σ denotes the semi-exclusive cross section but for a specific ^3He spin direction \vec{S} . We consider only A_{\parallel} for $\vec{S} \parallel \hat{z}$ and A_{\perp} for $\vec{S} \parallel \hat{x}$:

$$A_{\perp} = A(\theta^* = 90^\circ, \phi^* = 0^\circ), \quad A_{\parallel} = A(\theta^* = 0^\circ, \phi^* = 0^\circ) \quad (8.17)$$

Sample results are presented in Figure 8.8. We see that the chiral bands and the line representing the AV18 predictions overlap for all cases. Inclusion of the TPE contributions in the current operator leads to broader bands, especially for the lower Q value and at smaller energy E_p .

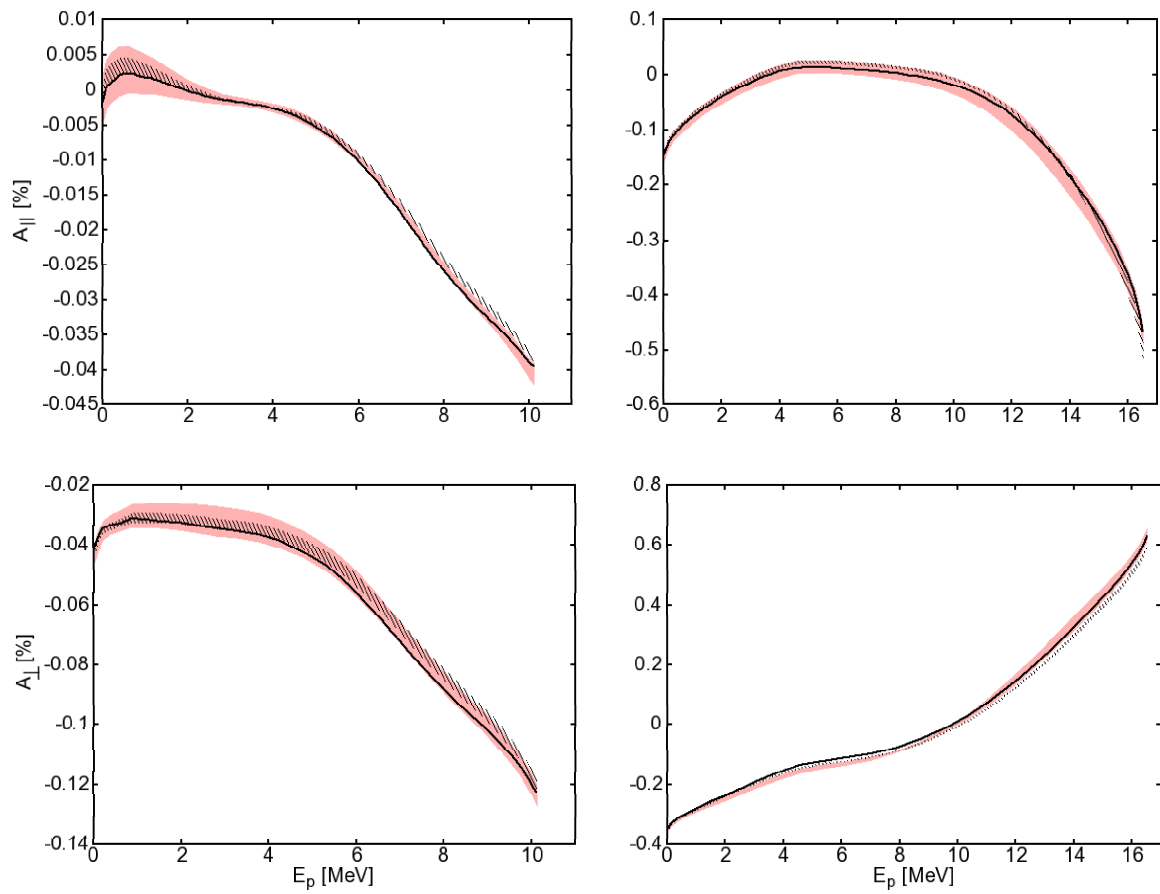


Figure 8.8: Helicity asymmetry A_{\parallel} (upper row) and A_{\perp} (lower row) as functions of the outgoing proton energy E_p . Both the electron kinematics and the final proton angles are the same in the left and in the right panels as in Figure 8.7. The meaning of lines and bands are the same as in Figure 8.2.

Chapter 9

Photodisintegration of ^3He

Photodisintegration of ^3He has been studied experimentally and theoretically for a long time [54, 142]. Two-body and three-body photon induced breakup of ^3He has been investigated with the aim to search for three nucleon force effects [143, 144]. Photodisintegration observables are more sensitive to meson-exchange contributions in the nuclear current operator. This is due to the fact that the charge density operator, which often dominates low energy electrodisintegration and is mostly given by the single nucleon current does not play any role in this reaction. Thus we hope that our results will show more sensitivity to smaller components of the nuclear current operator. In Ref.[54], the description of the photodisintegration reactions employed the Siegert approximation. In this thesis, we use for the first time current operators derived, within ChEFT [42].

In this chapter we present our results for two- and three-body photodisintegration of ^3He . We restrict ourselves to two photon laboratory energies $E_\gamma=12$ and 50 MeV. The Coulomb force between two-protons in three-nucleon scattering states is not taken into account. The three nucleon matrix elements N^μ are obtained using partial wave decomposition, with the total angular momentum of the three-nucleon system $J \leq \frac{15}{2}$ and including all partial waves with the subsystem total angular momentum $j \leq 3$.

The kinematics for this process is very similar to the one for electrodisintegration: one should only remember that $Q = \omega$ for real photons. As in the previous chapter, we check first that the nonrelativistic treatment of kinematics is justified. In particular, in Figure 9.1, we see that deuteron momenta calculated for two-body breakup relativistically and nonrelativistically as a function of the deuteron scattering angle θ_d are very similar. The same good agreement can be found also for other kinematical quantities for the two considered laboratory energies. The nuclear matrix elements $N_{\pm 1}$ are obtained according to the formalism described in Chapter 7. Given $N_{\pm 1}$, one can calculate cross sections and any polarization observables. They are expressed through the nuclear matrix elements with different spin projections carried by the initial photon, the ^3He nucleus, and by the outgoing nucleons and/or the outgoing deuteron. For more details we refer to [54]. In the following we just present our sample results.

We start with the exclusive unpolarized cross section for two body breakup of ^3He , $d^2\sigma/d\Omega_d$, where the final deuteron is measured. It is shown as a function of the deuteron

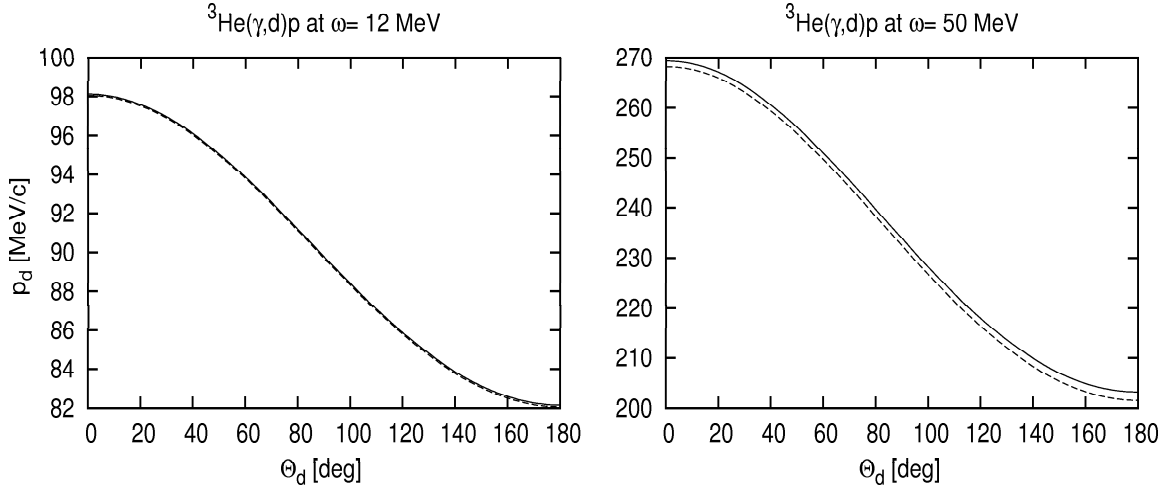


Figure 9.1: Final deuteron momentum calculated relativistically (solid line) and nonrelativistically (dashed line) for $E_\gamma=12$ MeV (left panel) and 50 MeV (right panel) as a function of the deuteron scattering angle θ_d .

scattering angle θ_d measured with respect to the initial photon direction. In the left panel, we put the results for $E_\gamma=12$ MeV and in the right panel for $E_\gamma=50$ MeV. We compare the same types of predictions (the AV18, the chiral including leading OPE current operator and the chiral with the additional long-range TPE current operator).

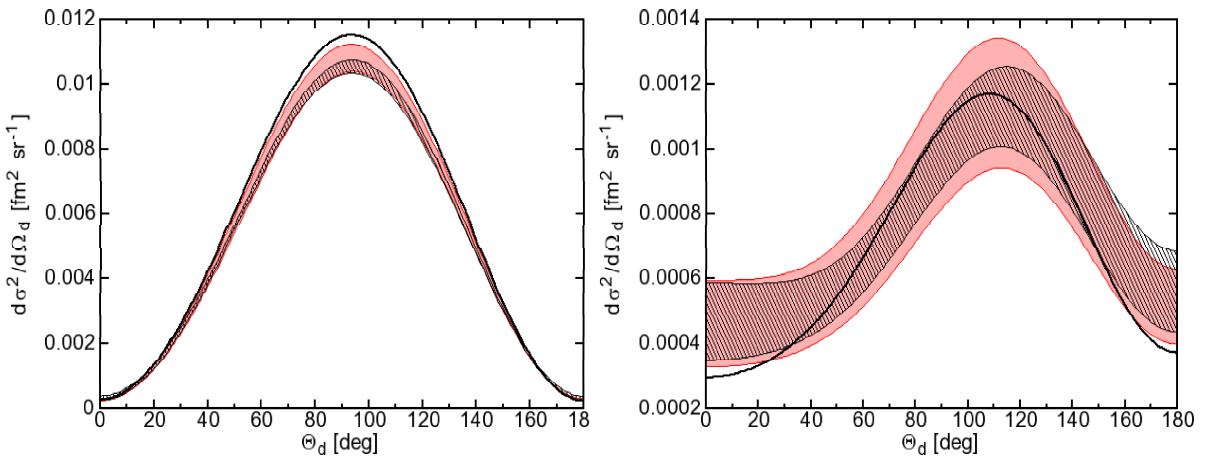


Figure 9.2: Differential cross section in the laboratory frame for ${}^3\text{He}$ two-body photodisintegration at the photon laboratory energies $E_\gamma = 12$ MeV (left panel) and $E_\gamma = 50$ MeV (right panel). The dark band covers N²LO chiral predictions for different cut-off parameter values. The current operator is taken as a sum of the single nucleons current and one-pion exchange current. The pink band covers N²LO chiral predictions for different cut-off parameter values and the current operator is taken as a sum of the single nucleons current, one-pion exchange current and two-pion exchange current. The solid line represents predictions obtained with the AV18 nucleon-nucleon potential and the related exchange currents.

Further, we show the results for a few polarization observables using the definitions from [142]. We choose the \hat{z} -axis to be the direction of the incoming photon, consider a linear photon polarization P_0^γ along the \hat{x} -axis, with the polarization component $P_0^\gamma = -1$, and the ^3He target nucleus polarization $P_0^{^3\text{He}}$ along the \hat{y} -axis. Then the cross section in the $\bar{\gamma}(^3\text{He}, d)p$ reaction, when the outgoing deuteron is detected at angles (θ_d, ϕ_d) is given by [142]

$$\begin{aligned} \sigma_{\gamma, ^3\text{He}}^{pol}(\theta_d, \phi_d) &= \sigma_{\gamma, ^3\text{He}}^{unpol}(\theta_d)[1 + P_0^\gamma \cos(2\phi_d) A_x^\gamma(\theta_d) + P_0^{^3\text{He}} \cos(\phi_d) A_y^{^3\text{He}}(\theta_d) + \\ &P_0^\gamma \cos(2\phi) P_0^{^3\text{He}} \cos(\phi_d) C_{x,y}^{\gamma, ^3\text{He}}(\theta_d) + P_0^\gamma \sin(2\phi_d) P_0^{^3\text{He}} \sin(\phi_d) C_{y,x}^{\gamma, ^3\text{He}}(\theta_d)]. \end{aligned} \quad (9.1)$$

Here the non-vanishing spin observables are the photon ($A_x^\gamma(\theta_d)$) and the ^3He ($A_y^{^3\text{He}}(\theta_d)$) analyzing powers, and the spin correlation coefficients $C_{x,y}^{\gamma, ^3\text{He}}(\theta_d)$ and $C_{y,x}^{\gamma, ^3\text{He}}(\theta_d)$. They can be obtained by measuring the spectra of the outgoing deuteron using a proper combination of ϕ_d angles and are expressed through the nuclear matrix element $N_\tau \equiv N_{m_p, m_d, \tau, m_{bs}}$ by (m_p, m_d, τ, m_{bs} are the spin projections of the proton, deuteron, photon and the initial three-nucleon bound state, respectively):

$$\begin{aligned} A_x^\gamma(\theta_d) &\equiv \frac{\sum_{m_p, m_d, m_{bs}} \left(2\text{Re} \left(N_{m_p, m_d - 1, m_{bs}} N_{m_p, m_d + 1, m_{bs}}^* \right) \right)}{\sum_{m_p, m_d, m_{bs}} (|N_{m_p, m_d + 1, m_{bs}}|^2 + |N_{m_p, m_d - 1, m_{bs}}|^2)} \\ A_y^{^3\text{He}}(\theta_d) &\equiv \frac{\sum_{m_p, m_d} \left(-2\text{Im} \left(N_{m_p, m_d - 1, -\frac{1}{2}} N_{m_p, m_d + 1, \frac{1}{2}}^* \right) - 2\text{Im} \left(N_{m_p, m_d + 1, -\frac{1}{2}} N_{m_p, m_d + 1, \frac{1}{2}}^* \right) \right)}{\sum_{m_p, m_d, m_{bs}} (|N_{m_p, m_d + 1, m_{bs}}|^2 + |N_{m_p, m_d - 1, m_{bs}}|^2)} \\ C_{x,y}^{\gamma, ^3\text{He}}(\theta_d) &\equiv \frac{\sum_{m_p, m_d} \left(-2\text{Re} \left(N_{m_p, m_d - 1, -\frac{1}{2}} N_{m_p, m_d + 1, \frac{1}{2}}^* \right) + 2\text{Re} \left(N_{m_p, m_d - 1, \frac{1}{2}} N_{m_p, m_d + 1, -\frac{1}{2}}^* \right) \right)}{\sum_{m_p, m_d, m_{bs}} (|N_{m_p, m_d + 1, m_{bs}}|^2 + |N_{m_p, m_d - 1, m_{bs}}|^2)} \\ C_{y,x}^{\gamma, ^3\text{He}}(\theta_d) &\equiv \frac{\sum_{m_p, m_d} \left(2\text{Im} \left(N_{m_p, m_d - 1, -\frac{1}{2}} N_{m_p, m_d + 1, \frac{1}{2}}^* \right) + 2\text{Im} \left(N_{m_p, m_d - 1, \frac{1}{2}} N_{m_p, m_d + 1, -\frac{1}{2}}^* \right) \right)}{\sum_{m_p, m_d, m_{bs}} (|N_{m_p, m_d + 1, m_{bs}}|^2 + |N_{m_p, m_d - 1, m_{bs}}|^2)} \\ . \end{aligned} \quad (9.2)$$

The photon analyzing power $A_x^\gamma(\theta_d)$ the ^3He analyzing power $A_y^{^3\text{He}}(\theta_d)$ as well as the spin correlation coefficients $C_{x,y}^{\gamma, ^3\text{He}}(\theta_d)$ and $C_{y,x}^{\gamma, ^3\text{He}}(\theta_d)$ are shown in Figures 9.3.

For the three-body breakup of ^3He we show only the semiexclusive differential cross section $\frac{d^3\sigma}{d\Omega_p dE_p}$ (detected single proton), at two photon laboratory energies $E_\gamma = 12$ and $E_\gamma = 50$ MeV. The cross section values are shown as functions of the outgoing proton energies. For the lower photon energy (left panel) the observed bands are relatively narrow, especially for higher proton energies, where they both coincide with the AV18 results. For lower proton energy, the bands are broader and the band representing the TPE contributions is narrower than the other one.

The situation is quite different for the higher photon energy (right panel). The shapes of the bands are more complicated and they become very broad. Especially, the band with TPE parts of the current operator is much broader than the band including only OPE contributions. This is true in the whole range of the proton energies.

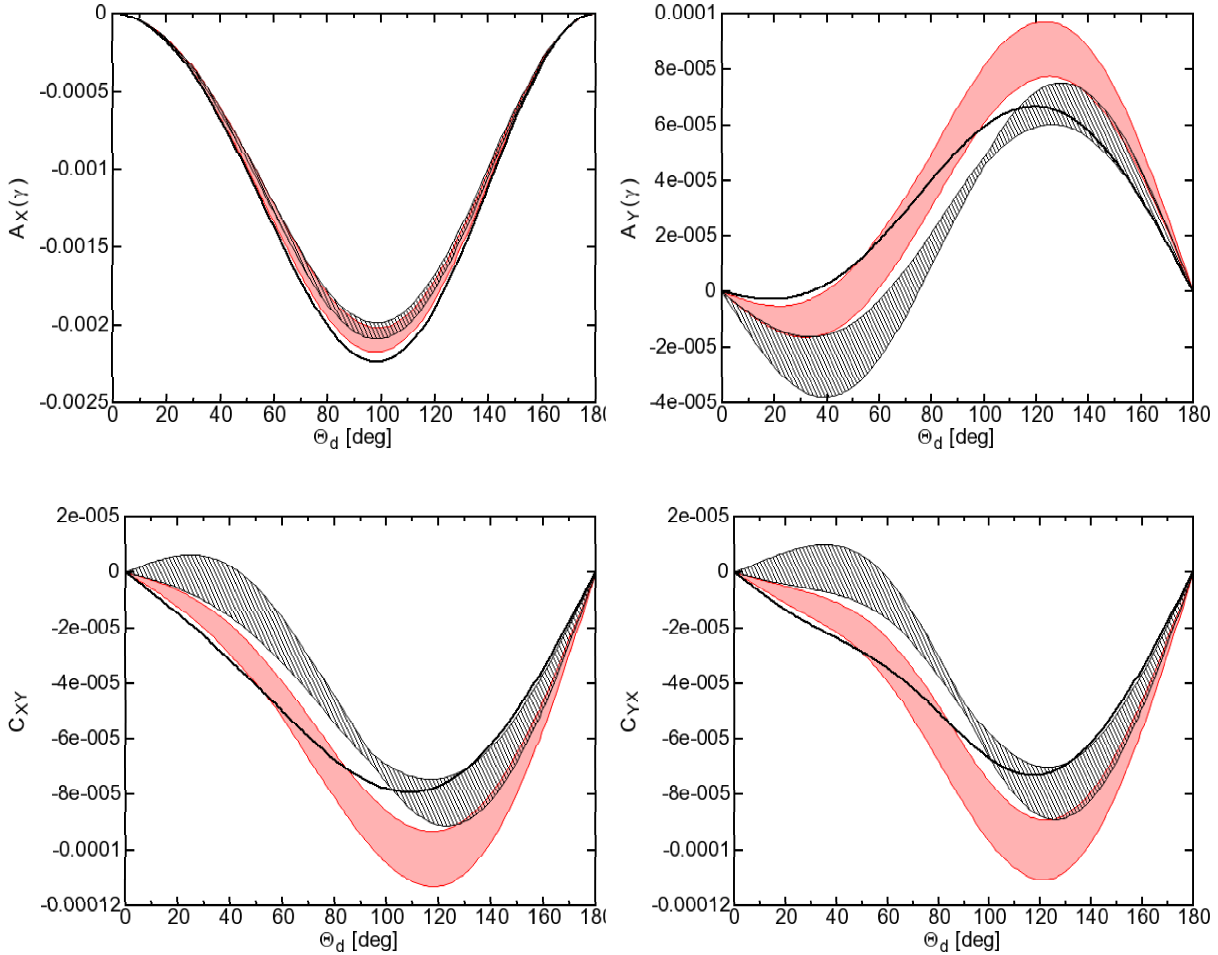


Figure 9.3: Spin observables for ${}^3\text{He}$ two-body photodisintegration at photon lab. energy $E_\gamma = 12$ MeV. The upper row shows the analyzing powers for photon ($A_x(\gamma)$, left) and ${}^3\text{He}$ ($A_y({}^3\text{He})$, right). The lower row shows spin correlation coefficients: C_{XY} (left) and C_{YX} (right). The bands and line have the same meaning as in Figure 7.

Having presented all our results for different electromagnetic reactions in the two- and three-nucleon systems we have to conclude that inclusion of the TPE contributions in the current operator does not lead to precise theoretical predictions for higher energy and momentum transfers. Especially, the band including the TPE contributions becomes so broad that we loose any predictive power. This happens practically for all observables. Only at very low values of the energy transfer we see cases with the “correct” behaviour of the bands. Namely, in these few cases the band including the TPE operators is narrower than the one, with OPE operators only.

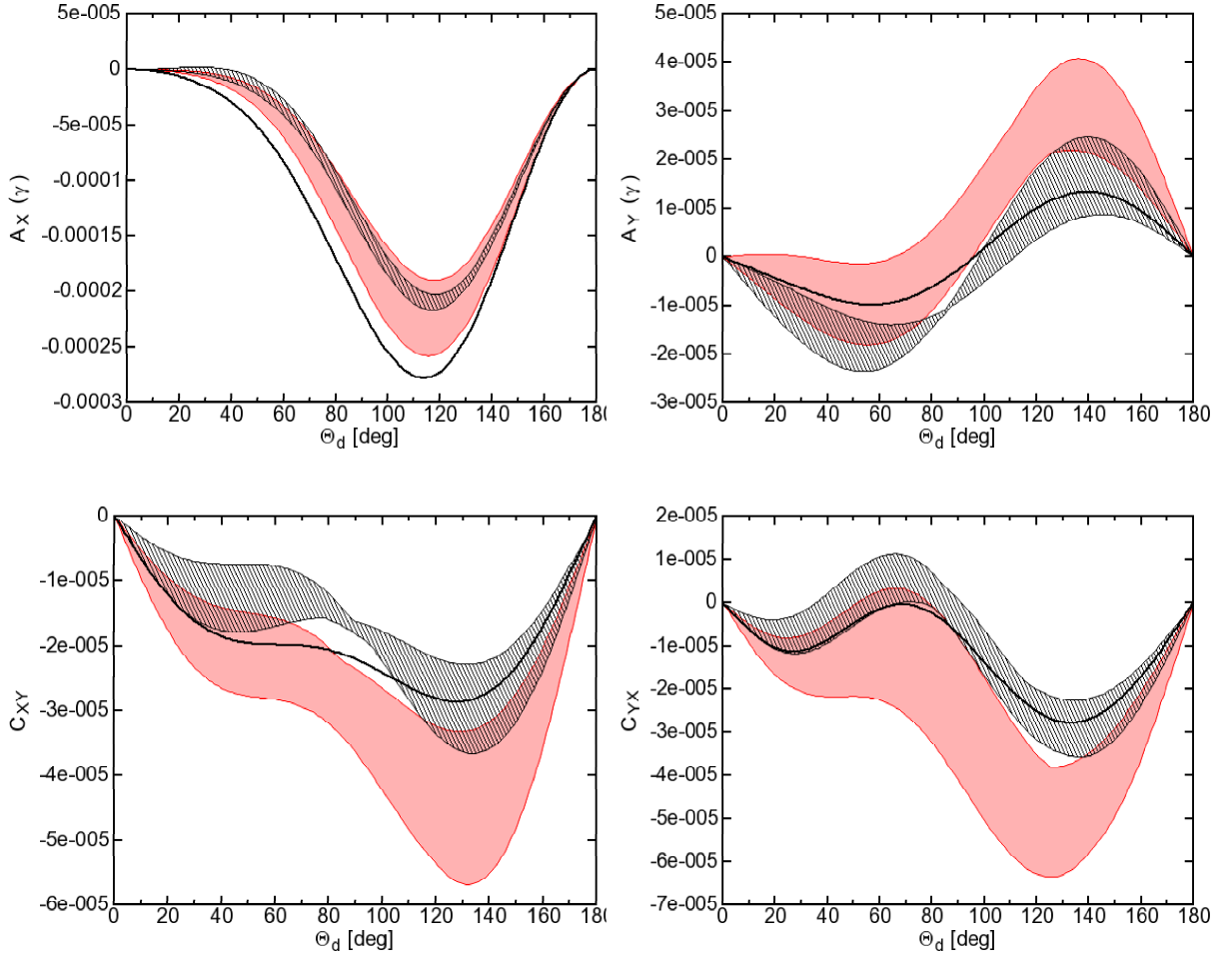


Figure 9.4: The same as in Figure 9.3 but for the photon laboratory energy $E_\gamma = 50$ MeV.

This agrees with the conditions given in Ref. [42], where the following restrictions on the magnitude of the photon momentum Q and the photon energy ω are given

$$Q \sim \mathcal{O}(M_\pi), \quad \omega \sim \mathcal{O}\left(\frac{M_\pi^2}{M_N}\right) \ll M_\pi. \quad (9.3)$$

This means that in the case of photodisintegration reactions, where $Q = \omega$ we are limited to very low photon energies. This also means that our present knowledge (at NLO) about the chiral current operator is far from being complete. First of all, one should study systematically the remaining contributions to the current operator at NLO. They have been partly taken into account for the two-nucleon reactions but are totally absent in our treatment in three nucleon reactions. These structures contain unknown parameters, which should be fixed in the two-nucleon sector. Only then they can be applied in the three-nucleon electromagnetic reactions. This is left for future work.

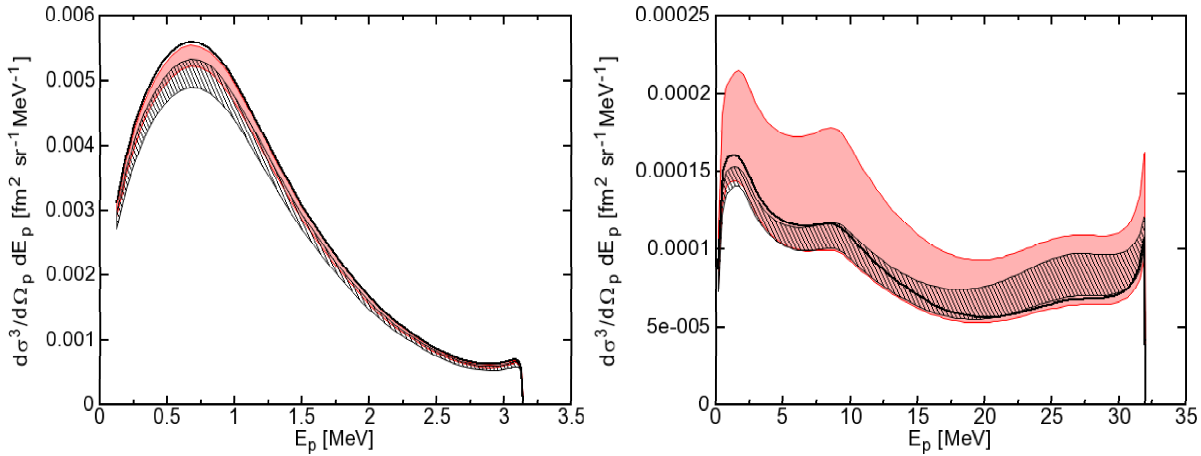


Figure 9.5: Differential cross section for semiexclusive ${}^3\text{He}$ three-body photodisintegration ${}^3\text{He}(\gamma, p)pn$ for proton emissions at $\theta = 15^\circ$ and photon lab. energy $E_\gamma = 12$ and $E_\gamma = 50$ MeV. The bands and lines have the same meaning as in Figure 9.3.

Further research in this field is necessary, which should lead to new components in the current operator. Only then a description of electromagnetic reactions in a wider kinematical range will be possible. Comparing this situation to the one for the few-nucleon forces, we can expect a significant improvement at higher orders of chiral expansion.

Chapter 10

Summary and conclusions

A pending problem in any theory dealing with electromagnetic reactions with atomic nuclei has been (full) consistence between the theoretical models of the forces and currents. Despite many efforts in the past the situation has changed only with the advent of the Chiral Effective Field Theory. This theory is strongly linked to QCD and offers a consistent picture of nucleon-nucleon potentials, many-nucleon potentials and current operators responsible for the photon absorption by the few-nucleon system.

Such an effective theory can be formulated in many different ways. We concentrate in this thesis on the work of Evgeny Epelbaum and collaborators, who have already published many important results concerning the two-nucleon potential [51], the three-nucleon potential [12, 145] and even the four-nucleon force [146, 13]. Recently the same group published results about the two-pion-exchange two-nucleon current operator [42] obtained, like earlier the few-nucleon forces, with the method of unitary transformation. For the first time this nontrivial contribution to the nuclear current operator is fully consistent with the two-pion-exchange nuclear force, including all calculational details. Pion physics is included exactly in this framework so the published expressions do not contain any free parameters.

In this thesis we used and tested these new important results. We had even a chance to work with some expressions prior to their official publication and reported to the authors about some numerical problems, which led to some modifications in the final published version.

We wanted to check the importance of these two-pion-exchange contributions to the nuclear current operator studying their role in various electromagnetic reactions on the deuteron and to some extent also on ${}^3\text{He}$. To this aim we first of all built our own consistent framework for description of elastic electron-deuteron scattering, electrodisintegration of the deuteron, photo-disintegration of the deuteron and radiative neutron-proton capture. Our programs can calculate not only the cross sections but also many polarization observables. We are of course aware that these electromagnetic reactions have been studied for a long time and carefully compared our results obtained with the older AV18 nucleon-nucleon potential [45] and the corresponding meson-exchange currents [46, 47, 53] to the results available in the literature. A special role in this comparison played publications of H. Arenhövel [147, 148]. However,

we wanted to have our own tool to study various inputs to the two-nucleon current operator.

An important part of this framework is our way of dealing with many spin-isospin structures present in the chiral current operator. In the traditional approach based on the so-called meson theory, the number of spin operators was very limited. It was possible to obtain and program analytical expressions for matrix elements of these operators in the commonly used partial wave representation. In ChEFT one should be prepared for very many different spin-isospin combinations (altogether more than one hundred). That is why we decided to use a totally different approach and prepared matrix elements by straightforward four fold integrations performed on the powerful parallel computers of the Jülich Supercomputing Centre in Germany. The computer codes for these integrations were produced in an "automated" (and thus very safe) way using the *Mathematica* software [49]. This method enables us to work efficiently with many different contributions to the two-nucleon current operator.

As mentioned above, the expressions for the leading two-pion-exchange part of the two-nucleon current operator do not contain any free parameters. However, all effective theories give eventually results with unknown parameters, which have to be determined from experimental data. This is also the case for ChEFT, where the so-called contact interactions and currents have to be fitted from data. In fact we are aware of the new results which will soon be officially available from Kölling and collaborators and even have started to work on them. They do contain expressions with unknown parameters, which should be fitted from experimental data. We hope very much that the set of codes we have prepared for this thesis will be also used for analyzing data from such facilities like the High Intensity Gamma-Ray Source (HIGS) at TUNL (USA) or the Superconducting Darmstadt Linear Accelerator (S-DALINAC) in Germany. Experimental groups from both these facilities are very interested in our results.

Compared to the chiral nucleon-nucleon force (available already at N3LO), the two-nucleon chiral current operator is known only at NLO. It means that many more parts of the current are needed to achieve the level of the nucleon-nucleon potential. It is then no wonder that our results for various observables in the electromagnetic reactions leave a lot of room for improvement and can be used for very limited values of the energy and momentum transfer.

In the case of elastic electron-deuteron scattering the leading one-pion-exchange and two-pion-exchange current operators do not contribute. On top of the single-nucleon operator we deal then with much smaller components of the current operator. Our goal has been here to check some effects of the new current operators.

For the deuteron electro- and photo-disintegration processes nearly all the two-nucleon current operators play a role, with the exception of the structures with the T_1 isospin operator. Here we can see clearly effects from the recently published two-pion-exchange operators and even additional structures. The "bands", characteristic for the chiral physics, become very broad with the increasing energy and momentum transfer, which clearly demonstrates the need of inclusion of further components in the current operator. We believe in the quest for the nuclear current operator one should

concentrate on the deuteron, the simplest system, where the contributions beyond the single-nucleon operator can be tested.

With the established two-nucleon current operator we can then go over to the three-nucleon system. We show in this thesis how the approach to two-nucleon current operators in [54] can be extended to incorporate many more spin-isospin operators, which appear in ChEFT. One should note that the so-called "non-local" operators will pose additional (mostly numerical) problems due to their dependence on the total initial two-nucleon momentum, which is not fixed in the three-nucleon system. In the case of the ^3He electro- and photo-disintegration reactions we give only very few results but in principle, using the framework prepared in [54], we are able to cover many different observables. In the reactions with three nucleons all isospin operators must be included. We see again that the "bands" depend on the energy and momentum delivered to the three-nucleon system. We would be also able to include in the future the three-nucleon potential and the corresponding three-nucleon current operator, which appear at next-to-next-to-leading order of the chiral expansion.

Summarizing, we would like to express our hope that the results of this thesis will be useful in studying electromagnetic reactions with two- and three-nucleon systems.

Appendix A

Schrödinger equation for the deuteron

In this appendix we will explain how we solve the non-relativistic Schrödinger equation for the deuteron bound state,

$$H |\Psi_{deut} m_d\rangle \equiv (H_0 + V) |\Psi_{deut} m_d\rangle = E_{deut} |\Psi_{deut} m_d\rangle , \quad (\text{A.1})$$

in the partial wave representation in the momentum space and discuss properties of the resulting S -component ($\varphi_0(p)$) and D -component ($\varphi_2(p)$) of the deuteron wave function. Since we know already that only two basis states with $s = j = 1$ and $t = 0$ contribute to the deuteron state, we can use a simplified notation

$$|pl\rangle \equiv |p(l1)1\rangle |00\rangle . \quad (\text{A.2})$$

Note that the deuteron wave function does not depend on the projection of the total angular momentum, so we skip m_d in the following considerations.

By projecting from the left with $\langle pl |$ Equation (A.1) reads

$$\frac{p^2}{M_N} \varphi_l(p) + \sum_{l',l=0,2} \int dp' p'^2 \langle pl | V | p'l' \rangle \varphi_{l'}(p') = E_{deut} \varphi_l(p), \quad (\text{A.3})$$

where of course

$$\varphi_l(p) \equiv \langle pl | \Psi_{deut} \rangle . \quad (\text{A.4})$$

For a numerical treatment of Equation (A.3) we assume that the integral over p' will be carried out with some choice of Gaussian points and weights (p_j, w_j) with $j = 1, 2, \dots, N_P$ given in the interval $(0, \bar{p})$, where the upper limit \bar{p} depends on the nucleon-nucleon potential used. For all the chiral potentials we considered it was sufficient to take $N_P = 40$ Gaussian points up to $\bar{p} = 4.5 \text{ fm}^{-1}$. In the case of the AV18 potential we took a similar number of points but the upper integral limit had to be shifted to 40 fm^{-1} in order to guarantee convergence of the results. We get

$$\frac{p_i^2}{M_N} \varphi_l(p_i) + \sum_{l'=0,2} \sum_{j=1}^{N_P} w_j p_j^2 \langle p_i l | V | p_j l' \rangle \varphi_{l'}(p_j) = E_d \varphi_l(p_i) , \quad l = 0, 2 . \quad (\text{A.5})$$

This can be written as an eigenvalue problem $A\xi = E_{deut}\xi$, where the components of the $2N_P$ dimensional vector ξ and the $2N_P \times 2N_P$ matrix A are given as

$$\begin{aligned} \xi_{i+\frac{l}{2}N_P} &= \varphi_l(p_i), \\ A(i + \frac{l}{2}N_P, j + \frac{l'}{2}N_P) &= \delta_{ij}\delta_{ll'}\frac{p_i^2}{M_n} + w_j p_j^2 \langle p_i l | V | p_j l' \rangle, \\ i &= 1, \dots, N_P, \quad j = 1, \dots, N_P, \quad l, l' = 0, 2. \end{aligned} \quad (\text{A.6})$$

We used the routines from *Numerical Recipes* [149] to get the numerical solutions for the five choices of the NLO chiral potential, for the five choices of the N2LO chiral potential and the AV18 potential. Each choice of the chiral potential is characterised by two parameters, $(\Lambda, \tilde{\Lambda})$ listed in Table 2.2. The resulting S - and D - components of the deuteron wave function in momentum space, for the chiral potentials, are shown in Figure A.1. In Figure A.2, we show the corresponding results for the AV18 potential.

In each case the components are normalised as

$$\int_0^\infty dp p^2 (\varphi_0^2(p) + \varphi_2^2(p)) = 1. \quad (\text{A.7})$$

Very often properties of the deuteron components are discussed in the coordinate space. In order to compare our results with the ones given in literature [78]–[75], we made a transformation to the coordinate space using the spherical Bessel functions, $j_0(z)$ and $j_2(z)$

$$\begin{aligned} u(r) &= \sqrt{\frac{2}{\pi}} r \int_0^\infty dp p^2 \varphi_0(p) j_0(pr) \\ w(r) &= -\sqrt{\frac{2}{\pi}} r \int_0^\infty dp p^2 \varphi_2(p) j_2(pr), \end{aligned} \quad (\text{A.8})$$

where $u(r)$ ($w(r)$) is the S - (D -)component of the deuteron wave function in the coordinate space. The results of the transformation are shown in Figure A.3. The normalisation condition reads now

$$\int_0^\infty dr (u^2(r) + w^2(r)) = 1. \quad (\text{A.9})$$

Among the many properties of the deuteron wave function we calculate first the S - and D -state probabilities

$$\begin{aligned} P_S &= \int_0^\infty dp p^2 \varphi_0^2(p) = \int_0^\infty dr u^2(r) \\ P_D &= \int_0^\infty dp p^2 \varphi_2^2(p) = \int_0^\infty dr w^2(r). \end{aligned} \quad (\text{A.10})$$

The other quantities are the so-called root mean square (RMS) radius of the deuteron

$$r_d = \frac{1}{2} \left[\int_0^\infty dr r^2 [u(r)^2 + w(r)^2] \right]^{1/2} \quad (\text{A.11})$$

and the deuteron quadrupole moment

$$Q_d = \frac{1}{20} \int_0^\infty dr r^2 w(r) [\sqrt{8}u(r) - w(r)]. \quad (\text{A.12})$$

Note that none of these quantities is actually an observable. Finally, we fit the deuteron components in order to extract the asymptotic S -wave normalisation (A_S)

$$u(r) \rightarrow A_S e^{-\gamma r} \quad \text{for } r \rightarrow \infty \quad (\text{A.13})$$

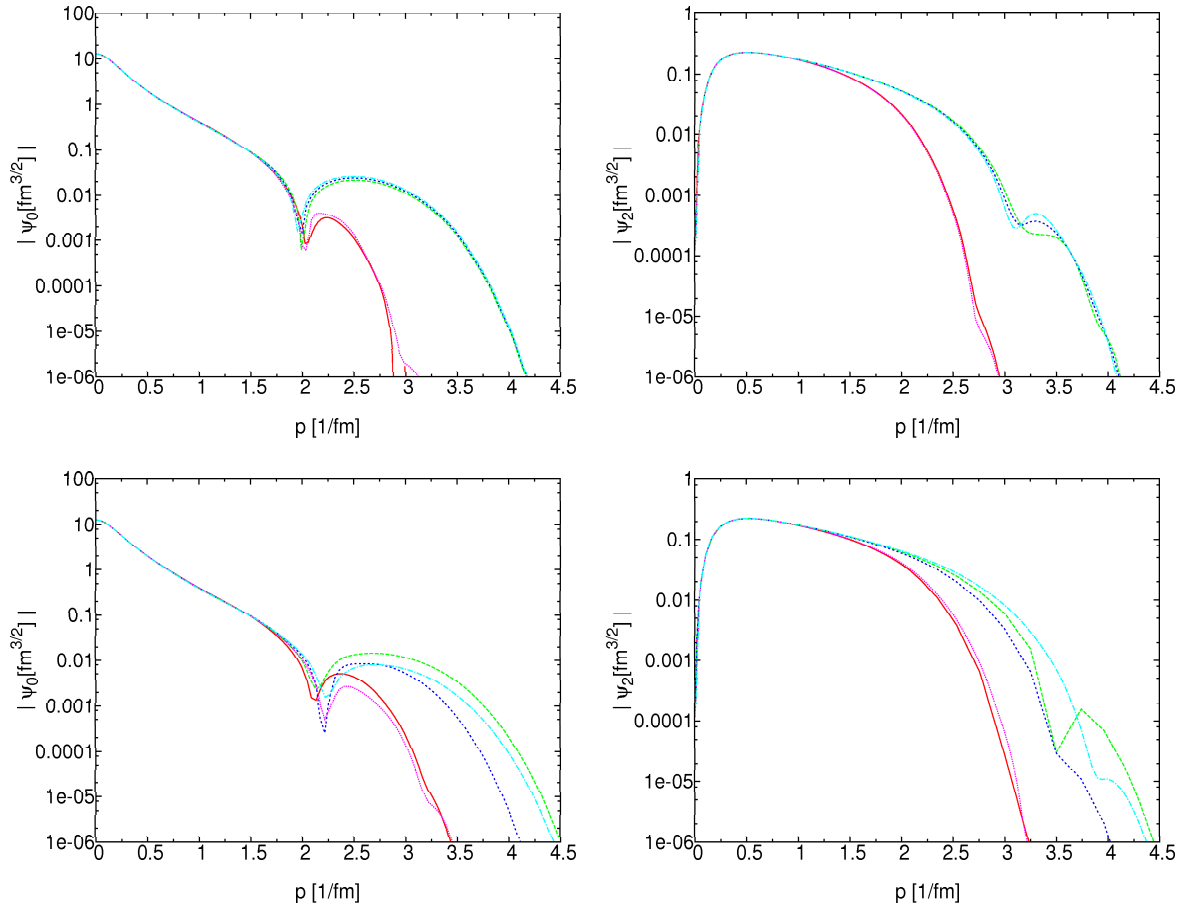


Figure A.1: Deuteron wave functions for different cutoff values at two orders of chiral expansion: NLO (upper row) and N2LO (lower row) as given by Table 2.2. The plots on the left display the S-wave components as a function of p . In the right plots we see D-wave components as a function of p .

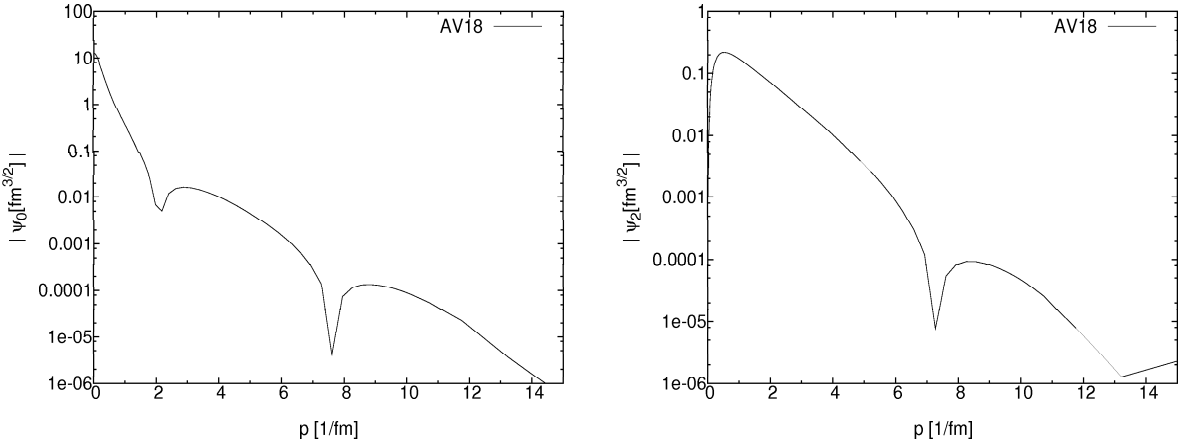


Figure A.2: Deuteron wave function with the AV18 potential. The left (right) panel shows S-(D-) component of the wave functions as a function of p .

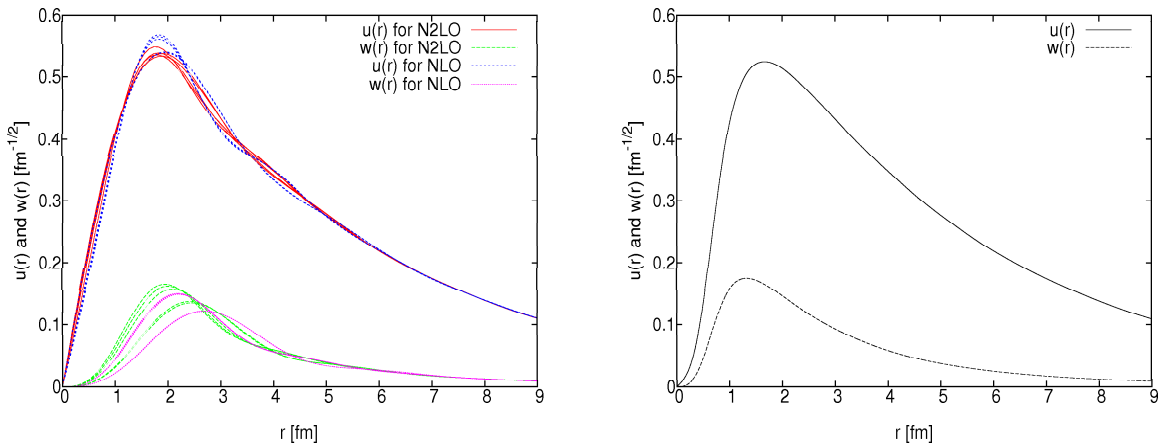


Figure A.3: S-wave ($u(r)$) and D-wave ($w(r)$) component of the deuteron wave functions in the co-ordinate space as a function of r . The left panel contains wave function components for the chiral NLO and N2LO potentials. The right panel shows components of the wave function obtained with the AV18 potential.

and the asymptotic D/S -ratio (η)

$$w(r) \rightarrow \eta A_S \left(1 + \frac{3}{\gamma r} + \frac{3}{(\gamma r)^2} \right) e^{-\gamma r} \quad \text{for } r \rightarrow \infty, \quad (\text{A.14})$$

with $\gamma = \sqrt{M_n |E_d|} \approx 45.7$ MeV, where for M_N we used the average mass of the proton and the neutron, $M_N = 938.918$ MeV. In order to get η we first obtained A_S . Both fits were carried out in the interval $(10, 30)$ fm. All calculated results are collected in Table A.1.

Table A.1: Deuteron properties derived from chiral potential at NLO and N2LO for different cut-off values. Here, E_d is the binding energy, the D-state probability, Q_d the quadrupole moment, η the asymptotic D/S ratio, r_d the root-mean-square matter radius and A_S the strength of the asymptotic S-wave normalisation.

V-CUT	$ E_d $ [MeV]	D[%]	Q_d [fm 2]	$\eta[10^{-2}]$	r_d [fm]	A_S [fm $^{-1/2}$]
NLO-1	2.16988	3.08683	0.27058	2.56101	1.97491	0.86800
NLO-2	2.18335	4.08341	0.27447	2.55631	1.97287	0.87208
NLO-3	2.18092	4.04863	0.27451	2.55669	1.97335	0.87132
NLO-4	2.16465	3.06678	0.27076	2.56230	1.97559	0.86638
NLO-5	2.17929	4.01726	0.27448	2.55682	1.97374	0.87081
N2LO-1	2.19239	3.53628	0.27150	2.55693	1.97183	0.87506
N2LO-2	2.18443	4.56609	0.27562	2.55069	1.97223	0.87321
N2LO-3	2.18889	4.38325	0.27491	2.55093	1.97161	0.87454
N2LO-4	2.20211	3.61314	0.27110	2.55257	1.97056	0.87806
N2LO-5	2.19986	4.70944	0.27474	2.54781	1.97013	0.87769
AV18	2.22422	5.77590	0.26982	2.53732	1.96226	0.87879
Exp. [28]	2.22458	–	0.2859	2.5600	1.9734	0.885

Appendix B

Numerical solutions of the Lippmann-Schwinger equation

For the calculation of the rescattering matrix elements of the full two-nucleon current element given in Equation (4.40), we need the half-shell elements of the T -matrix,

$$\left\langle p_0 \alpha_2 \left| T \left(\frac{p_0^2}{M_N} + i\epsilon \right) \right| p' \alpha_{2'} \right\rangle .$$

Due to the rotational invariance, parity conservation, spin and isospin conservation of the nucleon-nucleon potential these matrix elements may be written as

$$\begin{aligned} & \left\langle p_0(ls)jm_j; lm_t \left| T \left(\frac{p_0^2}{M_N} + i\epsilon \right) \right| p'(l's')j'm'_j; l'm'_t \right\rangle = \\ & \delta_{j,j'} \delta_{m_j,m'_j} \delta_{(-1)^l,(-1)^{l'}} \delta_{s,s'} \delta_{t,t'} \delta_{m_t,m'_t} \left\langle p_0(ls)j; l \left| T \left(\frac{p_0^2}{M_N} + i\epsilon \right) \right| p'(l's)j; l \right\rangle , \end{aligned} \quad (\text{B.1})$$

which means that either $l = l'$ (uncoupled channel) or $l - l' = \pm 2$ (two coupled channels). We will show how the Lippmann-Schwinger equation

$$T = V + TG_0V \quad (\text{B.2})$$

is solved numerically for the more demanding case of the coupled channels which is possible for $j > 0$ only if $s = 1$. Using a shorthand notation

$$\langle p_0 l | T | p' l' \rangle \equiv \langle p_0 \alpha_2 | T | p' \alpha'_2 \rangle , \quad (\text{B.3})$$

the partial-wave projected Equation (B.2) takes the following form:

$$\langle p_0 l | T | p' l' \rangle = \langle p_0 l | V | p' l' \rangle + \sum_{l''=j-1,j+1} \int_0^\infty dp'' \frac{p''^2 \langle p_0 l | T | p'' l'' \rangle \langle p'' l'' | V | p' l' \rangle}{\frac{p_0^2}{M_N} - \frac{p''^2}{M_N} + i\epsilon} \quad (\text{B.4})$$

with $\epsilon \rightarrow 0^+$. Treating the singularity by subtraction we obtain

$$\begin{aligned} \langle p_0 l | T | p' l' \rangle &= \langle p_0 l | V | p' l' \rangle \\ + M_N \sum_{l''} \int_0^{\bar{p}} dp'' p''^2 &\frac{\langle p_0 l | T | p'' l'' \rangle \langle p'' l'' | V | p' l' \rangle - p_0^2 \langle p_0 l | T | p_0 l'' \rangle \langle p_0 l'' | V | p' l' \rangle}{p_0^2 - p''^2} \\ &+ \frac{M_N p_0}{2} \left[\ln \left| \frac{\bar{p} + p_0}{\bar{p} - p_0} \right| - i\pi \right] \sum_{l''} \langle p_0 l | T | p_0 l'' \rangle \langle p_0 l'' | V | p' l' \rangle, \end{aligned} \quad (\text{B.5})$$

where we used the following formula

$$\lim_{\epsilon \rightarrow 0^+} \int_0^{\bar{p}} \frac{dp}{p_0^2 - p^2 + i\epsilon} = \frac{1}{2p_0} \left[\ln \left| \frac{\bar{p} + p_0}{\bar{p} - p_0} \right| - i\pi \right]. \quad (\text{B.6})$$

Here again we choose a set of Gaussian points and weights –different from the one used for the deuteron wave function (p_n, w_n) with $n = 1, 2, \dots, N_P$ given in the interval $(0, \bar{p})$ and supplement it with an additional pair $(p_0, w_0 = 0)$ and require that $p_n \neq p_0$ for $n > 1$. This is done because in Equation (B.5) we need also $\langle p_0 l | T | p_0 l'' \rangle$. Both the upper limit \bar{p} and the number of integral points N_P must be chosen in a way which yields stable results. With

$$\begin{aligned} Z &\equiv \frac{M_N p_0}{2} \left[\ln \left| \frac{\bar{p} + p_0}{\bar{p} - p_0} \right| - i\pi \right], \\ H &\equiv M_N p_0^2 \sum_{n=1}^{N_P} \frac{w_n}{p_0^2 - p_n^2}, \\ \tilde{w}_n &\equiv \begin{cases} 0 & n = 0 \\ \frac{M_N w_n p_n^2}{p_0^2 - p_n^2}, & n \neq 0 \end{cases} \end{aligned} \quad (\text{B.7})$$

we obtain a set of $2(N_P + 1)$ equations

$$\begin{aligned} \sum_{l''} \sum_{n=0}^{N_P} [\tilde{w}_n \langle p_n l'' | V | p_i l' \rangle - H \langle p_0 l'' | V | p_i l' \rangle \delta_{n0} \\ + Z \langle p_0 l'' | V | p_i l' \rangle \delta_{n0} - \delta_{in} \delta_{l'l''}] \langle p_0 l | T | p_n l'' \rangle = - \langle p_0 l | V | p_i l' \rangle \end{aligned} \quad (\text{B.8})$$

for $2(N_P + 1)$ unknown matrix elements $\langle p_0 l | T | p_n l'' \rangle$, which we solve for each l separately. To be explicit, we write it as

$$\sum_d A_{kd} \xi_d = B_k, \quad (\text{B.9})$$

where

$$\begin{aligned}
l, l', l'' &= j-1, j+1, \\
k = i + 1 + \frac{l' - j + 1}{2} (N_P + 1), \quad i &= 0, 1, 2, \dots, N_P, \\
d = n + 1 + \frac{l'' - j + 1}{2} (N_P + 1), \quad n &= 0, 1, 2, \dots, N_P, \\
\xi_d &\equiv \langle p_0 l | T | p_n l'' \rangle, \\
b_k &\equiv -\langle p_0 l | T | p_i l' \rangle, \\
A_{kd} &\equiv \tilde{w}_n \langle p_n l'' | V | p_i l' \rangle + (Z - H) \langle p_0 l'' | V | p_i l' \rangle \delta_{n0} - \delta_{in} \delta_{l'l''}. \tag{B.10}
\end{aligned}$$

We solved this system of equations numerically using the standard LU decomposition routines from *The Numerical Recipes* [149]. We used also for comparison routines from other scientific libraries, for example from *LAPACK* [150]. The case of the uncoupled channel is simpler, since $l = l' = l''$ and we deal with a system of $N_P + 1$ coupled equations for unknown $\langle p_0 l | T | p_n l \rangle$ matrix elements. Note that in both cases, as a “by-product”, we obtain the on-shell T -matrix elements, $\langle p_0 l | T | p_0 l' \rangle$, which are used to calculate the phase shifts and mixing parameters characterising the nucleon-nucleon potential.

For two values of the 2N laboratory energy (7 and 100 MeV) and for all the channels with $j \leq 1$, we show T -matrix elements in Figures B.1–B.6. From the inspection of these and similar plots for higher partial waves, it became clear that setting $\bar{p} = 4.5$ 1/fm is fully sufficient. We used $N_P = 40$.

In order to check our numerics, we made the standard transition from the on-shell T -matrix to the on-shell S -matrix. For the case of two coupled channels we obtain:

$$\begin{aligned}
S_{11} &\equiv \langle p_0 j - 1 | S | p_0 j - 1 \rangle = 1 - i p_0 M_N \pi \langle p_0 j - 1 | T | p_0 j - 1 \rangle \\
S_{12} &\equiv \langle p_0 j - 1 | S | p_0 j + 1 \rangle = i p_0 M_N \pi \langle p_0 j - 1 | T | p_0 j + 1 \rangle \\
S_{21} &\equiv \langle p_0 j + 1 | S | p_0 j - 1 \rangle = i p_0 M_N \pi \langle p_0 j + 1 | T | p_0 j - 1 \rangle \\
S_{22} &\equiv \langle p_0 j + 1 | S | p_0 j + 1 \rangle = 1 - i p_0 M_N \pi \langle p_0 j + 1 | T | p_0 j + 1 \rangle. \tag{B.11}
\end{aligned}$$

For the case of uncoupled channels the S -matrix is one dimensional:

$$S \equiv \langle p_0 l | S | p_0 l \rangle = 1 - i p_0 M_N \pi \langle p_0 l | T | p_0 l \rangle. \tag{B.12}$$

We checked numerically that, as expected, the S -matrix in the partial wave decomposition is indeed unitary

$$S^\dagger S = S S^\dagger = 1 \tag{B.13}$$

and calculated standard phase shifts and mixing parameters in order to compare with results well known from the literature. In the uncoupled case the S -matrix is parametrised by one real phase, δ ,

$$S = e^{2i\delta} \tag{B.14}$$

For the coupled-channel case, where the 2×2 S -matrix is unitary and symmetric, we used the so-called Stapp parametrisation [151]

$$S = \begin{pmatrix} \cos(2\epsilon) \exp(2i\delta_1) & i \sin(2\epsilon) \exp(i(\delta_1 + \delta_2)) \\ i \sin(2\epsilon) \exp(i(\delta_1 + \delta_2)) & \cos(2\epsilon) \exp(2i\delta_2) \end{pmatrix}, \quad (\text{B.15})$$

which requires three real parameters, δ_1 , δ_2 and ϵ . These parameters are called phase shifts and mixing parameters.

We show our results for the neutron-proton phase shift parameters in Figures B.7–B.8 as functions of the laboratory energy. We chose just the first few $2N$ states, which dominate low-energy nuclear physics. We made calculations with the standard AV18 potential as well as with the different parametrizations of the chiral NLO and N2LO potential given by the different $(\Lambda, \tilde{\Lambda})$ pairs. We see again the bands characteristic for all chiral results, which become wider and wider with the increasing energy. Although there is a clear improvement when one shifts from NLO to N2LO, generally, the AV18 potential describes the data better, especially at higher energies. Our results agree very well with the ones from [152], where a detailed discussion of the chiral results is presented. This provides an additional check of our numerics.

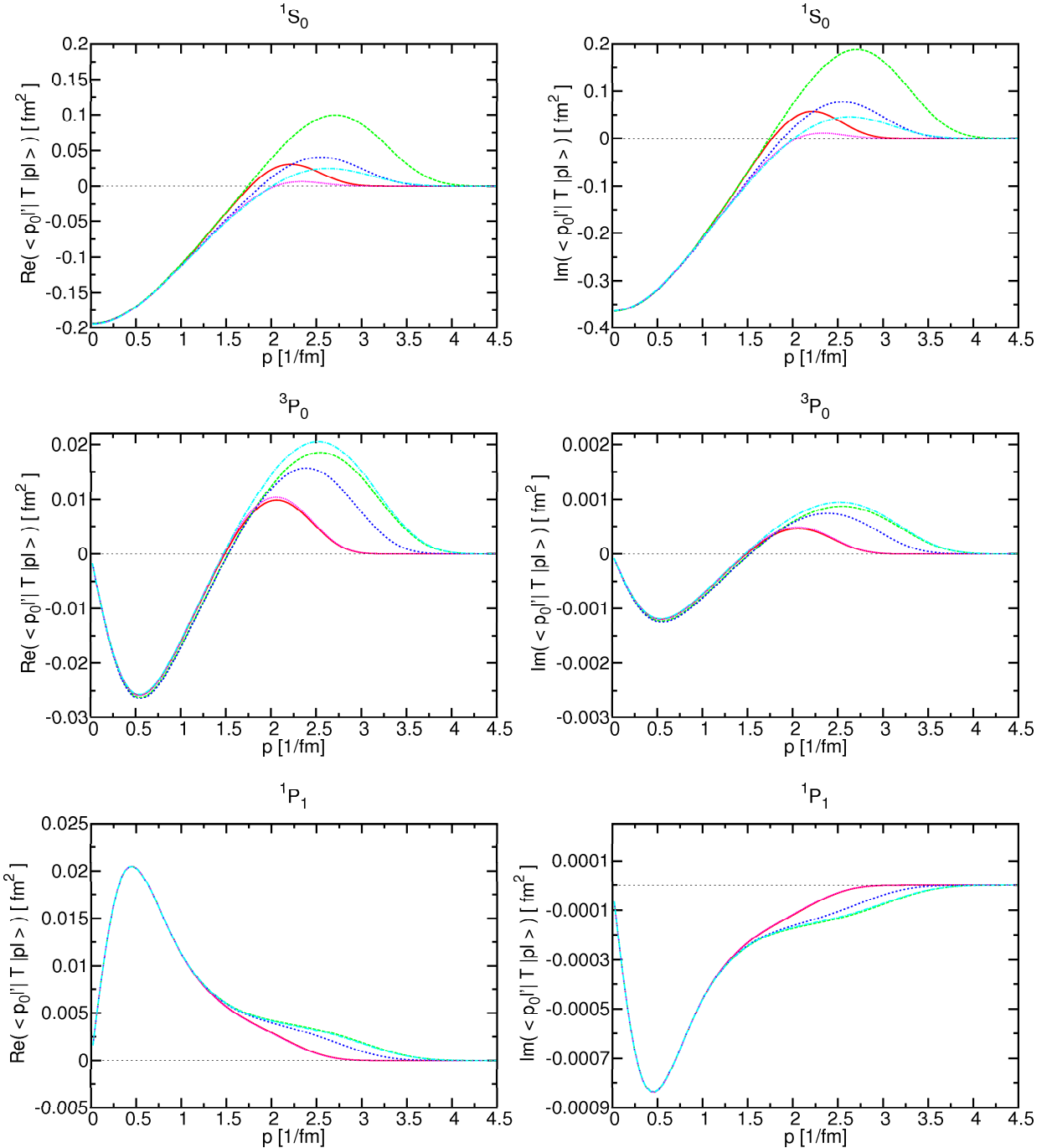


Figure B.1: Matrix elements of the T-operator for $p_0 = 0.3 \text{ fm}^{-1}$ (corresponding to the laboratory energy $E_{lab}=7 \text{ MeV}$) and for uncoupled channels with $j \leq 1$. The red lines show the results with the N2LO-1 potential. The green lines are the predictions based on the N2LO-2 potential. The blue lines are obtained with the N2LO-3 potential. The pink lines represent the results with the N2LO-4 case. The dark-blue lines stand for the N2LO-5 predictions. The cut-off values come from Table 2.2.

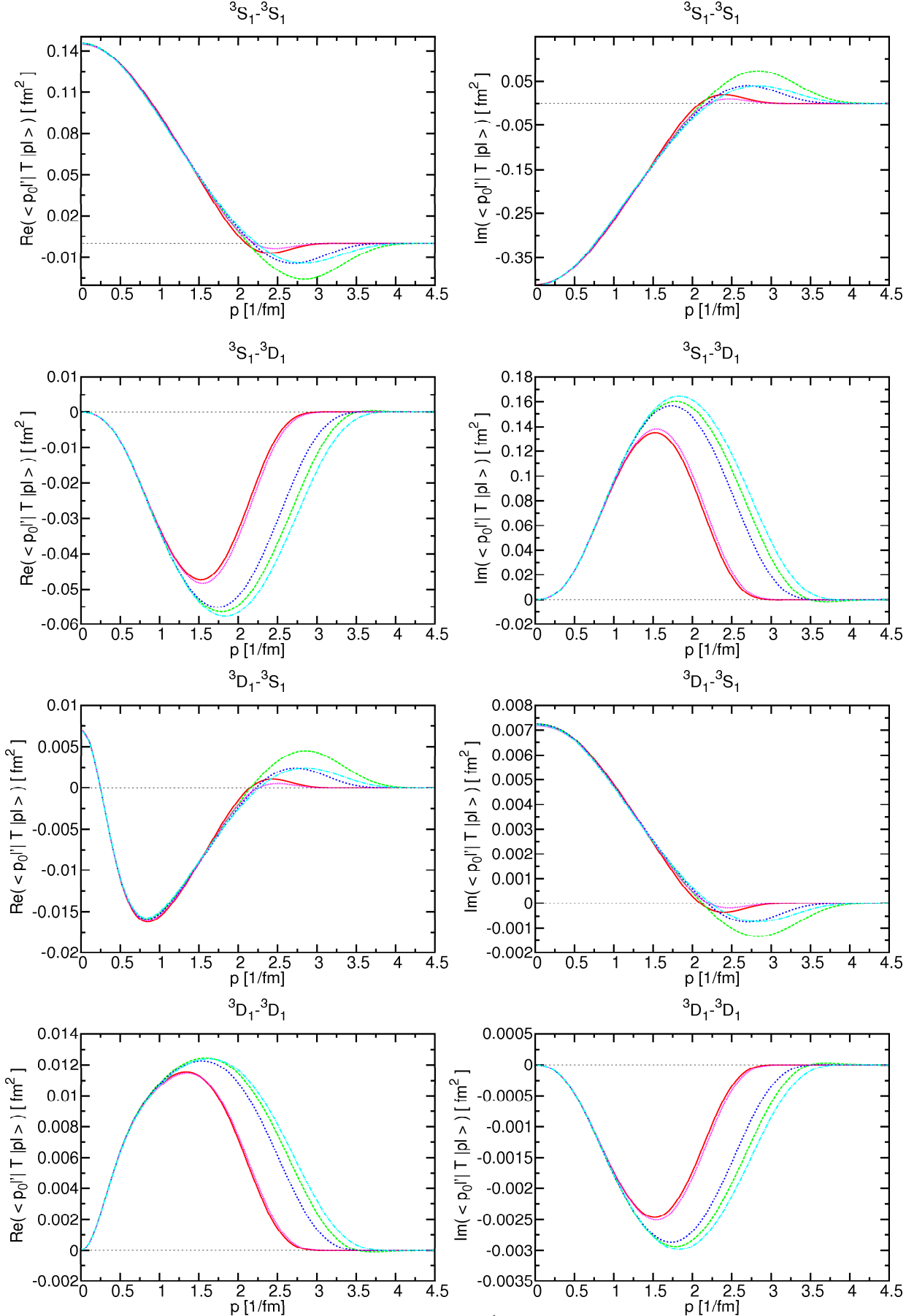


Figure B.2: T-matrix elements for $p_0 = 0.3 \text{ fm}^{-1}$ corresponding to the laboratory energy 7 MeV and coupled channels with $j \leq 1$. Lines as in Figure B.1.

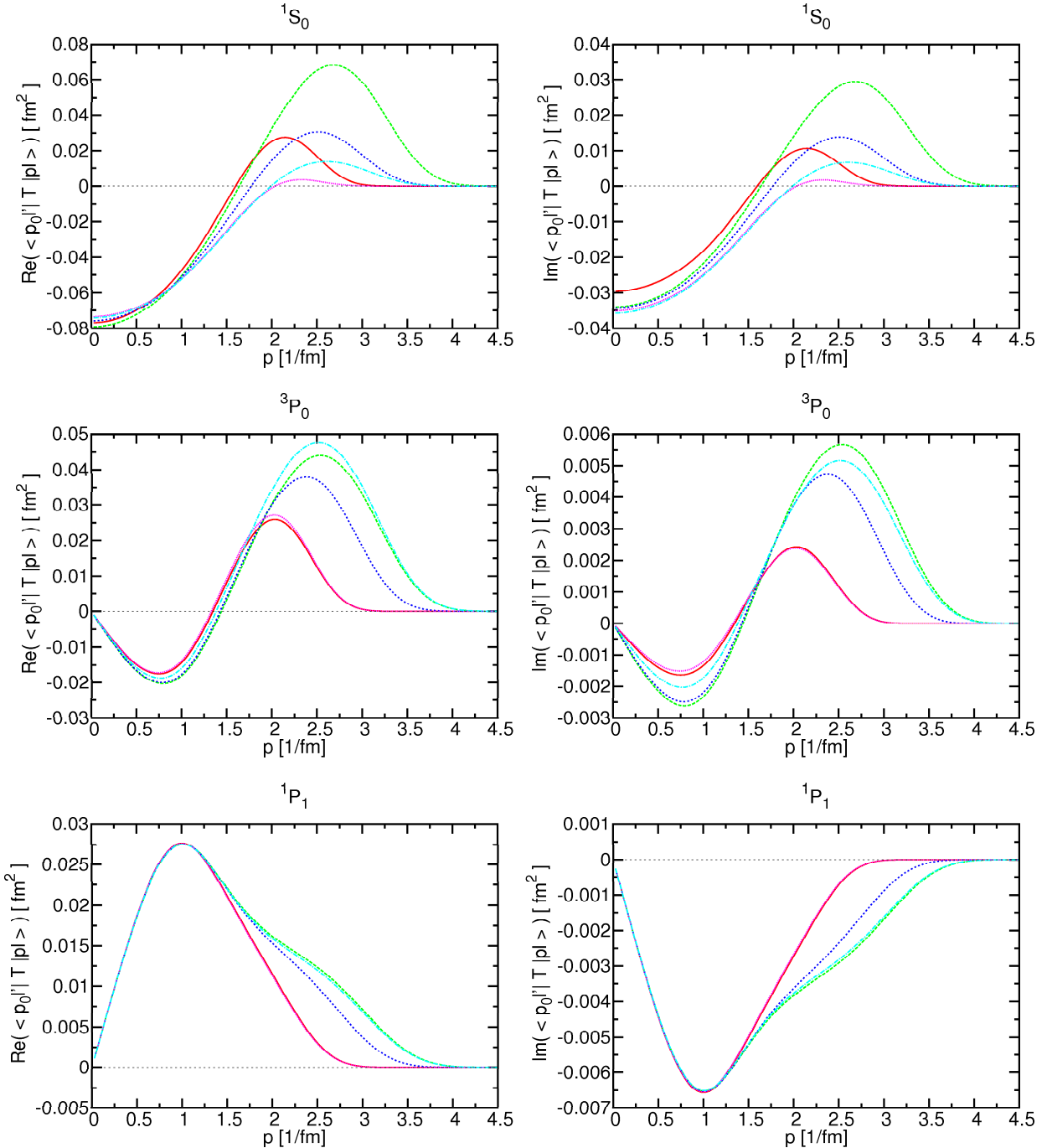


Figure B.3: T-matrix elements for $p_0 = 1.1 \text{ fm}^{-1}$ corresponding to the laboratory energy 100 MeV and uncoupled channels with $j \leq 1$ at N2LO. Lines as in Figure B.1.

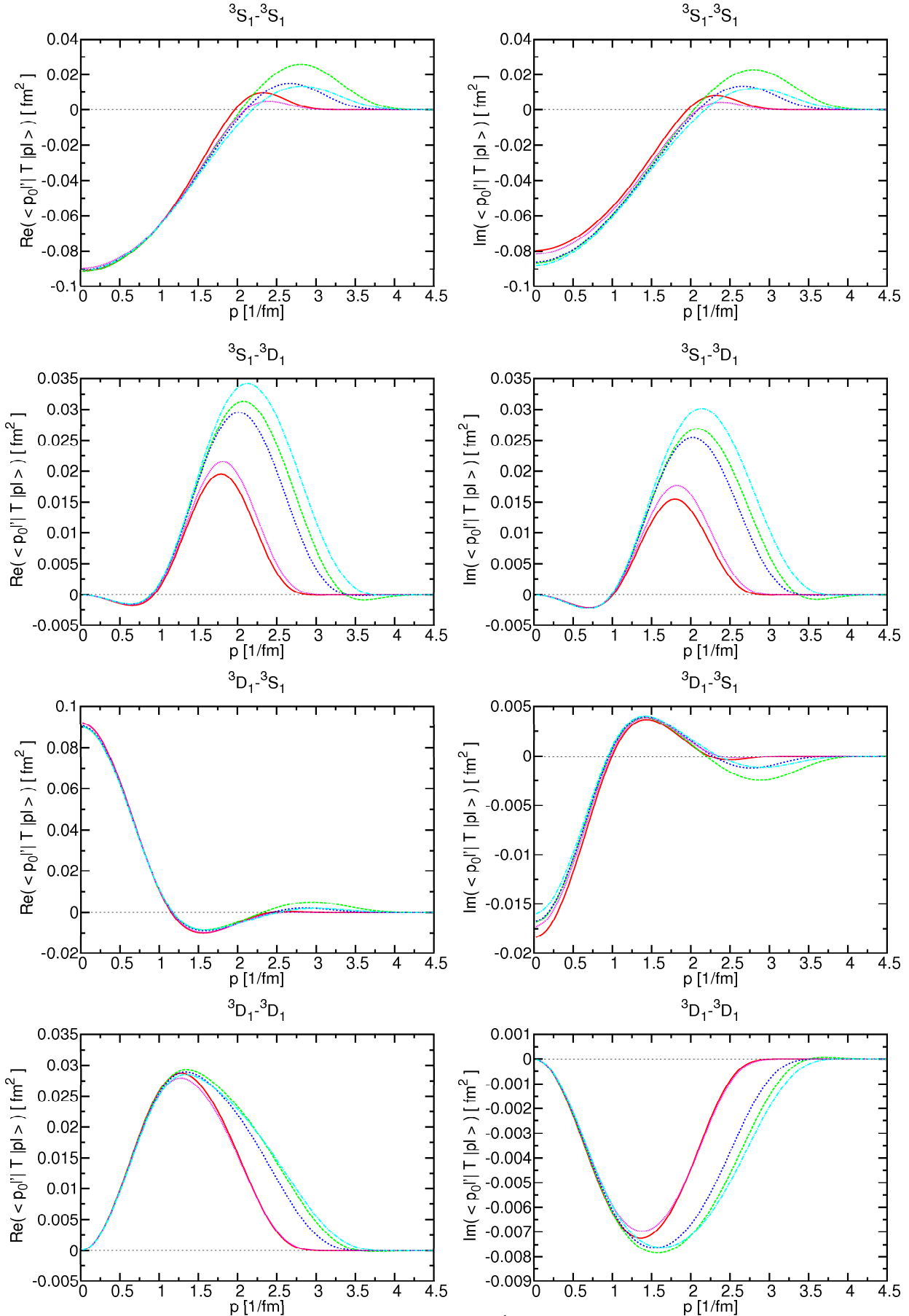


Figure B.4: T-matrix elements for $p_0 = 1.1 \text{ fm}^{-1}$ corresponding to the laboratory energy 100 MeV and coupled channels with $j \leq 1$ at N2LO. Lines as in Figure B.1.

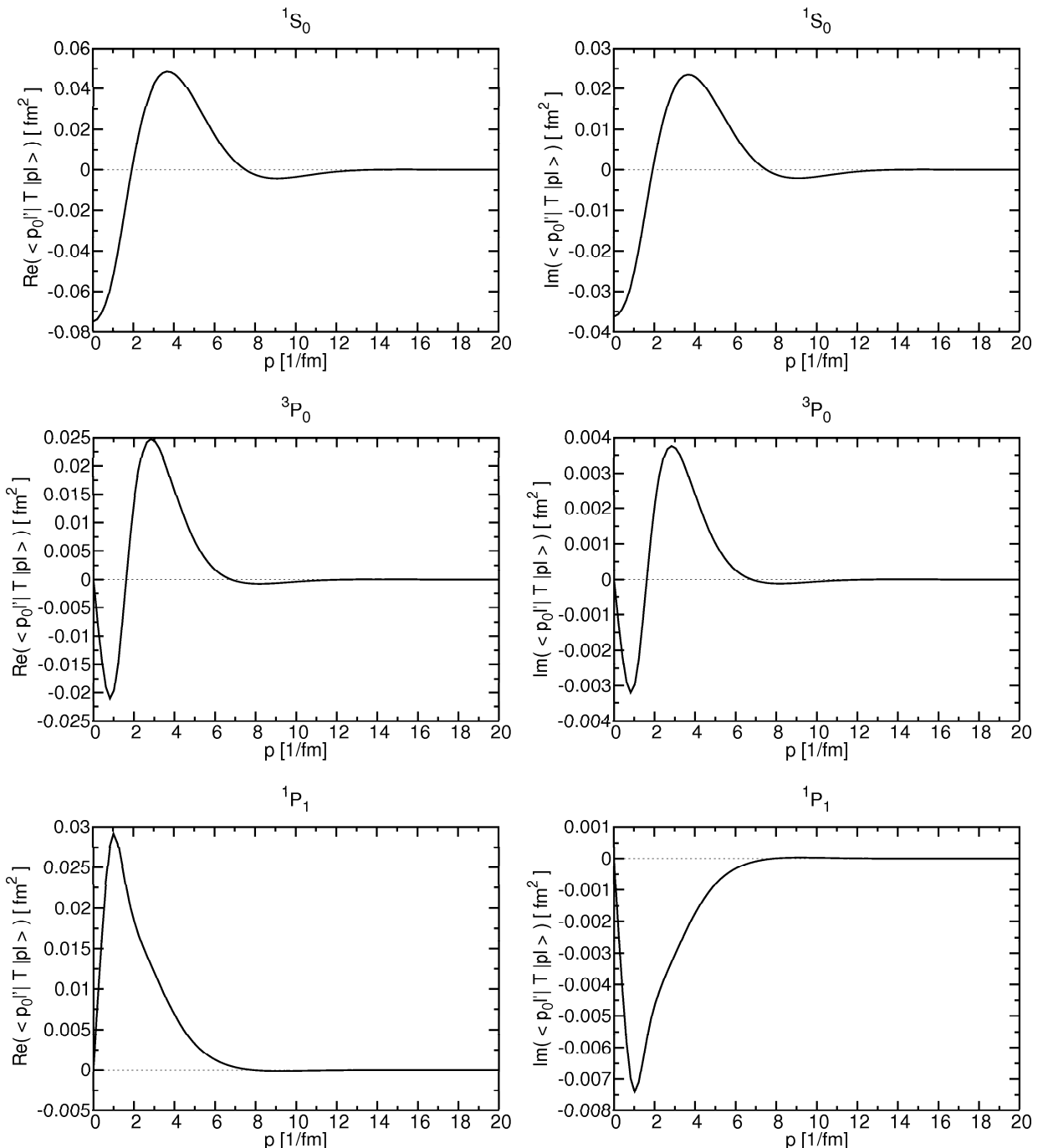


Figure B.5: T-matrix elements for $p_0 = 1.1 \text{ fm}^{-1}$ corresponding to the laboratory energy 100 MeV and uncoupled channels with $j \leq 1$ with AV18 potential.

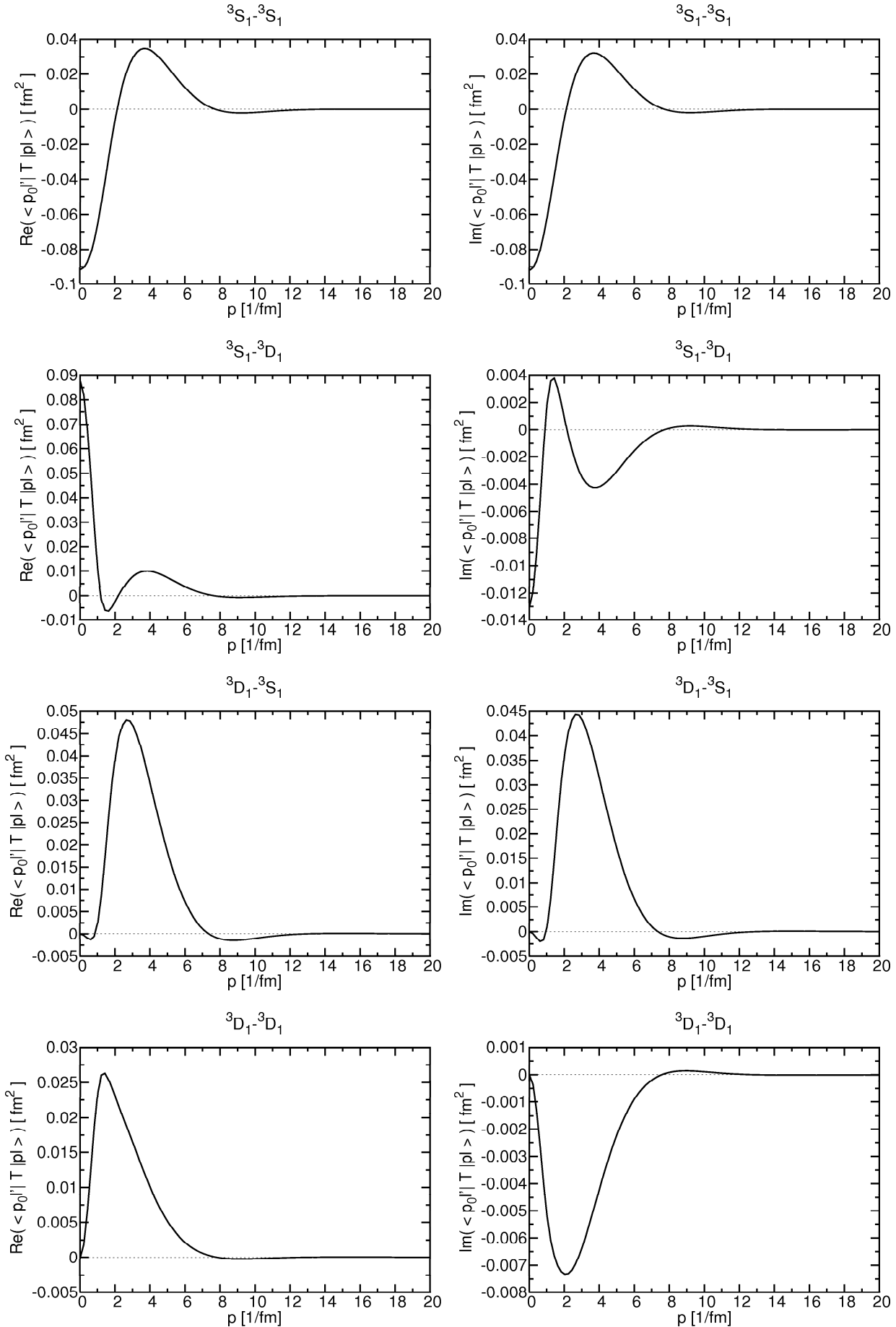


Figure B.6: T-matrix elements for $p_0 = 1.1 \text{ fm}^{-1}$ corresponding to the laboratory energy 100 MeV and coupled channels with $j \leq 1$ with AV18 potential.

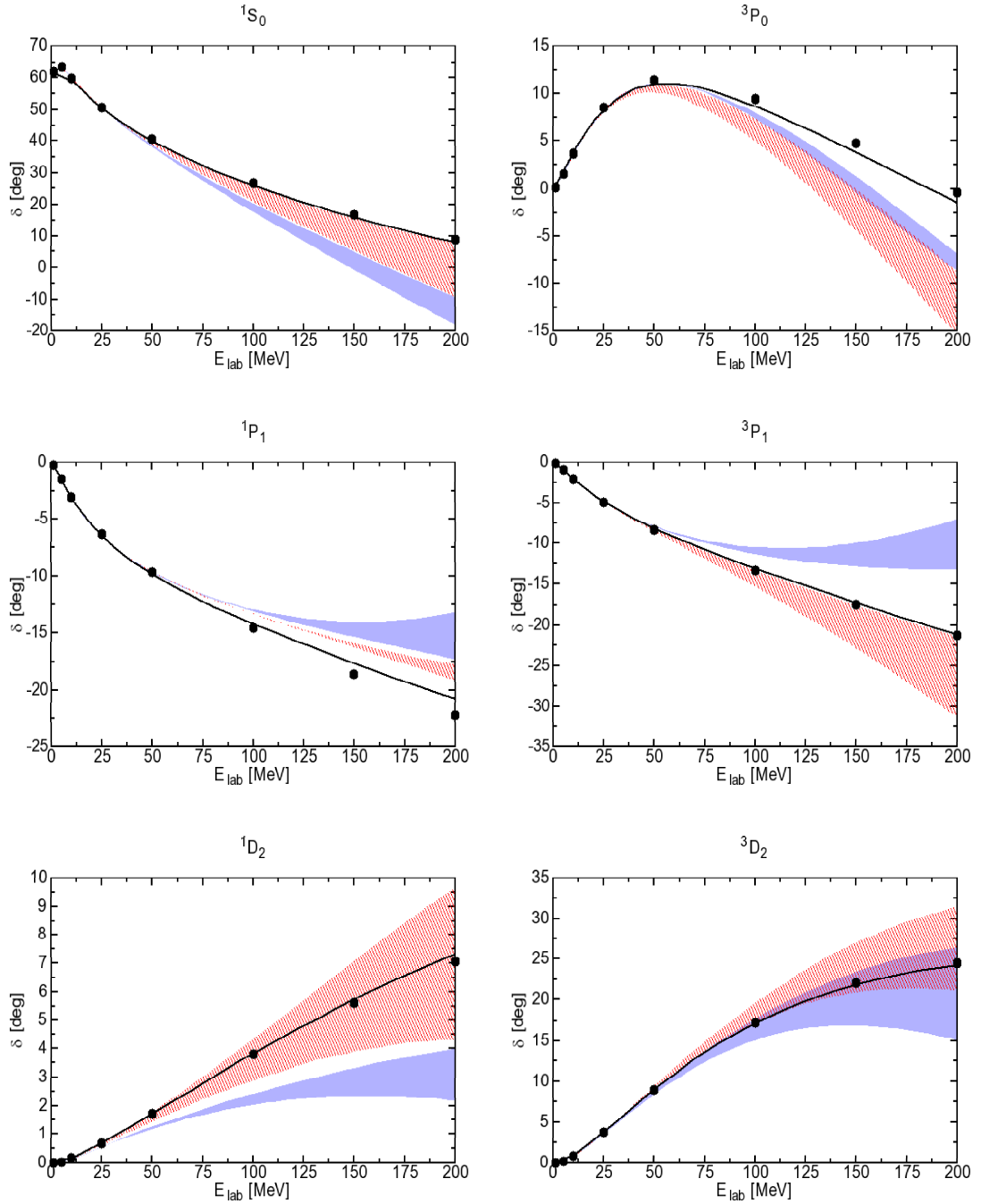


Figure B.7: Neutron-proton phase shifts for energies below 200 MeV and partial waves with total angular momentum $J \leq 2$. The solid line show the phase shift predicted by the AV18 potential. The cut-offs is chosen according to Tables 2.2 and leading to the band. The red band displayed predictions for N2LO potential and the blue band represents NLO potential. Solid dots represent the Nijmegen multienergy np phase shift analysis [153].

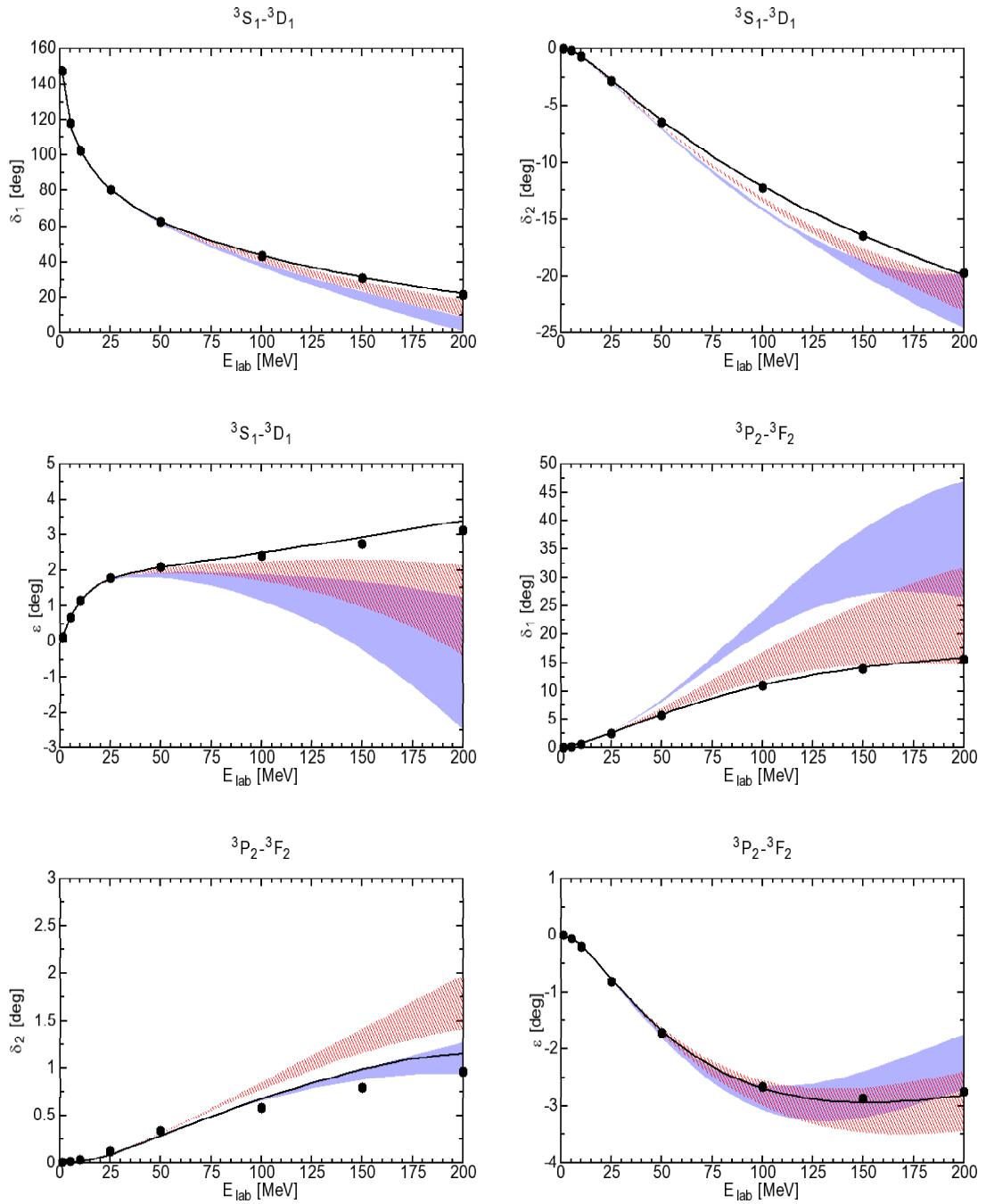


Figure B.8: Neutron-proton phase shift and mixing parameters for laboratory energies below 200 MeV and partial waves with total angular momentum $j \leq 2$. The solid line show the phase shift predicted by the AV18 potential. The cut-off values are chosen according to Tables 2.2. The blue band displays NLO predictions and the red band represents N2LO results. Solid dots represent the Nijmegen multienergy np phase shift analysis [153].

Appendix C

Symbolic algebra calculation of the nuclear matrix elements

Below we show an example of the *Mathematica* script which we use for generating integrals in the partial-wave decomposition of the two-nucleon current matrix elements. This particular case is prepared for the well known leading one-pion-exchange contribution, which consists of the "seagull" and "pion-in-flight" terms.

After first 16 lines, where we define the notation and give information about the particular part of the two-nucleon current operator in the spin-isospin space, we start with the redefinition of the way we will invoke the Clebsch-Gordan coefficients (lines 18–22). Next we define explicitly the 2×2 unit matrix and the standard Pauli matrices σ_i , $i = 1, 2, 3$ and prepare the spherical components σ_{+1} and σ_{-1} . Further we introduce the fractional momentum transfers \vec{k}_1 and \vec{k}_2 and their spherical components $(k_1)_{+1}$, $(k_1)_{-1}$, $(k_2)_{+1}$ and $(k_2)_{-1}$. It is then very straightforward, using standard *Mathematica* commands, to calculate the dot products like

$$\vec{\sigma} \cdot \vec{k}_i \tag{C.1}$$

and prepare two dimensional vectors

$$a \equiv \begin{pmatrix} 1 \\ 0 \end{pmatrix} \quad \text{and} \quad b \equiv \begin{pmatrix} 0 \\ 1 \end{pmatrix}, \tag{C.2}$$

which are used to represent the one-nucleon spin (and isospin) states $| \frac{1}{2}m \rangle$ for $m = \pm \frac{1}{2}$. (The null vector c is introduced in order to simplify the following summations and has no physical meaning.)

The following part of the script is most important. Here we prepare the two-nucleon spin (and isospin) states as well as the spin OS and isospin T operators specific for the considered two-nucleon operator. We use a very convenient idea of the Kronecker product, which is predefined in *Mathematica*. In this example, using obvious abbreviations,

$$\begin{aligned} OS &= v_\pi(k_1) \vec{\sigma}_1 \cdot \vec{k}_1 (\sigma_2)_{+1} - v_\pi(k_2) (\sigma_1)_{+1} \vec{\sigma}_2 \cdot \vec{k}_2 \\ &\quad + v(k_1, k_2) ((k_1)_{+1} - (k_2)_{+1}) \vec{\sigma}_1 \cdot \vec{k}_1 \vec{\sigma}_2 \cdot \vec{k}_2, \end{aligned} \tag{C.3}$$

$$T = i (\vec{\tau}_1 \times \vec{\tau}_2)_z . \quad (C.4)$$

It is then clear that going to another spin-isospin structure requires only simple changes in very few lines of the script. The quantity H corresponds exactly to the integrand in Equation (4.53). Note that the spherical harmonics ($Y_{l'm'_l}(\hat{p}')$ and $Y_{lm_l}(\hat{p})$) and other quantities will be calculated only in the main Fortran code. In the remaining parts of the script we define the (primed) basis states $|p'\alpha'_2\rangle$ and the two (unprimed) deuteron states with the isospin $t = 0$.

Finally, we write down to an output file the code of all nonzero integrands, which appear in the matrix elements of the two-nucleon current operator

$$\langle p'\alpha'_2(\mu') | J_{+1} | p\alpha_2(\mu) \rangle \quad (C.5)$$

for all possible $(\alpha_2, \mu, \alpha'_2)$ combinations, where μ is the projection of the total angular momentum in the initial state and $\mu' = \mu + 1$. The results are output in the so-called "Fortran form" which guarantees that our method is indeed simple and safe. The similar approach was used in the calculations of the two-nucleon and three-nucleon potential matrix elements [67].

Example of the *Mathematica* script:

```
(* < p'(l's')j'mu't'mt'|j_ + |p(ls)jmutmt >
```

one pion exchange : Seagull term

```
j = (vpi(k1)sigma1.k1sigma2 - vpi(k2)sigma2.k2sigma1) * i(tau1 x tau2)_z
```

one pion exchange : Pion – in – flight term

```
j = (k1 - k2)sigma1.k1sigma2.k2(vpi(k2) - vpi(k1))/(k1^2 - k2^2) * i(tau1 x tau2)_z
= (k1 - k2)sigma1.k1sigma2.k2(vpi(k1) * vpi(k2)) * i(tau1 x tau2)_z
```

```
vpi1 = 1/(mpi^2 + k1^2)
```

```
vpi2 = 1/(mpi^2 + k2^2)
```

```
v12 = 1/((mpi^2 + k1^2) * (mpi^2 + k2^2))
```

```
k1 = -p + p' + Q/2
```

```
k2 = p - p' + Q/2 *)
```

(*“corrected”Clebsch – Gordan coefficients are defined*)

```
myClebschGordan[j1_, j2_, j3_, m1_, m2_, m3_]:=
```

```
If[(Abs[m1] ≤ j1)&&(Abs[m2] ≤ j2)&&(Abs[m3] ≤ j3)&&(m1 + m2 == m3)
```

```
&&(j1 + j2 ≥ j3)&&(Abs[j1 - j2] ≤ j3), ClebschGordan[{j1, m1}, {j2, m2}, {j3, m3}], 0];
```

```
Um = Array[U, {2, 2}];
```

```
U[1, 1] = 1;
U[1, 2] = 0;
U[2, 1] = 0;
U[2, 2] = 1;
```

```
Sigma1m = Array[Sigma1, {2, 2}];
Sigma2m = Array[Sigma2, {2, 2}];
Sigma3m = Array[Sigma3, {2, 2}];
```

```
Sigma1[1, 1] = 0;
Sigma1[1, 2] = 1;
Sigma1[2, 1] = 1;
Sigma1[2, 2] = 0;
```

```
Sigma2[1, 1] = 0;
Sigma2[1, 2] = -I;
Sigma2[2, 1] = I;
Sigma2[2, 2] = 0;
```

```
Sigmam = {Sigma1m, Sigma2m, Sigma3m};
Sigmaplusm = -1/Sqrt[2] * (Sigma1m + I * Sigma2m);
Sigmaminusm = 1/Sqrt[2] * (Sigma1m - I * Sigma2m);
```

```
K1m = Array[K1, 3];
```

```
K1M = K1m.Sigmam;
```

```
K2m = Array[K2, 3];
```

```
K2M = K2m.Sigmam;
```

```
K1plus = -1/Sqrt[2] * (K1m[[1]] + I * K1m[[2]]);
```

```
K2plus = -1/Sqrt[2] * (K2m[[1]] + I * K2m[[2]]);
```

```
K1minus = 1/Sqrt[2] * (K1m[[1]] - I * K1m[[2]]);
```

```
K2minus = 1/Sqrt[2] * (K2m[[1]] - I * K2m[[2]]);
```

```
a1m = Array[a1, 2];
```

```
a1[1] = 1;
```

```
a1[2] = 0;
```

```
b1m = Array[b1, 2];
```

```
b1[1] = 0;
```

```
b1[2] = 1;
```

```
c1m = Array[c1, 2];
```

```
c1[1] = 0;
```

```
spin2N[s_, ms_]:=ArrayFlatten[Sum[myClebschGordan[1/2, 1/2, s, m1, ms - m1, ms]*KroneckerProduct[w[[-m1 + 3/2]], w[[-ms + m1 + 3/2]]], {m1, -1/2, 1/2, 1}], 1];
```

```

T = Simplify[I * (KroneckerProduct[Sigmam[[1]], Sigmam[[2]]]-
KroneckerProduct[Sigmam[[2]], Sigmam[[1]]])];

OS = Simplify[vpi1 * KroneckerProduct[K1M, SigmaPlusm-
vpi2 * KroneckerProduct[SigmaPlusm, K2M]+
v12 * (K1plus - K2plus) * KroneckerProduct[K1M, K2M]];

H[pp_, lp_, sp_, jp_, mup_, tp_, mtp_, p_, l_, s_, j_, mu_, t_, mt_]:= 
(spin2N[tp, mtp].T.spin2N[t, mt]) * Sum[myClebschGordan[l, s, j, ml, mu - ml, mu]* 
myClebschGordan[lp, sp, jp, mlp, mup - mlp, mup]* 
(spin2N[sp, mup - mlp].OS.spin2N[s, mu - ml])* 
CONJGYLM[lp, mlp, ithpp, iphpp] * YLM[l, ml, ithp, iphp], {ml, -l, l, 1}, {mlp, -lp, lp, 1}];

lm1 = Array[lm, 2];
sm1 = Array[sm, 2];
jm1 = Array[jm, 2];
tm1 = Array[tm, 2];
lm[1] = 0;
sm[1] = 1;
jm[1] = 1;
tm[1] = 0;
lm[2] = 2;
sm[2] = 1;
jm[2] = 1;
tm[2] = 0;
nindex2 = 2;
JMAX = 10;

lm2 = Array[lpm, 100];
sm2 = Array[spm, 100];
jm2 = Array[jpm, 100];
tm2 = Array[tpm, 100];

nindex2p = 0;
Do[{Do[{Do[{itp = ((-1)^(lp + isp) + 1)/2;
nindex2p = nindex2p + 1;
lpm[nindex2p] = lp;
spm[nindex2p] = isp;
jpm[nindex2p] = jp;
tpm[nindex2p] = itp; }, {lp, Abs[jp - isp], jp + isp, 1}]; }, {isp, 0, 1, 1}]; }, {jp, 0, JMAX, 1}];

```

```

out = OpenWrite["J1pi_eff_1i2.v9.gauss.KroneckerProduct.nb.output",
FormatType → FortranForm, PageWidth → 64];
Write[out, "nindex2= ", nindex2];
Do[{l = lm[ial];
s = sm[ial];
j = jm[ial];
t = tm[ial];
Write[out, " ial= ", ial, " l,s,j,t= ", l, ", ", s, ", ", j, ", ", t]; }, {ial, 1, nindex2, 1}];

Write[out, "  ];
Write[out, "  ];

Write[out, "nindex2p= ", nindex2p];
Do[{lp = lpm[ialp];
sp = spm[ialp];
jp = jpm[ialp];
tp = tpm[ialp];
Write[out, " ialp= ", ialp, " lp,sp,jp,tp= ", lp, ", ", sp, ", ", jp, ", ", tp]; }, {ialp, 1, nindex2p, 1}];

Write[out, "  ];
Write[out, "  ];
(*Only non - zero cases are considered*)IALPNONZEROm = Array[IALPNONZERO, 500];
IALNONZEROm = Array[IALNONZERO, 500];
MUNONZEROm = Array[MUNONZERO, 500];

counter = 0;
Do[{lp = lpm[ialp];
sp = spm[ialp];
jp = jpm[ialp];
tp = tpm[ialp];
Do[{l = lm[ial];
s = sm[ial];
j = jm[ial];
t = tm[ial];
Do[{me1 = H[pp, lp, sp, jp, mu + 1, tp, 0, p, l, s, j, mu, t, 0];
me2 = Simplify[me1];
If[me2 == 0, {counter = counter; }, {counter = counter + 1;
IALPNONZERO[counter] = ialp;
IALNONZERO[counter] = ial;
MUNONZERO[counter] = mu;
Write[out, " ME(", counter, ")= ", me2];
Write[out, " SME(", counter, ")= SME(", counter, ") + ME(", counter, ")"];
Write[out, "  ];
Write[out, "  ]; }, {counter = counter + 1;

```

```
IALPNONZERO[counter] = ialp;
IALNONZERO[counter] = ial;
MUNONZERO[counter] = mu;
Write[out, " ME(", counter, ")= ", me2];
Write[out, " SME(", counter, ")= SME(", counter, ") + ME(", counter, ")"];
Write[out, " "];
Write[out, " "];
{mu, -j, j}]; }, {ial, 1, nindex2, 1}]; }, {ialp, 1, nindex2p, 1}];
Write[out, " "];
Write[out, " "];
Write[out, " counter= ", counter];
Do[{Write[out, " IALPNONZERO(", ic, ")= ", IALPNONZERO[ic]];
Write[out, " IALNONZERO(", ic, ")= ", IALNONZERO[ic]];
Write[out, " MUNONZERO(", ic, ")= ", MUNONZERO[ic]]; }, {ic, 1, counter}];
Close[out];
```

Appendix D

Low energy constants C'_1 and d_9 – estimation procedure

As it was already mentioned in previous chapters, two low energy constants in the new part of the 2N current operator have to be established by a fit to the experimental data. These are C'_1 and d_9 parameters. Here we try to find the estimation of their values with the elastic electron scattering on deuterons. In the elastic scattering, the observables depend only on the deuteron wave function. We performed the calculation with N2LO wave functions.

The best estimates for the two parameters C'_1 , d_9 were obtained by minimizing the quantity

$$\chi^2(C'_1, d_9) = \sum_{Q_i=1}^n \left(\frac{D_1(Q_i, C'_1, d_9) - D_{1;exp}(Q_i)}{\Delta D_{1;exp}(Q_i)} \right)^2 + \sum_{Q_i=1}^n \left(\frac{D_2(Q_i, C'_1, d_9) - D_{2;exp}(Q_i)}{\Delta D_{2;exp}(Q_i)} \right)^2 \quad (\text{D.1})$$

where Q_i indicates the selected photon momentum Q . D_1 represents the structure function A and D_2 – differential cross section. The experimental data are from Ref. [84]. These observables have been selected because of a very good accuracy of the measurement.

The LECs depend on the choice of the regularization parameter Λ , therefore, we obtain five pairs of values (C'_1, d_9) depending on the regularization used as listed in Table 2.2. The fit results are summarized in Table D.1. Contour plots of χ^2 surfaces for three calculations with the cut-off pairs N2LO-1, N2LO-2 and N2LO-3 are shown in Figure D.1. The calculations with N2LO-4 and N2LO-5 give practically the same results as N2LO-1 and N2LO-2, respectively. One can observe that the values of the two constants are highly correlated as evidenced by straight valleys in the χ^2 surfaces. Moreover, the values of χ^2 in the valley are very large which means that the calculations poorly describe the experimental data. Although the new current components improve the description, the theory seems to be incomplete yet.

Having in mind that for elastic electron scattering on deuteron we have included all parts of the current operator that appear at NLO, this result suggests that, in order to improve the description, one has to consider higher-order currents (e.g. N2LO).

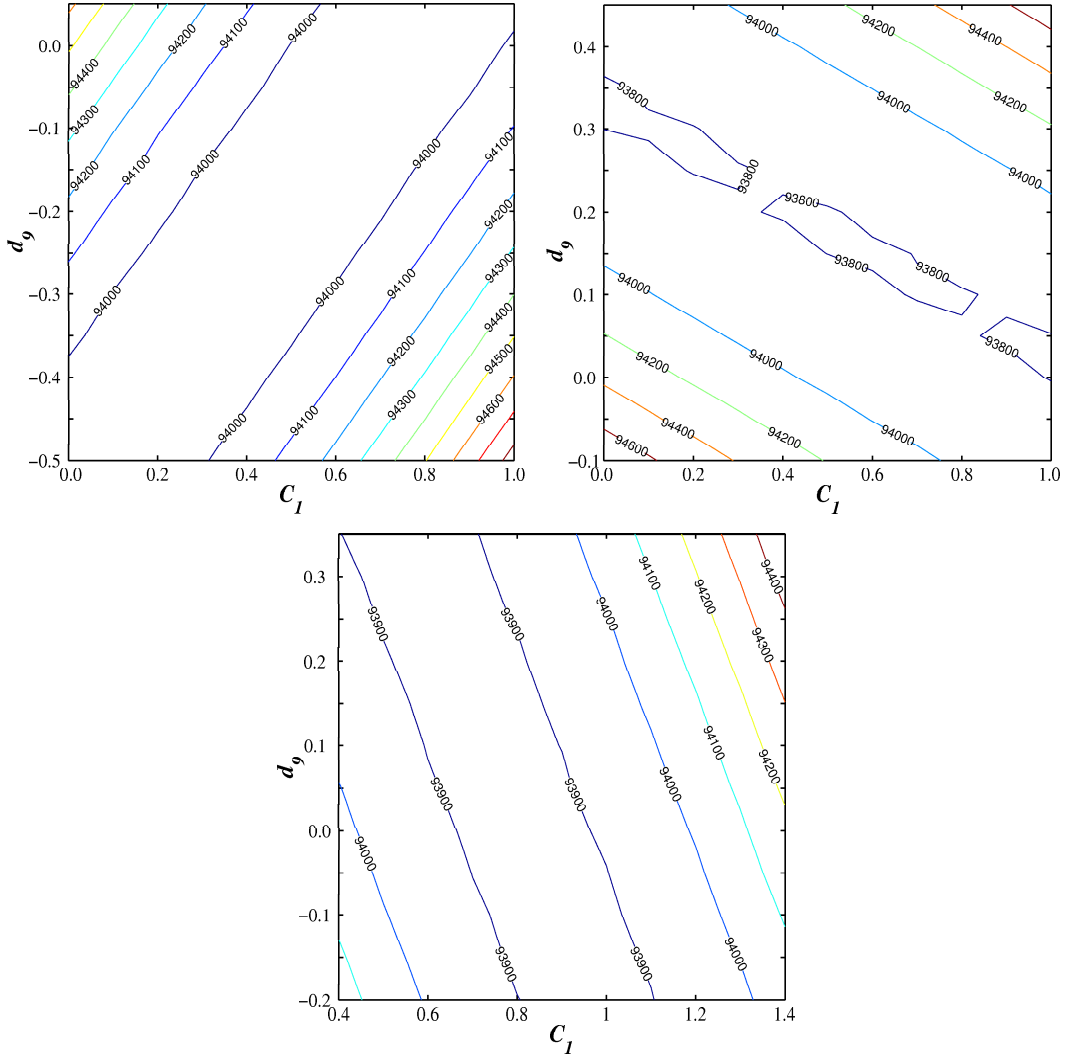


Figure D.1: Contour plots of χ^2 surfaces for first three pairs of cut-off parameters $(\Lambda, \tilde{\Lambda})$ listed in Table D.1, respectively.

Table D.1: N2LO cut-off values as listed in Table 2.2 together with optimal values of the LEC parameters C'_1 and d_9 obtained from fit to the experimental data. Note that C'_1 and d_9 are strongly correlated so one of them was arbitrarily chosen.

V-CUT	Λ [MeV]	$\tilde{\Lambda}$ [MeV]	C'_1 [fm] $^{-4}$	d_9 [fm] $^{-2}$
N2LO-1	450	500	+0.500	+0.210
N2LO-2	600	500	+0.900	-0.045
N2LO-3	550	600	+0.200	-0.195
N2LO-4	450	700	+0.500	+0.210
N2LO-5	600	700	+0.900	-0.045

Bibliography

- [1] S. Weinberg, Physica **A96**, 327 (1979).
- [2] S. Weinberg, Phys. Lett. **B251**, 288 (1990).
- [3] S. Weinberg, Nucl. Phys. **B363**, 3 (1991).
- [4] C. Ordonez, L. Ray, U. van Kolck, Phys. Rev. **C53**, 2086-2105 (1996).
- [5] J. L. Friar and S. A. Coon, Phys. Rev. **C49**, 1272 (1994).
- [6] N. Kaiser, R. Brockmann and W. Weise, Nucl. Phys. **A625**, 758 (1997).
- [7] E. Epelbaum, W. Glöckle and U.-G. Meißner, Nucl. Phys. **A637**, 107 (1998).
- [8] E. Epelbaum, W. Glöckle and U.-G. Meißner, Nucl. Phys. **A671**, 295 (2000).
- [9] E. Epelbaum, U.-G. Meißner and W. Glöckle, Nucl. Phys. **A714**, 535 (2003).
- [10] E. Epelbaum, *et al.*, Nucl. Phys. **A689**, 111-118 (2001).
- [11] E. Epelbaum, *et al.*, Phys. Rev. Lett. **86**, 4787-4790 (2001).
- [12] E. Epelbaum, A. Nogga, W. Glöckle, H. Kamada, Ulf-G. Meißner, H. Witała, Phys. Rev. **C66**, 064001 (2002).
- [13] E. Epelbaum, Eur. Phys. J. **A34**, 197 (2007).
- [14] S. R. Beane, V. Bernard, E. Epelbaum, *et al.*, Nucl.Phys. **A720**, 399-415 (2003).
- [15] T. S. Park, D. P. Min and M. Rho, Phys. Rept. **233**, 341 (1993).
- [16] T. S. Park, D. P. Min and M. Rho, Nucl. Phys. **A596**, 515 (1996).
- [17] Y. H. Song, R. Lazauskas, T. S. Park and D. P. Min, Phys. Lett. **B656**, 174 (2007).
- [18] R. Lazauskas, Y. H. Song and T. S. Park, arXiv:0905.3119 [nucl-th].
- [19] Y. H. Song, R. Lazauskas and T.-S. Park, Phys. Rev. **C79**, 064002 (2009).
- [20] T. S. Park, K. Kubodera, D. P. Min and M. Rho, Phys. Lett. **B472**, 232 (2000).
- [21] T. S. Park, K. Kubodera, D. P. Min and M. Rho, Astrophys. J. **507**, 443 (1998).
- [22] T. S. Park *et al.*, arXiv: nucl-th/0107012.
- [23] S. Ando, T. S. Park, K. Kubodera and F. Myhrer, Phys. Lett. **B533**, 25 (2002).
- [24] T. S. Park *et al.*, Phys. Rev. **C67**, 055206 (2003).
- [25] K. Kubodera and T. S. Park, Ann. Rev. Nucl. Part. Sci. **54**, 19 (2004).

- [26] D. R. Phillips and T. D. Cohen, Nucl. Phys. **A668**, 45 (2000).
- [27] M. Walzl and U.-G. Meißner, Phys. Lett. **B513**, 37 (2001).
- [28] D. R. Phillips, Phys. Lett. **B567**, 12 (2003).
- [29] D. R. Phillips, J. Phys. **G34**, 365 (2007).
- [30] M. P. Valderrama, A. Nogga, E. Ruiz Arriola and D. R. Phillips, Eur. Phys. J. **A36**, 315 (2008).
- [31] S. R. Beane, M. Malheiro, J. A. McGovern, *et al.*, Nucl. Phys. **A747**, 311 (2005).
- [32] D. Choudhury and D. R. Phillips, Phys. Rev. **C71**, 044002 (2005).
- [33] D. Shukla, A. Nogga and D. R. Phillips, Nucl. Phys. **A819**, 98 (2009).
- [34] S. R. Beane, V. Bernard, T. S. H. Lee, U.-G. H. Meißner and U. van Kolck, Nucl. Phys. A **618**, 381 (1997).
- [35] V. Bernard, H. Krebs and U.-G. Meißner, Phys. Rev. **C61**, 058201 (2000).
- [36] H. Krebs, V. Bernard and U.-G. Meißner, Nucl. Phys. **A713**, 405 (2003).
- [37] H. Krebs, V. Bernard and U.-G. Meißner, Eur. Phys. J. **A22**, 503 (2004).
- [38] A. Gardestig and D. R. Phillips, Phys. Rev **C73**, 014002 (2006).
- [39] V. Lensky *et al.*, Eur. Phys. J. **A33**, 339-348 (2007).
- [40] S. Pastore, R. Schiavilla and J. L. Goity, Phys. Rev. **C78**, 064002 (2008).
- [41] S. Pastore, L. Girlanda, R. Schiavilla, M. Viviani and R. B. Wiringa, Phys. Rev. **C80**, 034004 (2009).
- [42] S. Kölling, E. Epelbaum, H. Krebs, Ulf-G. Meißner, Phys. Rev. **C80**, 045502 (2009).
- [43] E. Epelbaum, Prog. Part. Nucl. Phys. **57**, 654 (2006).
- [44] S. Kölling, private communication.
- [45] R. B. Wiringa, V. G. J. Stoks, R. Schiavilla, Phys. Rev. **C51**, 38 (1995).
- [46] D. O. Riska, Phys. Scr. **31**, 107 (1985).
- [47] D. O. Riska, Phys. Scr. **31**, 471 (1985).
- [48] R. Schiavilla, V.R. Pandharipande, D.O. Riska, Phys. Rev. **C40**, 2294 (1989).
- [49] Wolfram Research, Inc., *Mathematica*©, Version 7.0 (Wolfram Research, Inc., Champaign, 2008).
- [50] E. Epelbaum, H.-W. Hammer, Ulf-G. Meißner, Rev. Mod. Phys. **81**, 1773 (2009).
- [51] E. Epelbaum, W. Glöckle, Ulf-G. Meißner, Nucl. Phys. **A747**, 362 (2005).
- [52] E. Epelbaum, private communication.
- [53] J. Carlson, R. Schiavilla, Rev. Mod. Phys. **70**, 743 (1998) and references therein.
- [54] J. Golak *et al.*, Phys. Rept. **415**, 89-205 (2005) and references therein.

- [55] J. Arrington, C. D. Roberts, J.M. Zanotti, *J. Phys.* **G34**, S23-S52 (2007).
- [56] J. Jourdan, *Nucl. Phys.* **A721**, 395c (2003).
- [57] H. Schmieden, *Nucl. Phys.* **A737**, 147 (2004).
- [58] Kees de Jager, *Eur. Phys. J.* **A191**, s01267 (2004).
- [59] L. L. Foldy and J. A. Lock, in M. Rho, D. Wilkinson, *Mesons In Nuclei*, Vol.II, Amsterdam 1979, 465-493.
- [60] M. Gari and H. Hyuga, *Z. Phys.* **A277**, 291 (1976).
- [61] J. Golak, H. Kamada, H. Witala *et al.*, *Phys. Rev.* **C62**, 054005 (2000).
- [62] D. Rozpedzik, J. Golak, *CPC(HEP & NP)* **34**, 9 (2010).
- [63] L. Girlanda, S. Pastore, R. Schavilla, and M. Viviani, *nucl-th:/0912.2753v1* (2009).
- [64] W. Glöckle, Ch. Elster, J. Golak, R. Skibinski, H. Witala, H.K amada, *Few Body Syst.* **47**, 25-38 (2010).
- [65] A. R. Edmonds, *Angular Momentum in Quantum Mechanics*, Princeton University Press 1960.
- [66] V. V. Kotlyar, H. Kamada, W. Glöckle, J. Golak, *Few-Body Systems* **28**, 35 (2000).
- [67] J. Golak, D. Rozpedzik, R. Skibinski *et al.*, *Eur. Phys. J.* **A43**, 2 (2010).
- [68] E. Guth, *Phys. Rev.* **68**, 279–280 (1945).
- [69] M. E. Rose *Elementary Theory of Angular Momentum*, Dover Publication 1995.
- [70] L. I. Schiff *et al.*, *Phys. Rev. Lett.* **11**, 387 (1963).
- [71] L. R. B. Elton and Daphne F. Jackson, *Phys. Rev.* **155**, 1070–1072 (1967).
- [72] T. deForest, J. D. Walecka, *Adv. Phys.* **15**, 1 (1966).
- [73] C. J. Horowitz, B. D. Serot, *Nucl. Phys.* **A368**, 503 (1981).
- [74] J. Carlson and R. Schiavilla *Rev. Mod. Phys.* **70**, 743 (1998).
- [75] R. Gilman *et al.*, *J. Phys G* **28**, R37-R116 (2002).
- [76] M. Garcon *et al.*, *Phys. Rev C5*, 49 (1994).
- [77] H. Arenhövel, W. Leidemann, E. L. Tomusiak, *Eur. Phys. J.* **A23**, 147-190 (2005).
- [78] M. Garcon, W. Van Orden. *Adv. Nucl. Phys.* **26**, 293 (2001).
- [79] J. D. Bjorken and S. D. Drell, *Relativistic Quantum Mechanics*, McGraw-Hill Book. Company, New York (1964).
- [80] T. W. Donnelly and A. S. Raskin, *Ann. Phys.* **169**, 247 (1986).
- [81] M. Walzl and U. G. Meißner. *Phys. Lett.* **B513**, 37 (2001).
- [82] M. N. Rosenbluth, *Phys. Rev.* **79**, 615-619 (1950).
- [83] R. W. Berard, *et al.*, *Phys. Lett.* **B47**, 355 (1973).

- [84] G. G. Simon, *et al.*, Nucl. Phys. **A364**, 285 (1981).
- [85] S. Platchkov, *et al.*, Nucl. Phys. **A510**, 740 (1990).
- [86] D. Benaksas, *et al.*, Phys. Rev. **148**, 1327 (1966).
- [87] I. Sick and D. Trautmann, Phys. Lett. **B375**, 16 (1996); Nucl. Phys. **A637**, 559 (1998).
- [88] D. Abbott, *et al.*, Eur. Phys. J **A7**, 421 (2000).
- [89] L. C. Alexa, *et al.*, Phys. Rev. Lett. **82**, 1374 (1999).
- [90] D. Abbott, *et al.*, Phys. Rev. Lett. **82**, 1379 (1999).
- [91] R. Cramer, *et al.*, Z. Phys. **C29** 513 (1985).
- [92] R. Machleidt, K. Holinde, and C. Elster, Phys. Rep. **149**, 1 (1987).
- [93] E. E. Salpeter and H. A. Bethe, Phys. Rev. **84**, 1232 (1951), J. W. van Orden, N. Devine, and F. Gross, Phys. Rev. Lett. **75**, 4369 (1995), J. Carbonell, B. Desplanques, V. A. Karmanov, and J.-F. Mathiot, Phys. Rep. **300**, 215 (1998).
- [94] E. Lomon et al., Ann. Phys. **125**, 309 (1980).
- [95] E. Witten, Nucl. Phys. **B223**, 422 (1983).
- [96] E. Nyman and D. O. Riska, Nucl. Phys. **A468**, 473 (1987).
- [97] C. D. Buchanan and R. Yearian, Phys. Rev. Lett. **15**, 303 (1965).
- [98] J. Goldemberg and C. Schaerf, Phys. Rev. Lett. **12**, 298 (1964).
- [99] B. Grossette, D. Drickey, and P. Lehmann, Phys. Rev. **141**, 1425 (1966).
- [100] E. C. Jones, W. L. Bendel, L. W. Fagg and R A Lindgren, Phys. Rev. **C21** 1162 (1980).
- [101] G. Ohlsen, Rep. Prog. Phys. **35**, 717 (1972).
- [102] G. G. Ohlsen, Nucl. Instr. Meth. **37**, 240 (1965).
- [103] W. Glöckle, H. Witała, D. Hüber *et al.*, Phys. Rept. **274**, 107 (1996).
- [104] D. M. Bishop, L. M. Cheung, Phys. Rev. **C20**, 381 (1979).
- [105] I. Lindgren. In: K. Siegbahn, Editor, Alpha Beta, and Gamma-Ray Spectroscopy 2, North-Holland, Amsterdam (1965).
- [106] D. Schildknecht, Phys. Lett **10**, 254 (1964), Z. Phys. **185**, 382 (1965).
- [107] R. G. Arnold, C. Carlson and F. Gross Phys. Rev. **C223**, 363 (1981).
- [108] T-S H. Lee, Few Body Syst. Sup. **6**, 526 (1992).
- [109] A. Arriaga, R. Schiavilla, Phys. Rev. **C76**, 014007 (2007).
- [110] H. Arenhövel, W. Leidemann, E. L. Tomusiak, Phys. Rev. **C46**, 455-470 (1992).
- [111] H. Arenhövel, W. Leidemann, E. L. Tomusiak, Few Body Syst. **15**, 109-127 (1993).

- [112] H. Arenhövel, W. Leidemann, E. L. Tomusiak, Phys. Rev. **C52**, 1232 (1995).
- [113] H. Arenhövel, W. Leidemann, E. L. Tomusiak, Nucl. Phys. **A641**, 517-527 (1998).
- [114] H. Arenhövel, W. Leidemann, E. L. Tomusiak, Few Body Syst. **28**, 147-188 (2000).
- [115] H. Arenhövel, W. Leidemann, E. L. Tomusiak, Eur. Phys. J. **A14**, 491-509 (2002).
- [116] W. Fabian and H. Arenhövel, Nucl. Phys. **A314**, 253-286, (1979).
- [117] A. Buchmann, W. Leidemann, H. Arenhövel, Nucl. Phys. **A443**, 726 (1985).
- [118] K.-M. Schmitt, H Arenhövel , Few Body Syst. **11**, 33-72 (1991).
- [119] K.-M. Schmitt, P. Wilhelm, H Arenhövel , Few Body Syst. **10**, 105-133, (1991).
- [120] R. Gilman F. Gross Journal Phys G: Nucl Particle Physics **28**, R37 (2002).
- [121] H. Arenhövel, M. Sanzone, "Photodisintegration of the deuteron" in Few-Body Systems Suppl. **3**, 1 (1991).
- [122] Shuqian Ying, E. M. Henley, and G. A. Miller, Phys. Rev. **C38**, 1584-1600 (1988).
- [123] I. A. Racheck *et al.*, Phys. Rev. Lett. **98**, 182303 (2007).
- [124] T. S. Suzuki *et al.*, Astrophys. J. Lett. 439, L59 (1995).
- [125] Y. Nagai, T. S. Suzuki, T. Kikuchi, T. Shima, T. Kii, H. Sato, and M. Igashira, Phys. Rev. C 56, 3173 (1997).
- [126] K. Y. Hara *et al.*, Phys. Rev. D 68, 072001 (2003).
- [127] R. Moreh, T. J. Kennett, and W. V. Prestwich, Phys. Rev. **C39**, 1247 (1989).
- [128] G. Rupak, Nucl. Phys. **A678**, 405 (2000).
- [129] S. Nakamura, T. Sato, V. Gudkov, and K. Kubodera, Phys. Rev. bf C63, 034617 (2001); S. Nakamura *et al.*, Nucl. Phys. **A707**, 561 (2002).
- [130] G. M. Hale (private communication); A. S. Johnson and G. M. Hale, Nucl. Phys. **A688**, 566 (2001).
- [131] S. Ando *et al.*, Phys. Rev. **C74**, 025809 (2006).
- [132] S. Ando and C. H. Hyun, Phys. Rev. **C72**, 014008 (2005).
- [133] G. Xu, S. F. Pate, C. Bloch, *et al.*, Phys. Rev. **C52**, 6 (1995).
- [134] H. Kamada, W. Glöckle, J. Golak, Nuovo Cimento **A105**, 1425(1992).
- [135] S. Ishikawa, H. Kamada, W. Glöckle *et al.*, Nuovo Cimento **A107**, 305(1994).
- [136] S. Ishikawa, H. Kamada, W. Glöckle *et al.*, Phys. Lett **B339**, 293 (1994).
- [137] J. Golak, H. Kamada, W. Glöckle and S. Ishikawa, Phys. Rev. **C51**, 1638 (1995).
- [138] J. Golak, H. Witala, H. Kamada, *et al.*, Phys Rev. **C52**, 1216 (1995)
- [139] H. Witala and W. Glöckle, Eur. Phys. J. **A37** (2008) 87
- [140] H. Collard, R. Hofstadter, E. B. Hughes, A. Johansson, M. R. Yearian, R. B. Day, R. T. Wagner, Phys Rev. **B57**, 38 (1965).

- [141] H. Kamada, W. Glöckle, J. Golak, Nuovo Cimento **105A**, 1435 (1992).
- [142] R. Skibinski, J. Golak, H. Witala *et al.*, Acta Phys. Polon. **B37**, 2905-2918 (2006).
- [143] R. Skibinski, J. Golak, H. Witala, *et al.*, Phys. Rev. **C72**, 044002 (2005).
- [144] R. Skibinski, J. Golak, H. Witala, *et al.*, Phys. Rev. **C67**, 054002 (2003).
- [145] V. Bernard, E. Epelbaum, H. Krebs, Ulf-G. Meißner, Phys. Rev. **C77**, 064004 (2008).
- [146] E. Epelbaum, Phys. Lett. **B639**, 456 (2006).
- [147] W. Leidemann, E. L. Tomusiak, Eur. Phys. J. **A23**, 147 (2005).
- [148] H. Arenhövel, M. Sanzone, Photodisintegration of the deuteron, in Few-Body Systems Suppl. 3 (1991) 1.
- [149] W. Press *et al.*, Numerical Recipes (CUP, 2007).
- [150] LAPACK – The Linear Algebra PACKage; <http://www.netlib.org/lapack/index.html>
- [151] H. P. Stapp, T. J. Ypsilantis, N. Metropolis, Phys. Rev. **105**, 302 (1957).
- [152] R. Machleidt, Nucl. Phys. **A790**, 17, (2007)
- [153] V. G. J. Stoks *et al.*, Phys. Rev. **C48**, 792 (1993).

Acknowledgements

My adventure with ChEFT started a few years ago thanks to Professor W. Glöckle, who turned my scientific interests into this direction. Today, I would like sincerely thank him for that. My supervisor, Dr. habil. J. Golak, has helped me in pursuing these interests. I would like to thank him for introducing me into the field of few-nucleon interactions and electromagnetic currents. Thank you for trust and care during the studies.

Besides, it is my great pleasure to acknowledge the scientific collaboration with Professor E. Epelbaum and Msc Stefan Kölling. Without their kind collaboration on the TPE currents this thesis would not have been completed. Thank you for suggestions, discussion and feeding me with your preliminary results. Stefan, thank you for bringing the TPE currents to the form of numerically stable expressions.

I would also like to express my appreciation to Professor K. Bodek for important suggestions and remarks which influenced the final shape of this thesis.

During this few years, I had a chance to present my results on international conferences which would not be possible without the financial support from Professor B. Kamys, Head of Nuclear Physics Division of the Institute of Physics. Thank you for understanding, support and providing me with comfortable conditions for work and scientific development.

I want to express my gratitude to Professor H. Witała for giving me the opportunity to work in his group and Dr. R. Skibiński for the explanation of the dynamics of 3N interactions.

I am not going to make a list of my colleagues and friends, because I do not want to miss anyone. Therefore, I would like to express my thanks to all of you from the Institute of Physics, Jagiellonian University, and from different corners of Poland who helped and supported me in any way. I could always count on you.

Last but not least, I would like to thank my family for the love, having faith in me and unceasing support during the whole period of study.

This thesis was supported by the Polish Ministry of Science and Higher Education under Project No. 1045/B/H03/2009/36.

Dagmara Rozpedzik